2026 | Faculty of Sciences

Doctoral dissertation submitted to obtain the degree of
Doctor of Sciences: Physics, to be defended by

Fernando Francisco Silva Filho

DOCTORAL DISSERTATION

Optimization and phase transitions in stochastic thermodynamics: from singular engines to collective effects

Promoters: Prof. Dr Carlos E. Fiore dos Santos | University of São Paulo
Prof. Dr Bart Cleuren | UHasselt

2026 | Faculty of Sciences

Doctoral dissertation submitted to obtain the degree of
Doctor of Sciences: Physics, to be defended by

Fernando Francisco Silva Filho

DOCTORAL DISSERTATION

Optimization and phase transitions in stochastic thermodynamics: from singular engines to collective effects

Promoters: Prof. Dr Carlos E. Fiore dos Santos | University of São Paulo
Prof. Dr Bart Cleuren | UHasselt

D/2026/2451/9

The PhD researcher and the UHasselt supervisor hereby formally declare that the research conducted for the purpose of this PhD thesis was executed in accordance with the principles of good scientific conduct, as stipulated in the UHasselt Integrity charter, the UHasselt charter supervisor – PhD Researcher, the UHasselt Integrity Policy and the UHasselt guidelines for the use of (generative) AI in research.

The author asserts that this PhD thesis is made Open Access immediately upon submission. The full text is publicly available without restrictions.

Dedicatory

To My wife, Dalila.

Acknowledgements

As John Donne famously wrote, no single person is an island but a part of the whole. There is no human goal reached by an individual himself, but rather through collective effort. Under the realm of such a philosophy, it is my pleasure and honor to acknowledge everyone who contributed to the successful completion of this thesis.

First and foremost, I thank my wife Dalila. We went through really hard times, but also fantastic moments that I will never forget. We spent the best of our time together even when the Atlantic Ocean was separated us during some of my research travels. She always showed me simple solutions in the moments of despair, told me to cry when I was sad and convinced me to celebrate every small achievement, even when I did not consider those goals important. I am grateful for her support during the time when I was absent and during weekends devoted to work and study.

My parents, who invested in my education and supported my studies, always believing in my initiatives. After finishing my bachelor's degree, I was convinced that I should give up from a research career. It was my mom who convinced me to keep trying and to give it at least another shot. As a result, here I am, finishing something I did not expect to finish when I was younger.

My advisor, Fiore, who taught me valuable lessons in research, writing, publications and professional conduct. He also provided financial during difficult times, for which I will always be grateful. I also thank my advisor Bart Cleuren, who accepted me into his research group at UHasselt and supported me during my stay in Hasselt. I also thank Thomas Speck, who accepted me to work as a visiting researcher in ITP4 (Stuttgart University). I am very grateful for the recommendation letters that the three of you wrote for me.

I thank all my collaborators, Gustavo Forão, Pedro Paraguassú, Carlos Noa, Bart Wijns, Daniel Busiello, André Vieira and Bruno Akasaki. You guys are great researchers and I learned a lot from you.

I thank all the employees from the Postgraduate Committee (CPG) of IFUSP and also the staff from PhD administration of UHasselt, for their technical and administrative support during my stay at both universities.

I acknowledge National Council for Scientific and Technological Development (CNPq) for the financial support under the process 146224/2021-3. I also acknowledge CAPES for the financial support of my stay in Stuttgart University (Germany) through the CAPES-DAAD program. The double degree program was financed by Special Research Fund (BOF-BILA) of UHasselt (BOF23DOCBL14).

Abstract

The rapid progress of nanotechnology and of experimental techniques in fields such as biophysics, chemistry, and neuroscience has raised fundamental questions about thermodynamics on the small scale, where thermal fluctuations become unavoidable. Stochastic thermodynamics provides a theoretical framework to describe key energetic quantities such as work, heat, dissipation, and efficiency in such fluctuating small systems, offering insights into the operation of nanoscale engines found in both artificial and natural setups. This thesis investigates optimization strategies to enhance the performance of these engines by fine-tuning time-dependent driving protocols, modifying thermodynamic cycles, and exploring rare trajectory fluctuations in two representative models under the sequential (or collisional) approach: Brownian particles and quantum dot pumps, each interacting with two or more thermal reservoirs. Extending beyond single-unit systems, a thermal engine based on a set of interacting spins with up-down (Z_2) spontaneous symmetry breaking is introduced, exhibiting collective (ordered) and independent (disordered) phases governed by interaction strength and external biases. This model also reveals novel nonequilibrium phase transitions, including non-classical critical exponents in the mean-field limit and distinct transition points according to which phase dominates initially. Together, this study advances the understanding of the optimization of microscopic and collective energy flux conversion processes in nonequilibrium systems. In addition, it explores new phenomena in the realm of nonequilibrium phase transitions.

Keywords : thermodynamics, phase transitions, non-equilibrium phenomena, stochastic processes, thermal engines

Resumo

O rápido progresso da nanotecnologia e de métodos experimentais em áreas como biofísica, química e neurociência tem feito surgir questões fundamentais a respeito da termodinâmica em escalas pequenas. A termodinâmica estocástica fornece uma estrutura teórica para descrever quantidades energéticas fundamentais como trabalho, calor, dissipação e eficiência em sistemas pequenos com flutuações, contribuindo para o entendimento sobre a operação de máquinas térmicas em nanoescalas que são encontradas tanto em configurações artificiais quanto naturais. Esta tese investiga estratégias de otimização de desempenho dessas máquinas pelo ajuste fino de protocolos externos dependentes do tempo, modificando ciclos termodinâmicos e explorando trajetórias raras nas flutuações térmicas em dois modelos representativos na abordagem sequencial (ou colisional): partículas Brownianas e bombas de quantum dots, com cada um interagindo com dois ou mais reservatórios térmicos. Estendendo-se além de sistemas com uma única unidade, introduzimos uma máquina térmica baseada em um conjunto de spins interagentes com quebra espontânea de simetria de dois estados (Z_2), exibindo uma fase coletiva (ordenada) e uma fase independente (desordenada) governadas pela intensidade das interações entre os spins e os vieses externos. Este modelo também revela um novo tipo de transição de fase, incluindo expoentes críticos não clássicos no limite do campo médio e pontos distintos de transição de acordo com qual fase inicialmente domina a dinâmica. Juntos, esses estudos avançam o entendimento da otimização de processos de conversão energética em sistemas microscópicos e coletivos. Adicionalmente, exploram novos fenômenos no âmbito das transições de fase fora do equilíbrio.

Palavras-chave: termodinâmica, transições de fase, fenômenos de não equilíbrio, processos estocásticos, máquinas térmicas

Contents

Chapter 1

Introduction

Thermodynamics is successful in explaining the relationship between heat and work and how these fluxes are converted and transformed in terms of macroscopic variables. The link between these macroscopic quantities and the particles that compose the system is provided by statistical mechanics, which uses probability theory and statistical methods as a fundamental framework to describe large sets of particles in thermodynamic equilibrium. However, nature is abundant in systems that are far from equilibrium due to the exchange of fluxes with subsystems or with the environment, which are not described by classical equilibrium statistical mechanics and therefore require an alternative approach.

Each technological breakthrough is related to the development of thermodynamics in some way. Starting from the invention of the steam engine in the first industrial revolution, which is directly linked to the study of fundamental aspects of heat engines and the Carnot efficiency [1], passing through the development of nuclear energy production in the 20th century and the first preliminary results on finite-time optimization [2,3], the advent of telecommunications and information theory, which rewrote the interpretation of entropy [4,5], and the development of deep learning and generative diffusion models that use

nonequilibrium methods developed by Jarzynski [6] to compute backward probability distributions in order to generate artificial images and videos (each day more surprisingly realistic) from Gaussian noise [7]. In particular, the advent and novelty of nanotechnology and the advanced experimental methods incorporated in fields such as biological cell physiology, physical chemistry, neuroscience, the origins and evolution of life, and other areas have introduced questions about thermodynamics in small-scale systems [8,9].

At such scales, fluctuations due to the thermal environment are unavoidable, making it necessary to develop an alternative theoretical approach different from traditional equilibrium statistical mechanics in order to obtain a more precise description. Stochastic thermodynamics is a contemporary area of statistical mechanics that incorporates nonequilibrium thermodynamics elements to describe quantities such as dissipation, energy, and transport fluxes in the microscopic realm under the influence of thermal fluctuations, which can radically change the state of microscopic units. Stochastic thermodynamics defines thermodynamic quantities at the level of single units by associating them with transitions between microstates and by introducing trajectory-based definitions of quantities such as work and heat at each each step. In the thermodynamic limit, for a large number of units, these definitions recover the standard macroscopic expressions. The microstate transitions themselves are specified according to a chosen level of description, for instance through a coarse-grained representation based on discrete Markovian dynamics. This description is developed through the use of fluctuation theorems [8], thermodynamic uncertainty relations (TURs) [10], and entropy production (EP), a key nonequilibrium concept that estimates heat dissipation and is associated with the energetic compensation that occurs when a transition violates detailed balance. Since its mean value is non-negative and vanishes only at equilibrium, EP is an important quantity that characterizes not only the nonequilibrium regime but also its irreversibility.

In addition to fluctuations, small-scale systems can be subject to external deterministic forces that drive the system far from equilibrium. In a particular case where these forces are periodic or constant, the system reaches a nonequilibrium steady state (NESS) in the long-time limit, where all thermody-

namic quantities are constant on average. There are two important dynamical approaches that capture these features. Using a Langevin equation, we describe the motion of a particle as the sum of a deterministic force and a random noise, which is suitable for describing Brownian motion. The probability distribution of the particle in phase space is a solution of a Fokker–Planck equation, which has the Boltzmann–Gibbs distribution as a particular (equilibrium) solution. On the other hand, an approach based on master equations considers a coarse-grained modeling of stochastic discrete jumps of a microscopic unit among known states (describing, for example, electric currents through a quantum dot), which also admits the equilibrium distribution as a particular solution. From both approaches, it is possible to obtain analytically (or numerically) all key thermodynamic quantities. Both approaches are successful in describing nanoscale engines that compose natural and artificial setups, such as molecular motors, Brownian ratchets, and thermal engines based on nanoscale particle pumps, among others [11]. In contrast to their macroscopic counterparts, small-scale engines are not composed of moving parts such as pistons moved by fluid expansions. Instead, they are realized through changes in probability currents induced by external forces applied directly to individual units or by particle fluxes between occupation states connected to reservoirs.

Despite the reliability of these nanoscale devices in converting one form of energy into another in various scenarios, they can operate rather inefficiently depending on how they are designed. Hence the importance of developing strategies to enhance their performance. In this thesis, we explore several optimization routes by considering different parameters, such as fine-tuning time-dependent external drives, introducing different strokes in sequential models, and exploring fluctuations of rare events in the context of single trajectories for two relevant setups: Brownian particles and quantum-dot pumps. In both cases, we employ the collisional (or sequential) approach, which consists of sequentially placing the system in contact with distinct and uncorrelated thermal baths, subject to different external drivings and, in the quantum-dot case, different occupation energies. The switches between reservoirs are assumed to be instantaneous, resulting in adiabatic transitions between baths. The Brownian case involves a single particle interacting with one reservoir, with distinct external forces applied at each stage. In this setup, the system operates only

as a work-to-work converter, transforming one form of work into another over the cycle while dissipating heat into the reservoirs. We show how to improve its performance by fine-tuning the external drives, obtaining analytical expressions for the optimized quantities in terms of Onsager coefficients in the linear regime. In the quantum-dot pump, the system is described by a nonequilibrium multistage model that interacts with several thermal environments, each characterized by a distinct occupation energy. Although the system can also function as a work-to-work converter, our main focus is on the heat engine regime, where a heat flux is converted into external work with unavoidable dissipation. In this context, we reveal the nontrivial relationship between the number of stages, thermodynamic currents, chemical potentials of the reservoirs, and the engine performance.

Both previous cases are examples of engines composed of a single unit interacting with two or more reservoirs. However, nature is abundant in complex systems composed of many interacting entities, in which cooperative effects often play a crucial role. Examples span multiple biological scales, from microbes [12] to the human brain [13], and have been studied in a broad range of research fields, from nonequilibrium effects in chemical processes [14–16] to synchronization in biological networks [17–21]. This vast spectrum of applications highlights that the demand for implementable and robust optimal strategies to engineer collective engines is both important and timely. In the quantum realm, the interplay between collective effects and system performance has been extensively studied [22–26], although the development of classical setups built from interacting units is comparatively much less known and still remains at a preliminary stage [27–32]. In order to fill this gap and explore a simple yet robust classical example of a cooperative setup, we introduce a nonequilibrium collective engine composed of a system of spins interacting as described by the Ising model [33]. The system consists of N spins that interact simultaneously with two reservoirs, which also impose biased external forces that individually "rotate" each spin according to its state. This system exhibits two phases: a collective (ordered) phase, in which spins are macroscopic aligned, and an independent (disordered) phase, where the state is completely random and the total magnetization vanishes. In the latter state, the system operates only as a dud or a pump. On the other hand, the collective phase displays an engine

regime within a region where the system remains strongly ordered. In addition, the introduction of these nonequilibrium ingredients into the spin system gives rise to unique phenomena without any analog in traditional equilibrium or nonequilibrium phase transitions. The uniqueness lies in several features that will be further discussed throughout this work, such as the order–disorder phase transition occurring at different points, with different orders, depending on which ordered phase initially dominates.

This thesis is organized as follows: In Chapter 2, we introduce the basic concepts of nonequilibrium thermodynamics, also exploring the engine regime and discussing essential aspects of optimization, such as efficiency at maximum power, the Curzon–Ahlborn efficiency, and others. In Chapter 3, we introduce stochastic thermodynamics, taking as examples three fundamental setups that compose this research: Brownian particles described by Langevin equations, two-level systems described by master equations, and spin models with order–disorder phase transitions (Z_2 symmetry). In Chapter 4, we apply the theoretical framework to study optimization routes for power and efficiency of a Brownian particle in a collisional setup under time-dependent drivings. Chapter 5 is dedicated to the nonequilibrium spin system, describing the optimization of output performance in the presence of a nonequilibrium phase transition and a collective phase. We also analyze nonequilibrium phase transitions for different configurations and interactions. Finally, in Chapter 6, we study a new strategy involving the introduction of different strokes in a collisional quantum-dot pump in order to improve its performance.

Chapter 2

Introduction to Nonequilibrium Thermodynamics

Systems driven by ”forces” that ”remove” the system from equilibrium constitute the majority of observed phenomena in nature, appearing in fields such as biology [34, 35], chemistry [36], materials science [37–39], quantum systems [30], and even in artificial intelligence and diffusion models [40, 41]. In contrast to traditional equilibrium thermodynamics, its nonequilibrium counterpart lacks a general theory, and a rigorous derivation of its fundamental principles is still incomplete. Although nonequilibrium thermodynamics (and stochastic thermodynamics in particular) does not yet have a closed theoretical framework as well established as equilibrium thermodynamics, it has attracted considerable attention by partially filling this gap. In this chapter, we approach nonequilibrium thermodynamics as an extension and adaptation of the equilibrium theory: we examine an extension of the second law of thermodynamics to nonequilibrium regimes and its role in describing the dynamics and thermodynamic properties of such systems.

2.1 Entropy Production

The thermodynamic equilibrium of an isolated system is determined by the principle of maximum entropy [42]. Consider an isolated system $A + B$ composed of two subsystems, A and B. Due to the extensivity of entropy, we write $S_T = S_{A+B} = S_A + S_B$. Any change in the total entropy of the system can be expressed as $\Delta S_T = \Delta S_A + \Delta S_B$. Since the total entropy evolves toward its maximum value at equilibrium, we always have $\Delta S_T \geq 0$. For subsystem A (or B), we can write

$$\Delta S_A = \Delta S_T - \Delta S_B. \tag{2.1.1}$$

An important particular case is a system composed of a subsystem that interacts with a reservoir R much larger than the subsystem itself. Let A denote the subsystem and $B \gg A$ the reservoir R. Here, for a fixed energy U, the equilibrium state is reached by maximizing the entropy S, which characterizes equilibrium through a fundamental relation $S = S(\{V_k\})$ [43,44], with $\{V_k\}$ the set of extensible variables of the system and $U \in \{V_k\}$. However, when thermodynamic fluxes induced by one or several reservoirs drive the system out of equilibrium, this static description is no longer appropriate and one must adopt a dynamical viewpoint in which the internal energy and the entropy become time-dependent quantities, $U = U(t)$ and $S = S(t)$. We first start by defining $\Delta S_B = \Delta S_R = \frac{\Delta Q_R}{T}$, and Eq.(2.1.1) becomes

$$\Delta S = \Delta S_i - \Delta S_R, \tag{2.1.2}$$

where ΔS is the entropy change of the subsystem, and $\Delta S_i := \Delta S_T$ is what we call the entropy production, a non-negative quantity, $\Delta S_i \geq 0$ [45] that is related by the thermal interaction between A and B (the subscript i stands for "internal"). The entropy production vanishes only when the system reaches equilibrium (or undergoes a reversible process). From Eq.(2.1.2) we conclude that the total entropy change of the subsystem is given by the sum of an external contribution, $-\Delta S_R$, and an internal contribution ΔS_i that is "produced" by the irreversible nature of the system's dynamics.

As we already discussed, the entropy of the system is a function of time in the dynamics of a nonequilibrium process. Returning to the general case of the

total system $A+B$, let $\{V_k^{(A)}\}$ and $\{V_k^{(B)}\}$ be the sets of extensive variables (e.g., volume) of the subsystems A and B. These extensive variables also evolve in time, but their dynamics occur in such a way that the overall system remains isolated, implying $V_k^{(A)} + V_k^{(B)} =$ constant at any instant, and consequently

$$dV_k^{(A)} + dV_k^{(B)} = 0. \tag{2.1.3}$$

The differentials of the entropies S_A and S_B are given by

$$dS_A = \sum_k \frac{\partial S_A}{\partial V_k^{(A)}}\, dV_k^{(A)}; \qquad dS_B = \sum_k \frac{\partial S_B}{\partial V_k^{(B)}}\, dV_k^{(B)}, \tag{2.1.4}$$

where each partial derivative $\frac{\partial S_\alpha}{\partial V_k^{(\alpha)}}$ corresponds to an intensive variable of subsystem $\alpha \in \{A, B\}$, in accordance with the Gibbs relations [44]. For example, if $V_k^{(\alpha)}$ is the volume, then $\frac{\partial S_\alpha}{\partial V_k^\alpha} = \frac{P_\alpha}{T_\alpha}$, where P_α is the pressure and T_α the temperature of subsystem α.

From Eq.(2.1.2), the total entropy variation dS_i (the entropy production) can be written as

$$dS_i = \sum_k \left(\frac{\partial S_A}{\partial V_k^{(A)}}\, dV_k^{(A)} + \frac{\partial S_B}{\partial V_k^{(B)}}\, dV_k^{(B)} \right), \tag{2.1.5}$$

and using Eq.(2.1.3), we obtain

$$dS_i = \sum_k \left(\frac{\partial S_A}{\partial V_k^{(A)}} - \frac{\partial S_B}{\partial V_k^{(B)}} \right) dV_k^{(A)} = \sum_k f_k\, dV_k^{(A)}, \tag{2.1.6}$$

where f_k is defined as a thermodynamic force (sometimes called "affinity" in the literature). Outside the equilibrium regime, we assume that the entropy of the system is time-dependent, so we can write

$$\dot{S}_i = \sum_k f_k J_k, \tag{2.1.7}$$

where $J_k = \dot{V}_k^{(A)} = -\dot{V}_k^{(B)}$ is a thermodynamic flux (or current).

Let us return to the reservoir case, where A is a subsystem interacting with a reservoir $B = R$, much larger than A. Rewriting Eq.(2.1.2), we note that $dS_R = dQ_R/T_R$ is the entropy change of the reservoir, and dQ_R is the (inexact) differential of the heat exchanged between the system and the reservoir. Thus, $\dot{Q}_R$ denotes the heat flux entering (or leaving) the system through the reservoir.

We define $\phi = \dot{S}_R = \dot{Q}_R/T$ as the entropy flux. The entropy production is then $\sigma = \dot{S}_i$, and we write

$$\dot{S} = \sigma - \phi. \tag{2.1.8}$$

The entropy production σ is an important quantity in the study of nonequilibrium phenomena. Its non-negativity, $\sigma \geq 0$, represents a generalization of the second law of thermodynamics to nonequilibrium systems [45]. Moreover, under constant or periodically driven forces (which, as we shall see later, are related to the thermodynamic forces f_k), the system reaches a nonequilibrium steady state where $\dot{S} = 0$. In this case, the entropy production equals the rate of heat dissipation, and we have

$$\sigma = \phi. \tag{2.1.9}$$

2.2 Engine Regime

We now turn our attention to the main topic of this thesis: the engine regime and different routes for its optimization. Engines are thermodynamic cycles that convert one form of energy into another. Here, we examine two main examples of such devices: the heat engine and the work-to-work converter. The former transforms a heat flux into useful work, while the latter converts one form of work into another. Both types of engines unavoidably waste heat in the form of dissipation, as required by the second law of thermodynamics. In general, engine setups must involve at least two reservoirs: one for the input heat or work and another to absorb the dissipated heat. In fact, such transformations may be inefficient, or may not even occur, depending on the physical conditions imposed on the cycle, highlighting the importance of identifying optimization routes to overcome inefficiency and improve performance. Briefly, the quantities of interest are the maximization of power output and efficiency, and the minimization of heat dissipation (which is related to the entropy production in the nonequilibrium steady state). However, simultaneous optimization of these quantities is typically hindered by trade-off relations. In general, one must sacrifice power output in order to improve efficiency. The most famous example is the Carnot engine itself, for which the power output vanishes because a reversible (quasi-static) process requires the engine period

to tend to infinity. This trade-off is also present in nanoscale engine setups and has attracted significant interest, as described by various thermodynamic uncertainty relations (TURs) [46, 47].

When the system is close enough of the equilibrium state, the linear regime can be applied and these relations are straightforwardly expressed in an analytical form. From now on, we consider the simplest engine setup, involving two reservoirs. (In Chap.(6), we will study a special case with more than two reservoirs). We now rewrite Eq.(2.1.7) for reservoirs 1 and 2:

$$\sigma = f_1 J_1 + f_2 J_2 = \sigma_1 + \sigma_2, \tag{2.2.1}$$

where J_i are the thermodynamic fluxes associated with reservoir $i \in \{1, 2\}$. The engine regime occurs when one flux, say J_1 with $\sigma_1 = J_1 f_1 > 0$, drives the system against an opposing force and flux, such that $\sigma_2 = J_2 f_2 < 0$. The intuition behind this definition is best understood through the classical example of a heat engine [44], where input heat expands a working fluid against a mechanical resistance, for instance, a weighted piston. We define the efficiency η as the ratio

$$\eta = -\frac{\sigma_2}{\sigma_1}, \tag{2.2.2}$$

with the power output given by $\langle \mathcal{P} \rangle = -\sigma_2 \geq 0$.

Before proceeding with the optimization within a linear description, we must first define the conditions under which the system operates as an engine, i.e., what are the conditions for the input σ_1 to be transformed into the output σ_2. Our analysis will focus on the nonequilibrium steady state (NESS). As discussed in Sec.(2), this particular state is reached when periodic (or constant) forces act on the system for a long time, and its state functions (S and U) become constant ($\dot{S} = \dot{U} = 0$). In this case, according to Eq.(2.1.8), we always have $\sigma = \phi$. Since ϕ represents the entropy flux arising from the system–reservoir interaction, it can be expressed in a Clausius-like form:

$$\sigma = \frac{\dot{Q}_1}{T_1} + \frac{\dot{Q}_2}{T_2}, \tag{2.2.3}$$

and using the first law of thermodynamics,

$$\dot{Q}_1 + \dot{Q}_2 = -\dot{W}, \tag{2.2.4}$$

where $\dot{W}$ is the work flux (power) extracted from the thermodynamic cycle. Equation (2.2.1) then becomes

$$\sigma = \left(\frac{1}{T_2} - \frac{1}{T_1}\right)\dot{Q}_2 - \frac{\dot{W}}{T_1}. \tag{2.2.5}$$

Defining $T = (T_1 + T_2)/2$ as the mean temperature and $\Delta T = T_2 - T_1$ as the temperature difference between reservoirs 1 and 2, we can rewrite Eq.(2.2.5) as

$$\sigma = \frac{4T^2}{4T^2 - \Delta T^2}\left[(\dot{Q}_1 - \dot{Q}_2) - \frac{\dot{W}}{T}\right], \tag{2.2.6}$$

which is a general expression valid for both heat engines and work-to-work converters.

For a system to operate as an engine, certain criteria must be satisfied. For a heat engine, we define the efficiency as

$$\eta = -\frac{\dot{W}}{\dot{Q}_{\text{in}}}, \tag{2.2.7}$$

where $\dot{W} > 0$ is the extracted work and $\dot{Q}_{\text{in}} > 0$ is the heat input, which may come from reservoir 1 or 2 depending on their temperatures. According to the second law of thermodynamics, the efficiency of a heat engine is bounded by that of a Carnot engine [1, 44], i.e., $0 < \eta \leq \eta_C$, where $\eta = \eta_C$ corresponds to the reversible limit. Equivalently, we may write $0 < \hat{\eta} \leq 1$, with $\hat{\eta} = \eta/\eta_C$.

For a work-to-work converter, each reservoir imposes an external force, and the total work flux is written as $\dot{W} = \dot{W}_1 + \dot{W}_2$, with $\dot{W}_{\text{in}}$ and $\dot{W}_{\text{out}}$ denoting the input and output work fluxes, respectively. The efficiency of a work-to-work converter is given by

$$\eta = -\frac{\dot{W}_{\text{out}}}{\dot{W}_{\text{in}} + \dot{Q}_{\text{in}}}, \tag{2.2.8}$$

where the conditions $\dot{Q}_{\text{in}} \leq 0$ and $\dot{W}_{\text{out}} > 0$ must be satisfied for the system to operate as an engine. As will be discussed in more detail in Chap.(4), the best-case scenario for this type of engine occurs when there is no heat input, i.e., when $T_1 = T_2$ and consequently $\dot{Q}_{\text{in}} = 0$. Under these conditions, a reversible regime (global maximum efficiency) can be achieved depending on the physical setup. In this case, the efficiency is bounded by $0 \leq \eta \leq 1$.

2.2.1 Linear Thermodynamics and Onsager Coefficients

Consider the system–reservoir interaction described in Sec.(2.1). For each nonzero thermodynamic force f_k, there is an associated nonzero flux J_k. In other words, a set of different affinities $\{f_j\}$ gives rise to a set of fluxes $\{J_k\}$ that are generally not independent; rather, each flux depends on all affinities, i.e., $J_k = J_k(\{f_j\})$ [48]. An example of such coupling occurs in thermoelectric effects, such as the Peltier effect, where a temperature difference induces a voltage [49]. In particular, at equilibrium, all affinities vanish, and consequently $J_k(\{f_j\}) = 0$ for all k. For affinities sufficiently close to zero, we can expand J_k around $f_k = 0$ (for all k) and write

$$J_k = \sum_n L_{kn} f_n, \tag{2.2.9}$$

where L_{kn} are the Onsager coefficients [48]. Using Eq.(2.1.7), we obtain

$$\sigma = \sum_n f_n J_n = \sum_m \sum_n L_{mn} f_n f_m \geq 0. \tag{2.2.10}$$

From this expression we conclude that the entropy production assumes a non-negative bilinear form, also known as non-negative quadratic form [50]. An especial form is obtained when one considers the case with two affinities f_1 and f_2,

$$J_1 = L_{11} f_1 + L_{12} f_2, \tag{2.2.11}$$

$$J_2 = L_{21} f_1 + L_{22} f_2, \tag{2.2.12}$$

with a entropy production given by

$$\sigma = L_{11} f_1^2 + L_{22} f_2^2 + (L_{12} + L_{21}) f_1 f_2. \tag{2.2.13}$$

There are some conditions that the coefficients L_{ij} must obey to garantee that $\sigma \geq 0$,

$$\begin{cases} L_{11} > 0, L_{22} > 0, \\ 4L_{11}L_{22} - (L_{12} + L_{21})^2 \geq 0. \end{cases} \tag{2.2.14}$$

In the constant forces case, Onsager shown that there is an equality between the coefficients (the Onsager reciprocity relation) [48],

$$L_{12} = L_{21}. \tag{2.2.15}$$

On the other hand, in the case of some periodic or time-dependent forces the conditiond expressed by Eq.(2.2.15) can not be valid and if this is the case, this relation is undo by another weaker one, $L_{21} = \tilde{L}_{12}$ where $\sim$ corresponds to a symmetry in relation to a temporal inversion [51]. In the Chap. (4), we show the non-vality of the Eq.(2.2.15) for some examples of external drivings.

According to Eq.(2.2.13), we can write

$$\sigma_1 = J_1 f_1 = L_{11} f_1^2 + L_{12} f_1 f_2, \tag{2.2.16}$$

and

$$\sigma_2 = J_2 f_2 = L_{22} f_2^2 + L_{21} f_1 f_2, \tag{2.2.17}$$

and the efficiency in Eq.(2.2.2) becomes

$$\eta = -\frac{L_{22} f_2^2 + L_{21} f_1 f_2}{L_{11} f_1^2 + L_{12} f_1 f_2}, \tag{2.2.18}$$

with σ_2 representing the output.

The linear expressions for the power and efficiency lead to straightforward relations when we impose maximization conditions. A method adopted throughout this thesis is to fix one thermodynamic force, f_1, and manipulate the other in order to find a value for f_2 that offers the best output. Before exploiting the optimization of the output performance, we start by searching for criteria for the engine regime itself, finding an interval for values of f_2 in which the system transforms the input into useful power output for a fixed value of f_1. In general, the engine regime will operate while $\sigma_2 \geq 0$, and according to Eq.(2.2.17), the output σ_2 has two zeros: $f_2 = 0$ and $f_2 = -L_{21} f_1 / L_{22}$. Assuming that σ_2 is a concave curve within this interval, the system will work as an engine for the interval $0 < |f_2| \leq f_m$, with $f_m = -L_{21} f_1 / L_{22}$. We now establish the first relation between the engine regime and the entropy production, since the minimum value for Eq.(2.2.13) is given by the equation $\frac{d\sigma}{df_2}\Big|_{f_2 = f_{2mS}} = 0$, where f_{2mS} is the value of f_2 that minimizes the entropy production. Solving this equation we find the relation

$$f_{2mS} = f_m - \frac{(L_{12} - L_{21}) f_1}{2 L_{22}}. \tag{2.2.19}$$

When the Onsager reciprocity relation is verified ($L_{12} = L_{21}$), we have $f_m = f_{2mS}$.

Now we start to find a value of f_2 that maximizes the output quantities. In the linear description, we can simply impose $\frac{d\sigma}{df_2} = 0$ and $\frac{d\eta}{df_2} = 0$ to find the maximum power and efficiency, respectively. From the differentials of Eq.(2.2.17) and Eq.(2.2.18) with respect to f_2, we obtain

$$\frac{f_{2\mathsf{ME}}}{f_1} = \frac{L_{11}}{L_{12}}\left(\sqrt{1-\frac{L_{12}L_{21}}{L_{11}L_{22}}}-1\right), \tag{2.2.20}$$

$$\frac{f_{2\mathsf{MP}}}{f_1} = -\frac{1}{2}\frac{L_{12}}{L_{22}}, \tag{2.2.21}$$

where $f_{2\mathsf{ME}}$ and $f_{2\mathsf{MP}}$ are the values of f_2 that maximize the efficiency and power, respectively. The corresponding maximum values of efficiency and power, η_{ME} and $\mathcal{P}_{\mathsf{MP}}$, can be found by substituting Eqs.(2.2.20) and (2.2.21) into Eqs.(2.2.18) and (2.2.17):

$$\eta_{\mathsf{ME}} = -\frac{L_{21}}{L_{12}} + \frac{2L_{11}L_{22}}{L_{12}^2}\left(1-\sqrt{1-\frac{L_{21}L_{12}}{L_{11}L_{22}}}\right), \tag{2.2.22}$$

and

$$\mathcal{P} = \frac{L_{21}^2 f_1^2}{4L_{22}}. \tag{2.2.23}$$

We can also find two other optimized quantities known as the efficiency at maximum power and the power at maximum efficiency, respectively given by η_{MP} and $\mathcal{P}_{\mathsf{ME}}$,

$$\eta_{\mathsf{MP}} = \frac{L_{21}^2}{4L_{11}L_{22}-L_{21}L_{12}}, \tag{2.2.24}$$

$$\mathcal{P}_{\mathsf{ME}} = \frac{f_1^2 L_{11}}{L_{12}^2}\left(\sqrt{1-\frac{L_{12}L_{21}}{L_{11}L_{22}}}\left[L_{12}L_{21}+L_{11}L_{22}\left(\sqrt{1-\frac{L_{12}L_{21}}{L_{11}L_{22}}}\right)\right]\right). \tag{2.2.25}$$

The above results produce interesting relations between them when the Onsager relation $L_{12} = L_{21}$ is valid [52]. First, from direct manipulation of Eqs.(2.2.24), (2.2.25) and (2.2.25) we obtain:

$$\eta_{\mathsf{MP}} = \frac{\mathcal{P}_{\mathsf{MP}}}{2\mathcal{P}_{\mathsf{MP}}-\mathcal{P}_{\mathsf{ME}}}, \tag{2.2.26}$$

also, after some algebra from Eqs.(2.2.25) and (2.2.25) we also have that

$$\frac{\mathcal{P}_{\mathsf{ME}}}{\mathcal{P}_{\mathsf{MP}}} = 1-\eta_{\mathsf{ME}}^2. \tag{2.2.27}$$

By combining both equations above we also obtain

$$\eta_{\mathsf{MP}} = \frac{\eta_{\mathsf{ME}}}{1+\eta_{\mathsf{ME}}^2}. \tag{2.2.28}$$

The above relations and expressions are useful for systems close to equilibrium and have been broadly applied to several problems in the context of stochastic thermodynamics and general nonequilibrium phenomena [52–55]. In this thesis, we apply such equations, but we also perform analyses that go beyond these limits, approaching results for cases far from equilibrium.

2.2.2 Thermal engines and the Curzon-Albohrn efficiency

As stated before, the Carnot efficiency is a cornerstone of thermodynamics, being equivalent to its second law by stating that no engine can have an efficiency superior to that of Carnot's when operating between the same cold T_C and hot T_H temperatures:

$$\eta \leq \eta_{\mathsf{C}} = 1 - \frac{T_{\mathsf{C}}}{T_{\mathsf{H}}}, \tag{2.2.29}$$

This limit was introduced by the French engineer Sadi Carnot in 1824 [1] and corresponds to a reversible engine composed of two quasi-static adiabatic and two isothermal processes forming a thermodynamic cycle. Equation (2.2.29) does not depend on the nature, format, or type of cycle the engine operates on. However, any engine that reaches the reversible regime will have zero power output, since quasi-static processes take an infinite time to produce a finite amount of work.

A more realistic model for a thermal engine reaches a fast cycle limit, implying that the engine becomes more dissipative and its efficiency decreases. In this regime, it is possible to find an optimized (and finite) power output value. The study of engines under such conditions introduces the concept of "endoreversible engines": a part of the system operates reversibly, while the thermal interaction with the environment is accelerated and becomes irreversible. This idea was discovered and rediscovered several times in the history of thermodynamics. In 1929, Henri Reitlinger introduced an expression for the efficiency at maximum power based on a practical sketch of a heat engine driven by coal combustion [56], which presented his original formula as

$$\eta_{\mathsf{MP}} = \frac{\sqrt{T_1} - \sqrt{T_2}}{\sqrt{T_1}}, \tag{2.2.30}$$

with $T_1 > T_2$. About 30 years later, independently, the French physicist P. Chambadal [57] and the Soviet physicist I. Novikov [2] arrived at the same result as Reitlinger, motivated by the modeling of nuclear power plants. Two decades later, physicists F. Curzon and L. Ahlborn rediscovered Reitlinger's expression in their seminal work published in 1975 [58], which considered a speed-up of a Carnot engine (increasing its cycle velocity, making it irreversible, while keeping the interaction of the working fluid with the environment reversible). The so-called Curzon–Ahlborn (or Chambadal–Novikov) efficiency is given by

$$\eta_{\mathsf{CA}} = 1 - \sqrt{\frac{T_{\mathsf{C}}}{T_{\mathsf{H}}}}, \tag{2.2.31}$$

which is clearly equivalent to the original Eq.(2.2.30).

The derivation of the expression given by Eq.(2.2.31) will be presented in the following paragraphs. The main idea behind the procedure of Curzon and Ahlborn is to increase the useful power of a Carnot cycle by reducing the time allocated to each step of the cycle. However, if the cycle is too fast, the thermal interaction between the system and the reservoirs will not be sufficient to produce a substantial power output. Between the fast and slow time regimes, there exists an optimal time duration that maximizes the power output in a finite-time setting [58].

Let us consider T_1 and T_2 as the temperatures of the reservoirs, with $T_1 > T_2$, and T_{1S} and T_{2S} as the temperatures of the working fluid when in contact with reservoirs 1 and 2, respectively. Curzon and Ahlborn assume that the heat flux exchanged during each isothermal process is proportional to the temperature difference between the working fluid and the reservoir (Newtonian heat flux):

$$\langle \dot{Q}_1 \rangle = \alpha_1 (T_1 - T_{1S}), \tag{2.2.32}$$

$$\langle \dot{Q}_2 \rangle = \alpha_2 (T_{2S} - T_2), \tag{2.2.33}$$

where α_1 and α_2 are non-negative constants with units of energy per time per temperature. We define $\Delta T_1 = T_1 - T_{1S}$ and $\Delta T_2 = T_{2S} - T_2$, always satisfying $\Delta T_j > 0$, which implies $T_1 > T_{1S} > T_{2S} > T_2$; otherwise, the system would not exchange heat in a way that allows for a positive output. Some assumptions about the system–reservoir interaction must be made. First, the duration of each interaction must be short, since the goal is to speed up the Carnot cycle.

However, if this time is too short, the system will not have enough time to exchange heat properly. Additionally, it must be short enough to assume that T_{jS} remains constant throughout the process.

Since the working fluid and reservoirs interact cyclically over infinitely many cycles, we expect the system to reach a nonequilibrium steady state (NESS), making the following relation valid in this limit:

$$\langle \mathcal{P} \rangle = \langle \dot{Q}_1 \rangle - \langle \dot{Q}_2 \rangle, \tag{2.2.34}$$

where $\langle \mathcal{P} \rangle$ is the power output, which must be non-negative for the system to be producing useful work.

We now pause to discuss a cornerstone concept of the Curzon–Ahlborn work. The interaction between the working fluid and both reservoirs is irreversible. However, all processes inside the working fluid are reversible, as stated by the endoreversibility hypothesis. This assumption relies on the fact that the irreversible interaction between the working fluid and the reservoir is confined to their contact surface. Since the total system (working fluid plus reservoirs) is in a nonequilibrium steady state (NESS), it is reasonable to assume that the working fluid itself is also in a steady state. Because the working fluid is internally reversible, it does not produce entropy (which arises only at the interface between the subsystem and the reservoirs). According to Eq.(2.1.9), we have $\langle \phi \rangle = 0$ around a complete cycle, and thus

$$\frac{\dot{Q}_1}{T_{1S}} - \frac{\dot{Q}_2}{T_{2S}} = 0, \tag{2.2.35}$$

which means that the total entropy change during the cycle inside the working fluid is zero (reversible). Equation (2.2.35) is a direct consequence of the endoreversibility hypothesis. From it, we rewrite Eq.(2.2.34) as

$$\langle \mathcal{P} \rangle = \alpha_2 \Delta T_2 \left(\frac{T_1 - \Delta T_1}{T_2 + \Delta T_2} - 1 \right). \tag{2.2.36}$$

The efficiency of the engine is given by

$$\eta = \frac{\langle \mathcal{P} \rangle}{\langle \dot{Q}_1 \rangle} = 1 - \frac{\langle \dot{Q}_2 \rangle}{\langle \dot{Q}_1 \rangle} = 1 - \left(\frac{T_2 + \Delta T_2}{T_1 - \Delta T_1} \right). \tag{2.2.37}$$

We now recap the necessary conditions for the system to operate as an engine:

i The temperatures must satisfy $T_1 > T_{1S} > T_{2S} > T_2$ in order for the heat fluxes in Eqs.(2.2.32) and (2.2.33) to have the correct sign;

ii $\langle \mathcal{P} \rangle > 0$ and $0 < \eta < \eta_C$;

Physically, we expect $\mathcal{P} \geq 0$ to be a concave function, which implies that there is a maximum point between its zeros. The reason for this is that the engine regime, in which the system produces power while absorbing heat, is sensitive to extreme values of the temperature gradient or to the duration of the interactions along the cycle. It is always possible to find two values of these quantities for which the power vanishes before the system transitions to the pump or dud regime. For example, the power will be null if ΔT_1 and ΔT_2 are too close to zero, since this would imply that little heat is exchanged between the working fluid and the reservoirs. We also expect the power to vanish for large ΔT_1 and ΔT_2, because this would correspond to a long interaction time between the working fluid and the reservoirs, resulting in a slow and therefore a thermalized cycle. We therefore conclude that there exists a critical point ΔT_{2MP} at which $\mathcal{P}$ reaches its maximum value. To find it, we impose

$$\frac{\partial \mathcal{P}}{\partial \Delta T_2} = 0 \tag{2.2.38}$$

and solve for $\Delta T_2 = \Delta T_{2MP}$, which yields $\Delta T_{2MP} = \sqrt{T_1 T_2} - T_2$. Substituting this value into Eq.(2.2.37) and after some algebra, we obtain

$$\eta_{\mathrm{MP}} = 1 - \sqrt{\frac{T_2}{T_1}}, \tag{2.2.39}$$

which reproduces Eq.(2.2.31). This limit is not universal, unlike the Carnot efficiency bound. There are examples in the literature of efficiencies at maximum power exceeding the Curzon–Ahlborn efficiency [59, 60]. Nevertheless, this expression provides a good approximation for several real-world systems, as demonstrated in the original work by Curzon and Ahlborn themselves. Equation (2.2.39) can be rewritten as

$$\eta_{\mathrm{CA}} = 1 - \sqrt{1 - \eta_C}, \tag{2.2.40}$$

which can be expanded around $\eta_C = 0$ (i.e., $T_1 = T_2$):

$$\eta_{\mathrm{CA}} = \frac{1}{2}\eta_C + \frac{1}{4}\eta_C^2 + \frac{3}{8}\eta_C^3 + \cdots, \tag{2.2.41}$$

which reduces to the following expression when $T_1 \approx T_2$:

$$\eta_{\mathsf{CA}} \approx \frac{1}{2}\eta_{\mathsf{C}}. \tag{2.2.42}$$

When $T_2 << T_1$,

$$\eta_{\mathsf{CA}} \approx \eta_{\mathsf{C}}. \tag{2.2.43}$$

Macroscopic thermal engines are composed of moving parts, such as pistons moved by fluid expansions. This setup is not feasible at small scales and does not accurately describe nanoscale thermodynamic cycles. Instead, nanoscale engines are typically realized by applying external forces to individual particles or by driving particle fluxes between reservoirs. The description of such systems must take into account that, at this scale, fluctuations play a central role and cannot be avoided. In the next chapter, we introduce stochastic thermodynamics, which will be the main tool used to describe the thermodynamics of small, fluctuating systems.

Chapter 3

Introduction to Stochastic Thermodynamics

The main goal of macroscopic thermodynamics (whether in equilibrium or not) is to describe energy transformation and its dissipation in terms of macroscopic observables. Statistical mechanics has been successful in interpreting heat (and entropy) in terms of the statistical behavior of microscopic units in the thermodynamic limit. Although classical thermodynamics is traditionally formulated for macroscopic systems with many degrees of freedom, stochastic thermodynamics provides a consistent framework to define heat, work and entropy production for single-particle systems evolving under stochastic dynamics. These quantities fluctuate from trajectory to trajectory due to the thermal interaction, but their ensemble averages correspond to the macroscopic thermodynamic observables in the appropriate limits. Throughout this chapter, we shall present the fundamental aspects of stochastic dynamics and how to apply it to define thermodynamics quantities.

3.1 Introduction to Stochastic Processes

A stochastic process is defined briefly as a set of indexed random variables (in general, this indexation is related to time) with a well-defined probability distribution. Let $t = 0, 1, 2, \ldots$ be a time index; the dynamics of state jumps given by the trajectory $\{n_0 \to n_1 \to n_2 \to \ldots\}$ is a stochastic process if each n_k is a random variable with the time dependent probability distribution $P_k(n_k)$. The element n_k can be used to describe any state of a random process, such as the occupation of a fermion in a quantum dot or the position of a random walker. One can also compute a probability of a given tractory starting from $t = 0$ until a given instant $t = l$ and its expression is given by the joint distribution $P_l(n_0, n_1, \ldots, n_l)$. Throughout this thesis, we will consider that any distribution can also be marginalized, and for the state n_l:

$$P_l(n_l) = \sum_{n_0} \cdots\cdots \sum_{n_{l-1}} P_l(n_0, ..., n_l) \tag{3.1.1}$$

with $\sum_{n_l} P_l(n_l) = 1$. Each probability $P_j(n_j)$ can be found by summing the probabilities of all possible trajectories with duration j. Now, if we consider the same trajectory as above, one should ask about the probability of a given state n_{l+1} after $l + 1$ steps, which is given by the conditional probability

$$P_{l+1}(n_{l+1}|n_0, ..., n_l) = \frac{P_{l+1}(n_0, ...n_{l+1})}{P_l(n_0, ..., n_l)}. \tag{3.1.2}$$

3.2 Markov Chains

Consider the same process described by the trajectory defined above. We call it a Markov process (or Markov chain) if for any time l the following equation is true

$$P_{l+1}(n_{l+1}|n_0, n_1, ..., n_l) = P_{l+1}(n_{l+1}|n_l). \tag{3.2.1}$$

In other words, a process is called ”Markovian” if the probability of any step depends only on the previous state. Now imposing the Markov chain definition

in Eq.(3.1.2),

$$P_{l+1}(n_0,...,n_{l+1}) = P_{l+1}(n_{l+1}|n_0,...,n_l)P_l(n_0,...,n_l) = P_{l+1}(n_{l+1}|n_l)P_l(n_0,...,n_l), \tag{3.2.2}$$

which is a valid equation for any step. We can apply the property defined by Eq. (3.1.2) recursively,

$$\begin{aligned} P_l(n_0,...,n_l) &= P_l(n_l|n_{l-1})P_{l-1}(n_0,...,n_{l-1}), \\ P_{l-1}(n_0,...,n_{l-1}) &= P_{l-1}(n_{l-1}|n_{l-2})P_{l-2}(n_0,...,n_{l-2}), \\ &\dots \\ P_1(n_0,n_1) &= P_1(n_1|n_0)P_0(n_0). \end{aligned} \tag{3.2.3}$$

From here, we claim that for each time step $l+1$, the probability $P_{l+1}(n_0,n_1,...,n_{l+1})$ is completely defined by the initial probability $P_0(n_0)$ and the transition probabilities $P_k(n_k|n_{k-1})$,

$$P_l(n_0,n_1,...,n_l) = P_l(n_l|n_{l-1})P_{l-1}(n_{l-1}|n_{l-2})...P_1(n_1|n_0)P_0(n_0). \tag{3.2.4}$$

We also apply marginalization, as done in Eq.(3.1.1),

$$P_l(n_l) = \sum_{n_0}\cdots\sum_{n_{l-1}} P_l(n_l|n_{l-1})P_{l-1}(n_{l-1}|n_{l-2})...P_1(n_1|n_0)P_0(n_0). \tag{3.2.5}$$

The property computed by Eq.(3.1.1) should be applied to Eq. (3.2.5) to evaluate the following

$$P_l(n_l) = \sum_{n_{l-1}} P_{l-1}(n_l|n_{l-1})P_{l-1}(n_{l-1}). \tag{3.2.6}$$

The probability $P_{l-1}(n_l|n_{l-1})$ is defined as the transition probability. From now on, we will simplify this transition as constant in time (valid for any step l). Calling $n_l \to m$ and $n_{l-1} \to n$, the probability $P(m|n) = T_{mn}$ expresses the transition probability between $n \to m$ and Eq.(3.2.6) is rewritten as

$$P_l(m) = \sum_n T_{mn}P_{l-1}(n), \tag{3.2.7}$$

which can also be represented in matrix form,

$$P_l = TP_{l-1}, \tag{3.2.8}$$

where P_l and P_{l-1} are vectors with the probabilities (the sum of their entries is unity) and $T = [T_{ij}]$ is a square matrix with the following properties

$$\begin{cases} T_{ij} \geq 0, \ \forall i,j, \\ \sum_i T_{ij} = 1, \ \forall j. \end{cases} \tag{3.2.9}$$

The second property is given by the normalization of the conditional probabilities. The matrix T is defined as a stochastic matrix or transition matrix [61]. From Eq.(3.2.8), we write

$$P_1 = TP_0, \tag{3.2.10}$$

$$P_2 = TP_1, \tag{3.2.11}$$

$$\cdots \tag{3.2.12}$$

$$P_l = TP_{l-1}, \tag{3.2.13}$$

in a recursive way:

$$P_l = TP_{l-1} = T^2P_{l-2} = \cdots = T^lP_0, \tag{3.2.14}$$

and then

$$P_l = T^lP_0, \tag{3.2.15}$$

for any time step l. The equation above implies that once we have a stochastic matrix T, we are capable of describing the dynamics of any Markov process starting from its initial condition.

We now pause to make an important remark. In general, we are interested in the long-term solution of Eq. (3.2.15). If we model a system in contact with a reservoir as a Markov chain, we expect that the equilibrium solution (Boltzmann–Gibbs) corresponds to the long-time limit solution of Eq.(3.2.15). Thus, we expect that

$$\lim_{l\to\infty} P_l = P^{\text{st}} \tag{3.2.16}$$

with P^{st} being the expected equilibrium stationary solution, which also implies that the following condition must hold:

$$TP^{\text{st}} = P^{\text{st}}. \tag{3.2.17}$$

From Eq.(3.2.17) we conclude that the stationary solution P^{st} is also an eigenvector of T, with eigenvalue $\lambda = 1$. The existence and uniqueness of such a solution for Eq.(3.2.15) is guaranteed by the Perron–Frobenius theorem [61]. Also, a general method to find P^{st} for any regular T can be found in Tomé and Oliveira's textbook [61]. In this thesis, we will focus our attention on more generic and numerical methods, such as Newton–Raphson methods, to find its solution.

3.3 Master Equations

Equation (3.2.15) describes the stepwise evolution of the probability vector P_l under the linear application of T. Until this point, no information about the time scale of each transition is given by the matrix T. Therefore, we suppose that any transition $n \to m$ occurs in a mean time interval τ. We define the transition rate ω_{mn} as the probability of transition $n \to m$ per unit time,

$$\omega_{mn} = \frac{T_{mn}}{\tau}, \quad \text{if } m \neq n. \tag{3.3.1}$$

From the properties stated in Eq.(3.2.9), we can also write the diagonal elements of the matrix T in terms of the transition rates,

$$T_{mm} = 1 - \sum_{n \neq m} T_{nm} = 1 - \tau \sum_{n \neq m} \omega_{nm}. \tag{3.3.2}$$

Equation (3.3.1) defines the off-diagonal elements of an evolution matrix given by $W = [\omega_{ij}]$ that describes the time evolution of the probability vector P, since applying Eqs.(3.2.9) and (3.3.1) to Eq.(3.2.7) yields

$$\begin{aligned} P_l(m) &= \sum_n T_{mn} P_{l-1}(n) \\ &= \sum_{n \neq m} T_{mn} P_{l-1}(n) + T_{mm} P_{l-1}(m) \\ &= \sum_{n \neq m} \tau \omega_{mn} P_{l-1}(n) + \left(1 - \tau \sum_{n \neq m} \omega_{nm}\right) P_{l-1}(m), \end{aligned} \tag{3.3.3}$$

which can be rewritten as

$$\frac{P_l(m) - P_{l-1}(m)}{\tau} = \sum_{n \neq m} \left[\omega_{mn} P_{l-1}(n) - \omega_{nm} P_{l-1}(m)\right], \tag{3.3.4}$$

and since each transition has a mean time given by τ, we define a time scale $t = \tau l$ such that $P_l(m) - P_{l-1}(m)$ corresponds to $P_m(t) - P_m(t - \Delta t)$, where $\Delta t = \tau$. Taking the continuous limit ($\Delta t = \tau \to 0$), Eq.(3.3.4) becomes

$$\frac{dP_m}{dt} = \sum_{n \neq m} \left(\omega_{mn} P_n - \omega_{nm} P_m\right), \tag{3.3.5}$$

which is known as the master equation [61]. The master equation (3.3.5) can be rewritten in matrix form by properly defining the diagonal elements of the matrix $W = [\omega_{ij}]$:

$$\frac{d}{dt} P_t = W P_t, \tag{3.3.6}$$

with

$$\omega_{nn} = -\sum_{m \neq n} \omega_{mn}, \tag{3.3.7}$$

where $\frac{d}{dt}$ is the derivative operator acting on the probability vector P_t, and $W = [\omega_{ij}]$ is the evolution matrix. Equation (3.3.7) defines the diagonal elements of W to ensure the conservation of probability, consistent with the normalization condition in Eq.(3.2.9).

We also address a steady solution of Eq.(3.3.5) considering the long-time limit $t \to \infty$, in which the probability P^{st} is constant, obeying

$$\sum_{n \neq m} \left(\omega_{mn} P_n^{\text{st}} - \omega_{nm} P_m^{\text{st}} \right) = 0, \quad \text{for all states } m. \tag{3.3.8}$$

The existence and uniqueness of the stationary solution P^{st} are also guaranteed by the Perron–Frobenius theorem [61]. However, we will focus our attention on the physical argument for its existence. We first consider a canonical ensemble, where the system interacts with a reservoir at temperature T (as defined in Sec.(2.1)). Also, let us consider that the system is Markovian and that its microstates evolve solely through heat exchange with the reservoir. If the system starts from a given initial state, it will evolve until it reaches the stationary state that corresponds to the equilibrium distribution P^{eq} described by statistical mechanics [42]. Since it is also a steady solution, Eq.(3.3.8) must be valid, and we state that for each transition between m and n,

$$\frac{\omega_{mn}}{\omega_{nm}} = \frac{P_m^{\text{eq}}}{P_n^{\text{eq}}}, \quad \text{for all } m, n, \tag{3.3.9}$$

which is the condition of detailed balance, a necessary and sufficient condition for the evolution matrix W to reach the equilibrium state. In other words, the equilibrium solution is a property of the matrix W, and therefore one needs to properly define the entries ω_{ij} in order to describe the system–reservoir interaction. In Secs. (3.3.1) and (3.3.1) we define the transition rates for two important examples that also constitute one of the main topics of this thesis. The fundamental difference between Eqs.(3.3.8) and (3.3.9) is that the latter is a particular case of the former, since it is possible for an evolution matrix to obey Eq.(3.3.8) without satisfying Eq.(3.3.9). In such a case, we say that the system reaches a non-equilibrium steady state (NESS). In the following sections, we will show that the NESS has the important property of producing

entropy continuously. Furthermore, the NESS is a property of the evolution matrix W, and its components must also be defined properly, in such a way that detailed balance is "broken" by external forces and/or by simultaneous interaction with different reservoirs.

The difference between both solutions can be better understood by introducing the "currents" of transitions, defined as $J_{mn} := \omega_{mn}P_m - \omega_{nm}P_n$. In the steady state, we obtain from Eq.(3.3.8):

$$\sum_{n \neq m} J_{mn} = 0, \tag{3.3.10}$$

with the currents J_{mn} obeying the following properties:

$$J_{mn} = -J_{nm}, \tag{3.3.11}$$

and

$$J_{mm} = 0. \tag{3.3.12}$$

The current $J_{mn} > 0$ when there are more transitions $n \to m$ than the reverse. The NESS occurs when Eq.(3.3.10) holds and $J_{mn} \neq 0$ for some pair (m, n). The equilibrium probability distribution, in contrast, satisfies $J^{\text{eq}}_{mn} = 0$ for every m, n.

3.3.1 Models

We now introduce the equilibrium version of the main Markovian models used throughout this thesis. All of them are modelled using master equations such as Eq.(3.3.5), and in their non-equilibrium versions, the transition rates will break the detailed balance condition from Eq.(3.3.9) due to an external driving and/or due to the interaction with several reservoirs. More details on how to break detailed balance can be found in Sec.(3.4) and also in the subsequent chapters.

Two-state model

The two-state case is one of the simplest Markovian dynamics models, consisting of a system with two accessible random states. One of the most prominent

examples of an application of this model is the single-particle stochastic pump, which will be explored in its non-equilibrium version in Chapter (6). Single-particle stochastic pumps are models of transport of fermions (in general, electrons) between one or more occupation states. In particular, we will focus on the simplest two-state case. Experimentally, one of the most prominent devices for particle pumps are quantum dots (QDs) [62, 63], which comprise a nanoscale semiconductor with energy levels whose occupation is broadly used to transport electrons in several applications in quantum physics. The two-level system thermodynamics is a suitable model for nanoscale engines that extract useful work from electron reservoirs [51, 64, 65], and here we focus our attention on the classical approach, considering a two-state master equation, where the 0 state corresponds to deoccupation (when the electron leaves the QD and returns to the reservoir) and the 1 state corresponds to occupation (when the electron is delivered to the QD from the reservoir). The master equation for this dynamics is given by

$$\dot{p}(t) = [1 - p(t)]\omega_{01} - p(t)\omega_{10}, \tag{3.3.13}$$

where p is the probability that the QD is filled, ω_{01} is the rate for the transition $0 \to 1$, and ω_{10} is the rate for the transition $1 \to 0$. In equilibrium, the steady-state solution of Eq. (3.3.13) is obtained straightforwardly by setting $[1-p^{\mathsf{st}}]\omega_{01} - p^{\mathsf{st}}\omega_{10} = 0$, resulting in

$$p^{\mathsf{st}} = \frac{\omega_{01}}{\omega_{01} + \omega_{10}}, \quad \text{(occupation)}, \tag{3.3.14}$$

$$1 - p^{\mathsf{st}} = \frac{\omega_{10}}{\omega_{01} + \omega_{10}}, \quad \text{(deoccupation)}. \tag{3.3.15}$$

The transition rates ω_{01} and ω_{10} must obey Eq. (3.3.9) in order for the system to evolve to the equilibrium distribution. For a QD with occupation energy ϵ, interacting with one reservoir at temperature T and chemical potential μ, we expect a Fermi–Dirac distribution $p^{\mathsf{eq}} = (1 + e^{\beta(\epsilon-\mu)})^{-1}$, and therefore,

$$\ln\left(\frac{\omega_{10}}{\omega_{01}}\right) = \beta(\epsilon - \mu), \tag{3.3.16}$$

which leads to the following transition rates:

$$\omega_{01} = \frac{\Gamma}{1 + e^{\beta(\epsilon-\mu)}}, \qquad \omega_{10} = \frac{\Gamma e^{\beta(\epsilon-\mu)}}{1 + e^{\beta(\epsilon-\mu)}}, \tag{3.3.17}$$

where Γ defines the time scale.

Equilibrium Ising Model

Phase transitions and critical phenomena occur in several physical systems, such as fluids, magnetic materials, liquid crystals, and others. Generally speaking, in equilibrium systems, a phase transition occurs when there is a singularity in the free energy or in one of its derivatives [33]. The classical theory of phase transitions is interested in two quantities: one is the order parameter, a quantity that separates the phases, assuming a zero value (defining the disordered phase) and a nonzero value (defining the ordered phase). As examples, we cite the paramagnetic-to-ferromagnetic phase transition, with the order parameter being the magnetization m, and the gas–liquid phase transition in water, with the order parameter being the difference in densities of the two phases, $\rho_{\text{gas}} - \rho_{\text{liquid}}$. Critical (or second-order) phase transitions are marked by the existence of critical exponents, which characterize the asymptotic behavior of several thermodynamic quantities (such as the specific heat or magnetic susceptibility) near the critical points in continuous phase transitions. These exponents define universality classes, which depend on generic ingredients such as the dimensionality, the symmetry of the order parameter, range of interactions, and others [33, 42].

One of the simplest models with a phase transition is the Ising model, suggested by Wilhelm Lenz in 1920 [66] and developed by his student Ernst Ising in 1925 [67]. It is composed of a set of interacting spins on a lattice. The spins interact according to the energy (Hamiltonian)

$$E(S) = \epsilon \sum_{(ij)} s_i s_j - H \sum_{i=1}^{N} s_i, \tag{3.3.18}$$

where $S = (s_1, \ldots, s_N)$ is the set of spins that interacts with a reservoir at temperature T, with each element s_i being a random variable assuming the values $s_i = \pm 1$. Here, ϵ is the exchange energy, which can favor a ferromagnetic ($\epsilon < 0$) or an antiferromagnetic ($\epsilon > 0$) alignment, and H is an external field. The notation (ij) refers to the summation over nearest-neighbor spins.

In this thesis we introduce a general class of collective engines inspired by ferromagnetic equilibrium models, not only the Ising model but also the Potts model [33]. In order to tackle the optimization of engines based on collective

effects, we start by generalizing the Hamiltonian of Eq.(3.3.18) in the form

$$E(S) = \frac{1}{2k}\sum_{(ij)} \epsilon_{ij} s_i s_j + \Delta \sum_{i=1}^{N} s_i^2 - H\sum_{i=1}^{N} s_i, \tag{3.3.19}$$

in which each spin s_i can assume q states, but for simplicity, we will focus our attention on two specific cases: $s_i = \pm 1$ for $q = 2$ ($1/2$-Ising model) and $s_i = -1, 0, 1$ for $q = 3$ (1-Ising model). As in Eq.(3.3.18), the exchange energy ϵ_{ij} can favour a ferromagnetic ($\epsilon_{ij} < 0$) or an antiferromagnetic ($\epsilon_{ij} > 0$) alignment. The quantity Δ is the contribution of the individual energy of each spin, and H is an external field. The quantity k is the number of nearest neighbors. Here, we will also focus our attention on the 2D lattice case, with two possible interaction topologies: the square lattice ($k = 4$) and the all-to-all ($k = N$), in which each spin interacts with all the other spins. In the thermodynamic limit ($N \to \infty$), the all-to-all approach is analogous to the mean-field approximation. Now, a microstate transition occurs by flipping one spin per step, i.e., $S = (s_1, \ldots, s_j, \ldots, s_N) \to S' = (s_1, \ldots, \tilde{s}_j, \ldots, s_N)$, where the spin s_j changes to $\tilde{s}_j$ according to the energy interactions represented in Eq. (3.3.19). Each spin flip in the Ising model can be treated as a Markovian process and is described by a master equation:

$$\dot{p}_S = \sum_{S' \neq S} \omega_{SS'} p_{S'} - \omega_{S'S} p_S, \tag{3.3.20}$$

where the transition rates are defined as

$$\omega_{SS'} = \Gamma e^{-\tilde{\beta}[E(S) - E(S')]}, \tag{3.3.21}$$

where Γ is a quantity related to the time scale (for simplicity, we set $\Gamma = 1$) and $\tilde{\beta} = 1/T$ is the inverse of the temperature T of the reservoir. In the all-to-all approach, each spin interacts with all the other spins in the lattice, without any topological restriction. This approach is equivalent to taking the number of nearest neighbors $k = N$ and is also analogous to the mean-field approximation in the thermodynamic limit $N \to \infty$. The transition rates defined above obey the detailed balance condition expressed in Eq. (3.3.9), since the equilibrium probability is given by the canonical ensemble expression $p^{\text{eq}} = e^{-\tilde{\beta}E(S)}/Z$, with the partition function $Z = \sum_{(S)} e^{-\tilde{\beta}E(S)}$. Thus, the equilibrium solution $p^{\text{eq}}(S)$ for the master equation is guaranteed. Later on, we will break the detailed balance in Eq.(3.3.21) by introducing a biased external force and placing the system in contact with more than one reservoir.

Equation (3.3.20) describes the transitions in the set of microstates S, which makes it cumbersome to compute, since S can involve a huge number of spins. Each spin flip s_j leads to a change in the number of spins in a given state β. We therefore study such a system for all-to-all interactions, where the configuration of the microstate S is characterized by the number of spins in each state, N_β^S. Each spin flip leads to a transition $\beta' \to \beta$, which is equivalent to saying that in the transition $s' \to s$, we have $N_{\beta'}^{(S')} = N_{\beta'}^{(S)} - 1$ and $N_\beta^{(S')} = N_\beta^{(S)} + 1$. For $q = 2$, we have $\beta \in \{\downarrow, \uparrow\}$, and for $q = 3$, $\beta \in \{\downarrow, 0, \uparrow\}$. For the all-to-all case, we rewrite Eq. (3.3.19) in terms of the state β:

$$E(S) = \frac{1}{2N} \sum_{(\beta,\beta'<\beta)}^{q} [\epsilon_{\beta\beta} N_\beta^{(S)}(N_\beta^{(S)} - 1) + 2\epsilon_{\beta\beta'} N_\beta^{(S)} N_{\beta'}^{(S)}], \tag{3.3.22}$$

taking $H = \Delta = 0$ for simplicity. This approach is a coarse-grained procedure that has been effective in the description of several complex systems [68–70]. The interaction energies $\epsilon_{\beta\beta'}$ and $\epsilon_{\beta\beta}$ correspond to interactions between spins in different states and between spins in the same state, respectively. We can study different values for $\epsilon_{\beta\beta'}$ and how they affect the phase transition. In this model, we will consider two possibilities, which will be referred to as Model A and Model B later on. For Model A with $q = 3$, we define $\epsilon_{\uparrow\uparrow} = \epsilon_{\downarrow\downarrow} = \epsilon$, $\epsilon_{\uparrow\downarrow} = \epsilon_{\downarrow\uparrow} = -\alpha\epsilon$, and $\epsilon_{00} = \epsilon_{\uparrow 0} = \epsilon_{\downarrow 0} = 0$. Here, α represents the interaction strength between spins in different states. For Model B, we set $\epsilon_{\beta\beta'} = \epsilon\delta_{\beta\beta'}$, which resembles the Potts model [33]. The parameter α plays an important role in this model, since for $\alpha = 1$ the system exhibits a phase transition between ordered and disordered phases in the mean-field approximation, while for other values of α we observe a crossover (in Chapter 5 this will be discussed). In the all-to-all approach, we write the transition rates in Eq.(3.3.21) as

$$\omega_{S'S} = e^{-\tilde{\beta}\left[\mp\epsilon(1+\alpha)\left(1-\frac{2N_{\uparrow(\downarrow)}^{(S)}\mp 1}{N}\right)\right]}, \tag{3.3.23}$$

where the sign $\mp\epsilon(1+\alpha)$ corresponds to $N_\uparrow^{(S')} = N_\uparrow^{(S)} \pm 1$ and $N_\downarrow^{(S')} = N_\downarrow^{(S)} \mp 1$. Now we take the thermodynamic limit ($N \to \infty$), which together with the all-to-all interaction corresponds to the mean-field approximation. We define the state density p_β as $p_\beta = \left\langle \sum_S \frac{N_\beta^{(S)}}{N} \right\rangle$, leading to the following master equation:

$$\dot{p}_\beta = \sum_{\beta' \neq \beta} \omega_{\beta\beta'} p_{\beta'} - \omega_{\beta'\beta} p_\beta. \tag{3.3.24}$$

For Model A and $q = 2$, we have:

$$\omega_{\uparrow\downarrow} = e^{-\frac{\tilde{\beta}}{2}\{-\epsilon(1+\alpha)(1-2p_\uparrow)\}}, \tag{3.3.25}$$

and

$$\omega_{\downarrow\uparrow} = e^{-\frac{\tilde{\beta}}{2}\{\epsilon(1+\alpha)(1-2p_\uparrow)\}}. \tag{3.3.26}$$

Model B can be obtained by taking the transition rates above and setting $\alpha = 0$. Transition rates are evaluated in a similar fashion for $q = 3$. Starting with Model A, they are identical to the $q = 2$ case for transitions of type $\uparrow\to\downarrow$ and $\downarrow\to\uparrow$, whereas the energy difference reads $\epsilon(N_k^{(i)} - \alpha N_\ell^{(i)})/N$ for transitions like $0 \to\uparrow (\downarrow)$, where $k =\uparrow (\downarrow)$ and $\ell =\downarrow (\uparrow)$. All the remaining ones can be computed analogously. Likewise, for Model B, a given transition $N_\ell^{(j)} = N_\ell^{(i)} - 1$ and $N_k^{(i)} = N_k^{(i)}+1$ (where k, $\ell \in (\uparrow, 0, \downarrow)$) has an energy difference given by $\epsilon(N_k^{(i)}-N_\ell^{(i)}+1)/N$ [28, 29]. Numerical simulations are performed as before, but now there are $2q(q-1) = 12$ distinct transitions. As for $q = 2$, the limit $N \to \infty$ is promptly obtained and described by the master equation (3.3.24) for $\beta \in (\downarrow, 0, \uparrow)$. For Model A, some of the transition rates are:

$$\omega_{\uparrow\downarrow} = \Gamma e^{-\frac{\tilde{\beta}}{2}\{-\epsilon(1+\alpha)(p_\downarrow - p_\uparrow)\}}, \qquad \omega_{\uparrow 0} = \Gamma e^{-\frac{\tilde{\beta}}{2}\{\epsilon(p_\uparrow - \alpha p_\downarrow)\}} \quad \text{and} \quad \omega_{0\downarrow} = \Gamma e^{-\frac{\tilde{\beta}}{2}\{\epsilon(\alpha p_\uparrow - p_\downarrow)\}}. \tag{3.3.27}$$

For Model B, we have:

$$\omega_{\uparrow\downarrow} = \Gamma e^{-\frac{\tilde{\beta}}{2}\{\epsilon(p_\uparrow - p_\downarrow)\}}, \qquad \omega_{\uparrow 0} = \Gamma e^{-\frac{\tilde{\beta}}{2}\{\epsilon(p_\uparrow - p_0)\}} \quad \text{and} \quad \omega_{0\downarrow} = \Gamma e^{-\frac{\tilde{\beta}}{2}\{\epsilon(p_0 - p_\downarrow)\}}. \tag{3.3.28}$$

Before we proceed to understand the effects of nonequilibrium variables on the phase transition, we properly define the order parameter for the spin systems. We define the magnetization m as $m(S) = (N_\downarrow^{(S)} - N_\uparrow^{(S)})/N$, and the paramagnetic phase is characterized by $m(S) = 0$. Let us first consider the limiting case $N \to \infty$ in the all-to-all setting, and write $m(t) = p_\downarrow - p_\uparrow$. Using Eq. (3.3.24), we compute $\frac{dm(t)}{dt}$ and determine the steady state in the long-time limit.

3.4 Stochastic Thermodynamics for Markov Chains

Until now, we have described two apparently unrelated topics: macroscopic non-equilibrium thermodynamics in Chap.(2) and Markovian jump processes in the last sections. We will now combine these two approaches by introducing the thermodynamics of individual jumps between the states of the microscopic units that compose a system. Stochastic thermodynamics is a novel subarea of statistical mechanics that extends the non-equilibrium thermodynamics framework of Onsager and Prigogine [45,48,71] to define analogous thermodynamic quantities in the realm of microscopic transitions. At such scales, fluctuations due to thermal interaction are unavoidable and must be taken into account in these definitions. There are two approaches to describe thermodynamics and its fluctuations at small scales: the ensemble approach, where we define quantities such as the heat exchange flux $\dot{Q}$ as the average heat exchange over all Markovian jumps, and the trajectory approach, where we define the heat flux for each individual step $m \to n$, $\dot{q}_{nm}(t)$. Both approaches are connected, since $\dot{Q} = \langle \dot{q}_{nm}(t) \rangle$.

3.4.1 Ensemble Approach

To begin, let us first consider a grand canonical ensemble, where the equilibrium probability is given by

$$p_m^{\mathsf{eq}} = \frac{e^{-\beta(\epsilon_m - \mu n_m)}}{\mathcal{Z}}; \qquad \mathcal{Z} = \sum_m e^{-\beta(\epsilon_m - \mu n_m)}, \tag{3.4.1}$$

where $\mathcal{Z}$ is the grand canonical partition function, μ is the chemical potential of the reservoir, and ϵ_m and n_m are the energy and the number of particles occupying the state m, respectively. Of course, one can also define analogous quantities for a canonical ensemble (we will see this application in the example of Sec.(3.5)). From the detailed balance condition, Eq.(3.3.9), we write

$$k_{\mathsf{B}} \ln\left(\frac{\omega_{mn}}{\omega_{nm}}\right) = \frac{\epsilon_m - \epsilon_n - \mu(n_m - n_n)}{T}, \tag{3.4.2}$$

which describes a transition between states m and n. Any state hop results in dissipation [72]. Furthermore, the transition $m \to n$ results in a change in the energy, $\epsilon_m - \epsilon_n$, and we define the heat absorbed by the system from the reservoir during this transition, q_{mn}, inspired by the first law of thermodynamics on the macroscopic scale [44], as follows:

$$q_{mn} = \epsilon_m - \epsilon_n - \mu(n_m - n_n). \tag{3.4.3}$$

The internal energy is given by the average value of the energy of each state ϵ_m:

$$U = \sum_m \epsilon_m p_m, \tag{3.4.4}$$

which is a key definition in the ensemble approach, since the dynamics of the system will be described by mean values. Now, suppose that the system interacts with one heat reservoir and also with a work source: a fine-tuned external driving force that can continuously change the system's state, driving it away from equilibrium. This external agent will induce a change in the internal energy:

$$\dot{U} = \sum_m \dot{\epsilon}_m p_m + \dot{p}_m \epsilon_m, \tag{3.4.5}$$

where the first term on the right-hand side represents the change in energy of a given state m while the system remains in that state. The second term represents the change due to the probability of the system being in state m. This leads to a natural interpretation for each term. The time dependence $\epsilon_m = \epsilon_m(t)$ for each m is non-dissipative, since for a fixed state m we have $q_{mm} = 0$ from Eq.(3.4.3). This change in ϵ_m will be interpreted as work: a non-dissipative change in energy, a property that defines work in traditional thermodynamics [44]. Motivated by this, we define the work flux (power) as

$$\dot{W} = \sum_m \dot{\epsilon}_m p_m. \tag{3.4.6}$$

Due to external forces, we also expect a flux of energy and particles between states, suggesting the presence of a chemical work flux in addition to heat dissipation. Thus, we write the dissipative part of Eq. (3.4.5) as

$$\dot{Q} + \dot{W}_{\text{chem}} = \sum_m \dot{p}_m \epsilon_m, \tag{3.4.7}$$

and when combined with Eq. (3.4.5), we obtain

$$\dot{U} = \dot{W} + \dot{Q} + \dot{W}_{\text{chem}}, \tag{3.4.8}$$

which is the statement of the first law of thermodynamics. Before defining precise expressions for $\dot{Q}$ and $\dot{W}_{\text{chem}}$, we first turn to the entropy definition, given by the Gibbs expression [42]. Due to the nonequilibrium driving, we consider the entropy as a time-dependent function:

$$S(t) = -k_{\text{B}} \sum_m p_m(t) \ln p_m(t). \tag{3.4.9}$$

The time evolution of $S(t)$, denoted $\dot{S}$, is obtained from Eq.(3.4.9) as

$$\dot{S} = -k_{\text{B}} \sum_m \left[\dot{p}_m \ln p_m + p_m \frac{d}{dt} \ln p_m \right], \tag{3.4.10}$$

where the second term in the sum vanishes because

$$\sum_m p_m \frac{d}{dt} \ln p_m = \sum_m \dot{p}_m = 0, \tag{3.4.11}$$

by conservation of probability, Eq.(3.3.5). Equation (3.4.10) then simplifies to

$$\dot{S} = -k_{\text{B}} \sum_m \sum_n J_{mn} \ln p_m, \tag{3.4.12}$$

with $J_{mn} = \omega_{mn} p_n - \omega_{nm} p_m$. From now on, we will perform some algebraic manipulations using the properties of J_{mn} defined in Eqs.(3.3.11) and... (3.3.12)

$$\begin{aligned}
\dot{S} &= -\frac{k_{\text{B}}}{2} \left[\sum_m \sum_n J_{mn} \ln(p_m) + \sum_m \sum_n J_{mn} \ln(p_m) \right] \\
&= -\frac{k_{\text{B}}}{2} \left[\sum_m \sum_n J_{mn} \ln(p_m) + \sum_m \sum_n (-J_{nm}) \ln(p_m) \right] \\
&= -\frac{k_{\text{B}}}{2} \left[\sum_m \sum_n J_{mn} \ln(p_m) + \sum_m \sum_n J_{nm} \ln\left(\frac{1}{p_m}\right) \right] \\
&= -\frac{k_{\text{B}}}{2} \left[\sum_n \sum_m J_{mn} \ln(p_m) + \sum_n \sum_m J_{mn} \ln\left(\frac{1}{p_n}\right) \right] \\
&= -\frac{k_{\text{B}}}{2} \left[\sum_m \sum_n J_{mn} \ln\left(\frac{p_m}{p_n}\right) \right] \\
&= -\frac{k_{\text{B}}}{2} \left[\sum_m \sum_n J_{mn} \ln\left(\frac{p_m}{p_n} \frac{\omega_{nm}}{\omega_{mn}} \frac{\omega_{mn}}{\omega_{nm}}\right) \right] \\
&= -\frac{k_{\text{B}}}{2} \left[\sum_m \sum_n J_{nm} \ln\left(\frac{\omega_{nm} p_m}{\omega_{mn} p_n}\right) + \sum_m \sum_n J_{nm} \ln\left(\frac{\omega_{mn}}{\omega_{nm}}\right) \right].
\end{aligned} \tag{3.4.13}$$

Equation (3.4.13) can be split into two expressions: on the left-hand side, we have a non-negative sum, since it is of the form $(x - y)\ln(x/y)$, which is

always non-negative for all real x and $y \neq 0$. The right-hand side, on the other hand, can assume either sign depending on the values of the currents J_{nm} and the transition rates. Thus, inspired by the macroscopic entropy flux (see Eq.(2.1)), we write

$$\dot{S} = \sigma - \phi, \tag{3.4.14}$$

with

$$\sigma = \frac{k_B}{2}\left[\sum_m \sum_n J_{mn} \ln\left(\frac{\omega_{mn} p_n}{\omega_{nm} p_m}\right)\right] \geq 0, \tag{3.4.15}$$

being the entropy production, and

$$\phi = \frac{k_B}{2}\left[\sum_m \sum_n J_{mn} \ln\left(\frac{\omega_{mn}}{\omega_{nm}}\right)\right], \tag{3.4.16}$$

the entropy flux.

Now, we recall Eq.(3.4.2), which is not globally valid outside the equilibrium realm, since the probability distribution no longer takes the form of Eq.(3.4.1) but instead becomes a time-dependent function in the presence of an external drive. However, we can assert a locally valid relation for the quantity $\ln(\omega_{mn}/\omega_{nm})$ that appears in the entropy flux expression, Eq. (3.4.16). Although the probability for each state m is time-dependent, the transition rates must also be, and for each state jump $m \leftrightarrow n$, they must satisfy locally the condition analogous to Eq.(3.4.2):

$$k_B T \ln\left(\frac{\omega_{nm}}{\omega_{mn}}\right) = q_{mn}(t), \quad \text{for each time } t, \tag{3.4.17}$$

where $q_{mn}(t) = \epsilon_m(t) - \mu n_m(t) - (\epsilon_n(t) - \mu n_n(t))$. This assumption in Eq.(3.4.17) is called local detailed balance. Equation (3.4.16) can then be rewritten as

$$\phi = \frac{1}{2}\sum_m \sum_n J_{nm} \frac{q_{nm}}{T}, \tag{3.4.18}$$

and since for each pair (i, j) in the summation above we have $J_{ij}q_{ij} + J_{ji}q_{ji} = 2J_{ij}q_{ij}$, using the property from Eq.(3.3.11) and the fact that $q_{ij} = -q_{ji}$, we obtain

$$\phi = \sum_n \sum_{m>n} J_{nm} \frac{q_{nm}}{T}. \tag{3.4.19}$$

In the macroscopic realm, the entropy flux is proportional to the heat flux, allowing us to write

$$\phi = \frac{\dot{Q}}{T}, \tag{3.4.20}$$

which can be used to finally obtain an explicit expression for the heat flux defined in Eq.(3.4.7). Applying Eq.(3.4.19) (or more directly from Eqs.(3.4.20), (3.4.18), and (3.4.16), and again using the properties of the currents J_{ij}), we find:

$$\begin{aligned}\dot{Q} &= \frac{1}{2}\sum_m \sum_n J_{nm} q_{nm} \\ &= \frac{1}{2}\sum_m \sum_n J_{nm}[\epsilon_n - \mu n_n - (\epsilon_m - \mu n_m)] \\ &= \frac{1}{2}\sum_m \sum_n [J_{nm}(\epsilon_n - \mu n_n) + J_{mn}(\epsilon_n - \mu n_n)] \\ &= \sum_{m,n} J_{nm}(\epsilon_n - \mu n_n). \end{aligned} \tag{3.4.21}$$

This yields explicit expressions for the thermodynamic quantities in terms of the probability fluxes:

$$\dot{W} = \sum_m \dot{\epsilon}_m p_m, \tag{3.4.22}$$

for the work flux (power);

$$\dot{Q} = \sum_m \sum_n J_{mn}(\epsilon_m - \mu n_m), \tag{3.4.23}$$

for the heat flux; and, applying the above to Eq.(3.4.7),

$$\dot{W}_{\text{chem}} = \sum_m \sum_n \mu n_m J_{mn}, \tag{3.4.24}$$

for the chemical work flux.

For a system that is under a periodic or constant force, we expect the system to reach a non-equilibrium steady state (NESS). In this state, the thermodynamic functions of state are constant, and therefore $\dot{U} = 0$ and $\dot{S} = 0$, resulting in

$$\dot{W} + \dot{Q} + \dot{W}_{\text{chem}} = 0, \tag{3.4.25}$$

and

$$\sigma = \phi = -\frac{\dot{Q}}{T}. \tag{3.4.26}$$

The equations above are powerful, as they allow us to describe, at the ensemble level, the thermodynamic properties in terms of the current fluxes in the non-equilibrium steady state, which can be obtained simply by imposing

$\dot{p}_m = 0$. The methods for solving this equation can vary depending on the system. Here, we explore two main methods in addition to analytical solutions (when possible): direct discretization of the master equation and the Gillespie algorithm [73].

3.4.2 Multiple Reservoirs

One feasible way to break detailed balance (see Eq.(3.3.9)) and drive a given system into a NESS is to place it in contact with multiple reservoirs. In this thesis we present two ways to do so: the collisional and the simultaneous approach. The collisional (or sequential) approach consists of maintaining the system in contact with only one reservoir during a time interval and, after that, switching to another one, typically via an adiabatic transformation [51, 60, 65, 74]. This approach is investigated in detail in Sec.(4) and in Sec.(6.1). In the simultaneous approach, the system interacts with two or more reservoirs at the same time, which is equivalent to the fast-switching limit of a "two-box" description. This consists of a diffusive system that is allowed to move back and forth between two thermal stages with a given transition rate [15].

We start by defining the transition rate for each reservoir, assuming that each transition in the microstate will be driven by one of the reservoirs independently. The transition $m \to n$ due to reservoir ν will be given by $\omega_{mn}^{(\nu)}$, which obeys a special case of detailed balance (see Eq.(3.4.17)):

$$k_{\mathsf{B}} \ln\left(\frac{\omega_{nm}^{(\nu)}}{\omega_{mn}^{(\nu)}}\right) = q_{mn}^{(\nu)}(t), \quad \text{for each reservoir } \nu. \tag{3.4.27}$$

For the simultaneous case, we write a total transition rate ω_{nm} considering the contribution of all reservoirs:

$$\omega_{nm} := \sum_{\nu} \omega_{nm}^{(\nu)}, \tag{3.4.28}$$

with the total probability current J_{nm} given by

$$J_{nm} = \sum_{\nu} J_{nm}^{(\nu)}, \tag{3.4.29}$$

rewriting Eq.(3.3.4) as

$$\dot{p}(t) = \sum_{\nu} \sum_{n \neq m} J_{mn}^{(\nu)}. \tag{3.4.30}$$

The total heat exchange is given by

$$q_{nm} = \sum_{\nu} q_{nm}^{(\nu)}, \tag{3.4.31}$$

which implies

$$\phi = \sum_{\nu} \sum_{n} \sum_{m>n} J_{nm}^{(\nu)} \frac{q_{nm}^{(\nu)}}{T}, \tag{3.4.32}$$

for the total entropy flux, and

$$\sigma = \frac{k_{\mathsf{B}}}{2} \left[\sum_{\nu} \sum_{m} \sum_{n} J_{mn}^{(\nu)} \ln \left(\frac{\omega_{mn}^{(\nu)}}{\omega_{nm}^{(\nu)}} \right) \right] \tag{3.4.33}$$

for the entropy production. For the heat fluxes exchanged with each reservoir, $\dot{Q}^{(\nu)}$, we simply apply Eq.(3.4.13) and write

$$\dot{Q}_{\nu} = \frac{1}{2} J_{nm}^{(\nu)} q_{nm}^{(\nu)} = \sum_{m} \sum_{n} J_{nm}^{(\nu)} (\epsilon_m - \mu_{\nu} n_m), \tag{3.4.34}$$

where μ_{ν} is the chemical potential of reservoir ν. The same generalization, now from Eq.(3.4.24), can be made for the chemical work fluxes:

$$\dot{W}_{\mathsf{chem}}^{(\nu)} = \sum_{m} \sum_{n} \mu_{\nu} n_m J_{nm}^{(\nu)}. \tag{3.4.35}$$

The total work is computed as the sum of all contributions from the reservoirs:

$$\dot{W} = \sum_{\nu} \dot{W}^{(\nu)}, \tag{3.4.36}$$

where each contribution $\dot{W}^{(\nu)}$ can be found by applying Eqs.(3.4.35) and (3.4.36) in the NESS or by computing Eq.(3.4.6) for each reservoir.

With the exception of Chapter (6), our main focus will be on the simplest case of two reservoirs. In the NESS, for two reservoirs we have

$$\dot{Q}_1 + \dot{Q}_2 + \dot{W} = 0, \tag{3.4.37}$$

As discussed in Sec.(2.2), we expect that certain conditions (generally expressed in terms of sign conventions) guarantee the engine regime. One reservoir will serve as an input (delivering heat or input work) and the other as an

output (receiving the output work and dissipation). In this case, we define the efficiency for the heat engine as

$$\eta = -\frac{\langle P \rangle}{\dot{Q}_{\text{in}}}, \tag{3.4.38}$$

where $\langle P \rangle := \dot{W} > 0$ is the power output and $\dot{Q}_{\text{in}}$ is the input heat, which can be either $\dot{Q}_1$ or $\dot{Q}_2$ depending on its sign. The efficiency expression in Eq.(3.4.38) must satisfy the same conditions discussed in Sec.(2.2) for the system to convert input heat into useful output work.

3.4.3 Trajectory Approach

The above description is suitable for the study of microscopic engines in the NESS, since Eqs.(3.4.22)–(3.4.24) should be analyzed under the conditions established in Chap.(2.2) in order to identify the regimes in which the system operates as an engine and to develop appropriate methods for improving its performance. In the following chapters, we apply these equations and methods to distinct scenarios in order to understand the engine regime at the small scale and to enhance its output, which can otherwise operate inefficiently under certain physical conditions.

The NESS is expected to be reached after a long time interval: under constant or periodic forces, the system ”thermalizes” under the combined action of external drives and thermal interaction with the reservoirs, and the probability distributions of its states reach constant values that do not correspond to the equilibrium ensemble distributions. The approach described above is suitable for this long-time assumption, and one can compute exact values for the currents J_{ij} and, consequently, for the thermodynamic quantities. However, due to recent advances in nanotechnology, measurements at even smaller scales have become possible [9]. Such precise measurements lead to a much deeper formulation of the second law of thermodynamics and, consequently, of heat dissipation and the engine regime as well. Suppose that a system (under the same conditions described above) follows a single trajectory in phase space, denoted by $m(t)$, among the set of all possible trajectories under the same physical conditions. The function $m(t)$ is a stochastic quantity with a well-defined prob-

ability distribution $p_{m(t)}(t)$ (which is also described by the master equation). In 2005, Udo Seifert [75] introduced the definition of entropy for a single trajectory $m(t)$,

$$s = -k_{\mathsf{B}} \ln(p_{m(t)}(t)). \tag{3.4.39}$$

Note that $S = \langle s \rangle$ corresponds to the Gibbs expression (3.4.9). We can repeat the decomposition of $\dot{s}$ as done in Eq.(3.4.14), making the fluctuations of entropy production and entropy flux explicit:

$$\dot{s} = \dot{s}_i + \dot{s}_e, \tag{3.4.40}$$

with

$$\dot{s}_e = -k_{\mathsf{B}} \sum_m \dot{\delta}_{m,m(t)} \ln \left(p_m^{\mathsf{eq}}(t)\right), \tag{3.4.41}$$

and

$$\dot{s}_i = -k_{\mathsf{B}} \sum_m \left\{ \dot{\delta}_{m,m(t)} + \delta_{m,m(t)} \frac{\dot{p}_m}{p_m(t)} \right\}, \tag{3.4.42}$$

according to [75]. Of course, these quantities correspond to the averages of the expressions in Eqs.(3.4.15) and (3.4.16).

We now consider two experiments: one that results in a trajectory $m(t)$ and another that results in the reverse trajectory $\tilde{m}(\tilde{t})$, where $m(t)$ starting at $t_i = 0$ corresponds to $\tilde{m}(\tilde{t})$ at the final time $\tilde{t}_i = \tau$, and *vice-versa*, with τ being the total duration of the experiment. The time $\tilde{t}$ is defined as $\tilde{t} = \tau - t$. We define the cumulative entropy production Δs_i as the difference between the entropy production of the two experiments, given by

$$\Delta s_i = k_{\mathsf{B}} \ln \left(\frac{p(m)}{\tilde{p}(\tilde{m})} \right), \tag{3.4.43}$$

where $\tilde{p}(\tilde{m})$ is the probability distribution of the reverse trajectory. The quantity Δs_i is a stochastic variable, and we describe its probability distribution $P(\Delta s_i)$ as [72]:

$$P(\Delta s_i) = \int_m \delta \left(\Delta s_i - k_{\mathsf{B}} \ln \frac{p(m)}{\tilde{p}(\tilde{m})} \right) p(m)\, dm, \tag{3.4.44}$$

where the integral is taken over the space of all trajectories $m(t)$, and δ denotes the Dirac delta function. Performing the change of variables $m \to \tilde{m}$, we obtain

$$P(\Delta s_i) = \int_{\tilde{m}} \delta \left(-\Delta s_i - k_{\mathsf{B}} \ln \frac{\tilde{p}(\tilde{m})}{p(m)} \right) \tilde{p}(\tilde{m})\, d\tilde{m} = e^{\Delta s_i / k_{\mathsf{B}}}\, \tilde{P}(-\Delta s_i), \tag{3.4.45}$$

which yields

$$\frac{P(\Delta s_i)}{\tilde{P}(-\Delta s_i)} = e^{\Delta s_i / k_B}, \tag{3.4.46}$$

corresponding to the fluctuation theorem for entropy production. In Sec.(4.4), we apply this approach to understand fluctuations in power and efficiency outputs, proposing a new optimization route that increases the probability of rare events, such as "super-Carnot" efficiencies and the simultaneous maximization of power and efficiency.

3.5 Stochastic Thermodynamics for the Driven Ising Model

We now apply the ensemble approach to the nonequilibrium collective system. Consider a minimal model consisting of N interacting units, where each unit j is represented by a spin variable s_j taking values $s_j \in \{-1, 0, 1\}$ for $q = 3$ or $s_j \in \{-1, 1\}$ for $q = 2$, exactly as described in Sec.(3.3.1). However, we now introduce two nonequilibrium ingredients: the system is coupled simultaneously to two thermal baths at different temperatures T_1 and T_2, and is subject to opposite nonconservative (biased) driving forces acting at the level of individual units. As in the equilibrium case, each step of the dynamics corresponds to flipping the state of a single unit due to the interaction between spins with their nearest neighbors (with the interaction energy described by Eq.(3.3.19)), but also due to the action of one of the baths (with equal *a priori* probability) and to the driving forces. These forces act according to two factors: one reservoir induces a "rotation" in each individual spin (say s_j) in the clockwise direction ($-1 \to 0 \to +1 \to -1$), while the other reservoir drives the rotation in the opposite direction, creating a kind of competition between the two biased forces (see the Fig(3.1)).

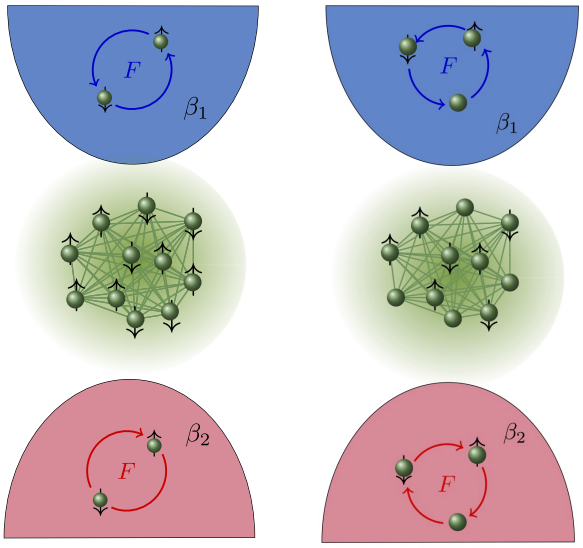

Figure 3.1: The figure above shows a schematic representation of a driven Ising model in the all-to-all setup for the states $q = 2$ and $q = 3$, from left to right, in contact with two work-source reservoirs and two thermal baths, where the blue bath represents the cold reservoir and the red bath the hot reservoir. The schematic arrows represent the bias of the force exerted by each reservoir.

As in Sec. (3.3.1), we represent each microstate by $S = (s_1, \ldots, s_j, \ldots, s_N)$, with transitions $S \to S' = (s_1, \ldots, \tilde{s}_j, \ldots, s_N)$ occurring via a flip of the j-th spin, where $\tilde{s}_j \neq s_j$. Using Eq.(3.4.17), we define the stochastic heat exchanged with each reservoir $\nu \in \{1, 2\}$, denoted $Q^{(\nu)}_{S'S}$, due to the transition $S \to S'$:

$$Q^{(\nu)}_{S'S} = \frac{1}{\beta_\nu} \ln\left(\frac{\omega_{S'S}}{\omega_{SS'}}\right) = E(S') - E(S) - W^{\nu}_{S'S}, \tag{3.5.1}$$

where $W^{(\nu)}_{S'S} = (-1)^{\nu-1} d_{s's} F$ is the work performed on the system due to the nonconservative force associated with reservoir ν. Here, F denotes the driving force strength, and $d_{s's}$ defines the bias: it equals $+1$ if the flip $s_j \to \tilde{s}_j$ follows the clockwise cycle $-1 \to 0 \to +1 \to -1$ for $q = 3$, and -1 otherwise. For $q = 2$, $d_{s's} = +1$ for transitions $-1 \to +1$ and $d_{s's} = -1$ for $+1 \to -1$. The bias satisfies $d_{s's} = -d_{ss'}$. This type of biased force is inspired by other engine setups [27, 28] and is compatible with models of biomolecular motors such as kinesin [76, 77], photo-acids [78], ATP-driven chaperones [79, 80], and also

appears in the mobility of active driven particles [81, 82]. The corresponding transition rate that satisfies the local detailed balance condition in Eq.(3.5.1) is given by $\omega^{\nu}_{s's} = \Gamma \exp\left(-\frac{\beta_\nu}{2} Q^{\nu}_{s's}\right)$, where Γ sets the time scale (for simplicity, we set $\Gamma = 1$).

This system is described by the master equation (3.3.20) considering two reservoirs:

$$\dot{p}_s(t) = \sum_{\nu=1}^{2} \sum_{s' \neq s} J^{(\nu)}_{s's}(t), \tag{3.5.2}$$

with $J^{(\nu)}_{s's}(t) = \omega^{(\nu)}_{s's} p_{s'}(t) - \omega^{(\nu)}_{s's} p_s(t)$ the probability current between microstates s and s'. Now, using Eq.(3.4.23), we write for each reservoir

$$\langle \dot{Q}_\nu \rangle = \sum_{(s's)} Q^{(\nu)}_{s's} J^{(\nu)}_{s's}, \tag{3.5.3}$$

where the sum over $(s's)$ runs over all distinct transitions between s and s'. Also, considering the NESS condition from Eq.(3.4.25), we have

$$\langle \dot{Q}_1 \rangle + \langle \dot{Q}_2 \rangle + \langle \mathcal{P} \rangle = 0, \tag{3.5.4}$$

with the power output given by

$$\langle \mathcal{P} \rangle = \sum_{(s's)} W^{(\nu)}_{s's} J^{(\nu)}_{s's}. \tag{3.5.5}$$

Finally, we define the efficiency for this system as

$$\eta = -\frac{\langle \mathcal{P} \rangle}{\langle \dot{Q}_j \rangle}, \tag{3.5.6}$$

where $\langle \dot{Q}_j \rangle$ is the heat absorbed from the hot reservoir. For definiteness, we take $j = 2$.

As discussed in Chap.(2.2), we impose conditions on the signs of the heat fluxes and power in order to identify a useful output. For this specific system, we adopt the following sign convention: the system operates as a heat engine when $\langle \mathcal{P} \rangle < 0$ and $\langle \dot{Q}_2 \rangle > 0$ (heat input from the hot reservoir), which by construction implies $0 \leq \eta \leq \eta_{\mathrm{C}}$. Sometimes we represent the efficiency in normalized form $\hat{\eta} = \eta_{\mathrm{C}}^{-1} \eta$, so that the engine regime corresponds to $0 \leq \hat{\eta} \leq 1$. Conversely, in the pump regime, heat from the hot reservoir is partially delivered to the cold reservoir in exchange for an input of external work, implying $\langle \mathcal{P} \rangle > 0$ and

$\langle \dot{Q}_2 \rangle < 0$, and by construction $\eta_C < \eta < \infty$ (or $1 < \hat{\eta} < \infty$). The dud regime occurs when $\eta < 0$, in which case the system produces no useful output or even reverses the heat flow from the hot reservoir (i.e., it is not useful).

The current $J^{\nu}_{s's}$ describes the flux of spin flips at the level of individual microstates $s = (s_1, \ldots, s_N)$, which is quite cumbersome to compute. As done in Sec.(3.3.1), we adopt a density approach, considering the number of spins in each state β, denoted N_β, and taking the thermodynamic limit ($N \to \infty$). In Chap.(5), we also address the finite-size spin case. The corresponding master equation in the mean-field approximation is the same as Eq.(3.3.24):

$$\dot{p}_\beta = \sum_{\nu} \sum_{\beta' \neq \beta} J^{(\nu)}_{\beta\beta'}, \tag{3.5.7}$$

where the current $J^{(\nu)}_{\beta\beta'}$ describes the flux of transitions from state β' to β induced by reservoir ν. The corresponding thermodynamic quantities are given by

$$\langle \dot{Q}_\nu \rangle = \sum_{(\beta'\beta)} Q^{(\nu)}_{\beta'\beta} J^{(\nu)}_{\beta'\beta}, \tag{3.5.8}$$

and

$$\langle \mathcal{P} \rangle = \sum_{\nu} \sum_{(\beta'\beta)} W^{(\nu)}_{\beta'\beta} J^{(\nu)}_{\beta'\beta}, \tag{3.5.9}$$

with $W_{\beta'\beta} = (-1)^{\nu-1} d_{\beta'\beta} F$, and $Q^{(\nu)}_{\beta'\beta}$ given by

$$Q^{(\nu)}_{\beta'\beta} = E(\beta') - E(\beta) - W^{(\nu)}_{\beta'\beta}. \tag{3.5.10}$$

The transition rates in the mean-field approximation are written as in Sec.(3.3.1), with the addition of distinct reservoirs and the external driving force F according to the corresponding bias, as given in Eqs.(3.3.25)–(3.3.28):

For $q = 2$ in Model A, we have:

$$\omega^{(1)}_{\uparrow\downarrow} = e^{-\frac{\beta_1}{2}\{-\epsilon(1+\alpha)(1-2p_\uparrow)-F\}} \quad \text{and} \quad \omega^{(2)}_{\uparrow\downarrow} = e^{-\frac{\beta_2}{2}\{-\epsilon(1+\alpha)(1-2p_\uparrow)+F\}}, \tag{3.5.11}$$

$$\omega^{(1)}_{\downarrow\uparrow} = e^{-\frac{\beta_1}{2}\{\epsilon(1+\alpha)(1-2p_\uparrow)+F\}} \quad \text{and} \quad \omega^{(2)}_{\downarrow\uparrow} = e^{-\frac{\beta_2}{2}\{\epsilon(1+\alpha)(1-2p_\uparrow)-F\}}. \tag{3.5.12}$$

For $q = 3$ in Model A, we have:

$$\omega^{(1)}_{\uparrow\downarrow} = e^{-\frac{\beta_1}{2}\{-\epsilon(1+\alpha)(p_\downarrow - p_\uparrow)+F\}}, \qquad \omega^{(1)}_{\uparrow 0} = e^{-\frac{\beta_1}{2}\{\epsilon(p_\uparrow - \alpha p_\downarrow)-F\}} \quad \text{and} \quad \omega^{(1)}_{0\downarrow} = e^{-\frac{\beta_1}{2}\{\epsilon(\alpha p_\uparrow - p_\downarrow)-F\}}. \tag{3.5.13}$$

For Model B with $q = 3$, we have:

$$\omega^{(1)}_{\uparrow\downarrow} = e^{-\frac{\beta_1}{2}\{\epsilon(p_\uparrow - p_\downarrow)+F\}}, \qquad \omega^{(1)}_{\uparrow 0} = e^{-\frac{\beta_1}{2}\{\epsilon(p_\uparrow - p_0)-F\}} \quad \text{and} \quad \omega^{(1)}_{0\downarrow} = e^{-\frac{\beta_1}{2}\{\epsilon(p_0 - p_\downarrow)-F\}}. \tag{3.5.14}$$

Again, Model B for $q = 2$ is obtained by taking Model A with $\alpha = 0$. Moreover, to obtain the transition rates for reservoir 2, one simply needs to change the sign of F.

3.6 Langevin Equations

According to Langevin [83], a Brownian particle can be described as a small particle of mass m subject to two forces: a drag force (deterministic) that depends on the velocity, arising from the movement of the particle through the medium, and a stochastic force resulting from random collisions between the particle and the molecules of the fluid. The equation of motion for the dynamics described above is written as

$$\begin{cases} m\dfrac{dv}{dt} = -\alpha v + F_a(t), \\ v = \dfrac{dx}{dt}, \end{cases} \tag{3.6.1}$$

where α is the drag coefficient and $F_a(t)$ is a random force satisfying the following properties:

$$\langle F_a(t)\rangle = 0, \tag{3.6.2}$$

and

$$\langle F_a(t)F_a(t')\rangle = B\delta(t - t'), \tag{3.6.3}$$

where $\langle\cdot\rangle$ denotes an ensemble average.

The property stated in Eq. (3.6.2) implies that there is no preferred direction for the random forces; in other words, collisions of the molecules with the Brownian particle occur in all directions with equal probability. Equation (3.6.3) reflects the fact that collisions at different times are independent.

Equation (3.6.1) can be reduced to

$$\frac{dv}{dt} = -\gamma v + \zeta(t), \tag{3.6.4}$$

where $\gamma = \alpha/m$ is the drag coefficient per unit mass, and $\zeta(t) = F_a(t)/m$ is a random force per unit mass, satisfying the same properties as $F_a(t)$:

$$\langle \zeta(t) \rangle = 0, \tag{3.6.5}$$

$$\langle \zeta(t)\zeta(t') \rangle = \Gamma \delta(t - t'), \tag{3.6.6}$$

with $\Gamma = B/m^2$.

The solution of Eq.(3.6.4) can be easily obtained:

$$v(t) = v_0 e^{-\gamma t} + \int_0^t \zeta(t') e^{\gamma(t'-t)}\, dt'. \tag{3.6.7}$$

Since $\dot{x} = v$, we have

$$x(t) = x_0 + \frac{v_0}{\gamma}(1 - e^{-\gamma t}) + \int_0^t \left(\int_0^{t'} \zeta(t'')\, dt'' \right) e^{\gamma t'}\, dt', \tag{3.6.8}$$

which simplifies to

$$x(t) = x_0 + \frac{v_0}{\gamma}(1 - e^{-\gamma t}) + \frac{1}{\gamma} \int_0^t \zeta(t'') \left(1 - e^{\gamma(t''-t)} \right) dt''. \tag{3.6.9}$$

The integral involving $\zeta(t)$ is a stochastic integral, which lies outside the scope of this thesis. Since we are initially interested in the ensemble averages of velocity and position, the stochastic terms in Eqs. (3.6.9) and (3.6.7) vanish, yielding

$$\langle x(t) \rangle = x_0 + \frac{v_0}{\gamma}(1 - e^{-\gamma t}), \tag{3.6.10}$$

$$\langle v(t) \rangle = v_0 e^{-\gamma t}. \tag{3.6.11}$$

The same approach can be applied to the mean square velocity $\langle v^2(t) \rangle$, using the properties given in Eqs.(3.6.5) and (3.6.6):

$$\langle v^2(t) \rangle = v_0^2 e^{-2\gamma t} + \frac{\Gamma}{2\gamma}(1 - e^{-2\gamma t}). \tag{3.6.12}$$

The variance $b(t)$ is then given by

$$b(t) = \langle v^2(t) \rangle - \langle v(t) \rangle^2 = \frac{\Gamma}{2\gamma}(1 - e^{-2\gamma t}). \tag{3.6.13}$$

In the long-time regime, $\langle v(t) \rangle \to 0$ and

$$\langle v^2 \rangle = \frac{\Gamma}{2\gamma}. \tag{3.6.14}$$

Using the equipartition theorem [42], for one degree of freedom we have $(1/2)m\langle v^2\rangle = (1/2)k_{\mathrm{B}}T$. Together with expression (3.6.14), this yields an explicit value for Γ (often referred to as the "reduced temperature" [84, 85]):

$$\Gamma = \frac{2k_{\mathrm{B}}\gamma T}{m}. \tag{3.6.15}$$

3.7 Fokker–Planck and Fokker–Planck–Kramers equations

The Langevin equation (3.6.4) is a stochastic differential equation whose solution is a stochastic process. The probability distribution $P(v,t)$ associated with this process satisfies a Fokker–Planck equation [61], which can be written as

$$\frac{\partial P}{\partial t} = -\frac{\partial J(v,t)}{\partial v}, \tag{3.7.1}$$

which has the form of a continuity equation, where $J(v,t)$ is the probability current, given by

$$J(v,t) = -\gamma v P(v,t) - \frac{\Gamma}{2}\frac{\partial P(v,t)}{\partial v}. \tag{3.7.2}$$

A detailed derivation of Eq.(3.7.1) can be found in Ref. [61]. An important special case is the description of a Brownian particle interacting with a reservoir at temperature T, for which Eq.(3.7.1) yields the well-known Maxwell–Boltzmann distribution:

$$P(v) = \frac{1}{Z}e^{-\beta m v^2/2}, \tag{3.7.3}$$

where Z is the partition function and $\beta = (k_{\mathrm{B}}T)^{-1}$.

Equation (3.7.1) is the Fokker–Planck equation for a single variable (velocity), corresponding to a Langevin equation of the form (3.6.4). We now consider another important case that describes experimental setups such as particles trapped in harmonic potentials. In this case, the Langevin equation takes the form

$$m\frac{dv}{dt} = -\alpha v + F(x) + F_a(t), \tag{3.7.4}$$

where $F_a(t)$ is a random force satisfying the properties in Eqs.(3.6.2) and (3.6.3), and $F(x)$ is an external position-dependent force, typically representing a harmonic trapping potential. We can also rewrite Eq.(3.7.4) in a reduced form:

$$\frac{dv}{dt} = -\gamma v + f(x) + \zeta(t), \tag{3.7.5}$$

where $f(x) = F(x)/m$, and $\zeta(t)$ obeys the conditions (3.6.5) and (3.6.6). Now, we need to consider the full phase space (x, v). The continuity equation written in Eq.(3.7.1) becomes more complex, since we must account not only for the probability current in v, but also for the additional current in x arising from the presence of the force $f(x)$. The continuity equation for this case is given by the Fokker–Planck–Kramers equation [61]:

$$\frac{\partial P}{\partial t} = -\left[v\frac{\partial P}{\partial x} + f(x)\frac{\partial P}{\partial v} + \frac{\partial J}{\partial v}\right], \tag{3.7.6}$$

where the current J is given by Eq.(3.7.2).

3.8 Stochastic Thermodynamics for Brownian particles

We now turn to the description of stochastic thermodynamics for a system governed by the Langevin equations (3.6.4) and (3.7.4). The approach begins with the same premise as in Sec.(3.4): we first assume that the entropy (which will again be given by the Gibbs expression (3.4.9)) is a function of time, and from its time derivative we will be able to identify the entropy production and dissipation. We now write the continuous form of Eq.(3.4.9) as

$$S(t) = -k_B \int_\Omega P(\Omega, t)\, \ln P(\Omega, t)\, d\Omega, \tag{3.8.1}$$

where Ω denotes the phase space of the particle, which may be x for the Fokker–Planck case or (x, v) for the Fokker–Planck–Kramers case. The time derivative of the entropy is then given by

$$\begin{aligned} \dot{S} &= -\int_\Omega \frac{\partial}{\partial t}\left[P(\Omega, t)\ln P(\Omega, t)\right] d\Omega \\ &= -\int_\Omega \frac{\partial P}{\partial t}\ln P(\Omega, t)\, d\Omega. \end{aligned} \tag{3.8.2}$$

For the Fokker–Planck case, Ω is the one-dimensional velocity space, and using Eq.(3.7.1) we obtain

$$\dot{S} = \int_{-\infty}^{\infty} \frac{\partial J}{\partial v} \ln P(v,t)\, dv. \tag{3.8.3}$$

The integral above can be evaluated by integration by parts:

$$\dot{S} = J \ln P(v,t)|_{-\infty}^{\infty} - \int_{-\infty}^{\infty} J \frac{\partial}{\partial v} \ln P(v,t)\, dv. \tag{3.8.4}$$

The boundary term vanishes because both the probability current J and the probability P tend to zero as $v \to \pm\infty$. After some algebra and another integration by parts (now applied to $J \ln P$), we obtain

$$\dot{S} = \int_{-\infty}^{\infty} \frac{2J^2}{\Gamma P}\, dv + \int_{-\infty}^{\infty} \frac{vJ}{\Gamma}\, dv. \tag{3.8.5}$$

The first term on the right-hand side is always non-negative, vanishing when $J = 0$. This is easy to see: $\frac{J^2}{P}$ is a convex function that tends to zero at the boundaries ($v \to \pm\infty$). On the other hand, there is no sign restriction for the second term in Eq.(3.8.5). Thus, we identify

$$\sigma = \int_{-\infty}^{\infty} \frac{2J^2}{\Gamma P}\, dv \geq 0, \tag{3.8.6}$$

and

$$\phi = -\int_{-\infty}^{\infty} \frac{v}{\Gamma} J\, dv, \tag{3.8.7}$$

as the entropy production and entropy flux, respectively.

For the Fokker–Planck–Kramers case, the approach is similar, although the integral becomes more cumbersome:

$$\dot{S} = -\frac{\partial}{\partial t} \left[\int_{-\infty}^{\infty} \int_{-\infty}^{\infty} P(x,v,t) \ln P(x,v,t)\, dx\, dv \right], \tag{3.8.8}$$

which can be rewritten as

$$\dot{S} = \int_{-\infty}^{\infty} \int_{-\infty}^{\infty} \frac{\partial P}{\partial t} \ln P(x,v,t)\, dx\, dv. \tag{3.8.9}$$

Substituting Eq.(3.7.6) yields

$$\dot{S} = \int_{-\infty}^{\infty} \int_{-\infty}^{\infty} \left[v \frac{\partial P}{\partial x} + f(x) \frac{\partial P}{\partial v} + \frac{\partial J}{\partial v} \right] \ln P(x,v,t)\, dx\, dv. \tag{3.8.10}$$

The same integration by parts can be applied, with the same consequences: the current and the probability vanish in the limits $v \to \pm\infty$ and $x \to \pm\infty$. After performing these steps, we obtain

$$\dot{S} = \int_{-\infty}^{\infty}\int_{-\infty}^{\infty} \frac{2J^2}{\Gamma P}\, dx\, dv + \int_{-\infty}^{\infty}\int_{-\infty}^{\infty} \frac{vf(x)}{\Gamma} J\, dx\, dv, \tag{3.8.11}$$

with

$$\sigma = \int_{-\infty}^{\infty}\int_{-\infty}^{\infty} \frac{2J^2}{\Gamma P}\, dx\, dv \geq 0, \tag{3.8.12}$$

and

$$\phi = -\int_{-\infty}^{\infty}\int_{-\infty}^{\infty} \frac{vf(x)}{\Gamma} J\, dx\, dv. \tag{3.8.13}$$

We now derive the heat flux and work. These quantities can be obtained for both cases using Eqs.(3.8.7) and (3.8.13), or by considering the dynamics of the internal energy $\dot{U} = \frac{d}{dt}\langle E(t)\rangle$ and applying the NESS condition. One can compute the time derivative of the total energy $E(t) = K(v) + V(x)$ by using the Langevin equation. For the Fokker–Planck–Kramers system, we have

$$\dot{U} = \int_{-\infty}^{\infty}\int_{-\infty}^{\infty} \frac{d}{dt}(EP)\, dx\, dv = \frac{m}{2}\int_{-\infty}^{\infty}\int_{-\infty}^{\infty} v^2 \frac{\partial P}{\partial t}\, dx\, dv + \int_{-\infty}^{\infty}\int_{-\infty}^{\infty} V(x)\frac{\partial P}{\partial t}\, dx\, dv. \tag{3.8.14}$$

we have If the potential $V(x)$ is purely harmonic, the contribution of the second term on the right-hand side of the integral above vanishes, leaving only the first term. Applying the Fokker–Planck and Fokker–Planck–Kramers equations and using the first law of thermodynamics, $\dot{U} = -(\dot{W} + \dot{Q})$, we obtain

$$\dot{W} = -mf(t)\langle v\rangle, \tag{3.8.15}$$

and

$$\dot{Q} = \gamma\left(m\langle v^2\rangle - k_{\mathsf{B}}T\right), \tag{3.8.16}$$

for the work and heat fluxes, respectively.

Chapter 4

Brownian Collisional Engines

The collisional (or sequential) approach has been widely used in several examples in quantum mechanics [86]. Here, we adapt the idea of sequential interactions between a system and uncorrelated reservoirs to a single Brownian particle. Such an adaptation is straightforward when taking into account the molecular chaos hypothesis: a Brownian particle immersed in a fluid interacts only with a small fraction of the environment over a given time interval and each fraction with which the particle collides is uncorrelated with the previous one. An engine under this framework consists of sequentially placing the Brownian particle in contact with distinct thermal reservoirs and subjecting it to external driving forces during each stroke. This procedure must occur in cycles: the particle begins its dynamics at a given point in phase space and returns to exactly the same point at the end of the process. Each change of reservoir must occur as rapidly as possible, making each transition effectively adiabatic.

This framework was described in [74] and under an appropriate choice of parameters it can operate as a work-to-work converter, where an input work is transformed into another form of work at the output. For example, a molecular

motor uses the chemical work extracted from ATP hydrolysis to generate mechanical work, allowing the protein to take a step forward along a filament [8]. Despite its reliability in various scenarios, this framework can operate rather inefficiently depending on how it is designed. For instance, the duration of each stroke may be too short, preventing the system from thermalizing with the environment or too long, causing all thermodynamic currents to vanish during the stroke (see 2.2.2). Other physical quantities also influence the output, such as the temperatures of the reservoirs and the shape of the external forces. Hence, it is important to search for strategies that ensure the cycle operates as an engine under an optimal choice of parameters.

In this chapter, we exploit several maximization methods for this system. We begin by determining the optimal output through fine-tuning the external force (drive) applied during each stroke, which can be modified in both shape and amplitude. We first consider a simple case under the overdamped approximation. In this regime, the effect of the particle's inertia is negligible, in contrast to the underdamped approximation.

To investigate the role of distinct drives in each stroke and their respective consequences for the thermodynamics of the system, two representative examples are considered: harmonic and power-law drivings. The simplest and most feasible way to drive the Brownian particle out of equilibrium is through power-law expressions, since they include the linear drive. This case is not only the simplest, but also, perhaps surprisingly, the most efficient among all choices of drives under the same physical conditions, as will be shown later in this chapter. The thermodynamic quantities of the Brownian work-to-work converter can be obtained analytically, as well as the corresponding optimal parameters, which can be expressed in terms of the Onsager coefficient in the linear regime.

Despite the reliability of the conditions discussed in the previous paragraph, the overdamped approximation is limited, since the corresponding Langevin equation does not exhibit explicit dependence on the position (see Sec. 3.6). This restricts the model in practical applications where the particle's position plays an essential role. To overcome this limitation, we also consider the un-

derdamped regime, in which both inertia and position are explicitly taken into account. As a result, we observe an interesting phenomenon of resonance: periodic drives can pull the system in such a way that the amplitude of the mean velocity increases, leading to an enhancement of both power and efficiency with a relatively low trade-off cost.

In the problems summarized in the previous paragraphs, we restrict our analysis to the NESS regime, in which the set of periodic strokes imposes a non-equilibrium steady state. As discussed in previous chapters, the NESS is reached in the long-time regime under periodic (or constant) driving of the system. When an optimal value of power or efficiency is obtained, the analysis is limited to their mean values. However, at small scales, fluctuations are large and rare events become significant, including the occurrence of "super-Carnot" engines. Here, we show that fluctuations in small-scale engines can offer statistical advantages, in some cases even boosting the output. To capture this essential feature, we study the collisional Brownian work-to-work converter in terms of the joint probability distribution of power and efficiency, addressing questions such as: what is the probability distribution associated with outputs that locally or globally maximize both efficiency and power simultaneously? In this chapter, we address these and other questions related to probability distributions and the thermodynamics of fluctuations in Brownian engines.

4.1 Overdamped Case

As discussed in Chap. 3.6, we briefly recap the Langevin equation that describes the dynamics of a Brownian particle. Here, we focus on the simplest realization of an engine composed of two strokes. More precisely, we consider a Brownian particle that sequentially interacts with two reservoirs, labeled 1 and 2, with $T_2 > T_1$. The particle starts in reservoir 1, interacts with it during a given time interval and then instantaneously switches to the second reservoir, eventually returning to the initial configuration in the first reservoir.

The total time required to complete one cycle is denoted by τ, with each

stroke $i \in \{1, 2\}$ lasting for $\tau/2$. This choice of equal time intervals is referred to as the symmetric protocol. In general, the duration of each stroke influences the engine output [47, 60]. However, we restrict ourselves to the simplest case in which both strokes have the same duration, since our objective is to investigate the role of fine-tuning the external drives in the optimization process while keeping the stroke duration fixed.

During stroke i, the Brownian particle of mass m, in contact with a thermal bath at temperature T_i, is described by the Langevin equation

$$\frac{dv_i(t)}{dt} = -\gamma_i v_i(t) + \tilde{f}_i(t) + \zeta_i(t), \tag{4.1.1}$$

where γ_i is the viscous coefficient of the fluid and $\tilde{f}_i(t)$ is an external force that depends only on time, not on position or velocity. The stochastic force per unit mass, $\zeta_i(t)$, represents the thermal interaction between the system and the reservoir and satisfies the Gaussian noise properties

$$\langle \zeta_i(t) \rangle = 0$$

for $i = 1, 2$ and all t and

$$\langle \zeta_i(t')\zeta_j(t) \rangle = \frac{2\gamma_i k_\mathrm{B} T_i}{m}\, \delta_{ij}\, \delta(t' - t).$$

As discussed in Sec. 3.6, the probability distribution in phase space for a particle described by a Langevin equation obeys a Fokker–Planck (FP) equation. Since Eq. (4.1.1) does not depend on the particle position, the corresponding FP equation reads

$$\frac{\partial P_i}{\partial t} = -\frac{\partial J_i}{\partial v} - \tilde{f}_i(t)\frac{\partial P_i}{\partial v}, \tag{4.1.2}$$

where J_i is the probability current, given by

$$J_i = -\gamma_i v P_i - \frac{\gamma_i k_\mathrm{B} T_i}{m}\frac{\partial P_i}{\partial v}. \tag{4.1.3}$$

Once again we recover an already discussed property of the bondaries of the probability distribution $P_i(v, t)$, assuming that $\lim_{|v|\to\infty} P_i = \lim_{|v|\to\infty} J_i = 0$ and as made in the Sec.(3.8), the time evolution of the internal energy for each stroke $U_i = m\langle v_i^2 \rangle/2$ is given by a a sum of two terms

$$\frac{d}{dt}U_i(t) = -[\dot{W}_i(t) + \dot{Q}_i(t)], \tag{4.1.4}$$

with the mean power $\dot{W}(t)$ and heat $\dot{Q}_i(t)$ computed by the following expressions,

$$\dot{W}_i(t) = -m\langle v_i\rangle(t)\tilde{f}_i(t), \tag{4.1.5}$$

and

$$\dot{Q}_i(t) = \gamma_i(m\langle v_i^2\rangle(t) - k_{\mathsf{B}}T_i). \tag{4.1.6}$$

By averaging the expression 4.1.4 over a complete period, one recovers the 1st law of thermodynamics, $\sum_{j\in\{1,2\}} \overline{\dot{W}}_j + \overline{\dot{Q}}_j = 0$, where we define the averages by

$$\overline{\dot{W}}_j := \int_{\tau_{j-1}}^{\tau_j} \dot{W}_j(t)dt, \qquad \overline{\dot{Q}}_j := \int_{\tau_{j-1}}^{\tau_j} \dot{Q}_j(t)dt. \tag{4.1.7}$$

where $\tau_j = j\tau/2$. The time evolution of the entropy $S(t)$ can proceed following the same steps presented in Chap. 3.8. As proved in the same section, such an evolution is expressed in the form,

$$\frac{d}{dt}S_i = \sigma_i(t) - \Phi_i(t), \tag{4.1.8}$$

where $\sigma_i(t)$ and $\Phi_i(t)$ are the entropy production rate and the entropy flux, respectively, whose expressions are given by

$$\sigma_i(t) = \frac{m}{\gamma_i T_i}\int \frac{J_i^2}{P_i}dv \qquad \text{and} \qquad \Phi_i(t) = \frac{\dot{Q}_i(t)}{T_i}. \tag{4.1.9}$$

One can also compute the average of the expressions above. In the NESS, we expect that the entropy (and also the internal energy U_i) becomes a constant value on average. Hence, from Eq. (4.1.8) we have $\overline{\sigma} = \overline{\Phi}$. In general, computing the expression of $\overline{\Phi}$ is more feasible than integrating the left-hand side of Eq. (4.1.9). We then find an expression for $\overline{\sigma}$ following the procedure that consists of integrating the right-hand side of the equation, $\overline{\Phi} = \overline{\sigma} = \int_0^{\tau/2}\Phi_1(t)\,dt + \int_{\tau/2}^{\tau}\Phi_2(t)\,dt$

$$\overline{\sigma} = \frac{4T^2}{4T^2 - \Delta T^2}\left[-\frac{1}{T}(\overline{\dot{W}}_1 + \overline{\dot{W}}_2) + (\overline{\dot{Q}}_1 - \overline{\dot{Q}}_2)\frac{\Delta T}{2T^2}\right], \tag{4.1.10}$$

where $T = (T_1+T_2)/2$ is the mean temperature of the system and $\Delta T = T_2 - T_1$ is the temperature difference. This expression is similar to Eq. (2.2.6) in Chap. 2.

The probability of the system is given by the solution of the FP equation presented in expression (4.1.2). Once we have an expression for $P_i(v,t)$, we can obtain all relevant thermodynamic quantities we need. For this special case,

the distribution for each stroke is still Gaussian (even outside equilibrium), given by the expression

$$P_i(v,t) = \exp\{-[v-\langle v_i(t)\rangle]^2/2b_i(t)\}/\sqrt{2\pi b_i(t)}, \tag{4.1.11}$$

in which the mean $\langle v_i(t)\rangle$ and variance $b_i(t)$, given by Eq. (3.6.13), are time-dependent and determined by the following equations:

$$\frac{d\langle v_i\rangle(t)}{dt} = -\gamma_i\langle v_i\rangle(t) + \tilde{f}_i(t), \tag{4.1.12}$$

and

$$\frac{db_i(t)}{dt} = -2\gamma_i b_i(t) + \frac{2\gamma_i k_B T_i}{m}. \tag{4.1.13}$$

Since the particle must return to the initial state after the end of a cycle, the external forces are always periodic with period τ, $f_i(t) = f_i(t+\tau)$. A convenient manner to define a periodic function is to express it in terms of two quantities: an amplitude, which will be denoted here as a strength X_i and a function $g_i(t)$, which defines the kind of driving (piece-wise linear, sinusoidal, etc.). It is worth mentioning that the definitions of these drivings do not depend on the velocity or position of the Brownian particle. We define the drivings for each stroke as follows

$$\tilde{f}_i(t) = \begin{cases} X_1 g_1(t), & t \in [0,\tau/2] \\ X_2 g_2(t), & t \in [\tau/2,\tau]. \end{cases} \tag{4.1.14}$$

Another condition we impose is the continuity of the probability distribution defined in Eq. 4.1.11 at the moments of the reservoir changes, i.e., at times $t = \tau/2$ and $t = \tau$. This condition can be expressed in terms of the variance $b_i(t)$ and the average velocity $\langle v_i(t)\rangle$, obtained by computing the mean value of Eq. (4.1.1),

$$\langle v_1\rangle(\tau/2) = \langle v_2\rangle(\tau/2), \quad b_1(\tau/2) = b_2(\tau/2), \tag{4.1.15}$$

$$\langle v_1\rangle(0) = \langle v_2\rangle(\tau), \quad b_1(0) = b_2(\tau). \tag{4.1.16}$$

The solution of the differential Eqs. (4.1.12 and 4.1.13) with the boundary conditions defined above leads to the following general expressions (evaluated for $k_B = 1$ and $\gamma_1 = \gamma_2 = \gamma$):

$$\langle v_1\rangle(t) = X_1\int_0^t e^{\gamma(t'-t)}g_1(t')dt' + \frac{1}{e^{\gamma\tau}-1}\left\{X_1\int_0^{\tau/2} e^{\gamma(t'-t)}g_1(t')dt' + X_2\int_{\tau/2}^{\tau} e^{\gamma(t'-t)}g_2(t')dt'\right\}, \tag{4.1.17}$$

$$\langle v_2\rangle(t) = X_2\int_{\tau/2}^{t} e^{\gamma(t'-t)}g_2(t')dt' + \frac{1}{e^{\gamma\tau}-1}\left\{e^{\gamma\tau}X_1\int_0^{\tau/2} e^{\gamma(t'-t)}g_1(t')dt' + X_2\int_{\tau/2}^{\tau} e^{\gamma(t'-t)}g_2(t')dt'\right\}, \tag{4.1.18}$$

$$b_1(t) = -\frac{1}{m}\frac{(T_1-T_2)}{(1+e^{-\gamma\tau})}e^{-2\gamma t} + \frac{T_1}{m}, \quad b_2(t) = -\frac{1}{m}\frac{(T_2-T_1)}{(1+e^{-\gamma' tau}}e^{-2\gamma(t-\tau/2)} + \frac{T_2}{m} \tag{4.1.19}$$

$$\overline{\dot{W}}_1 = -\frac{m}{\tau(e^{\gamma\tau}-1)}\Bigg[X_1^2\Bigg((e^{\gamma\tau}-1)\int_0^{\tau/2} g_1(t)e^{-\gamma t}\int_0^t g_1(t')e^{\gamma t'}\,dt'dt + \int_0^{\tau/2} g_1(t)e^{-\gamma t}\,dt\int_0^{\tau/2} g_1(t')e^{\gamma t'}\,dt'\Bigg) + X_1X_2\int_0^{\tau/2} g_1(t)e^{-\gamma t}\,dt\int_{\tau/2}^{\tau} g_2(t')e^{\gamma t'}\,dt'\Bigg], \tag{4.1.20}$$

$$\overline{\dot{Q}}_1 = \frac{\gamma m}{\tau}\left[\int_0^{\tau/2}\langle v_1\rangle^2 dt - \frac{1}{2\gamma m}\tanh(\gamma\tau/2)(T_1-T_2)\right] \tag{4.1.21}$$

$$\overline{\dot{W}}_2 = -\frac{m}{\tau(e^{\gamma\tau}-1)}\Bigg[X_2^2\Bigg(\int_{\tau/2}^{\tau} g_2(t)e^{-\gamma t}dt\int_{\tau/2}^{\tau} g_2(t')e^{\gamma t'}dt' + (e^{\gamma\tau}-1)\int_{\tau/2}^{\tau}[g_2(t)e^{-\gamma t}\int_{\tau/2}^{t} g_2(t')e^{\gamma t'}dt']dt\Bigg) + X_1X_2e^{\gamma\tau}\Bigg(\int_{\tau/2}^{\tau} g_2(t)e^{-\gamma t}\,dt\int_0^{\tau/2} g_1(t')e^{\gamma t'}\,dt'\Bigg)\Bigg], \tag{4.1.22}$$

$$\overline{\dot{Q}}_2 = \frac{m\gamma}{\tau}\left[\int_{\tau/2}^{\tau}\langle v_2\rangle^2 dt + \frac{1}{2\gamma m}\tanh(\gamma\tau/2)(T_1-T_2)\right], \tag{4.1.23}$$

It is worth emphasizing that Eqs. (4.1.20)–(4.1.23) are general and valid for any kind of driving and temperatures. Close to equilibrium, the entropy production (Eq. (4.1.9)) assumes the familiar flux-times-force form $\overline{\sigma} \approx J_1f_1 + J_2f_2 + J_Tf_T$, where

$$f_1 = X_1/T \;\;;\;\; f_2 = X_2/T \;\;;\;\; f_T = \Delta T/T^2 \tag{4.1.24}$$

($\Delta T = T_2 - T_1$) and fluxes defined by

$$\overline{\dot{W}}_1 = -TJ_1f_1 \;\;;\;\; \overline{\dot{W}}_2 = -TJ_2f_2 \;\;;\;\; \overline{\dot{Q}}_1 - \overline{\dot{Q}}_2 = 2J_T. \tag{4.1.25}$$

The thermodynamic currents J_j are written as a linear combination of the Onsager coefficients and the thermodynamic forces (see Sec. (2.2)), $J_1 = L_{11}f_1 + L_{12}f_2$ and $J_2 = L_{22}f_2 + L_{21}f_1$, leading to a bilinear form for Eqs. (4.1.20) and (4.1.22),

$$\overline{\dot{W}}_1 = -T(J_1f_1) = -T(L_{11}f_1^2 + L_{12}f_1f_2), \tag{4.1.26}$$

$$\overline{\dot{W}}_2 = -T(J_2f_2) = -T(L_{22}f_2^2 + L_{21}f_1f_2). \tag{4.1.27}$$

As discussed in Sec. (2.2.1), in general the following symmetric relation is valid: $L_{12} = L_{21}$. However, as we will see in the next paragraphs, this relation is not universal (see, for example, the Onsager-Casimir relation [51]). In our particular case, the choice of the driving shape given by the function $g_i(t)$ strongly affects the symmetry of the Onsager coefficients, reducing the latter equality to a particular scenario obtained by a proper choice of the kind of driving. We compute the general expression for the Onsager coefficients as follows,

$$\begin{aligned} L_{11} &= \frac{mT}{\tau\left(e^{\gamma\tau}-1\right)}\Bigg[\left(e^{\gamma\tau}-1\right)\int_0^{\tau/2} g_1(t)e^{-\gamma t}\int_0^t g_1(t')e^{\gamma t'}\,dt'dt \\ &+ \int_0^{\tau/2} g_1(t)e^{-\gamma t}dt\int_0^{\tau/2} g_1(t')e^{\gamma t'}\,dt'\Bigg], \end{aligned} \tag{4.1.28}$$

$$\begin{aligned} L_{22} &= \frac{mT}{\tau\left(e^{\gamma\tau}-1\right)}\Bigg[\int_{\tau/2}^{\tau} g_2(t)e^{-\gamma t}\,dt\int_{\tau/2}^{\tau} g_2(t')e^{\gamma t'}\,dt' \\ &+ \left(e^{\gamma\tau}-1\right)\int_{\tau/2}^{\tau} g_2(t)e^{-\gamma t}\int_{\tau/2}^{t} g_2(t')e^{\gamma t'}\,dt'dt\Bigg], \end{aligned} \tag{4.1.29}$$

$$L_{12} = \frac{mT}{\tau\left(e^{\gamma\tau}-1\right)}\int_0^{\tau/2} g_1(t)e^{-\gamma t}\,dt\int_{\tau/2}^{\tau} g_2(t')e^{\gamma t'}\,dt' \tag{4.1.30}$$

$$L_{21} = \frac{mTe^{\gamma\tau}}{\tau\left(e^{\gamma\tau}-1\right)}\int_0^{\tau/2} g_1(t')e^{\gamma t'}\,dt'\int_{\tau/2}^{\tau} g_2(t)e^{-\gamma t}\,dt, \tag{4.1.31}$$

$$L_{TT} = \frac{T^2}{2\tau}\tanh\left(\frac{\gamma\tau}{2}\right), \tag{4.1.32}$$

which are the general expressions for this description: using the above expressions, one can compute the Onsager coefficients for any choice of (at least continuous) shape of protocol $g_i(t)$.

We also address a particular case of a work-to-work converter, when its operation occurs in an isothermal environment (both reservoirs have the same temperature). In our model, the heat flux does not contribute to the final work output, being responsible only for increasing the dissipation without any performance gain. Hence, as we will also see later in this chapter, the existence of a temperature gradient only makes the engine less efficient, pointing to an isothermal scenario as a candidate for the best efficiency. In such a case, $T_1 = T_2 = T$ and $\Delta T = 0$ and Eq. (4.1.10) is reduced to,

$$\overline{\sigma} = -\frac{\overline{\dot{W}}_1 + \overline{\dot{W}}_2}{T} = L_{11}f_1^2 + L_{22}f_2^2 + (L_{12}+L_{21})f_1f_2, \tag{4.1.33}$$

which is the same expression discussed in Sec. (2.2.1).

4.1.1 Engine regime and efficiency

Since our main goal is to find an optimization criterion for both power output and efficiency, we must find an expression for both quantities in terms of the external driving shape $g_j(t)$ and amplitude X_j. For this particular problem, one can use directly the expressions 2.2.21 and 2.2.20 in the expressions for power and efficiency and optimize the resulting expressions. However, before we start to compute each component individually, we must define a sign convention. The system receives from the reservoir the work flux $\overline{\dot{W}_{\text{in}}} < 0$ and the heat flux $\overline{\dot{Q}}_{\text{in}} < 0$. The system will work as an engine if and only if it imposes against the system an output $\mathcal{P} := \overline{\dot{W}}_{\text{out}} > 0$ and the efficiency defined in the expression below is in the interval $0 < \eta \leq 1$,

$$\eta = -\frac{\mathcal{P}}{\overline{\dot{W}_{\text{in}}} + \overline{\dot{Q}_{\text{in}}}}. \tag{4.1.34}$$

If these conditions are not met, the system rather works in another regime (pump or dud, for example) or is not physically possible due to the second law of thermodynamics []. Thus, given an amount of energy injected into the system, whether in the form of $\overline{\dot{W}}_{\text{in}} := \overline{\dot{W}}_1 < 0$ and/or $\overline{\dot{Q}}_{\text{in}} = \overline{\dot{Q}}_1\Theta(-\overline{\dot{Q}}_1) + \overline{\dot{Q}}_2\Theta(-\overline{\dot{Q}}_2)$ (with $\Theta(x)$ denoting a Heaviside function), it is partially converted into power $\mathcal{P} := \overline{\dot{W}}_2$. To gain some insight into the role of the drivings in the power output $\mathcal{P}$ and in the efficiency η, we shall split the analysis into two parts, focusing first on the simplest (and most efficient) scenario: the isothermal setup.

4.1.2 Brownian work-to-work converters and distinct maximization routes

Fixing the input thermodynamic force f_1, we can decide which variable will be fine-tuned in order to find an optimal result for the engine output. There are two open variables that can be used in such a search: the output thermodynamic force f_2, which is also related to the amplitude of the driving X_2 and a generic variable related to the shape of the protocol, named δ. The former variable can assume any quantity related to $g_i(t)$ and the results discussed below are general. Two examples of quantities that δ can assume are discussed in Sec. (4.1.3).

With these variables, we have three distinct routes of optimization: i) optimization in terms of f_2 (keeping f_1 and δ fixed); ii) maximization in terms of the driving parameter δ for fixed thermodynamic forces f_1 and f_2; iii) simultaneous optimization for both f_2 and δ (fixing f_1).

The former case (maximization with respect to the output force) is similar to the findings from Sec. 2.2.1, in which the maximum power $\mathcal{P}_{\mathsf{MP},f_2}$ (with the efficiency η_{MP,f_2}) and maximum efficiency η_{ME,f_2} (with power $\mathcal{P}_{\mathsf{ME},f_2}$) are obtained via the optimal search for the values f_{2MP} and f_{2ME}. We now recap the equations derived in Sec. 2.2.1 and repeat them here only for the sake of clarity. From Eqs. (2.2.20) and (2.2.21) we have,

$$\frac{f_{2ME}}{f_1} = \frac{L_{11}}{L_{12}}\left(\sqrt{1-\frac{L_{12}L_{21}}{L_{11}L_{22}}}-1\right) \quad \text{and} \quad \frac{f_{2MP}}{f_1} = \frac{-L_{21}}{2L_{22}}, \tag{4.1.35}$$

and their respective efficiencies are given by Eqs. (2.2.22) and (2.2.24),

$$\eta_{ME,f_2} = -\frac{L_{21}}{L_{12}} + \frac{2L_{11}L_{22}}{L_{12}^2}\left(1-\sqrt{1-\frac{L_{12}L_{21}}{L_{11}L_{22}}}\right), \tag{4.1.36}$$

and

$$\eta_{MP,f_2} = \frac{L_{21}^2}{4L_{11}L_{22}-2L_{12}L_{21}}, \tag{4.1.37}$$

respectively. With these expressions in hand, we can find the power at maximum efficiency and the maximum power, namely $\mathcal{P}_{\mathsf{ME},f_2}$ and $\mathcal{P}_{\mathsf{MP},f_2}$, by applying directly the expressions $f_{2\mathsf{ME}}$ and $f_{2\mathsf{MP}}$ into the expression for $\mathcal{P}$.

In fact, the expressions above are valid considering the driving parameter δ fixed, which can be initially adjusted before the maximization above. Now, we investigate the opposite case: fixing f_1 and f_2 and varying only δ. Using the same approach as in the case above, we obtain the driving parameter that maximizes the power output δ_{MP} and the driving parameter that maximizes the efficiency δ_{ME}, which fulfill the following expressions:

$$\frac{L'_{21}(\delta_{MP})}{L'_{22}(\delta_{MP})} = -\frac{f_2}{f_1}, \tag{4.1.38}$$

and

$$\Delta_{2212}(\delta_{ME})f_2^2 + \Delta_{2111}(\delta_{ME})f_1^2 + \left[\Delta_{2211}(\delta_{ME}) + \Delta_{2112}(\delta_{ME})\right]f_1 f_2 = 0, \tag{4.1.39}$$

where $L'_{ij} \equiv \nabla L_{ij}(\delta)/\nabla\delta$ is the derivative of the coefficient L_{ij} with respect to the driving parameter δ and $\Delta_{ijkl}(\delta) = L'_{ij}(\delta)L_{kl}(\delta) - L'_{kl}(\delta)L_{ij}(\delta)$. The maximum values for the power and efficiency are given by

$$\mathcal{P}_{MP,\delta} = \frac{L'_{21}(\delta_{MP})}{L'^{2}_{22}(\delta_{MP})}\left[L_{21}(\delta_{MP})L'_{22}(\delta_{MP}) - L_{22}(\delta_{MP})L'_{21}(\delta_{MP})\right] f_1^2, \tag{4.1.40}$$

and

$$\eta_{ME,\delta} = -\frac{L_{22}(\delta_{ME})f_2^2 + L_{21}(\delta_{ME})f_1 f_2}{L_{11}(\delta_{ME})f_1^2 + L_{12}(\delta_{ME})f_1 f_2}, \tag{4.1.41}$$

respectively. The power at maximum efficiency, $\mathcal{P}_{\mathsf{ME},\delta}$ and the efficiency at maximum power, $\eta_{\mathsf{MP},\delta}$, can be obtained directly by substitution of the above results into the expressions for $\mathcal{P}$ and η.

With the two methods discussed above, we shall find the local maxima for both power and efficiency. Naively speaking, we are assuming that the surfaces given by the functions $\mathcal{P}(\delta, f_2)$ and $\eta(\delta, f_2)$, which are mapped into a 2D heat map as we will show in Sec. (4.1.3), can be examined through two "curves of maximization" composed of the points $(\delta, f_{2\mathsf{MP/ME}})$ and $(\delta_{\mathsf{MP/ME}}, f_2)$ for the δ-fixed maximization and for the f_2-fixed maximization, respectively. Depending on the system or the kind of driving, these curves may have an intersection point that will be referred to as a global maximization, which means that the power/efficiency has simultaneous maximization in terms of the pair δ and f_2. When it exists, this intersection will always coincide with the global maximum of the output quantities when the system operates as an engine. We will denote such an intersection point as $(\delta^*_{\mathsf{MP/ME}})$ and for the power, for instance, it can be obtained using Eqs. (4.1.35) and (4.1.38) simultaneously,

$$\frac{L'_{21}(\delta^*_{MP})}{L'_{22}(\delta^*_{MP})} = \frac{1}{2}\frac{L_{21}(\delta^*_{MP})}{L_{22}(\delta^*_{MP})} \quad \text{and} \quad \frac{f^*_{2MP}}{f_1} = -\frac{1}{2}\frac{L_{21}(\delta^*_{MP})}{L_{22}(\delta^*_{MP})}, \tag{4.1.42}$$

with the global maximum power value and efficiency value given, respectively, by

$$\mathcal{P}^* = \frac{1}{4}\frac{L^2_{21}(\delta^*_{MP})}{L_{22}(\delta^*_{MP})} f_1^2, \tag{4.1.43}$$

and

$$\eta^* = \frac{L^2_{21}(\delta^*_{MP})}{4L_{11}(\delta^*_{MP})L_{22}(\delta^*_{MP}) - 2L_{21}(\delta^*_{MP})L_{12}(\delta^*_{MP})}. \tag{4.1.44}$$

4.1.3 Applications

Until now, we have introduced some main expressions and also some theoretical tools to find an optimal route for a Brownian sequential work-to-work converter for any kind of external driving. From now on, we intend to apply these general results to two specific kinds of external forces that are useful for a practical/experimental setup: harmonic and power-law drivings. The former appears in several experimental contexts, such as Brownian particles under optical beam traps and optical tweezers [87], electrophoresis processes in colloidal gels [88], or measuring heat capacity experimentally by means of oscillating temperatures [89] and the latter refers to a generalization of the result obtained in Ref. [84], which exhibits complementary features to the harmonic setup.

General harmonic driving forces

In this section, we apply the sequential engine to a general function that converges to a Fourier series. Due to the fact that the engine runs in a cycle, we also assume that the drivings are periodic and, if well behaved, can be written in terms of Fourier components. Thus, our general results here consider only periodic functions, despite the fact that there are non-periodic functions that also converge to Fourier series (and therefore have components that can be applied to the results of this section), such as the Heaviside step function or the Riemann prime counting function. For each half stage we write:

$$g_i(t) = \sum_{n=0}^{\infty} \left[a_n^{(i)} \cos\left(\frac{4\pi n}{\tau} t\right) + b_n^{(i)} \sin\left(\frac{4\pi n}{\tau} t\right) \right], \tag{4.1.45}$$

for the ith stage ($i = 1, 2$), where the coefficients $a_n^{(i)}$ and $b_n^{(i)}$ are given by

$$a_0^{(i)} = \frac{2}{\tau} \int_{(i-1)\tau/2}^{i\tau/2} g_i(t')dt', \tag{4.1.46}$$

$$a_n^{(i)} = \frac{4}{\tau} \int_{(i-1)\tau/2}^{i\tau/2} g_i(t') \cos\left(\frac{4\pi n}{\tau} t'\right) dt', \tag{4.1.47}$$

$$b_n^{(i)} = \frac{4}{\tau} \int_{(i-1)\tau/2}^{i\tau/2} g_i(t') \sin\left(\frac{4\pi n}{\tau} t'\right) dt'. \tag{4.1.48}$$

The thermodynamic quantities and maximization values can be written directly in terms of these coefficients, which implies that once one has computed the Fourier expansion for both $g_1(t)$ and $g_2(t)$, all results are obtained by direct substitution. In Appendix A.1, we show all the evaluated quantities in terms of the Fourier coefficients.

In order to have a feasible and simple example to illustrate our results, we restrict our case to a simple sinusoidal function, with the same frequencies but a difference in phase given by ϕ:

$$g_1(t) = \sin\left(\frac{4\pi}{\tau}t\right) \tag{4.1.49}$$

$$g_2(t) = \sin\left(\frac{4\pi}{\tau}t - \phi\right), \tag{4.1.50}$$

where ϕ is a lag that has the role of controlling the efficiency [90], the dissipation [91] and also guiding the operation mode of the engine [90]. Note that the lag ϕ corresponds to the generic driving variable δ mentioned before. In Fig.(4.1) we show some features considering ϕ fixed and varying Tf_2. It is worth noticing

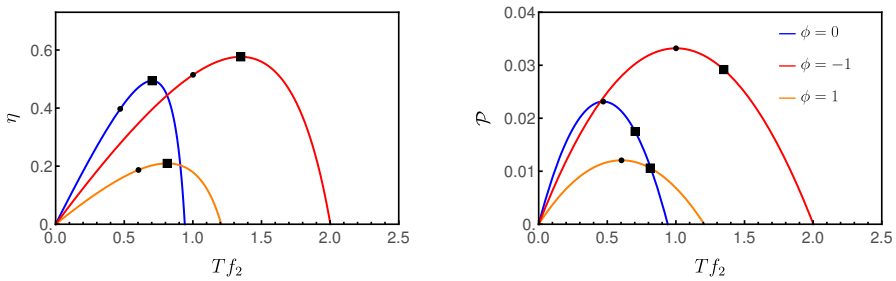

Figure 4.1: For harmonic drivings, the depiction of efficiency η and power output $\mathcal{P}$ versus force Tf_2 for distinct ϕ values. In each panel, from left to right curves, results for $\phi = 0, -1$ and 1, respectively. Squares and circles denote the maximum efficiencies and powers, according to Eqs. (4.1.35)-(4.1.36). In all cases, we set $X_1 = Tf_1 = 1$, $\tau = 2$, $\gamma = k_B = m = 1$ and $T = 1/2$.

that ϕ affects not only both power and efficiency, but also has a role in the engine regime interval. In fact, given a fixed ϕ, we compute the regime $0 < Tf_2 < Tf_m$ where the system operates as an engine ($0 < \eta \leq 1$ and $\mathcal{P} > 0$). We also observe both maxima for power and efficiency (and also other relevant

quantities such as the efficiency at maximum power). Using Eq.(2.2.21), we derive the following expression for $f_{2\mathrm{MP}}$

$$\frac{f_{2\mathrm{MP}}}{f_1} = \frac{4\pi(e^{\gamma\tau}+1)[2\pi\cos(\phi)-\gamma\tau\sin(\phi)]}{\gamma\tau[(e^{\gamma\tau/2}-1)(\gamma^2\tau^2+4\pi^2)-4\gamma\tau(e^{\gamma\tau/2}+1)\sin^2(\phi)]+16\pi^2(e^{\gamma\tau}+1)\cos^2(\phi)}, \tag{4.1.51}$$

A similar (but cumbersome) expression for $f_{2\mathrm{ME}}$ can be obtained. It is important to mention that in the long-period limit, i.e., $\tau\gamma \gg 1$, $f_{2\mathrm{MP}} \to 0$ independent of the lag. On the other hand, $f_{2\mathrm{MP}} \to f_1/(2\cos(\phi))$ for $\tau\gamma \ll 1$.

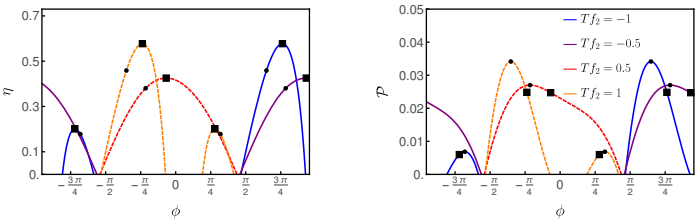

Figure 4.2: For $\tau = 2$ and distinct Tf_2 values, the depiction of efficiency η and power output $\mathcal{P}$ versus ϕ. In each panel, from left to right curves, results for $Tf_2 = -0.5, -1, 0.5$ and 1, respectively. Squares and circles denote the maximum efficiencies and powers, respectively, according to Eqs. (4.1.38) and (4.1.39). In all cases, we set $X_1 = Tf_1 = 1$, $\gamma = k_B = m = 1$ and $T = 1/2$.

We now point to the opposite case, fixing Tf_2 and varying ϕ. In Fig.(4.2) we reveal an additional (and new) feature arising from the lag in the second stage. The inclusion of a lag makes the system present two distinct engine regimes, delimited between two intervals $\phi_{1m} \leq \phi \leq \phi_{2m}$ and $\phi_{3m} \leq \phi \leq \phi_{4m}$ (fulfilling $\mathcal{P} = 0$ at $\phi = \phi_{im}$). Also, this interval depends on the sign of Tf_2, as plotted in Fig.(4.2): the engine regime occurs for positive (negative) output forces when $-\pi/2 < \phi \leq \pi/2$ ($\pi/2 < \phi \leq \pi$).

Finally, the lag also controls the engine performance, having optimal ϕ_{ME} and ϕ_{MP} at which $\eta_{\mathrm{ME},\phi}$ and $\mathcal{P}_{\mathrm{MP},\phi}$ are maximized. The relation between the external driving f_2 and ϕ for the power can be established by applying Eqs. (2.2.20, 2.2.21),

$$\frac{f_2}{f_1} = \frac{\pi[\gamma\tau\,\mathrm{csc}(\phi_{MP})+2\pi\,\mathrm{sec}(\phi_{MP})]}{\gamma^2\tau^2+4\pi^2}, \tag{4.1.52}$$

and a more cumbersome expression for ϕ_{ME} that will be omitted for the sake

of space. In the limits $\gamma\tau \ll 1$ and $\gamma\tau \gg 1$, Eq. (4.1.52) results in $\phi_{\mathsf{MP}} \to \cos^{-1}(f_1/2f_2)$ and zero, respectively. A more complete analysis can be made when we consider a density plot of power and efficiency in terms of Tf_2 and ϕ. In Fig. (4.3) we plot how the choice of Tf_2 and ϕ affects not only the power and efficiency but also the engine regime interval itself. Also, we leave the two maximization routes explicit in the dashed and continuous lines, which represent the optimization with respect to ϕ and f_2, respectively. If we fix, for example, $\phi = 0$, we obtain $\mathcal{P}_{\mathsf{MP},\delta=0} \approx 0.0231$ and $\eta_{\mathsf{ME},\delta=0} \approx 0.494$. A simultaneous optimization corresponds to the point where the curves intersect, equivalently to the intersections between Eqs. (4.1.51) and (4.1.52). In Fig. (4.3) we can see an intersection at the points $\mathcal{P}^* \approx 0.0398$ and $\eta^* \approx 0.581$, both global maxima.

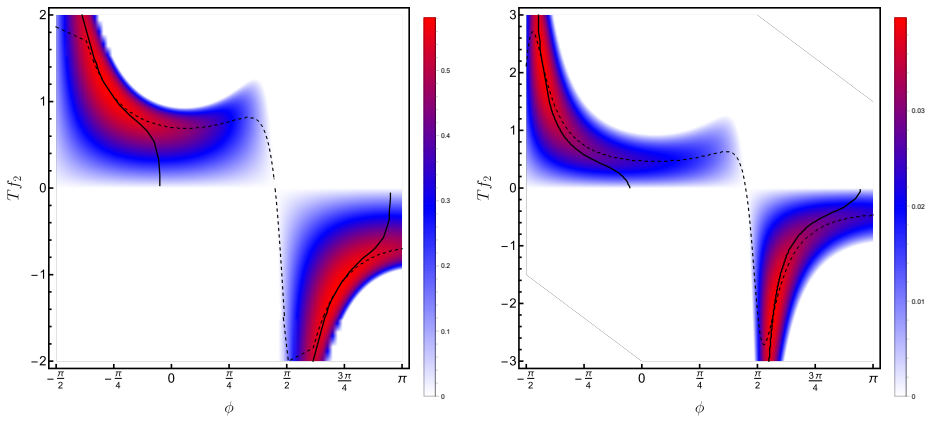

Figure 4.3: For the set of drivings given by Eq. (4.1.50) and $\tau = 2$, the left and right panels depict the phase diagram of the output force $X_2 = Tf_2$ versus the phase difference ϕ for the efficiency and power output, respectively. Continuous and dashed lines denote the maximization with respect to f_2 and ϕ, respectively. Their crossings provide the simultaneous maximizations. In all cases, we set $X_1 = Tf_1 = 1$, $\gamma = k_B = m = 1$ and $T = 1/2$.

Power Law drivings

Next we consider a general algebraic driving acting at each half stage:

$$g(t) = \begin{cases} \left(\frac{2t}{\tau}\right)^{\alpha}, & \text{for } t \in [0, \tau/2] \\ \left(1 - \frac{2t}{\tau}\right)^{\beta}, & \text{for } t \in [\tau/2, \tau], \end{cases} \tag{4.1.53}$$

where α and β assume non-negative integer values. In principle, we could also define half-integer values; however, an inspection of the exact expressions reveals that the Onsager coefficients assume imaginary values when β is a half-integer. A careful analysis also shows that for α as a half-integer, no substantial changes in the computed quantities are present. For these reasons, we will focus our analysis on the simplest case of integer exponents. Eqs. (4.1.20-4.1.32) can be applied in general to such a case and be computed as analytical expressions, although the results are cumbersome and not useful for a more practical analysis of the thermodynamic quantities. Therefore, our analysis will be focused on some remarkable values of α and β. Nonetheless, general expressions for the thermodynamic quantities for any integer α and β are plotted in Appendix (A.2). These drivings will be addressed here as power-law functions and they are a generalization of the analysis made in Ref. [84], which was focused on the particular cases $\alpha = \beta = 0$ and $\alpha = \beta = 1$.

In Fig. (4.4) we show the main portraits of the engine performance by varying the output force for some representative values of Tf_2, α and β. The influence of the choices of α and β on the output values and the engine regime interval is clear. The number α smoothly affects the power and efficiency, reducing the former and enhancing the latter as α increases, also reducing the range in which the system can operate as an engine. In other words, increasing α results in enhanced efficiency, while a loss in power and in the engine range is observed, showing a trade-off relation when this maximization route is adopted. On the other hand, β strongly affects both the output values and the engine regime interval, revealing another trade-off relation. Both power and efficiency decrease as β increases, in exchange for an increase in the engine regime interval $0 \leq f_2 \leq |f_{2m}|$. The sign of the second half of the external driving is highly affected by the choice of β, being positive (negative) when β is odd (even).

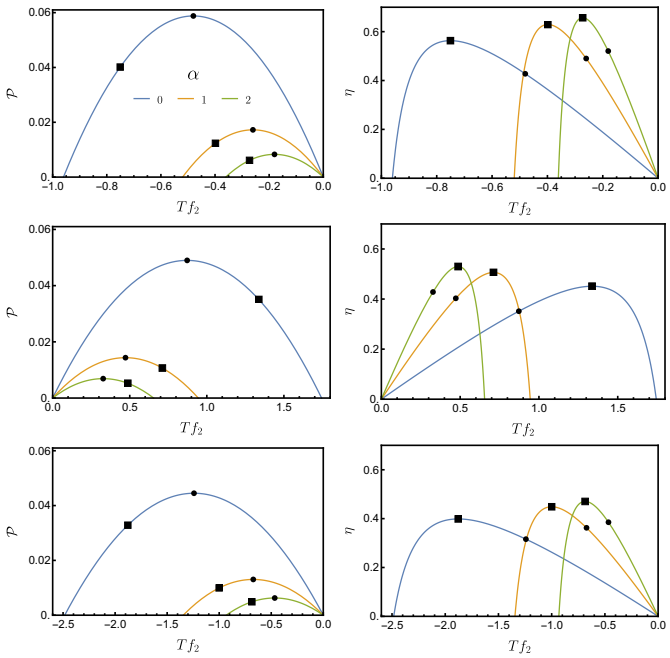

Figure 4.4: For power-law drivings, the depiction of power output $\mathcal{P}$ and efficiency η versus $X_2 = Tf_2$ for representative values of α and β (from top to bottom, $\beta = 0, 1$ and 2). From left to right (left side), the results for $\alpha = 0, 1$ and 2, respectively. Squares and circles denote the maximum efficiencies and powers, according to Eqs. (4.1.35)-(4.1.36). In all cases, we set $X_1 = Tf_1 = 1$, $\tau = \gamma = k_B = m = 1$ and $T = 1/2$.

The global maxima for power and efficiency occur in the simplest scenario, where $\alpha = \beta = 0$ and the g_i are time independent (we call this scenario the "linear case").

Now we do the opposite, searching for a maximization route by fixing Tf_2 and varying α and β. This analysis is plotted in Fig. (4.5) and the maxima points correspond to Eqs. (4.1.38) and (4.1.39). As shown in Fig. (4.5a) and (4.5b), the efficiency is maximized as α increases for $\beta = 0$ and fixed Tf_2, while the optimal power still occurs in the linear case, decreasing for $\alpha > 0$ for any fixed Tf_2, showing once more the trade-off relation in the optimization in terms of the coefficients. Fixing $\alpha = 0$ and varying β, we see that the maximization is

f_2-dependent (see Figs. (4.5c) and (4.5d)). The optimal β ensuring maximum efficiencies $\eta_{\mathrm{mE},\beta}$ and powers $\mathcal{P}_{\mathrm{mP},\beta}$ also follow Eqs. (4.1.38) and (4.1.39), being f_2-dependent and even (odd) for negative (positive) f_2.

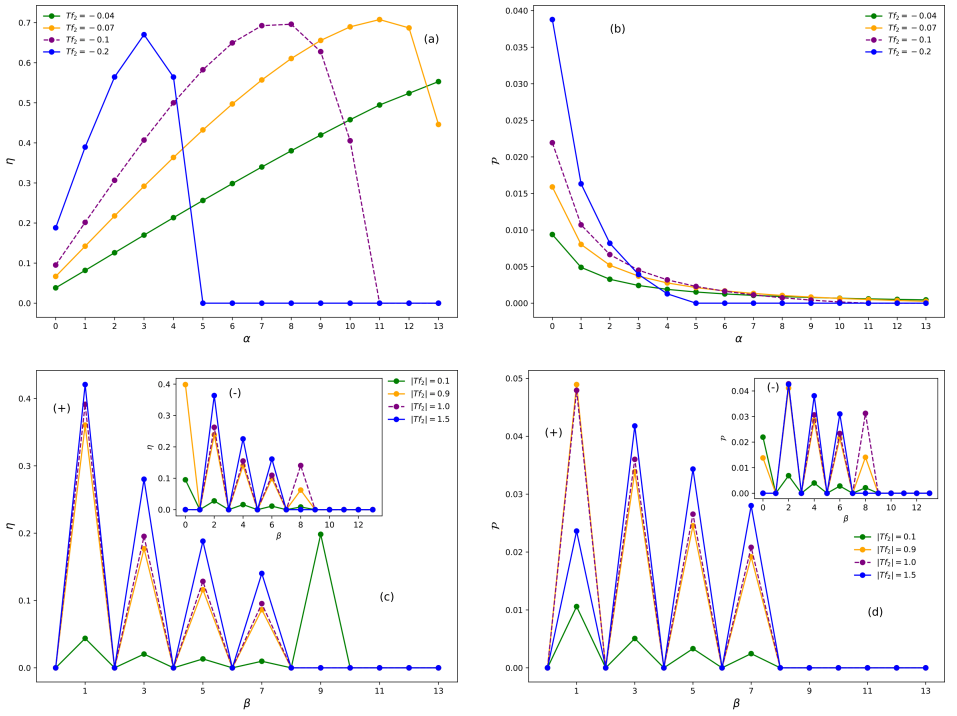

Figure 4.5: For fixed forces $X_2 = Tf_2$, the depiction of efficiency η (a) and $\mathcal{P}$ (c) versus α ($\beta = 0$). Panels (b) and (d) show the same, but β is varied (for fixed $\alpha = 0$). Main panels (insets) in (c) and (d) show results for odd (even) β. In all cases, we set $X_1 = Tf_1 = 1$, $\tau = \gamma = k_B = m = 1$ and $T = 1/2$.

In Fig. (4.6), we extend the aforementioned findings to several values of α and β. In the opposite direction from the harmonic drivings, a global optimization has not been found due to the fact that we are dealing only with integer values of α and β.

Recapping the above results: lower values of α are always more advantageous for enhancing the power output, while for the efficiency, there is a non-trivial compromise between the force $|f_2|$ and both coefficients. This non-

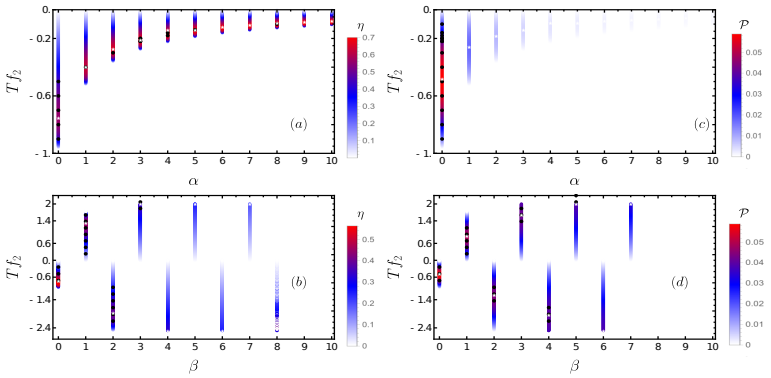

Figure 4.6: Panels (a) and (c) depict, for $\beta = 0$, the phase diagram $X_2 = Tf_2$ versus α considering the efficiency (a) and power (c). In (b) and (d), the opposite case is shown (β is varied for fixed $\alpha = 0$). White and black symbols denote some representative maximizations with respect to f_2 and the driving (for f_2 held fixed), respectively. In all cases, we set $X_1 = Tf_1 = 1$, $\tau = \gamma = k_B = m = 1$ and $T = 1/2$.

trivial relation between the three variables defines trade-off relations: one can enlarge the engine regime by increasing β, while increasing dissipation and losing power output; or increase the power output by imposing the linear case, with the engine operating at less than optimal efficiency and within a limited range of operation.

4.1.4 Difference of temperatures

Until now, we focused our attention on the isothermal case, when the two reservoirs have the same temperature. In this section, we examine the effects of different drivings at each stroke when the temperatures are different. On close inspection of Eq. (4.1.34), one reveals a dependence on the temperature gradient ΔT in the denominator, while the numerator $\mathcal{P}$ is temperature independent because it depends only on the driving and on the velocities. Thus, the increase of ΔT makes the system less efficient, dissipating more heat without any gain in the power output. One natural question is whether the external drivings and/or the driving parameter δ would compensate for the above

point. Both $\overline{\dot{Q}}_1$ and $\overline{\dot{Q}}_2$ depend on f_1 and f_2. For small ΔT, the system will only receive heat from reservoir 1 (2) if $2m\gamma \int_0^{\tau/2} \langle v_1 \rangle^2 dt < \tanh(\gamma\tau/2)(T_1 - T_2)$ [$2m\gamma \int_{\tau/2}^{\tau} \langle v_2 \rangle^2 dt < \tanh(\gamma\tau/2)(T_2 - T_1)$]. There is a driving value $|f_h| > 0$ such that $\overline{\dot{Q}}_i(f_h) = 0$, which therefore splits the system into two regimes according to the inequalities presented above: an interval $0 \leq |f_2| \leq |f_h|$ where the system does not receive heat ($\overline{\dot{Q}}_i = 0$) and an interval $|f_h| < |f_2| \leq |f_m|$, where the system receives heat ($\overline{\dot{Q}}_i < 0$). The treatment for the regime in the first interval is the same as that made here for the work-to-work case. For large ΔT, $\overline{\dot{Q}}_i$ is always negative and the engine is always less efficient than the work-to-work converter.

In Figs. (4.7) and (4.8) we exemplify thermal engines for harmonic drivings. As stated before, the system will operate in a similar way to a work-to-work converter until a value f_h (represented by an "X" symbol in Fig. (4.7)) when the system starts to receive heat from the external reservoir. Also, the efficiency decreases as ΔT increases in magnitude, illustrating that there is no conversion of heat into output work. Interestingly, the system placed in contact with the hot thermal bath in the first stage leads to somewhat higher efficiencies than in the second stage. This slight difference in the maximum efficiency can be understood by examining the right-hand sides of Eqs. (4.1.21) and (4.1.23). The interplay between the lag ϕ and the external driving forces leads $\int_0^{\tau/2} \langle v_1 \rangle^2(t) dt$ to be larger than $\int_{\tau/2}^{\tau} \langle v_2 \rangle^2 dt$, thus conferring some advantage when $T_1 > T_2$.

Finally, in Fig. (4.9) we extend the results for heat engines to the power-law drivings. For every pair α and β, $\Delta T \neq 0$ will always result in a loss of efficiency, being more substantial as α is increased and less sensitive to an increase of driving in the second stage (increase of β). There are also small differences in the maximum efficiency when the hot bath acts over the first or the second interaction, being slightly larger when $\Delta T > 0$. In such a case, the interplay between the driving forces leads $\int_0^{\tau/2} \langle v_1 \rangle^2 dt$ to be lower than $\int_{\tau/2}^{\tau} \langle v_2 \rangle^2(t) dt$, offering a small advantage when $T_1 < T_2$.

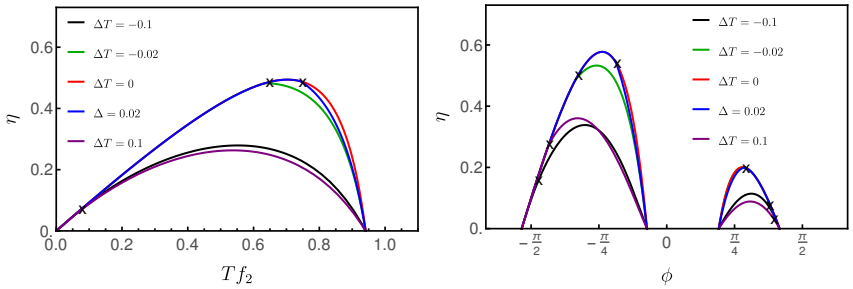

Figure 4.7: For $\tau = 2$, $\phi = 0$ and $Tf_2 = 1$, the depiction of efficiency η versus Tf_2 and ϕ for distinct temperature differences ΔT between thermal baths. From top to bottom in each panel, results for distinct temperature differences $\Delta T = 0, 0.02, -0.02, -0.1$ and 0.1. Symbols $\times$ refer to the separatrix f_h/ϕ_h between the work-to-work and thermal engines, respectively. In all cases, we set $T_1 = 1/2$, $T_2 = 1/2 + \Delta T$, $X_1 = Tf_1 = 1$ and $\gamma = k_B = m = 1$.

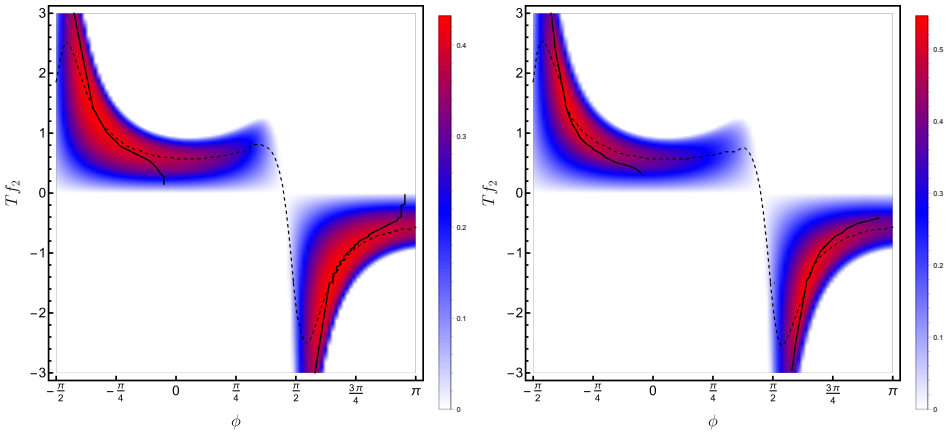

Figure 4.8: For the set of drivings given by Eq. (4.1.50) and $\tau = 2$, the left and right panels depict efficiency phase diagrams of the output force $X_2 = Tf_2$ versus the phase difference ϕ for $\Delta T = 0.1$ and -0.1, respectively. Continuous and dashed lines denote the maximization with respect to f_2 and ϕ, respectively. Their crossings provide the simultaneous maximizations. In all cases, we set $X_1 = Tf_1 = 1$, $\gamma = k_B = m = 1$ and $T = 1/2$.

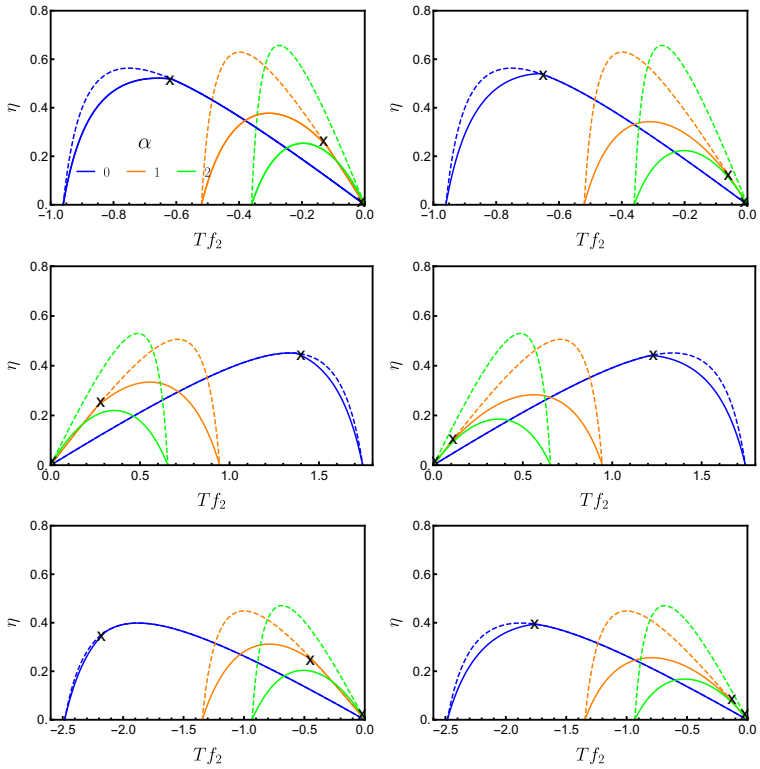

Figure 4.9: Left and right panels show the efficiency η versus Tf_2 for distinct α values for $\Delta T = 0.025$ and $\Delta T = -0.025$, respectively. From left to right (left side), the results for $\alpha = 0, 1$ and 2, respectively. Dashed lines denote the corresponding $\Delta T = 0$ (work-to-work) engines. Symbols $\times$ denote the separatrix f_h between regimes in which the particle receives heat from the thermal bath. In such a case, the efficiencies are different. From top to bottom, $\beta = 0, 1$ and 2.

4.2 Underdamped case and the ressonance phenomenon

We now extend the previous main results to the underdamped case. In the overdamped setup, the inertia of the particle is neglected. Since the inertia is not present in the overdamped case, its equation has the form of Eq. (3.6.1) (see Sec. 3.6). While the former is more theoretically simple, the absence of the mass results in an incomplete analysis. First, Eq. (4.1.1) does not include a position dependence, which implies that all boundary conditions and all dynamics computed by Eqs. (4.1.12 and 4.1.13) do not include any assumption about the position x of the particle, limiting applications to setups that require a confined particle, such as experiments with Brownian particles under optical traps [92] and general Langevin dynamics applied to biological transport [93, 94]. Also, the underdamped case captures distinct and essential aspects of the particle dynamics and stochasticity, emphasizing the effect of inertia along the process, while the overdamped case is limited to systems with rapid relaxation.

Despite the extensive research on both approximations [95–102], little is known about their thermodynamic implications. In this Section, we explore the role of inertia in a work-to-work converter under the same conditions addressed in Sec. (3.6) and in its related publication [85]. This setup is composed of a Brownian particle sequentially placed in contact with a given thermal reservoir and subject to an external force per mass given by $\tilde{f}_i(x,t)$ at each state i ($i \in \{1,2\}$). The first contact has a duration given by τ_1 and the second contact with the reservoir has a duration of $\tau - \tau_1$. In each stroke, the system is again described by the Langevin dynamics,

$$\frac{d}{dt}v_i(t) = \overline{f}_i(x,t) - \gamma_i v_i(t) + \zeta_i(t), \tag{4.2.1}$$

$$\frac{d}{dt}x_i(t) = v_i(t), \tag{4.2.2}$$

where γ_i is the viscous coefficient per mass. $\zeta_i(t)$ is a white noise and obeys the same properties addressed for Eq. (4.1.1). The force $\overline{f}_i(x,t) = f_i^*(x) + \tilde{f}_i(t)$, where $f_i^*(x) = -\kappa x_i/m$ is due to a harmonic potential that "traps" the particle in a bound state and $\tilde{f}_i(t)$ is the external force that is defined in the same way as

Eq. (4.1.14). The probability distribution of the particle $P_i(x,v,t)$ at stroke i is described by a Fokker-Planck-Kramers equation (FPK) [61],

$$\frac{\partial P_i}{\partial t} = -\left[v\frac{\partial P_i}{\partial x} + \overline{f}_i(x,t)\frac{\partial P_i}{\partial v} + \frac{\partial J_i}{\partial v}\right], \tag{4.2.3}$$

where J_i is the probability current, given by the same expression as in Eq. (4.1.3). As stated in Sec. (4.1), the system will repeat its strokes with a period τ under a periodic force $\overline{f}_i(x,t) = \overline{f}_i(x,t+\tau)$ for both $i = 1, 2$. The results expressed in Eqs. (4.1.3 - 4.1.11) and Eqs. (4.1.24 - 4.1.37) are general and can be applied directly to this specific case. The simplest way to treat the underdamped case is to decompose the driving at each stroke, written in terms of a Fourier series as,

$$g_1(t) = \frac{a_0}{2} + \sum_{n=1}^{\infty} a_n \cos\left(\frac{2\pi nt}{\tau}\right) + b_n \sin\left(\frac{2\pi nt}{\tau}\right), \tag{4.2.4}$$

and

$$g_2(t) = \frac{c_0}{2} + \sum_{n=1}^{\infty} c_n \cos\left(\frac{2\pi nt}{\tau}\right) + d_n \sin\left(\frac{2\pi nt}{\tau}\right), \tag{4.2.5}$$

where the driving to be considered is characterized by the coefficients a_n, b_n, c_n and d_n under the conditions $c_n = d_n = 0$ for $i = 1$ and $a_n = b_n = 0$ for $i = 2$. We write the mean value of the velocity in a general form as

$$\langle v\rangle = \sum_{k=1}^{\infty}(X_1\cdot a_{1vk} + X_2\cdot a_{2vk})\cos\left(\frac{2\pi kt}{\tau}\right) + (X_1\cdot b_{1vk} + X_2\cdot b_{2vk})\sin\left(\frac{2\pi kt}{\tau}\right), \tag{4.2.6}$$

where a_{ivk} and b_{ivk} correspond to Fourier coefficients obtained for the mean velocity and depend on the driving form from Eqs. (4.2.4) and (4.2.5). The general expressions for these coefficients are given in Appendix A.3. In order to tackle this new problem, we repeat some maximization methods used previously in this Chapter, with some additional features. First, we repeat the maximization of $\mathcal{P}$ and η in terms of f_2 for the underdamped setup and compare it with the overdamped case. This comparison is made by choosing three different driving forces: a constant, where $g_1(t) = g_2(t) = 1$; a linear driving given by,

$$g_i(t) = \begin{cases} t, & 0 < t \leq \tau/2 \\ t - \tau/2, & \tau/2 < t \leq \tau, \end{cases} \tag{4.2.7}$$

and a trigonometric force given by,

$$g_i(t) = \begin{cases} \cos\left(\frac{2\pi}{\tau}t\right), & 0 \leq t \leq \tau/2, \\ \sin\left(\frac{2\pi}{\tau}t\right), & \tau/2 \leq t \leq \tau. \end{cases} \tag{4.2.8}$$

All these drivings are particular cases of the external forces studied in the Sec. (4.1.2): the constant driving is obtained by taking $\alpha = \beta = 0$ in the Eq. (4.1.53); the driving from the Eq.(4.2.7) is the Eq.(4.1.53) for $\alpha = \beta = 1$ and making $g_1(t) \to (\tau/2)g_1(t)$ and $g_2(t) \to -(\tau/2)g_2(t)$ and the Eq.(4.2.8) can be reobtained from Eq.(4.1.50) by taking $\phi = 3\pi/4$ and exchanging $g_1(t) \leftrightarrow g_2(t)$. Such a modification does not affect the generality of the results presented for the overdamped scenario.

Fixing f_1, we maximize in terms of f_2 for the constant and linear external drivings, as plotted in Fig. (4.10). To gain insights about this maximization route in an underdamped model, we compare it with an already known example of the overdamped case. This analysis assumes $\gamma = \kappa = 1$. In both cases, the system operates as a work-to-work converter by choosing f_2 in the interval between 0 and $|f_m|$. Both external drivings have totally different behaviors when the underdamped case is applied. First, for the underdamped setup under a constant protocol, the Onsager coefficients obey the following symmetry relations $L_{11} = L_{22} = -L_{12} = -L_{21}$, which imply that the system operates as a work-to-work converter in the interval $0 \leq f_2 \leq f_m = f_1$. The expressions for the power output and efficiency are relatively simple, given by $\mathcal{P} = L_{22}f_2(f_2 - f_1)$ and $\eta = f_2/f_1$, respectively. It is important to notice that the interval of operation and the thermodynamic quantities do not depend on κ or τ, nor do their maximization values, such as the values of f_2 where the maximum efficiency and power output are reached, namely $f_{2\mathsf{ME}} = f_1$ and $f_{2\mathsf{MP}} = f_1/2$. One can simply find the optimal thermodynamics by applying $f_{2\mathsf{ME}} = f_1$ and $f_{2\mathsf{MP}} = f_1/2$, resulting in $\eta_{\mathsf{ME}} = 1$, $\eta_{\mathsf{MP}} = 1/2$, $\mathcal{P}_{\mathsf{ME}} = 0$ and $\mathcal{P}_{\mathsf{MP}} = TL_{22}f_1^2/4$. Surprisingly, the underdamped model under the constant protocol reaches the reversible "Carnot" scenario, with the maximum global efficiency being equal to 1 and its efficiency at maximum power equal to $\eta_{\mathsf{MP}} = \eta_{\mathsf{ME}}/2$, analogous to the results observed in Ref. [58] for a fast Carnot cycle, but for the work-to-work scenario.

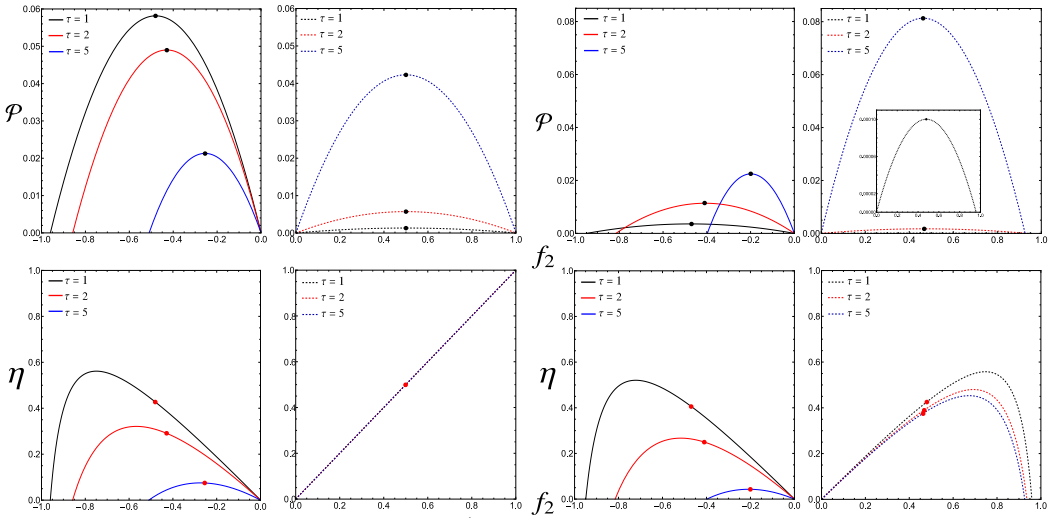

Figure 4.10: Depiction of the power output $\mathcal{P}$ (top) and efficiency η (bottom) as functions of f_2 for constant (left) and linear (right) drivings and different periods τ. Dashed and continuous lines correspond to the underdamped and overdamped regimes, respectively. Black and red dots represent $\mathcal{P}_{\mathsf{MP}}$ and η_{MP}, respectively. Parameters: $f_1 = T = 1$, $\gamma = 1$ and $\kappa = 1$.

For the linear protocol, the scenario is broadly different. We still observe some symmetries in the Onsager coefficients, $L_{11} = L_{22}$ and $L_{12} = L_{21}$; however, $L_{11} \neq -L_{12}$ and L_{11}/L_{22} increases "faster" with respect to τ. The optimal quantities $\mathcal{P}_{\mathsf{MP}}$, η_{MP} and $\mathcal{P}_{\mathsf{ME}}$ also depend strongly on τ and κ, two known quantities that are related and influence the particle when the inertia is not negligible. We also point out how the period τ affects the overdamped and underdamped scenarios differently (see Fig. (4.10)). Before we proceed with the particular role of κ in the underdamped approach, we further stress the role of the total period in the comparison between the overdamped and underdamped cases under both protocols.

First, we observe that the period τ affects the efficiency of the underdamped scenario according to the selected protocol. While the increase of τ slightly reduces the efficiency of the linear protocol, the efficiency for the underdamped model under the constant regime is constant, which offers a huge advantage

in selecting the best scenario for the power output with respect to time without any dissipation cost. In fact, the power output increases when we consider longer cycles for both protocols (see the left side of Fig. (4.10)), with a peak in the constant case at $\tau_0 = 6.311...$, when $\mathcal{P}_{\mathsf{MP}} = 0.05148$ for $f_1 = 1$. In the linear protocol, the peak is observed at $\tau_0 = 7.354...$, whose associated power and efficiency result in $\mathcal{P}_{\mathsf{MP}} = 0.170...$ and $\eta_{\mathsf{MP}} = 0.2765...$. In this scenario, the overdamped case for the constant protocol is remarkably different. Both power and efficiency decrease with the duration of the cycle. The overdamped case in the linear protocol has (qualitatively speaking) similar features to its counterpart in terms of power, since both exhibit the decay of the power output when the duration of the cycle increases. However, the power output for the underdamped case offers more advantages than that of the overdamped case. In summary: for the constant protocol, the underdamped case provides the best efficiency scenario, being able to reach a reversible cycle without any dissipation cost in terms of the cycle duration. The overdamped case in general surpasses the underdamped case in terms of power output, both presenting opposing behavior in relation to the increase of the cycle duration, with the overdamped being more powerful for small periods while the underdamped does the opposite. For the linear case, the underdamped surpasses the overdamped in both efficiency and power output.

For completeness, we show the same comparison with the trigonometric driving given by Eq. (4.2.8) in Fig. (4.11). While the power output for the overdamped case $\mathcal{P}$ increases with the duration of the cycle, the opposite is observed for the associated efficiencies and for the underdamped case. As observed for both linear and constant drivings, the underdamped case not only presents a substantial increase in efficiency but also exhibits a remarkably larger operation regime. Here, we propose a heuristic (less rigorous) explanation of the differences highlighted in the last paragraph. First, we notice that the driving forces (or the amplitudes X_j) are in opposite and the same directions for the overdamped and underdamped cases, respectively. This occurs because, in the underdamped case, the restoring force makes the particle restore its position (in an average sense) ideally without any additional dissipation, while the overdamped setup needs both drivings to run the engine and restore the cycle. However, the trigonometric case has some subtle details, in general due

to the phase difference ($\phi = 3\pi/4$ in Eq. 4.1.50). Another difference between both setups lies in the relation between f_m and τ, which can be directly analyzed through an inspection of the Onsager coefficients. Notwithstanding, if we stretch the heuristic interpretation slightly, we conclude that the mean velocity always aligns with the external force in both stages for the overdamped case if we wait long enough, due to the fact that both forces act as dissipative restoring forces, dragging the particle to its initial position when $t = \tau$. As stated in Chapter (2.2), the system can transform one kind of energy into another due to two opposing fluxes and forces. When the velocity, which is directly related to the mean flux of the particle, is aligned with the external drivings, there is no useful power output. Hence, the "production" of work flux to the outside is limited to smaller intervals when τ is larger.

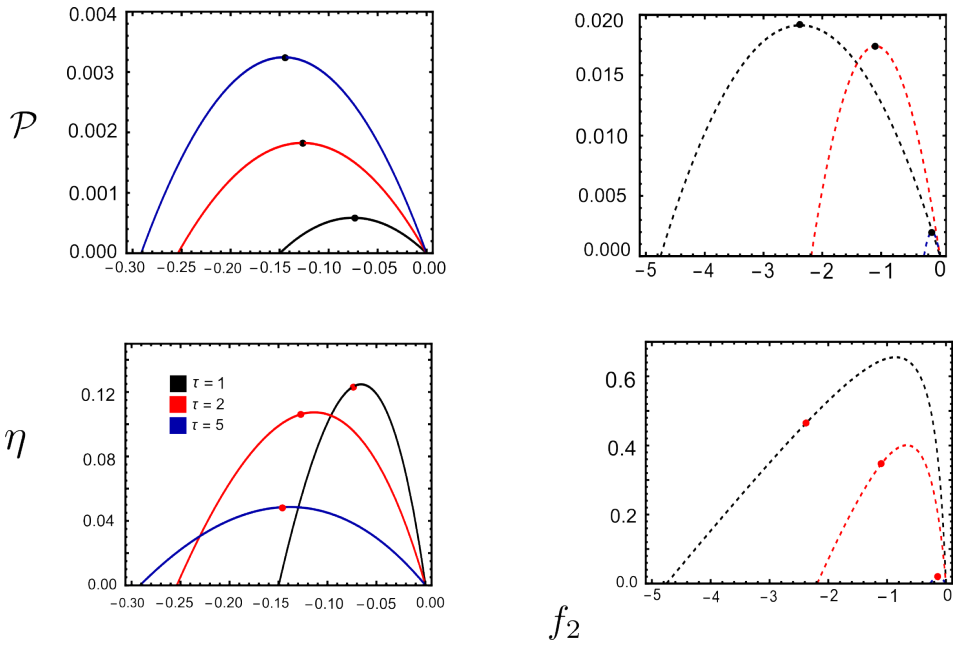

Figure 4.11: Power output (top) and efficiency (bottom) versus f_2 for sinusoidal protocols and different periods τ. Dashed lines represent the underdamped regime, while continuous lines represent the overdamped regime. Black bullets denote $\mathcal{P}_{\text{MP}}$ and red bullets denote η_{MP}. Parameters: $f_1 = 1$, $\gamma = 1$, and $\kappa = 1$.

4.3 Effects of the deterministic resonant phenomena in the underdamped setup

The presence of a restoring potential with an external force (which is also periodic, with frequency $\omega = 2\pi/\tau$) results in a resonant phenomenon, when the amplitude of the velocity exhibits a peak as the frequency of the external force approaches the natural frequency of the system. Here, we adjust the frequency of the restoring force by fine-tuning the spring constant κ. The interplay between the restoring potential and the external force is similar to a phenomenon coined stochastic resonance, when the response of the system to a weak external force is maximized by the noise, increasing the amplitude of oscillation between steady points [103]. Here, to avoid confusion with this specific behavior, we use the term "deterministic" resonance, since this phenomenon is not related to stochastic noise, but to an interplay between two deterministic quantities. We will denote κ_{res} as the resonant spring constant. In order to find it, we maximize the amplitude of the k-th mode in terms of time t and κ, given by,

$$\langle v(t)\rangle^{k\text{-th}} = (X_1 \cdot a_{1vk} + X_2 \cdot a_{2vk}) \cos\left(\frac{2\pi k t}{\tau}\right) + (X_1 \cdot b_{1vk} + X_2 \cdot b_{2vk}) \sin\left(\frac{2\pi k t}{\tau}\right). \quad (4.3.1)$$

The maximum amplitude is therefore obtained from the following relation:

$$\kappa_{\text{res}} = \left(\frac{2\pi k}{\tau}\right)^2, \qquad \text{k integer.} \quad (4.3.2)$$

Such a result is independent of the protocol, depending only on the natural frequency $\omega_0 = 2\pi/\tau$. In order to tackle the influence of the resonant phenomenon on the thermodynamic quantities, we start by studying its effect on the maximized quantities $\mathcal{P}_{\text{MP/ME}}$ and $\eta_{\text{MP/ME}}$. If we fix τ and κ, we can find the corresponding $f_{2\text{MP}}$ and $f_{2\text{ME}}$ and therefore the respective maximization of both power and efficiency. In Fig. (4.12) we draw heat maps for both maximum power and efficiency in the plane κ versus τ for the constant and linear cases. These results point to the role of both κ and τ in the optimization of the thermodynamic quantities and, more specifically, the heat maps show the peaks of the efficiency according to the resonance curves given by the relation in Eq. (4.3.2).

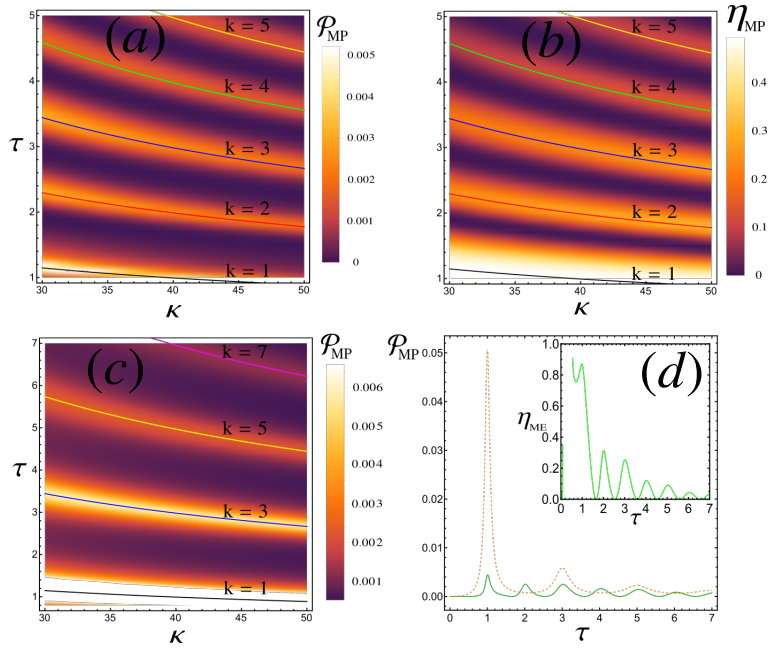

Figure 4.12: Top panels: (a) depicts the maximum power $\mathcal{P}_{MP}$ and (b) depicts the efficiency at maximum power η_{MP} heat maps for linear drivings. (c) shows the same, but for constant drivings. Continuous lines show the resonance lines according to Eq. (4.3.2). All maximizations have been carried out with respect to f_2. Since $\eta_{MP} = 1/2$ for constant drivings, the heat maps in this case are not shown. In (d), there is a plot of $\mathcal{P}_{MP}$ for constant (dashed) and linear (continuous) drivings for $\kappa = 4\pi^2$. Inset: the same, but for η_{ME} (linear). Parameters: $f_1 = T = 1$ and $\gamma = 1$.

The resonant patterns in Fig. (4.12) suggest that it is possible to overcome the previously known peaks obtained through maximization in terms of the external force. Thus, the underdamped setup offers a huge advantage over the overdamped one, since it is possible to maximize the power output without any cost in efficiency. These two quantities are related by a trade-off relation that does not allow their simultaneous maximization [104] unless some other thermodynamic quantity is sacrificed. Under these terms, we also examine the dissipation (entropy production) in the same configuration as in Fig. (4.12). In Fig. (4.13) we present a comparison of the entropy production for both under-

damped and overdamped setups under the constant and linear protocols and also the peaks of the entropy production at maximum power $\overline{\sigma_{\mathrm{MP}}}$. The same peak patterns are shown in the heat map in Fig. (4.13c) and (f), which suggest that the ”simultaneous” maximization also results in a peak in the dissipation. Also, it is important to mention that there is, in fact, no simultaneous maximization, since the resonance points are very close to the peaks of the power and efficiency, but do not precisely coincide.

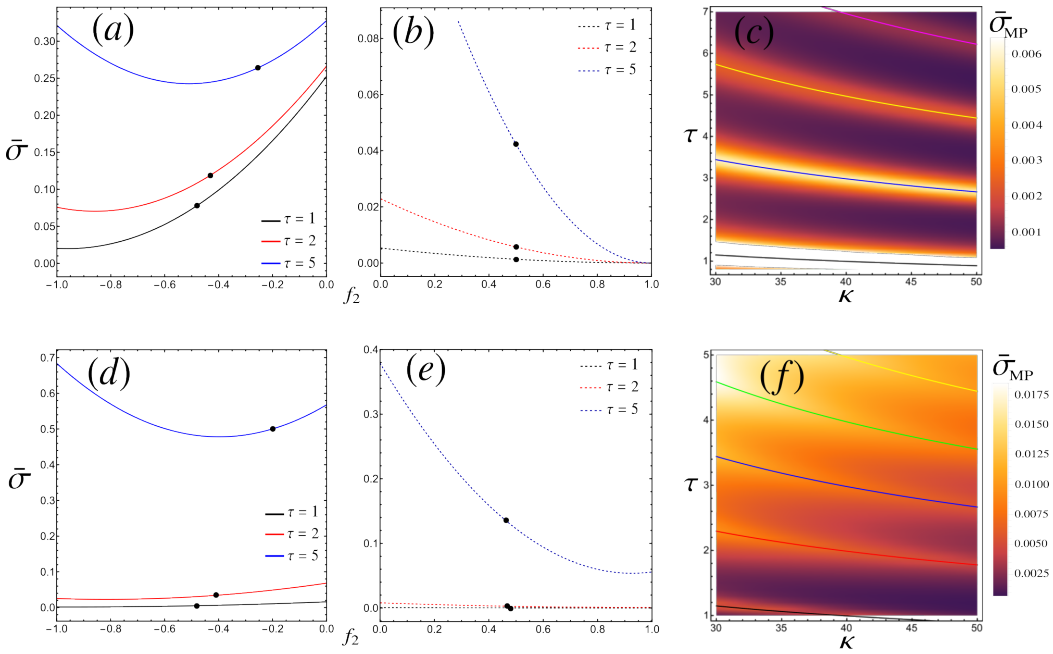

Figure 4.13: Left and center panels depict the mean entropy production $\bar{\sigma}$ for the overdamped ((a) and (d)) and underdamped ((b) and (e)) cases versus f_2, for the same range, resonance lines, and parameters as in Fig. (4.11). Black dots represent the maximum power. Panels (c) and (f) show entropy production heat maps for the same parameters as in Fig. (4.12). Top and bottom panels correspond to the constant and linear drivings, respectively. Parameters: $f_1 = 1$, $\gamma = 1$, and $T = 1$ in all plots and $\kappa = 1$ for the 2D plots.

We also estimate the experimental reliability of such a maximization due to the resonant phenomenon. In principle, our framework can be reproduced and tested using an optical tweezer system, in which the harmonic potential and the

harmonic drives can be generated via electric fields [105–108]. In Fig. 4.14 we plot the same heat map for $\mathcal{P}_{\text{MP}}$ (in J/s), applying some laboratory values: $m \approx 10^{-18}$ kg, $\gamma \approx 10^{-20}\,\text{s}^{-1}$, by imposing a thermodynamic force $X_1 \approx 0.003$ fN/kg in the underdamped case ($m/\gamma \gg 1$) at room temperature with $\kappa \approx 1\,\mu$N/m. Applying these quantities to our optimization methods, we find the resonant regime peaks at $X_2 \approx 0.5$ fN/kg with a period $\tau \approx 6\,\mu$s in the constant case. We also investigate the resonant phenomenon for the trigonometric external drives, which is shown in Fig. (4.15). The peaks due to the resonance are also observed, but they do not show remarkable improvements with respect to the constant and linear drivings.

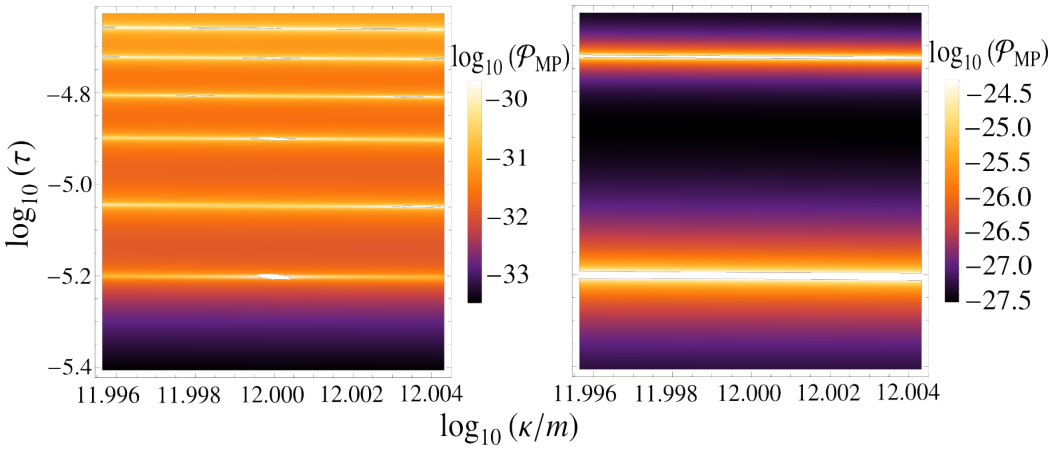

Figure 4.14: The power output for the linear (left) and constant (right) protocols in log base 10 scale considering some experimental quantities. Here, we use $m \approx 10^{-18}$ kg and $\gamma \approx 10^{-20}\text{s}^{-1}$.

4.4 Statistical fluctuations of power and efficiency

Until now, we have focused our attention on results in the NESS. Using the results from Sec. (3.4.3), we now tackle the maximization in terms of the fluctuations of the collisional engine. Here, we focus on the maximization of the

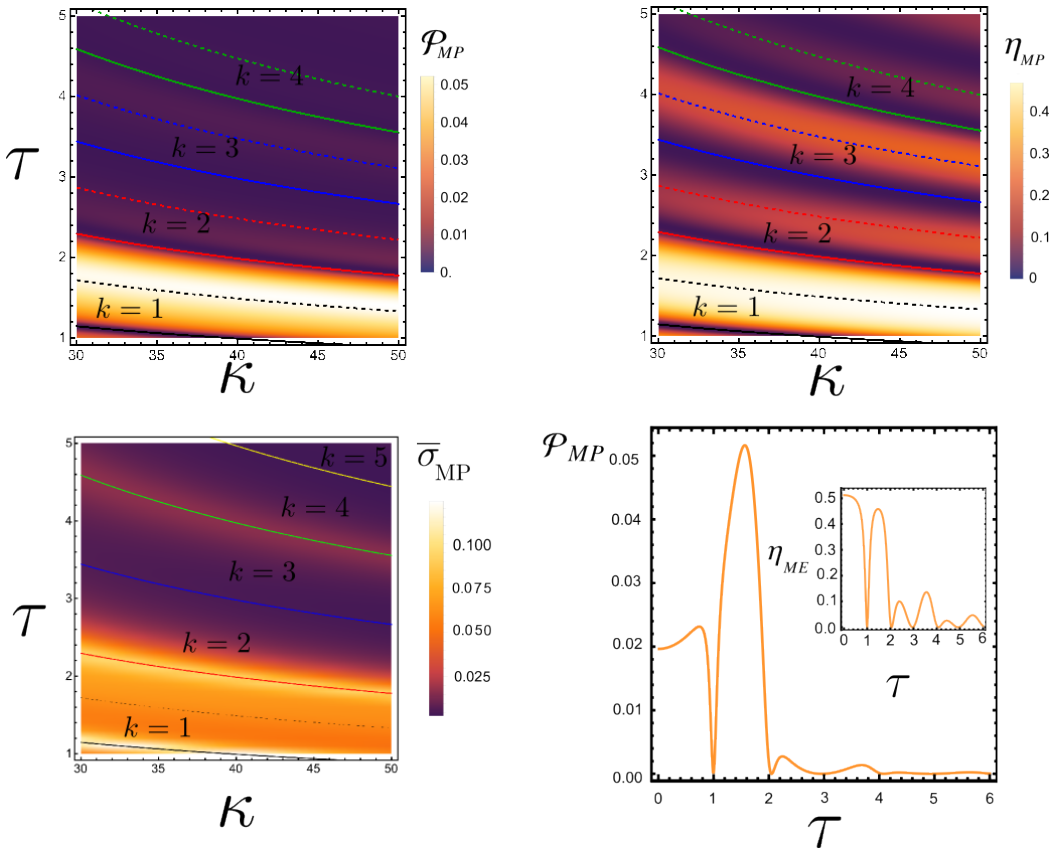

Figure 4.15: Depiction of $\mathcal{P}_{MP}, \eta_{MP}$ and $\bar{\sigma}_{MP}$ heat maps for harmonic drivings. Right bottom panels show $\mathcal{P}_{MP}$ and η_{ME} (inset) for $\kappa = 4\pi^2$. Parameters: f_1 and $\gamma = 1 = T = 1$.

joint probability of power and efficiency, searching for rare events and fluctuations of the thermodynamic quantities above their maximum values.

Let us define a flux of work per period τ for the Brownian particle along a single trajectory x, with velocity $v = \dot{x}$,

$$\overline{\dot{w}}_1 = -\frac{1}{\tau}\int_0^{\tau/2} \tilde{f}_1(t)v(t)dt, \tag{4.4.1}$$

$$\overline{\dot{w}}_2 = -\frac{1}{\tau}\int_{\tau/2}^{\tau} \tilde{f}_2(t)v(t)dt, \tag{4.4.2}$$

where the $\tilde{f}_j$ are the external drivings from the reduced Langevin Eq. (3.6.4). The mean values of the expressions (4.4.1) and (4.4.2) reproduce the well-known values from Eqs. (3.8.15) applied to both reservoirs,

$$\begin{aligned}\langle\overline{\dot{w}}_1[x]\rangle &= \left\langle -\frac{1}{\tau}\int_0^{\tau/2} \tilde{f}_1(t)v(t)dt \right\rangle \\ &= -\frac{1}{\tau}\int_0^{\tau/2} \tilde{f}_1(t)\langle v(t)\rangle dt \\ &= \overline{\dot{W}}_1,\end{aligned} \tag{4.4.3}$$

and the same can be done for $\langle\overline{\dot{w}}_2\rangle$. As already stated, the solution of this system is Gaussian and, since the fluctuating work is proportional to the Gaussian variable $v(t)$, we expect that $\overline{\dot{w}}_1$ and $\overline{\dot{w}}_2$ are also Gaussian variables. We describe this distribution by

$$P_G(\bar{\dot{w}}_1, \bar{\dot{w}}_2) = \frac{1}{\sqrt{\det(C)}}\exp\left(-\frac{1}{2}\sum_{i,j=1}^{2}\left(\bar{\dot{w}}_i - \bar{\dot{W}}_i\right)C_{ij}^{-1}\left(\bar{\dot{w}}_j - \bar{\dot{W}}_j\right)\right), \tag{4.4.4}$$

where $\overline{\dot{W}}_i = \langle\overline{\dot{w}}_i\rangle$. The covariance matrix C is defined as

$$C_{ij} = \langle\bar{\dot{w}}_i\bar{\dot{w}}_j\rangle - \langle\bar{\dot{w}}_i\rangle\langle\bar{\dot{w}}_j\rangle. \tag{4.4.5}$$

Following Ref. [109], we observe that the stochastic work is related to the stochastic entropy fluxes by

$$\sigma_1 = -\frac{\overline{\dot{w}}_1}{T}, \qquad \sigma_2 = -\frac{\overline{\dot{w}}_2}{T}. \tag{4.4.6}$$

The total entropy production should follow a fluctuation theorem in the asymptotic limit [109],

$$\frac{P(\sigma_1,\sigma_2)}{P^{\dagger}(-\sigma_1,-\sigma_2)} = \exp\left[(\sigma_1+\sigma_2)\,\tau/k_B\right], \tag{4.4.7}$$

where $P^{\dagger}$ is the probability distribution of the reversed process. Since everything is still Gaussian, obtaining the covariance matrix elements C_{ij} is straightforward and, once more using Ref. [109], we write the C elements in terms of the Onsager coefficients,

$$C_{ij} = \frac{T^2 k_B}{\tau} \left(L_{ij} + L_{ji}\right). \tag{4.4.8}$$

It is noteworthy that the results from Eq. (4.4.8) only depend on the Onsager coefficients and, since our only assumptions are the Gaussian solutions and the white noise from the Langevin equation, the result above is general and should be applied to other classes of collisional engines beyond the scope of this thesis. Also, assuming the marginalization of the expression for $P(\bar{\dot{w}}_j)$, we can easily obtain it from

$$P(\bar{\dot{w}}_2) = \int_{-\infty}^{\infty} P(\bar{\dot{w}}_1, \bar{\dot{w}}_2)\, d\bar{\dot{w}}_1. \tag{4.4.9}$$

Now, we start to approach the efficiency distribution, since its value also presents stochastic fluctuations. We define it inspired by Eq. (2.2.2),

$$\eta = -\frac{\bar{\dot{w}}_2}{\bar{\dot{w}}_1}. \tag{4.4.10}$$

The expressions $\bar{\dot{w}}_j$ present Gaussian distributions, which is not the case for η, which will be written in the form [110, 111],

$$P(\eta) = \int_{-\infty}^{\infty}\int_{-\infty}^{\infty} P(\bar{\dot{w}}_1, \bar{\dot{w}}_2)\, \delta\left(\eta + \frac{\bar{\dot{w}}_2}{\bar{\dot{w}}_1}\right) d\bar{\dot{w}}_1\, d\bar{\dot{w}}_2. \tag{4.4.11}$$

Besides the complexity of the above integral, Eq. (4.4.11) admits an analytical solution [54, 112]. To evaluate this integral, we rewrite the Dirac delta function as

$$\delta\left(\eta + \frac{\bar{\dot{w}}_2}{\bar{\dot{w}}_1}\right) = |\bar{\dot{w}}_1|\delta(\eta\bar{\dot{w}}_1 + \bar{\dot{w}}_2), \tag{4.4.12}$$

which is a feasible expression to apply to the integral in Eq. (4.4.11), yielding the result,

$$\begin{aligned} P(\eta) \;=\; & \frac{\sqrt{-C_{12}^2 + C_{11}C_{22}}}{\pi\left(C_{22} + \eta(2C_{12} + C_{11}\eta)\right)} \exp\left(\frac{C_{22}\bar{\dot{W}}_1^2 - 2C_{12}\bar{\dot{W}}_1\bar{\dot{W}}_2 + C_{11}\bar{\dot{W}}_2^2}{2C_{12}^2 - 2C_{11}C_{22}}\right) \\ & + \frac{e^{-\frac{(\bar{\dot{W}}_2 + \bar{\dot{W}}_1\eta)^2}{2(C_{22}+\eta(2C_{12}+C_{11}\eta))}}\left(C_{22}\bar{\dot{W}}_1 - C_{12}\bar{\dot{W}}_2 + C_{12}\bar{\dot{W}}_1\eta - C_{11}\bar{\dot{W}}_2\eta\right)}{\sqrt{2\pi}\left(C_{22} + \eta(2C_{12} + C_{11}\eta)\right)^{3/2}} \\ & \times \;\; \mathrm{Erf}\left[\frac{C_{22}\bar{\dot{W}}_1 - C_{12}\bar{\dot{W}}_2 + C_{12}\bar{\dot{W}}_1\eta - C_{11}\bar{\dot{W}}_2\eta}{\sqrt{2}\sqrt{\left(-C_{12}^2 + C_{11}C_{22}\right)\left(C_{22} + \eta(2C_{12} + C_{11}\eta)\right)}}\right]. \end{aligned} \tag{4.4.13}$$

This distribution exhibits a Cauchy-like behavior ($P(\eta) \sim 1/\eta^2$), meaning that all its moments are divergent (it is a distribution with a non-defined mean). This property is universal of efficiency distributions, observed in other results that also investigate their fluctuations [112]. Moreover, it depends solely on the statistical moments of the power variables, which are Gaussian with well-defined moments. Thus, all analysis related to the maximization of the efficiency will be written in terms of the average of Eq. (4.4.12).

With the distribution of the power output and efficiency well defined, we start to approach their joint relationship. We know that this relation always exists due to the trade-off relation between these two quantities [85, 113]. The joint distribution of power and efficiency is an important tool for this work because from it will be possible to compute a conditional probability analysis while capturing their fundamental thermodynamic "competition". We first derive the joint probability $P(\eta, \bar{\dot{w}}_2)$ from Eq. (4.4.14),

$$P(\eta, \bar{\dot{w}}_1, \bar{\dot{w}}_2) = P_G(\bar{\dot{w}}_1, \bar{\dot{w}}_2)\, \delta\left(\eta + \frac{\bar{\dot{w}}_2}{\bar{\dot{w}}_1}\right). \tag{4.4.14}$$

Therefore, to obtain the marginal $P(\eta, \bar{\dot{w}}_2)$, we need to integrate over $\bar{\dot{w}}_1$, which is simplified through the identity,

$$\delta\left(\eta + \frac{\bar{\dot{w}}_2}{\bar{\dot{w}}_1}\right) = \frac{|\bar{\dot{w}}_1|}{|\eta|}\delta\left(\bar{\dot{w}}_1 + \frac{\bar{\dot{w}}_2}{\eta}\right). \tag{4.4.15}$$

Now, integrating Eq. (4.4.14) over $\bar{\dot{w}}_1$ we have

$$P(\eta, \bar{\dot{w}}_2) = \frac{|\bar{\dot{w}}_2|}{\eta^2} P_G\left(-\frac{\bar{\dot{w}}_2}{\eta}, \bar{\dot{w}}_2\right), \tag{4.4.16}$$

which presents two simultaneous behaviors according to the variable: Eq. (4.4.16) is Gaussian in terms of $\bar{\dot{w}}_2$ but still a Cauchy-like distribution in terms of η. With this equation, we start to ask some questions about the joint behavior of both variables.

4.4.1 Optimization Beyond Mean Values

With Eq. (4.4.16), we start to investigate some topics concerned with the joint behavior of the "competition" between power and efficiency, and some specific

questions can be raised. Since these quantities are always fluctuating, there is a non-null probability to find a regime where the efficiency and/or the power overcome their mean value. This probability should be computed using the joint probability obtained in the previous paragraphs. The goal of this Section is to maximize the probability of such events by manipulating some external variable, f_2 for example.

We start by analyzing the probability of the power output overcoming its maximum mean value. The average value of the mean power output is constrained by an upper bound $\bar{\dot{W}}_2 \leq \bar{\dot{W}}_2^{\mathsf{MP}}$, however it is possible to find a fluctuating trajectory such that $\bar{\dot{W}}_2 > \bar{\dot{W}}_2^{\mathsf{MP}}$, with the following probability

$$\mathcal{P}\left(\bar{\dot{w}}_2 > \dot{W}_2^{\mathsf{MP}}\right) = \frac{1}{2}\left(1 + \mathsf{erf}\left(\frac{\dot{W}_2 - \dot{W}_2^{\mathsf{MP}}}{\sqrt{2}\sqrt{C_{22}}}\right)\right). \tag{4.4.17}$$

Notice that when $\bar{\dot{W}}_2 = \bar{\dot{W}}_2^{\mathsf{MP}}$, the error function vanishes, yielding a probability $p = 1/2$. We expect this result from the symmetry of the Gaussian distribution about its mean. Due to normalization, we expect that $\mathcal{P}(\bar{\dot{W}}_2 > \bar{\dot{W}}_2^{\mathsf{MP}}) < 1/2$. In Fig. (4.17), we plot the probability of the engine to overcome its maximum value *versus* the external driving f_2 for two time intervals, $\tau_1 = 0.1$ (fast cycling) and $\tau_2 = 1$ (slow cycling).

Another relevant statistical event is the probability of the power output falling between two intermediate values, the maximum power ($\overline{\dot{W}}_2^{\mathsf{MP}}$) and the power at maximum efficiency ($\overline{\dot{W}}_2^{\mathsf{ME}}$). In general, $\overline{\dot{W}}^{\mathsf{MP}} > \overline{\dot{W}}_2^{\mathsf{ME}}$, so we define the probability,

$$\mathcal{P}\left(\dot{W}_2^{\mathsf{MP}} > \bar{\dot{w}}_2 > \dot{W}_2^{\mathsf{ME}}\right) = \frac{1}{2}\left(\mathsf{erf}\left(\frac{\dot{W}_2 - \dot{W}_2^{\mathsf{ME}}}{\sqrt{2}\sqrt{C_{22}}}\right) - \mathsf{erf}\left(\frac{\dot{W}_2 - \dot{W}_2^{\mathsf{MP}}}{\sqrt{2}\sqrt{C_{22}}}\right)\right). \tag{4.4.18}$$

The "competition" between the power output and the efficiency is explicit in Eq. (4.4.18). If $\dot{W}_2 \sim \dot{W}_2^{\mathsf{MP}}$, the probability decreases, while the opposite occurs when $\dot{W}_2 \sim \dot{W}_2^{\mathsf{ME}}$. This behavior and its relation with the external driving f_2 are plotted in Fig. (4.17b).

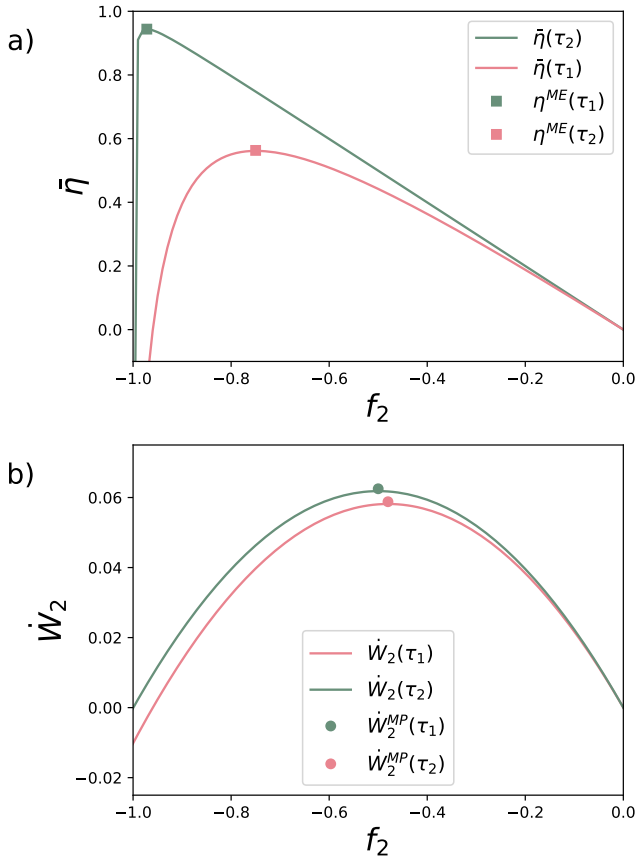

Figure 4.16: Depiction of the efficiency $\bar{\eta}$ (top) and mean power $\bar{\dot{W}}_2$ (bottom) versus different $X_2 = Tf_2$ for different τ's. Green curves show results for $\tau_1 = 0.1$, with $f_2^{\mathsf{ME}} = -0.972$, $\eta^{\mathsf{ME}} = 0.944$, $\dot{W}_2^{\mathsf{ME}} = 0.0068$ at maximum efficiency and $f_2^{\mathsf{MP}} = -0.500$, $\eta^{\mathsf{MP}} = 0.499$, $\dot{W}_2^{\mathsf{MP}} = 0.0625$ at maximum power. Pink curves show results for $\tau_2 = 1$, with $f_2^{\mathsf{ME}} = -0.750$, $\eta^{\mathsf{ME}} = 0.563$, $\dot{W}_2^{\mathsf{ME}} = 0.0401$ at maximum efficiency and $f_2^{\mathsf{MP}} = -0.480$, $\eta^{\mathsf{MP}} = 0.428$, $\dot{W}_2^{\mathsf{MP}} = 0.0588$ at maximum power. Symbols denote the corresponding maximum values $\bar{\dot{W}}_2^{\mathsf{MP}}$ and $\bar{\eta}^{\mathsf{ME}}$.

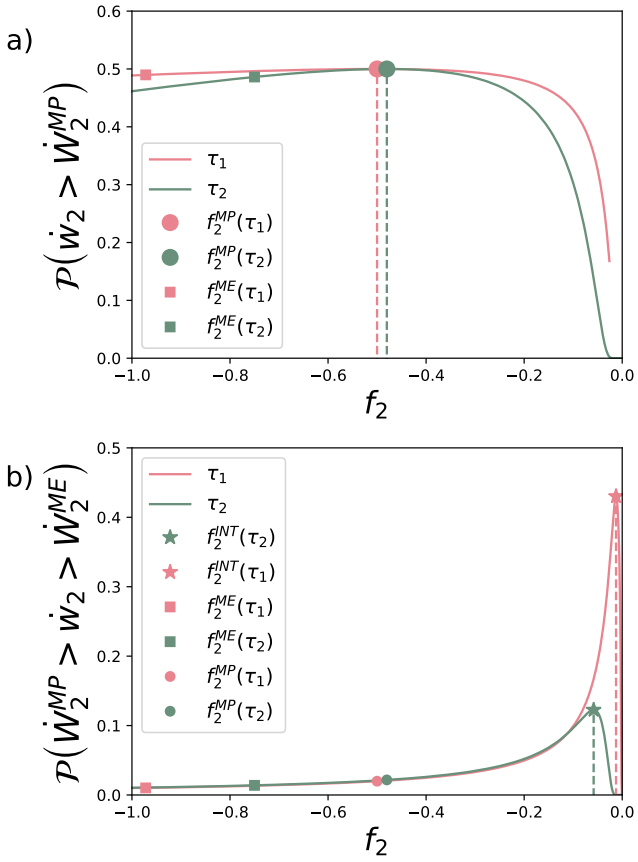

Figure 4.17: Probability distribution of power $\dot{W}_2$. (a) Probability that power exceeds its maximum mean value, which is maximized at the force corresponding to the maximum average power. (b) Probability that power falls within an intermediate range, which is maximized at a distinct value f_2^{INT}. For $\tau_1 = 0.1$ and $\tau_2 = 1$, the values of f_2^{INT} are approximately -0.0126 and -0.0583, yielding probabilities of 43% and 12%, respectively.

Now jumping to the efficiency optimization, the work-to-work converter operates within the well-defined efficiency range of $0 \leq \eta \leq 1$, with values exceeding $\eta > 1$ corresponding to another regime (pump) and the actual efficiency being redefined as $\eta_{\text{new}} \to 1/\eta$. Our first analysis is concerned with the probability of the efficiency surpassing its maximum value while still in the

work-to-work engine regime. Since the efficiency distribution is a Cauchy-like expression, we cannot compute its values analytically. Its numerical evaluation is found in Fig. (4.18), revealing that the probability $\mathcal{P}(1 > \eta > \eta^{\mathsf{ME}})$ presents peaks at $1/2$ when $f_2 = f_2^{\mathsf{ME}}$, mirroring the optimal condition for mean efficiency, showing some similarity with the power statistics, however hiding a crucial difference: while power fluctuations diminish with increasing time intervals, efficiency maintains significant probability density across a broader range of f_2 values. This fundamental distinction stems from the Cauchy-like nature of the efficiency distribution. [111].

Now, we investigate the probability of observing the efficiency within the range $\eta^{\mathsf{ME}} > \eta > \eta^{\mathsf{MP}}$. The results are plotted in Fig. 4.18. As expected, the maximizing values for this probability fall between f_2^{ME} and f_2^{MP}. As shown in Fig. (4.18a), the time dependence of the efficiency is stronger than that observed in the power output, revealing a fundamental difference between these two quantities. Our examination of independent probabilities for both power and efficiency sets the stage for the next step. Both quantities derive from the same underlying stochastic trajectories and therefore their statistical correlation becomes an important quantity to better understand simultaneous maximization and its "competition" along the engine cycling. We now start to investigate how these intrinsic correlations influence the joint probability structure and what implications they hold for the work-to-work regime.

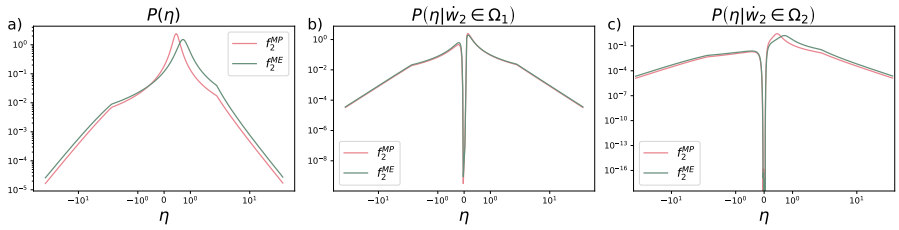

Figure 4.19: Probability distributions. (a) Probability distribution for the efficiency. (b) Conditional probability distribution for the efficiency with the condition $\dot{w}_2 \in \Omega_1 = [\bar{\dot{W}}_2^{\mathsf{ME}}, \bar{\dot{W}}_2^{\mathsf{MP}}]$. (c) Conditional probability distribution for the efficiency with the condition $\dot{w}_2 \in \Omega_2 = [\bar{\dot{W}}_2^{\mathsf{MP}}, \infty)$. All the distributions are compared for two thermodynamic force values, f_2^{MP} and f_2^{ME}. For all plots, we choose $\tau = \tau_2 = 1$.

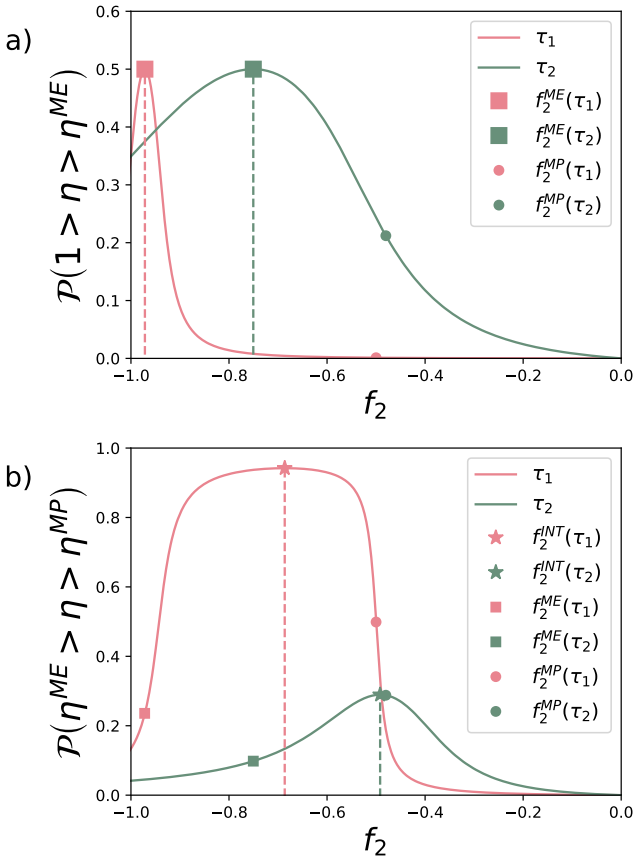

Figure 4.18: Probabilities for the efficiency. (a) Probability of having the efficiency greater than the efficiency at maximum mean power. For both time intervals, the maximum probability is 50%. (b) Probability of having the efficiency greater than the mean efficiency at maximum power, but less than the mean maximum efficiency. The optimal force values maximizing this probability are $f_2^{\text{INT}} = -0.686$ for $\tau_1 = 0.1$ and $f_2^{\text{INT}} = -0.492$ for $\tau_2 = 1$, yielding probabilities of approximately 90% and 20%, respectively.

4.4.2 Conditional probability of power and efficiency

We first define Ω as an arbitrary measurable event for the power variable, which could represent the power exceeding its maximum value ($\dot{w}_2 > \dot{W}_2^{\mathsf{MP}}$) or lying in the intermediate range ($\dot{W}_2^{\mathsf{ME}} < \dot{w}_2 < \dot{W}_2^{\mathsf{MP}}$). We define the conditional probability distribution for the efficiency given an event Ω of $\dot{w}_2$ as,

$$P(\eta|\bar{\dot{w}}_2 \in \{\Omega\}) = \frac{\int_\Omega P(\eta, \bar{\dot{w}}_2) d\bar{\dot{w}}_2}{\mathcal{P}(\bar{\dot{w}}_2 \in \{\Omega\})}, \tag{4.4.19}$$

with the denominator representing the total probability of the specific Ω event occurring. This conditional formulation provides a useful tool for examining any power constraint that the work-to-work engine can present. In Fig. (4.19) we present this analysis for different engine regimes and quantify how the power fluctuations affect the efficiency.

We start by defining the power condition $\Omega_1 = [\dot{W}_2^{\mathsf{ME}}, \dot{W}_2^{\mathsf{MP}}]$. Using the conditional probability defined in Eq. (4.4.19), we examine the probability of the efficiency exceeding the maximum value $\eta > \eta^{\mathsf{ME}}$. In Fig. (4.20a) we plot several important features of this conditional probability. There is a huge reduction of the maximum probability in comparison to the unconstrained case, falling from 50% to much lower values for both time intervals. We will denote f_2^{C1M} as the optimal force that maximizes this probability, where C1M indicates the force that maximizes the efficiency under the condition Ω_1. Now, for the intermediate range $\eta^{\mathsf{ME}} > \eta > \eta^{\mathsf{MP}}$ under the same power constraint, in Fig. (4.20b) we show that this probability is maximized by the optimal force f_2^{C1I}. Notably, these optimal forces lie closer to the maximum-power condition than to the maximum-efficiency condition, demonstrating how the constraint biases the system toward different operational regimes. These results show how the constraint on the power output also limits the system's ability to simultaneously achieve high efficiency values. Once more, the trade-off relation between power and efficiency is explicitly shown in these results. We now expand our investigation to a more broad conditions, $\Omega_2 = [\dot{W}_2^{\mathsf{MP}}, \infty}$. The conditional efficiency distribution for this case is presented in the Fig (4.19 c). This increased range presents a sharply difference in comparison with the intermediate-power results. When examining $\mathcal{P}(\eta \in [\eta^{\mathsf{ME}}, 1]|\dot{w}_2 \in \Omega_2)$, we observe a striking enhancement in probabilities consistently above 50 % across both time scales studied, reaching thein

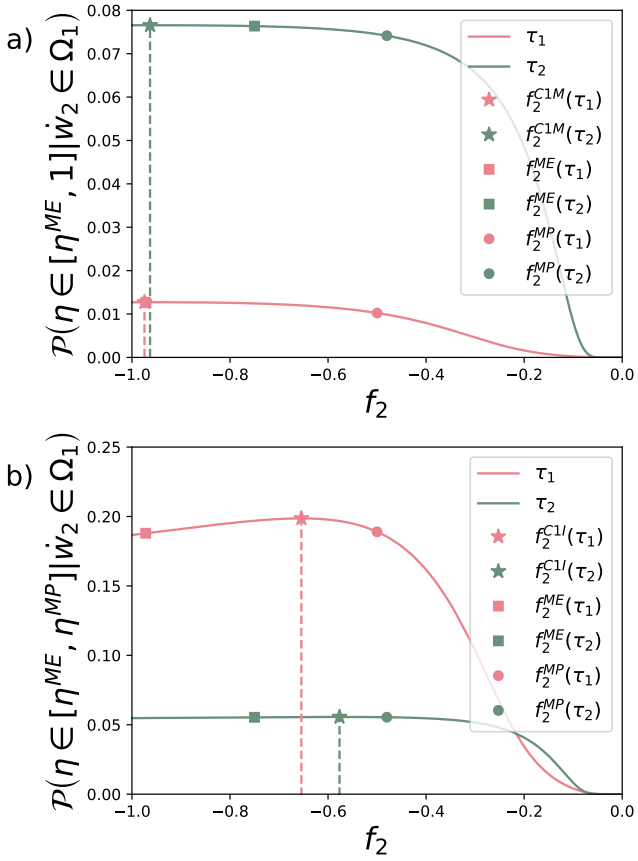

Figure 4.20: Conditional probability, with $\Omega_1 = [\dot{W}_2^{\mathrm{ME}}, \dot{W}_2^{\mathrm{MP}}]$. (a) Conditional probability for the efficiency being greater than the average maximum efficiency. For $\tau_1 = 0.1$, the optimal force is $f_2^{\mathrm{C1M}} = -0.974$ with maximum probability of $\sim 8\%$; for $\tau_2 = 1$, the optimal force is $f_2^{\mathrm{C1M}} = -0.963$ with maximum probability of $\sim 1.2\%$. (b) Conditional probability for the efficiency being in the intermediate range. For $\tau_1 = 0.1$, the optimal force is $f_2^{\mathrm{C1I}} = -0.654$ with maximum probability of $\sim 20\%$; for $\tau_2 = 1$, the optimal force is $f_2^{\mathrm{C1I}} = -0.577$ with maximum probability of $\sim 5\%$. For all cases, the forces that maximize these probabilities differ from the reference forces.

maxima at the optimal force value f_2^{MP}. This represents a significant increase from both the unconsrained case (50 % maximum) and the intermediate power condition. In particular, this peak is observed in the fast cycling regime ($\tau = \tau_1$), where the probabilities approach 90% for certain parameters. This particular results is interesting and contrast what we classicaly known about trade-off relations, suggesting that in regimes of strong pwer fluctuations, the system can achieve both high power and high efficiency by exploiting rare but favorable events where the energy conversion becomes exceptionally efficient.

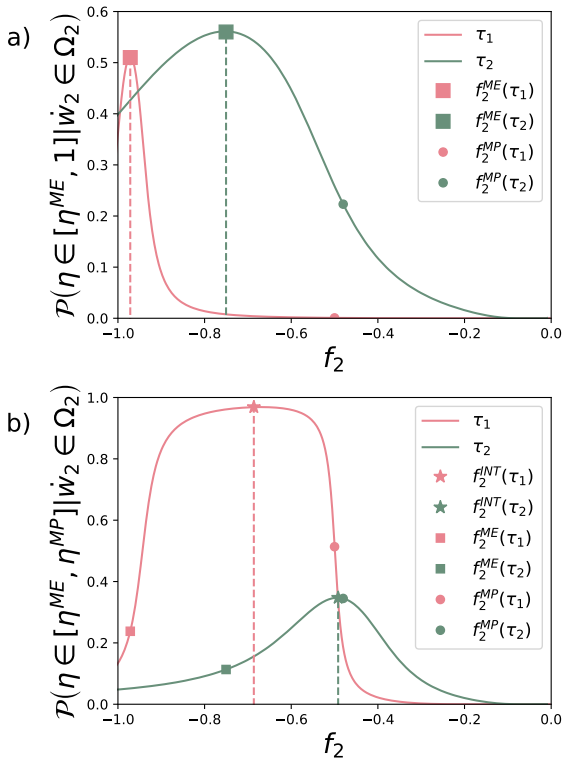

Figure 4.21: Conditional probability, with $\Omega_2 = [\dot{W}_2^{\mathrm{MP}}, \infty)$. (a) Conditional probability for the efficiency being greater than the average maximum efficiency. The probabilities are higher compared with condition 1 and the case without condition, reaching ~ 51% for $\tau_1 = 0.1$. (b) Conditional probability for the efficiency being in the intermediate range. For $\tau_1 = 0.1$, the maximum probability reaches ~ 97%. For all cases, the forces f_2 that maximize these probabilities are the same forces that maximize the probability in the unconditional efficiency case.

For intermediate efficiency values, we also observe an important relation with the time regime, since its probability decreases with increasing τ (see Fig. (4.21)). We also note that the optimal f_2 values match those maximizing the non-conditional intermediate efficiency probabilities, and these probabilities consistently exceed their non-conditional counterparts, demonstrating that high-power conditions enhance the probability of achieving higher efficiency values.

Chapter 5

Collective Heat Engines and Non-equilibrium Phase Transition in Driven Ising Models

The examples studied in the previous chapter deal with engines composed of a single Brownian particle operating as a work-to-work converter. However, nature is plentiful of complex systems composed of many interacting entities, in which cooperative effects often play a crucial role. Examples span multiple biological scales [114], from microbes [12] to the human brain [13], and have been studied in a broad range of research fields, from non-equilibrium effects in chemical processes [14–16] to synchronization in biological networks [17–21]. This vast spectrum of applications highlights that the demand for implementable and robust optimal strategies to engineer collective engines is important and timely. Although the interplay between collective effects and system performance has been extensively studied in quantum systems [23, 26, 115], the

development of classical setups built from interacting units is comparatively much less known and still remains at a preliminary stage [27–31].

We introduce a general class of collective engines, inspired by ferromagnetic equilibrium models [33, 116–118]. They have long-standing importance in the context of collective effects and are at the heart of numerous theoretical and experimental advances, having distinct models (e.g., the Ising, Potts, XY, and Heisenberg) as ideal platforms for describing ferromagnetism. Here we show that synchronized operations under ordered (ferromagnetic) arrangements play a central role in improving system performance by optimizing power and efficiency through fine-tuning of the external driving sources and the coupling parameters. The main features and optimization routes of the engine proposed here can be unveiled both by using a linear analysis close to equilibrium and an effective discrete-state model capturing all relevant effects. Finally, we highlight that our results are robust beyond the case of all-to-all interactions and pave the way for the construction of promising nonequilibrium thermal machines based on ordered structures. All the dynamics and thermodynamics are described exactly as in Sec. (3.3.1), where a set of N spins interacting in an all-to-all manner is considered, with the energy of a given microscopic configuration state given by Eq. (3.3.19). The dynamics of the microscopic states are described by a master equation modeling single-spin flips, as in Eq. (3.3.24). The nonequilibrium setup is realized by the same apparatus described in Sec. (3.5), in which the system is coupled to two thermal reservoirs that also act as a work source through a bias (non-conservative) force (See Fig.(3.1)). In the thermodynamic limit ($N \to \infty$), this system reduces to an effective q-state description, where q is the number of spin states accessible to each spin, with the energy of each mesostate $\beta \in \{-1, 1\}$ and $\beta \in \{-1, 0, 1\}$ for $q = 2$ and $q = 3$, respectively, given by Eq. (3.3.22), which we repeat below for clarity:

$$E_S = \sum_{\beta=1}^{q} \epsilon_\beta N_\beta^{(S)} + \frac{1}{2N} \sum_{(\beta,\beta'<\beta)} [\epsilon_{\beta\beta} N_\beta^{(S)} (N_\beta^{(S)} - 1) + 2\epsilon_{\beta\beta'} N_\beta^{(S)} N_{\beta'}^{(S)}], \tag{5.0.1}$$

for a mesostate S.

5.1 Optimizing power and efficiency in driven Ising models

We now start by optimizing the output performance of a collective heat engine. All thermodynamic quantities will be computed starting from the results of Sec.(3.4). Before moving on, it is important to briefly recall the definitions of models A and B introduced in Sec. (3.3.1). For Model A with $q = 3$, we define $\epsilon_{\uparrow\uparrow} = \epsilon_{\downarrow\downarrow} = \epsilon$, $\epsilon_{\uparrow\downarrow} = \epsilon_{\downarrow\uparrow} = -\alpha\epsilon$, and $\epsilon_{00} = \epsilon_{\uparrow 0} = \epsilon_{\downarrow 0} = 0$. Here, α characterizes the interaction strength between spins in different states. For Model B, we take $\epsilon_{\beta\beta'} = \epsilon\delta_{\beta\beta'}$. This distinction is particularly important here, since the system operates as an engine only when the interaction follows Model A. Fig. 5.1 shows the main features of models A and B for $q = 3$ and $N \to \infty$, in which $p^{\mathrm{st}}_{\beta} \in \{p^{\mathrm{st}}_{\uparrow}, p^{\mathrm{st}}_{\downarrow}, p^{\mathrm{st}}_{0}\}$. In such a mean-field limit, the system is described by a nonlinear master equation that must be self-consistently solved (see Sec.(3.5)). In Fig. 5.1(a)-(b), we show efficiency and power output per unit for model A. This setting allows for the existence of a collective ordered phase for large negative ϵ. In this regime, the system behaves as a heat engine (see Fig. 5.1(a)). As ϵ increases, units deviate from a synchronized phase and a pump behavior emerges. For $\alpha = 1$, units start operating independently after a phase transition, indicated by ♦ in Fig. 5.1(b), while for other α there is a crossover between these collective and independent regimes. Moreover, Fig. 5.1(c) shows that F can be used as a parameter to control the system, as when F increases a pump behavior emerges even in the collective ordered phase. As shown below in Section 5.5, power and heat fluxes are independent of ϵ when units operate independently, indicating that, in the collective phase, ϵ can be chosen appropriately to lead to better performance even as a pump, hence hinting at the relevance of a synchronous phase for this class of engines.

Conversely, no engine regime is present for model B (see Fig. 5.1(d)), when only Potts-like interactions are present. If units operate independently, the engine can only work as a pump in this case. Although model B has been proposed as a work-to-work converter, exhibiting maximum power in the collective regime [28], the absence of Ising-like interactions makes the synchronous phase useless for operating as a heat engine. For these reasons, model A will

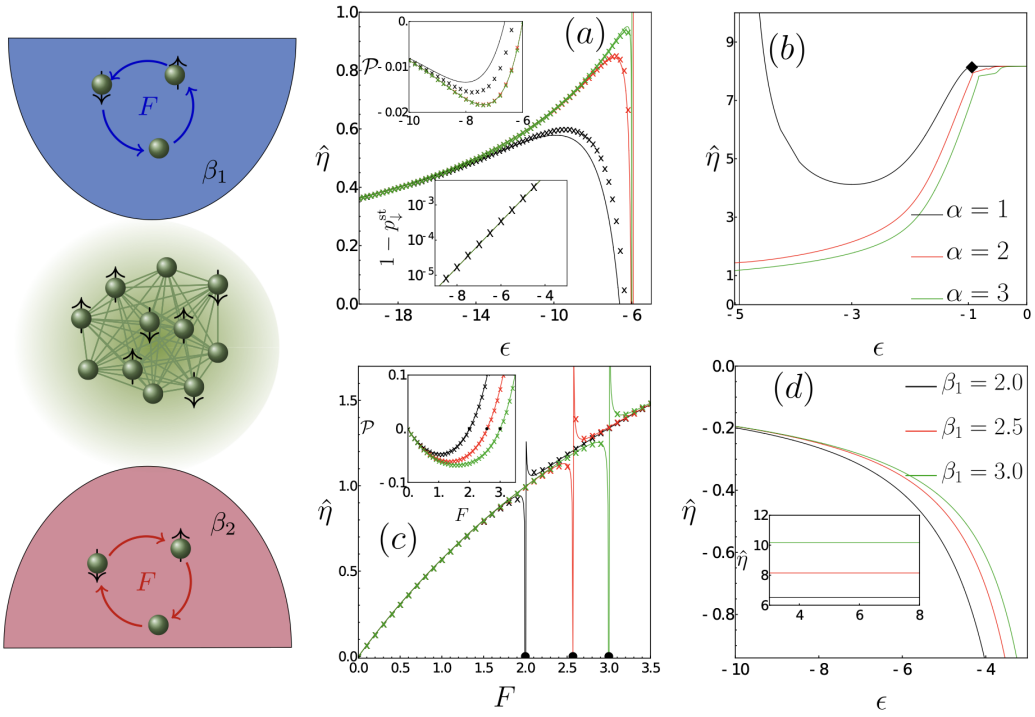

Figure 5.1: Left: Schematics of $q = 3$ engines. Arrows in the reservoirs indicate the direction of the driving F, which is clockwise at high temperature and counter-clockwise at low temperature. (a) Model A ($\epsilon_{\downarrow\uparrow} \neq 0$). The efficiency $\hat{\eta} = \eta/\eta_c$ is shown for different α as a function of the coupling strength ϵ in the strong collective phase (smaller ϵ). Lines are exact results, while dots represent the effective model (see Section 5.3). Power output per unit, $\mathcal{P}$, is presented in the upper inset, while the lower inset is a semilog plot of $1 - p_\downarrow^{\text{st}}$ to show the robustness of the effective description. (b) Same as (a), but in the presence of weak collective effects (larger ϵ). The symbol ♦ in (b) indicates the critical point ϵ_c separating the regimes of collective and independent units. As a result, collective ordered operations favor a heat engine behavior. Parameters in (a) and (b): $\beta_1 = 2$, $\beta_2 = 1$ and $F = 2$. (c) Model A. $\hat{\eta}$ and $\mathcal{P}$ (inset) versus F for different β_1. Vertical lines mark the crossover between heat engine and pump regimes, also indicated by •. Parameters in (c): $\alpha = 3$, $\epsilon = -6$, $\beta_2 = 1$. As previously, symbols correspond to the effective model. (d) Model B ($\epsilon_{\downarrow\uparrow} = 0$). For $F = 1$, $\beta_2 = 1$ and different β_1, the efficiency is shown as a function of ϵ, indicating only a dud regime in this case, as Ising-like interactions are absent. As ϵ increases, model B shows a pump behavior (inset).

be used as the reference model from now on. Analogous findings are also reported for $q = 2$ (model A) in Fig. 5.2. Indeed, we show the efficiency, $\hat{\eta}$, and the power per unit, $\mathcal{P}$, as a function of the interaction strength, ϵ, for different α's, highlighting the presence of the transition from the heat engine to the pump regime.

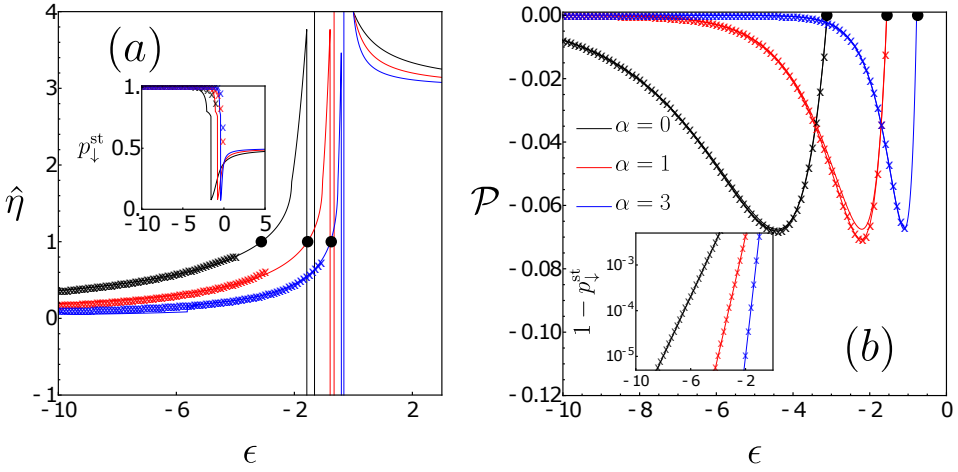

Figure 5.2: $q = 2$ engine (model A). For $\beta_1 = 2$, $\beta_2 = F = 1$ and distinct α, panels (a) and (b) respectively show the efficiency, $\hat{\eta}$, and the power per unit, $\mathcal{P}$, versus the interaction strength, ϵ. Black circles indicate the optimal efficiency, $\eta_{ME} = \eta_c$ ($\hat{\eta}_{ME} = 1$) in this setting (see Section 5.1). Symbols correspond to the effective two-state description, presented in Section 5.3. Insets: plot of $p_{\downarrow}^{st}$ (panel (a)) and semilog plot of $p_{\uparrow}^{st}$ (panel (b)) versus ϵ.

To investigate the optimal working regimes of the proposed model, we extend our results to a wider spectrum of values of the coupling parameter ϵ and the driving F. Figs. 5.3 and 5.4 show the resulting heat maps again for $q = 3$ and $q = 2$ (model A), respectively. Heat engine (blue-red) and pump (purple) regimes are separated by an intermediate region in which units operate as a dud regime (orange). Power and efficiency can be optimized with respect to F (solid lines) or ϵ (dashed lines), while the other quantity is held fixed. It is worth noting that the power output in the heat engine regime presents a global maximum where the two optimization lines cross (dark red spot). This point coincides with the power obtained by simultaneous optimization with respect to F and ϵ. Conversely, no optimal point exists for the efficiency in the (F, ϵ)

space, and the heat engine operates more efficiently as $|\epsilon|$ and F are increased. This result hints at the possibility of boosting the performance of a stochastic heat engine by favoring the emergence of collective order. We highlight that, when $q = 2$ (and $\alpha = 1$), the system exhibits qualitatively similar behavior to the $q = 3$ case.

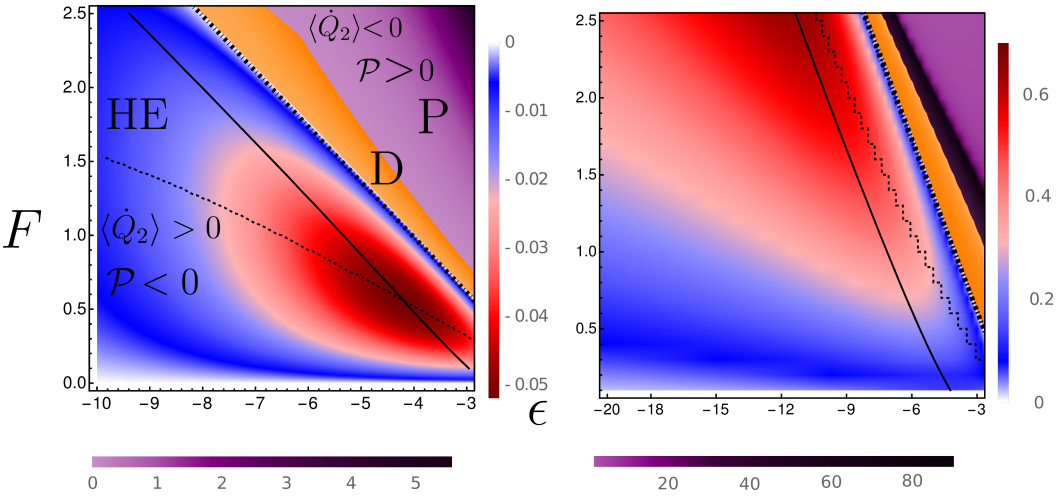

Figure 5.3: Model A and $q = 3$. Left panel depicts the power heat map as a function of driving F and coupling ϵ. HE, P and D indicate, respectively, heat engine, pump, and dud regimes. The solid line shows the maximum power with respect to F at fixed ϵ, while the dashed line accounts for the maximization with respect to ϵ. These two lines cross at the global maximum power. The right panel shows the efficiency $\hat{\eta}$ heat map as a function of F and ϵ. Solid and dashed lines again indicate maximization with respect to F and ϵ, respectively. In both panels, the dot-dashed lines only indicate the boundaries of heat engine regimes. Parameters: $\beta_1 = 2$, $\beta_2 = 1$, $\alpha = 1$.

As suggested by Fig.(5.5), an alternative route for optimization prescribes, at finite ϵ and F, to increase the value of the coupling between different states, α. In Fig. 5.5, we show the maximum efficiency, η_{ME}, the efficiency at maximum power, η_{MP}, and the one obtained by simultaneous optimization, η^*_{MP}, as a function of α for model A and $q = 3$. It is worth noting that η_{ME} approaches (and eventually reaches) the ideal Carnot efficiency η_c, while η^*_{MP} saturates the Curzon-Ahlborn bound, $\eta_{CA} = 1 - \sqrt{\beta_2/\beta_1}$, as the coupling strength is in-

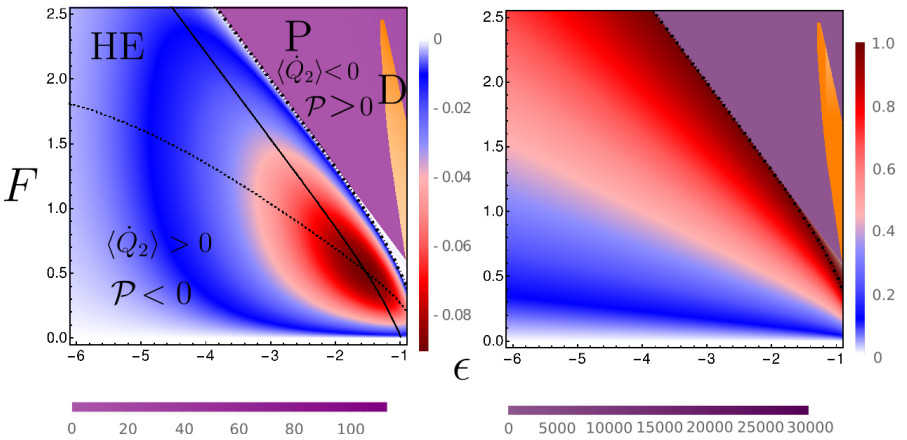

Figure 5.4: Heat maps for $\mathcal{P}$ and $\hat{\eta}$ for the same parameters as in Fig. 5.2. Heat engine, pump, and dud regimes are described by symbols HE, P, and D, respectively. Continuous and dotted lines denote the maximization of power, respectively holding F and ϵ fixed. The dot-dashed line corresponds to the crossover from heat engine to pump regimes, in which $\eta = \eta_c$ in this setup ($q = 2$).

creased. Furthermore, the efficiency at maximum power lies between these two bounds: $\eta_{CA} < \eta_{MP} < \eta_c$. It is worth noting that, for $q = 2$, the Carnot efficiency is reached for all values of α provided that $\mathcal{P} = \langle \dot{Q}_2 \rangle = 0$, as also shown by black circles in Fig. 5.2. Together with the results presented in the heat maps, we can state that, considering a general interacting model admitting an ordered phase, the performance as a heat engine benefits from a synchronized behavior, in combination with the presence of Ising-like couplings.

Systems operating collectively can offer significant advantages, such as reducing dissipated work [119, 120] and optimizing efficiency and/or power through tailored internal structures [27, 121, 122]. Here, we notice a crucial difference in behavior emerging from the existence of the two phases. Indeed, assuming $F > 0$, the system may only operate as a heat engine for $m > 0$ (phase A) and not for $m < 0$ (phase B), as illustrated in Fig. 5.6a. The engine regime occurs deep in the ordered phase with $m \approx 1$, in which case the majority of units are in the state $s_j = -1$. Due to the values of the transition amplitudes, only rarely does a unit flip, mostly to $s_j = 0$, under the action of the hot bath, flipping

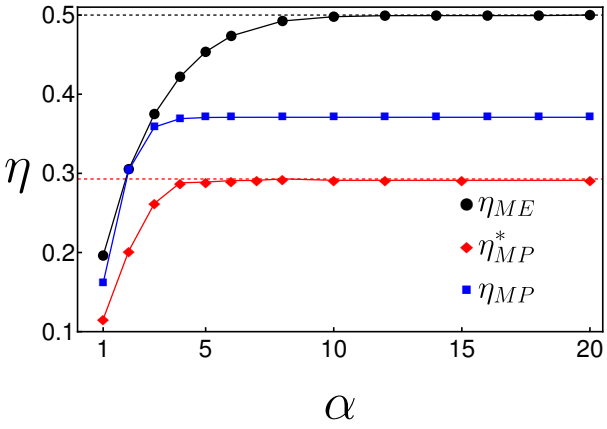

Figure 5.5: Maximum efficiency η_{ME} (black circles), efficiency at maximum power η_{MP} (blue squares), and efficiency at global maximum power η^*_{MP} (red diamonds) as a function of the coupling between different states, α. Solid lines are guides for the eye. The black and red dashed lines correspond to the Carnot η_c and Curzon-Ahlborn η_{CA} efficiencies, respectively.

back to $s_j = -1$ under the action of the cold bath. Both flips involve performing work on the surroundings. On the other hand, if $m \approx -1$, the most common excitation involves flips from the state $s_j = +1$ to $s_j = 0$ under the action of the hot bath, flipping back to $s_j = +1$ under the action of the cold bath. Both flips now involve work performed on the system. (If $F < 0$ the roles of the A and B phases are interchanged.)

Until now, we have focused our analysis on the interaction strength ϵ, on the coupling strength for different spin states α, and on the interplay of these quantities with the non-equilibrium variables. Now we add the effect of the energy of each individual spin by imposing $\Delta \neq 0$ in Eq.(3.3.19). As in the case $\Delta = 0$ and $\epsilon < 0$, there is a small region where the spin system operates as a heat engine. For simplicity, we will conduct this analysis considering Model A, fixing $\alpha = 1$. Also, as done in the equilibrium analysis, we split the solution for the magnetization of the system into two phases, denoted as A and B (not to be confused with Models A and B defined above), respectively characterized by a predominance of spins -1 and $+1$. Later on, we will examine the role of the non-

equilibrium characteristics on the magnetization and on the phase transition of each phase. Letting $m = -\langle s_i \rangle$ denote the order parameter, we have $m > 0$ for phase A and $m < 0$ for phase B, while $m = 0$ indicates independent operation of units. The "quadrupole moment" $q = \langle s_i^2 \rangle$ distinguishes between phases where units predominantly occupy states ± 1 ($q \approx 1$) and where they are in state 0 ($q = 0$).

Next, we extend the analysis to individual energies $\Delta \neq 0$, as depicted in Figs.(5.6) and (5.7). Note that the internal energy Δ substantially affects the engine output. In panel (a) of Fig.(5.6), we also address how the fine-tuning of β_1 (inverse of the cold reservoir temperature) affects the optimization of the efficiency. It is interesting to note how easily the efficiency at maximum power (η_{MP}) overcomes η_{CA}, reaching the limit $\eta_{\mathsf{MP}} \approx \eta_C = 1 - \frac{\beta_2}{\beta_1}$ in the direction of $\beta_1 \to \infty$. In panel (b), we begin to address the effect of $\Delta \neq 0$ on the engine regime itself. We denote Δ_{ME} and Δ_{MP} as the values of Δ that maximize the efficiency and the power output, respectively. We see that with the increase of β_1 in the limit $\beta_1 \to \infty$ (decreasing T_1), there is a convergence of the points Δ_{MP}, Δ_{ME}, and Δ_{A}, where Δ_{A} is the point of the order-disorder phase transition for a fixed ϵ, along with the reduction of the pump regime (P). In the limit $\beta_1 \to \infty$, the transition point Δ_A coincides with the global maximization point for both power and efficiency. This reveals a striking relationship between optimization and the occurrence of a phase transition.

The black dots in the heat map on the bottom-left of Fig. (5.7) represent the efficiency at maximum power η_{MP}, while the green dots are the maximum efficiency η_{ME}. The η_{MP} value is constrained between η_{CA} and η_C (the global maximum for the efficiency). Thus, as one increases Δ, the efficiency also improves, overcoming the Curzon-Ahlborn limit (which is not universal, as discussed in Sec.(2.2.2)). In the limit $\beta_1 \to \infty$, η_C and η_{MP} converge, matching the Carnot limit as ϵ and F increase (as already observed for fixed F and ϵ in Fig.(5.6)). As a consequence of such maximization, $\mathcal{P}_{\mathsf{MP}}$ reduces due to the trade-off relation (dissipation is maximized while the efficiency becomes greater).

Finally, we address the link between optimization and phase transitions (a detailed description and characterization of phase transitions will be depicted in

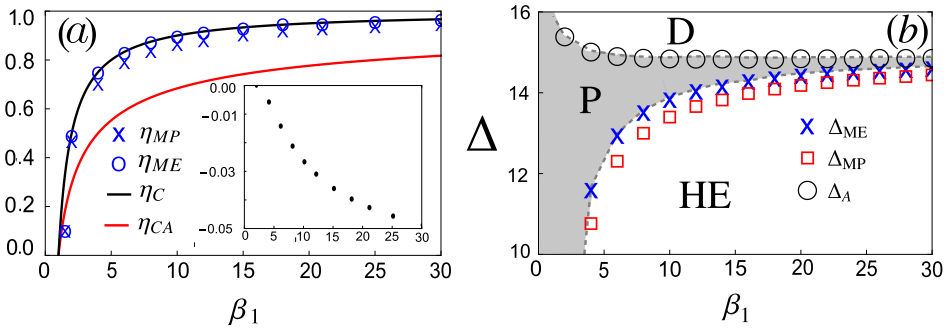

Figure 5.6: (a) η_{MP} (symbols $\times$) and η_{ME} (symbols $\circ$) versus β_1 for $\epsilon = -20$ and $F = 5$. For comparison, the continuous black and red curves represent the corresponding Carnot η_c and the Curzon-Ahlborn efficiency η_{CA}, respectively. The inset shows the corresponding maximum power values, $\mathcal{P}_{MP}$. (b) The convergence of Δ_{MP} and Δ_{ME} to Δ_A is shown as a function of β_1 for the same parameters as in panel (a). Dashed curves here separate the heat-engine (HE) and dud (D) regimes from the heat pump behavior (grey area). In all cases, $\beta_2 = 1$.

Sec.(5.6)). Although Δ_{MP} and Δ_{ME} do not necessarily coincide, both converge to the discontinuous transition value $\Delta = \Delta_A$ as β_1 increases (see Fig. 4.6c), revealing a connection between ideal operational conditions and phase transitions.

5.2 Linear thermodynamics for collective heat engines

We now apply the methods studied in Sec.(2.2.1), considering the non-equilibrium system to be sufficiently close to equilibrium, e.g., $\beta_1 - \beta_2 \ll 1$ and $F \ll 1$. By resorting to the ideas developed in Sec.(2.2.1), we introduce the following thermodynamic forces $f_1 = \beta_1 - \beta_2$ and $f_2 = \beta_1 F$, in such a way that the entropy production, $\langle \dot{\sigma} \rangle$, is expressed in the bilinear form as in Eq.(2.2.18), with $J_1 = \langle \dot{Q}_2 \rangle$ and $J_2 = \mathcal{P}/F$ denoting the thermodynamic fluxes. Such fluxes

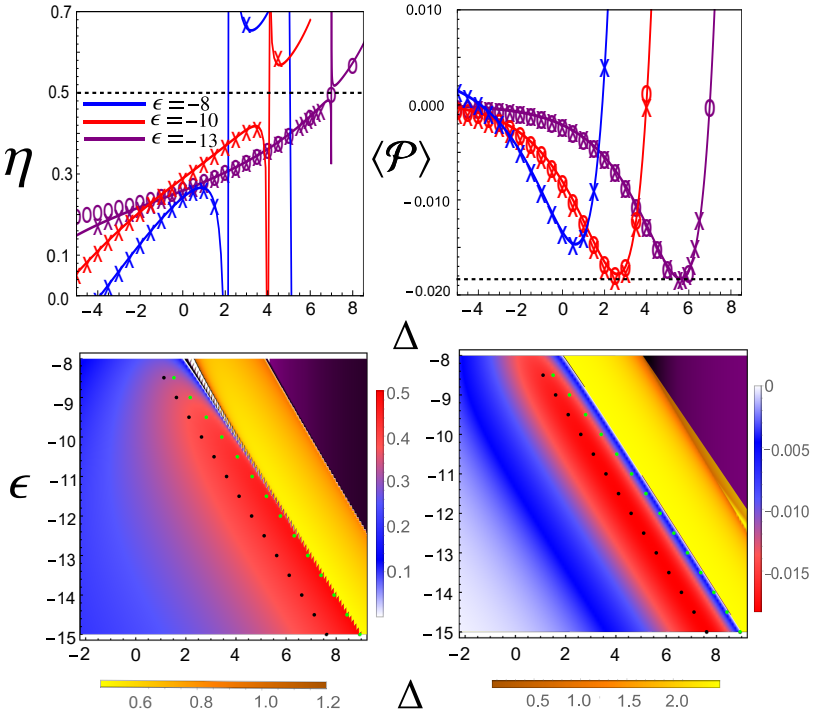

Figure 5.7: Upper panels: Plots of efficiency η (left) and power $\mathcal{P}$ (right) as functions of Δ for different values of ϵ, with driving $F = 2$. Solid lines represent all-to-all mean-field results, $\times$ symbols denote square lattice results, and circles show phenomenological predictions from Eqs. (5.3.9)-(5.3.10). Dashed lines mark ideal efficiency $\eta_c = 1 - \beta_2/\beta_1$ (left) and maximum power $\mathcal{P}_{mP} = -0.01831$ (right). Lower panels: Heat maps of efficiency and power. Black and green dots indicate MP and ME points, respectively. The transition from heat engine (red) to heat pump (yellow) approaches ideal efficiency $\eta = \eta_c$. Parameters: $\beta_1 = 2$, $\beta_2 = 1$, and $F = 2$.

can be expressed in terms of the Onsager coefficients, $J_1 = L_{11}f_1 + L_{12}f_2$ and $J_2 = L_{21}f_1 + L_{22}f_2$, which satisfy the conditions $L_{11}, L_{22} \geq 0$ and $L_{12} = L_{21}$. From Eqs.(2.2.5) and (2.2.18), the efficiency $\hat{\eta}$ promptly reads

$$\hat{\eta} = -\frac{\beta_1 \mathcal{P}}{(\beta_1 - \beta_2)\langle \dot{Q}_2 \rangle} = -\frac{L_{21}f_2f_1 + L_{22}f_2^2}{L_{11}f_1^2 + L_{12}f_1f_2}, \tag{5.2.1}$$

from which $\eta = \hat{\eta}\ \eta_c$ follows immediately. As previously, heat engine ($\mathcal{P} < 0$) and pump ($\mathcal{P} > 0$) regimes impose boundaries on the optimization with respect to f_2, whose absolute value must lie in the interval $0 \leq |f_2| \leq |f_m|$, where $f_m = -L_{21}f_1/L_{22}$, i.e., the so-called stopping force for which $\mathcal{P} = 0$. As previously, the optimization can be performed to obtain maximum power $\mathcal{P}_{\text{MP}}$ (with efficiency η_{MP}) or maximum efficiency η_{ME} (with power $\mathcal{P}_{\text{ME}}$), by changing the force f_2 to optimal values $f_{2,\text{MP}}$ and $f_{2,\text{ME}}$, respectively. These optimal output forces can be expressed in terms of the Onsager coefficients as

$$f_{2,\text{ME}} = \frac{L_{11}}{L_{12}}\left(-1 + \sqrt{1 - \frac{L_{12}^2}{L_{11}L_{22}}}\right) f_1, \tag{5.2.2}$$

and

$$f_{2,\text{MP}} = -\frac{1}{2}\frac{L_{12}}{L_{22}} f_1, \tag{5.2.3}$$

respectively, where the property $L_{21} = L_{12}$ has been considered. By inserting $f_{2,\text{ME}}$ or $f_{2,\text{MP}}$ into the expression for $\hat{\eta}$, we obtain $\hat{\eta}_{\text{ME}}$ and the efficiency at maximum power $\hat{\eta}_{\text{MP}}$ given by

$$\hat{\eta}_{\text{ME}} = -1 + \frac{2L_{11}L_{22}}{L_{12}^2}\left(1 - \sqrt{1 - \frac{L_{12}^2}{L_{11}L_{22}}}\right), \tag{5.2.4}$$

and

$$\hat{\eta}_{\text{MP}} = \frac{L_{12}^2}{4L_{11}L_{22} - 2L_{12}^2}, \tag{5.2.5}$$

Similarly, we can derive the expressions for $\mathcal{P}_{\text{MP}}$ and $\mathcal{P}_{\text{ME}}$. All these quantities are not independent of each other; instead, they satisfy the following relationships:

$$\hat{\eta}_{\text{MP}} = \frac{\hat{\eta}_{\text{ME}}}{1 + \hat{\eta}_{\text{ME}}^2} \qquad \text{and} \qquad \frac{\mathcal{P}_{\text{ME}}}{\mathcal{P}_{\text{MP}}} = 1 - \hat{\eta}_{\text{ME}}^2, \tag{5.2.6}$$

where the symmetry between crossed Onsager coefficients $L_{12} = L_{21}$ has been taken into account. It is convenient to introduce the *coupling parameter* $\kappa = L_{12}/\sqrt{L_{11}L_{22}}$ [123, 124], in such a way that the optimal efficiencies $\hat{\eta}_{\text{MP}}$ and $\hat{\eta}_{\text{ME}}$ are solely expressed in terms of this quantity as follows:

$$\hat{\eta}_{\text{ME}} = -1 + \frac{2}{\kappa^2}\left(1 - \sqrt{1 - \kappa^2}\right), \tag{5.2.7}$$

and

$$\hat{\eta}_{\text{MP}} = \frac{1}{2}\frac{\kappa^2}{2-\kappa^2}, \tag{5.2.8}$$

respectively. Since $\langle \dot{\sigma} \rangle \geq 0$, it follows that κ must be constrained in the interval $-1 \leq \kappa \leq 1$, implying that both $\hat{\eta}_{\text{MP}}$ and $\hat{\eta}_{\text{ME}}$ are confined to $0 \leq \hat{\eta}_{\text{MP}} \leq 1/2$ and $0 \leq \hat{\eta}_{\text{ME}} \leq 1$, respectively. Notice that $\kappa = \pm 1$ implies that the determinant of the (2×2) Onsager matrix is equal to zero. This, in turn, implies proportionality between the two thermodynamic fluxes, i.e., $J_1 \propto J_2$, for all forces f_1 and f_2. Fig. 5.8 shows that all the signatures of collective effects are also captured by the linear regime, describing very well the system behavior near equilibrium (panels (b) and (c)). Remarkably, the increase in efficiencies towards the Carnot bound as ϵ and F increase, as described in the main text, is understood from the interplay among Onsager coefficients, L_{ij} (shown in panel (a) as a function of ϵ), that leads to $\kappa \to -1$ (inset of panel (d)). Also, $\hat{\eta}_{ME}$ and $\hat{\eta}_{MP}$ closely follow the analytical expressions presented in Eqs. (5.2.7) and (5.2.8) (see Fig. 5.8d). Since $|\kappa|$ monotonically increases with ϵ, both η_{ME} and η_{MP} approach their ideal values when collective ordered effects are stronger, highlighting the importance of unit synchronization for increasing engine performance.

As a final comment, it is worth pointing out that there is no a priori advantage for the system when operating near criticality. Since κ, a measure of the degree of collective effects, vanishes as the system approaches criticality (as ϵ increases), both $\hat{\eta}$ and power $\mathcal{P}$ also decrease (see Fig. 5.8d). This is also consistent with Eqs. (5.2.4) and (5.2.5).

5.3 Effective description in the regime of strong collective effects

Despite being exact in the all-to-all case, the non-linear form of the master equation prevents the derivation of closed expressions for probabilities and clear insights into the influence of each parameter for all-to-all interactions. To grasp the main features of the system in the regime of strong collective effects, we develop an effective discrete-state description which is valid in the ordered

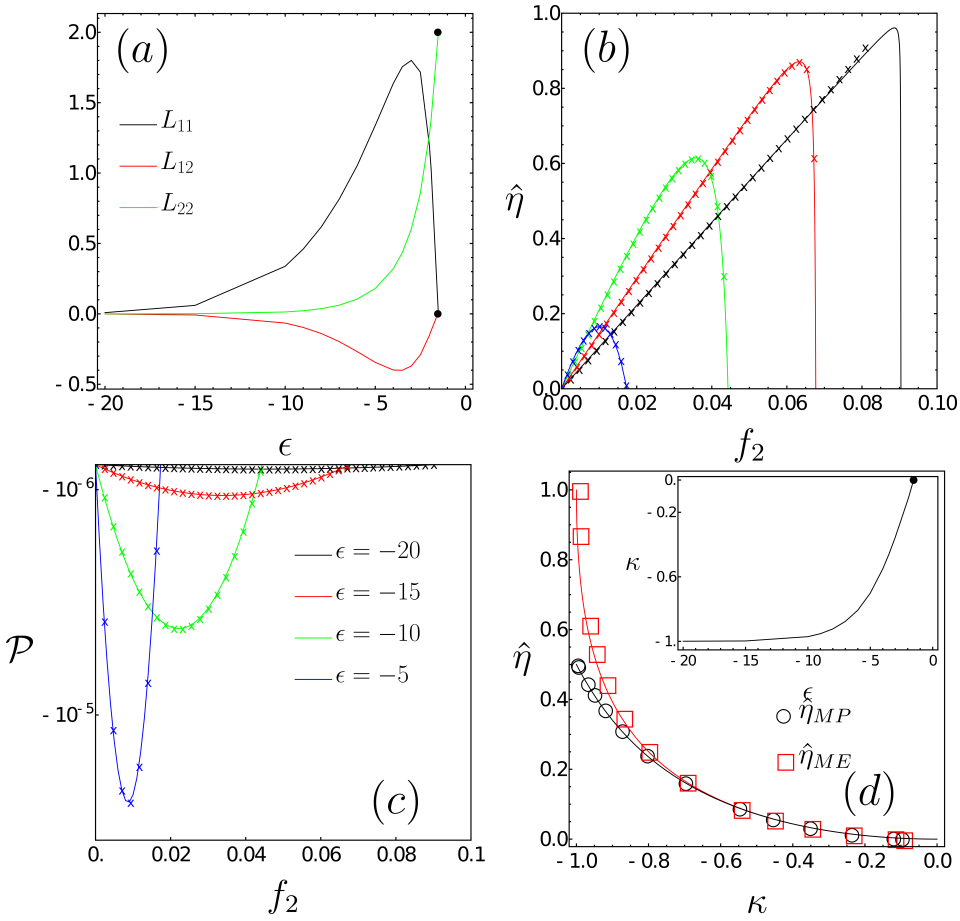

Figure 5.8: For model A, $q = 3$ and $\alpha = 1$, we show the thermodynamics of the system close to the equilibrium regime. Panel (a) shows the Onsager coefficients L_{ij} versus the interaction parameter ϵ. In (b) and (c), respectively $\hat{\eta}$ and $\mathcal{P}$ versus f_2 are reported for $f_1 = 9 \times 10^{-3}$. Continuous lines are exact results, while symbols correspond to Eq. (5.2.1). The heat engine behavior is delimited by $f_2 = f_m$. Panel (d) shows the behavior of maximum efficiency $\hat{\eta}_{\mathrm{ME}}$ and efficiency at maximum power $\hat{\eta}_{\mathrm{MP}}$ versus κ, where continuous lines follow Eqs. (5.2.7) and (5.2.8). The inset shows how κ changes as a function of ϵ, and $\bullet$ denotes the phase transition to the independent regime taking place at $\epsilon_c \approx -1.5$ (see also the same symbol in panel (a)).

collective regime. By taking $\alpha > 0$, $\epsilon < 0$, and $-\epsilon \gg F > 0$, this effective description can be derived employing the matrix-tree theorem [125]. A more detailed evaluation of the phenomenological and effective analysis for $\alpha = 1$ and $q = 3$ using the spanning tree theorem can be found in Appendix A.4. We start by describing the system as a coarse-grained q-state model. Starting with $q = 2$ to fix the ideas, the ordered phase is two-fold degenerate and characterized by the predominance of spins of one type ($\downarrow$ or $\uparrow$). As a consequence, a 2-state system exhibiting collective order can only be in two states, $\downarrow$ or $\uparrow$. It can be described using a coarse-grained master equation with two transition channels, i.e., driven by bath 1 or 2. The set of NESS solutions of the master equation for $q = 2$, $p_{\uparrow}^{st} + p_{\downarrow}^{st} = 1$, can be directly found by applying $\dot{p}_{\beta} = 0$ in Eq.(3.5.7), resulting in

$$p_{\downarrow}^{st} = \frac{\omega_{\downarrow\uparrow}^{(1)} + \omega_{\downarrow\uparrow}^{(2)}}{\omega_{\downarrow\uparrow}^{(1)} + \omega_{\downarrow\uparrow}^{(2)} + \omega_{\uparrow\downarrow}^{(1)} + \omega_{\uparrow\downarrow}^{(2)}} \,. \tag{5.3.1}$$

The explicit expressions for the transition rates are shown in Sec.(3.5). Equation 5.3.1 is an implicit equation, as the transition rates depend on $p_{\downarrow}$. By focusing on the case $p_{\downarrow}^{st} \approx 1$ (the opposite case can be immediately obtained by swapping $\downarrow$ with $\uparrow$), and performing the $\epsilon \to -\infty$ limit, we obtain:

$$p_{\downarrow}^{st} \approx \frac{1}{1 + e^{\frac{1}{2}\{(\beta_1+\beta_2)(\alpha+1)\epsilon + F(\beta_1-\beta_2)\}}}. \tag{5.3.2}$$

Taking into account that $\beta_2 < \beta_1$, $F > 0$, and $-\epsilon \gg F$, as we are in the regime of strong collective effects, we can approximate the above expression as $p_{\downarrow}^{st} \approx \frac{1}{2} e^{\{(\beta_1+\beta_2)(1+\alpha)\epsilon\}} e^{\frac{(\beta_1-\beta_2)F}{2}}$. This can also be derived from the fact that $p_{\downarrow}^{st} \approx 1 - (\omega_{\uparrow\downarrow}^{(1)} + \omega_{\uparrow\downarrow}^{(2)})/(\omega_{\downarrow\uparrow}^{(1)} + \omega_{\downarrow\uparrow}^{(2)}) \approx 1 - \omega_{\uparrow\downarrow}^{(1)}/\omega_{\downarrow\uparrow}^{(2)}$, under the aforementioned assumptions. By inserting the approximate expression for $p_{\downarrow}^{st}$ into the formulas in Eqs.(3.5.3) and (3.5.5), one arrives at the following expression for the effective power per unit, $\mathcal{P}_{\text{eff}}$, when $q = 2$:

$$\begin{aligned} \mathcal{P}_{\text{eff}} = \frac{F}{2} e^{-\frac{1}{2}\beta_2[(\alpha+1)\epsilon M + F]} \left[e^{\frac{1}{2}[(\beta_1+\beta_2)F - (\beta_1-\beta_2)(\alpha+1)\epsilon M]} - 1 \right] \\ \times \left[(1+M) e^{\frac{1}{2}[-(\beta_1-\beta_2)F + (\beta_1+\beta_2)(\alpha+1)\epsilon M]} - M + 1 \right] . \end{aligned} \tag{5.3.3}$$

Analogously, we obtain the following expression for the effective heat flux from bath 2, $\langle \dot{Q}_2 \rangle_{\text{eff}}$:

$$\begin{aligned} \langle \dot{Q}_2 \rangle_{\text{eff}} = -(F + (\alpha+1)M\epsilon) \Bigg[\sinh\left(\frac{\beta_2}{2}(F + (\alpha+1)M\epsilon) \right) \\ + M \cosh\left(\frac{\beta_2}{2}(F + (\alpha+1)M\epsilon) \right) \Bigg]. \end{aligned} \tag{5.3.4}$$

where $M = p_{\downarrow}^{\text{st}} - p_{\uparrow}^{\text{st}}$ is the order parameter. It is worth mentioning that $|M|$ reduces to $1 - 2e^{\beta(1+\alpha)\epsilon}$ in the equilibrium regime ($\beta_1 = \beta_2$ and $F = 0$), becoming equal to the magnetization per spin of the Ising model for sufficiently low temperatures $\beta \gg \beta_c = (1+\alpha)\epsilon/k_B$. Fig. 5.2 shows the validity of our approximate expressions for $p_{\downarrow}^{st}$ for distinct sets of α when $q = 2$ (symbols in the figure).

Our effective description can also be employed when $q = 3$, always considering model A. First, we consider the coarse-grained 3-state system, where each state corresponds to a spin state. Then, directly from the transition rates, we observe that, when the system is in one of the degenerate collective states, say $\downarrow$, i.e., $p_{\downarrow}^{st} \approx 1$, the transitions from $\uparrow$ to $\downarrow$ and 0 are almost unidirectional for $F > 0$ and $-\epsilon \gg F$. As a consequence, we can approximate the coarse-grained 3-state system as a 2-state model with only 0 and $\downarrow$. Finally, we deal with this system following the same steps as in the $q = 2$ scenario, obtaining:

$$p_{\downarrow}^{st} \approx \frac{1}{1 + e^{\frac{1}{2}\{(\beta_1+\beta_2)\epsilon + (\beta_1-\beta_2)F\}}} , \tag{5.3.5}$$

with $p_0^{st} \approx 1 - p_{\downarrow}^{st}$. Once again, as before, we can also write $p_{\downarrow}^{st} \approx 1 - \omega_{0\downarrow}^{(1)}/\omega_{\downarrow 0}^{(2)} = 1 - e^{\frac{1}{2}\{(\beta_1+\beta_2)\epsilon + (\beta_1-\beta_2)F\}}$, which gives our approximation for strong collective effects. Fig. 5.9 shows the validity of our approximate expressions for $p_{\downarrow}^{st}$ for distinct sets of temperatures β_1, β_2 and F, when $q = 3$. The corresponding expression for power per unit is given by

$$\begin{aligned} \mathcal{P}_{\text{eff}} &= F\Big[(1+M)\left(e^{\frac{\beta_1}{2}\Phi_-^{(\alpha)}} - e^{-\frac{\beta_2}{2}\Phi_+^{(\alpha)}} - e^{-\frac{\beta_1}{2}\Phi_-} + e^{\frac{\beta_2}{2}\Phi_+}\right) \\ &- M \left(e^{\frac{\beta_1}{2}\Phi_-} - e^{-\frac{\beta_2}{2}\Phi_+} - e^{-\frac{\beta_1}{2}(\Phi_+^{(\alpha)} + M\epsilon)} + e^{\frac{\beta_2}{2}(\Phi_-^{(\alpha)} - M\epsilon)}\right)\Big] , \end{aligned} \tag{5.3.6}$$

where $\Phi_\pm = F \pm M\epsilon$ and $\Phi_\pm^{(\alpha)} = F \pm \alpha M\epsilon$, with $M = p_{\downarrow}^{st} - p_{\uparrow}^{st} \approx 1 - e^{\frac{1}{2}\{(\beta_1+\beta_2)\epsilon + (\beta_1-\beta_2)F\}} > 0$. Also in this case, from Eq.(3.5.3), we obtain the following expression for $\langle \dot{Q}_2 \rangle_{\text{eff}}$:

$$\begin{aligned} \langle \dot{Q}_2 \rangle_{\text{eff}} &= -(1+M)\left[\Phi_+ e^{\frac{1}{2}\beta_2\Phi_+} - \Phi_+^{(\alpha)} e^{-\frac{1}{2}\beta_2\Phi_+^{(\alpha)}}\right] \\ &+ M\left[(\Phi_-^{(\alpha)} - M\epsilon)e^{\frac{1}{2}\beta_2(\Phi_-^{(\alpha)} - M\epsilon)} - \Phi_+ e^{-\frac{1}{2}\beta_2\Phi_+}\right]. \end{aligned} \tag{5.3.7}$$

The efficiency is readily evaluated by taking their ratio. In the limit of large α, it reads:

$$\eta_{\text{eff}} = \frac{F}{\Phi_+}\left[1 - \frac{\exp\left(-\frac{\beta_1}{2}\Phi_-\right) + 2M\cosh\left(\frac{\beta_1}{2}\Phi_-\right)}{\exp\left(\frac{\beta_2}{2}\Phi_+\right) + 2M\cosh\left(\frac{\beta_2}{2}\Phi_+\right)}\right]. \tag{5.3.8}$$

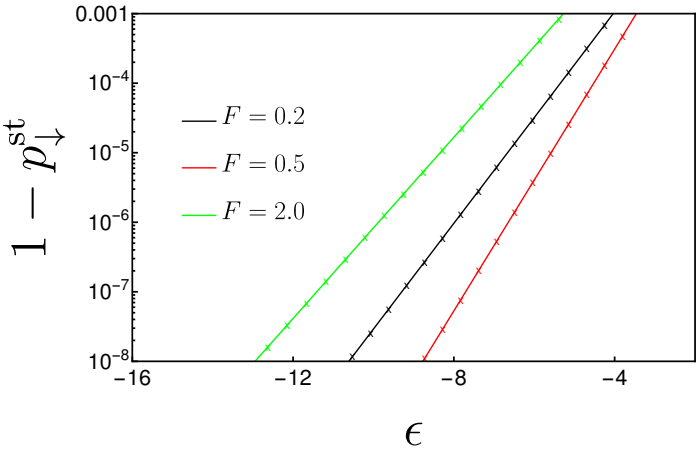

Figure 5.9: Model A, $q = 3$. Semilog plot of $1 - p_{\downarrow}^{st}$ versus ϵ for distinct sets of β_1 and F. Continuous lines are exact results for $N \to \infty$, while symbols correspond to the solution evaluated from the effective model. Black, red and green curves show results for $\beta_1 = 5/2, 10/3$ and 2, respectively. In all cases $\beta_2 = 1$.

The validity of this approach is also shown in Fig. 5.5 for different values of α (symbols). The effective discrete-state model provides a very good description of both the heat engine and pump regimes. However, small discrepancies arise when $p_{\uparrow}^{st}$ is not negligible (e.g., for small $-\epsilon$ and F).

The same effective approach must be applied to a scenario with the individual energy $\Delta \neq 0$, which also presents a collective case for both phases A ($m \approx 1$) and B ($m \approx -1$). As shown in Fig.(5.6), the system only works as an engine for $F > 0$ in phase A. Fixing $\alpha = 1$ and $q = 3$, we employ the effective case where phase A works as an engine ($m \approx 1$) by applying $|\beta_\nu(\epsilon + \Delta)| \gg 1$ and $|\beta_1 - \beta_2| \gg 0$,

$$\langle \mathcal{P}_{\rm eff}^{(A)} \rangle = \frac{2F\left(e^{\frac{1}{2}\beta_1(\Delta+\epsilon+F)} - e^{\frac{1}{2}\beta_2(\Delta+\epsilon-F)}\right)}{e^{\frac{1}{2}((\beta_1+\beta_2)(\Delta+\epsilon)+F(\beta_1-\beta_2))} + 1}, \tag{5.3.9}$$

and

$$\eta_{\rm eff}^{(A)} = \frac{2F}{F - \epsilon - \Delta}\left(e^{\frac{1}{2}\{(\beta_1+\beta_2)(\Delta+\epsilon)+F(\beta_1-\beta_2)\}} + 1\right). \tag{5.3.10}$$

Similar expressions for phase B show that $\langle \mathcal{P}_{\rm eff}^{(B)} \rangle > 0$ and $\eta_{\rm eff}^{(B)} < 0$, which is characteristic of a dud regime.

The phenomenological description employed in Sec.(5.3) allows the quantification of this effect via expressions for $\langle \mathcal{P} \rangle$ and η, valid when $|\beta_\nu(\epsilon + \Delta)| \gg 1$ and β_1 is sufficiently different from β_2 so that the system can operate as a heat engine, as presented in Eqs.(5.3.9) and (5.3.10). Similar expressions for phase B show that $\langle \mathcal{P}_{\text{eff}}^{(B)} \rangle > 0$ and $\eta_{\text{eff}}^{(B)} < 0$, so that, in this phase, the system never operates as a heat engine. On the other hand, for sufficiently distinct values of β_1 and β_2, there is a range of values of β_1 in which the system, in phase A, operates as a heat engine close to maximum power and maximum efficiency, as shown in Fig. 4.6b. While the second law of thermodynamics prevents ideal efficiency at finite power, the interactions and individual energy distributions allow for the maximization of power and efficiency at values of Δ denoted by Δ_{MP} and Δ_{ME}, respectively, with the other parameters held fixed. These values are close to each other, enabling near-ideal performance (i.e., near maximum power and efficiency). They converge toward the ideal efficiency $\eta_c = 1 - \beta_2/\beta_1$ as β_1 increases. These findings hold not only for all-to-all interactions but also in square lattice configurations (marked by $\times$ symbols in Fig. 4.6a), without requiring specialized optimization procedures, such as reward functions that balance power and efficiency.

5.4 Many versus few interacting units and beyond the all-to-all case

Although our findings have been derived in the $N \to \infty$ limit for all-to-all interactions, the main hallmarks have been found to be robust when finite-size effects and other topologies are considered. Panels (a) and (b) of Fig. 5.10 show, for model A and $q = 3$, numerical results for the all-to-all case at increasing N. We notice a reduced range of parameters for which the system operates as a heat engine, but no significant qualitative changes. In Appendix A.5, we also explore the limiting case $N = 2$ and find similar results, showing that a minimal setup of $N = 2$ interacting units already captures the essential ingredients of the model. It is worth noting that the system starts approaching the mean-field behavior already for $N \geq 10$, in similarity to work-to-work transducers [28]. A

very interesting feature is an increase in the finite-size efficiency at small ϵ, due to the fact that $\langle \dot{\mathrm{Q}}_2 \rangle / N$ monotonically decreases with N, while the absolute value of $\mathcal{P} = \langle \mathrm{P} \rangle / N$ increases within a certain range of parameters.

The all-to-all case also describes very precisely the behavior of interactions forming a regular arrangement. For simplicity, we restrict our analysis to model A and $q = 3$ in a square lattice of linear size L. Each site i is associated with a spin variable $\sigma_i = \pm 1, 0$, and Eq.(3.3.19) then becomes

$$E_i = \frac{1}{2k} \sum_{i=1}^{N} \sum_{j=1}^{k} \epsilon \sigma_i \sigma_{i+j} \Big[\delta_{\sigma_i, \sigma_{i+j}} + \alpha \delta_{\sigma_i, -\sigma_{i+j}} \Big], \tag{5.4.1}$$

where $k = 4$ for the square lattice. Despite the absence of exact results in such a case, the system's behavior and thermodynamic properties can be evaluated numerically by employing the Gillespie algorithm [73]. In panels (c) and (d) of Fig. 5.10 and in Fig. 5.11, we draw distinct comparisons with the all-to-all case, for different parameters and by increasing the system size. All of them agree almost perfectly, highlighting that the all-to-all case is also insightful when considering lattice models. This observation not only reinforces the generality of the model proposed here to capture the interplay between collective effects and system performance, but also the reliability of our results for finite-size systems.

5.5 Crossover from heat engine to pump regimes

Fig. 5.12 depicts the relationship between the degree of synchronization and system efficiency $\hat{\eta}$ for the same parameters as in Fig. 5.1. This result is consistent with the fact that the system operates as a heat engine and pump, respectively, when units operate collectively and almost (or completely) independently. In all cases, as ϵ increases towards positive values (arrows in Fig. 5.12), the system hits a threshold ϵ_c giving rise to the independent mode of operation. This threshold can emerge in different ways, such as via a discontinuous phase transition ($q = 2$, model A and B; $q = 3$, model B) or a continuous one ($q = 3$, model A, $\alpha = 1$), or even as a crossover with no phase transitions ($q = 3$, model A, $\alpha \neq 1$). Although our general findings are valid in all cases, in

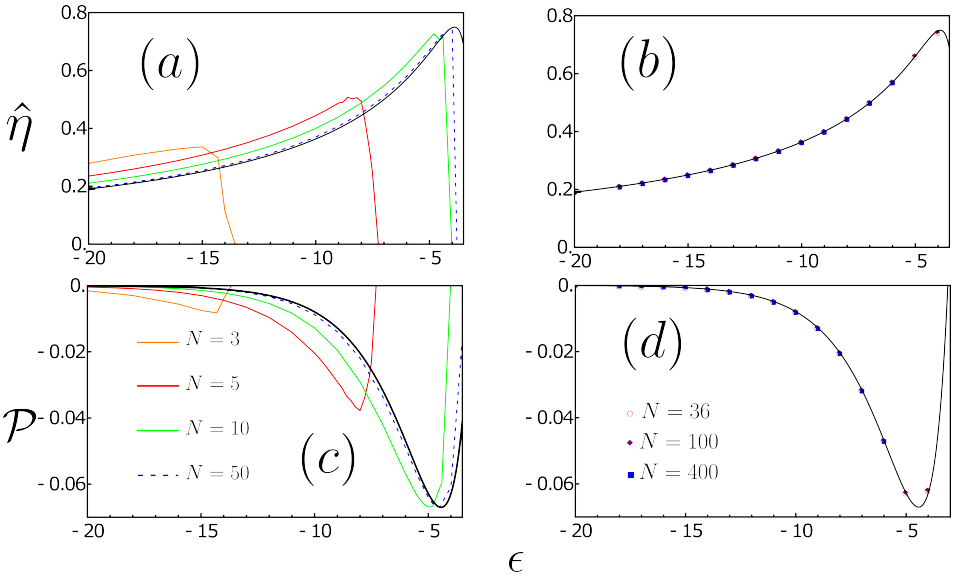

Figure 5.10: (a) Efficiency $\hat{\eta}$ in the heat engine regime for increasing system size N. The black continuous line represents the $N \to \infty$ case. (b) Same as (a) for the power output per unit $\mathcal{P} = \langle \mathrm{P} \rangle / N$. (c) The all-to-all case (continuous line) is compared with a square lattice of increasing size N (dots). (d) Same as (c) for $\mathcal{P}$. Numerical values have been obtained using the Gillespie algorithm. Parameters: $\beta_1 = 2$, $\beta_2 = 1$, $F = 1$, and $q = 3$.

the presence of a phase transition it is possible to obtain closed expressions for $\mathcal{P}$ and $\langle \dot{Q}_\nu \rangle$ per unit. As shown in Appendix A.7, the disordered regime in such cases is characterized by equal probabilities $p_\downarrow^* = p_0^* = p_\uparrow^* = 1/3$ for $\epsilon \geq \epsilon_c$. By inserting this condition into Eq. (3.5.9), it follows that:

$$\begin{aligned} \mathcal{P} &= 2F\Big[\sinh\Big(\frac{F\beta_1}{2}\Big) + \sinh\Big(\frac{F\beta_2}{2}\Big)\Big] \quad \text{and} \\ \langle \dot{Q}_\nu \rangle &= -2F \sinh\Big(\frac{F\beta_\nu}{2}\Big), \end{aligned} \tag{5.5.1}$$

both being independent of ϵ. Similar formulas can be obtained for $q = 2$ and $\epsilon \to \infty$, differing from them solely by a factor of 2. The corresponding efficiency, in both cases, is $\eta = 1 + \Big(\sinh(\beta_1 F/2)/\sinh(\beta_2 F/2)\Big)^{-1}$. All these expressions state that only a pump regime is possible when units operate independently. Although both collective and independent operations allow the emergence of a pump regime, power and heat fluxes are independent of ϵ when units oper-

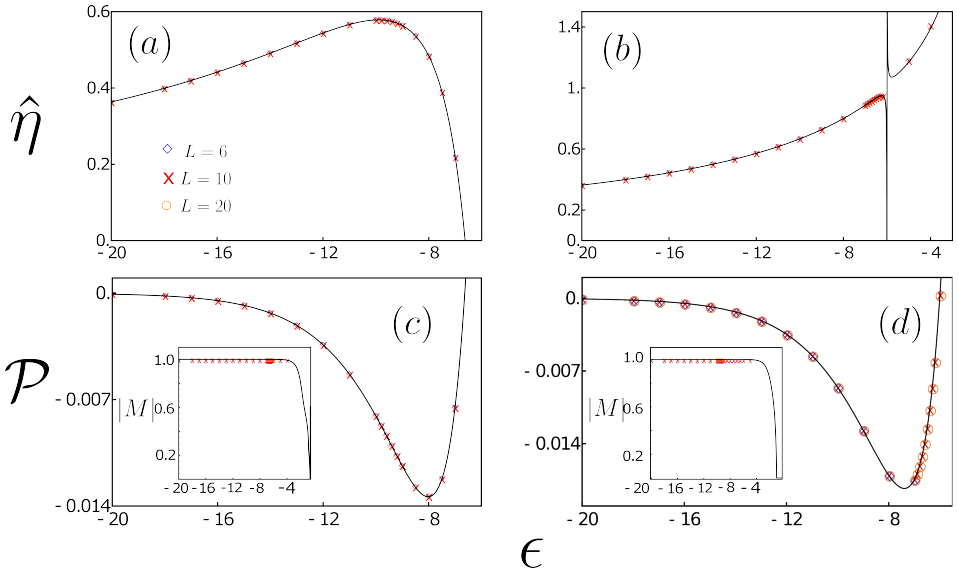

Figure 5.11: Performance of model A for $q = 3$ on a square lattice ($k = 4$ nearest neighbors). (a) Efficiency $\hat{\eta}$ as a function of ϵ for $\alpha = 1$, in the presence of a discontinuous transition between heat engine and pump regimes. (b) Efficiency as a function of ϵ for $\alpha = 3$, in the presence of a crossover behavior. (c) Power output per unit, $\mathcal{P}$, as a function of ϵ for $\alpha = 1$. The inset shows the behavior of $|M|$ with ϵ. (d) $\mathcal{P}$ as a function of ϵ for $\alpha = 3$. The inset shows the order parameter as a function of ϵ. In all panels, symbols indicate numerical results for the system size N, while continuous lines indicate the all-to-all case. Parameters: $\beta_1 = 2$, $\beta_2 = 1$, $F = 2$. Numerical results have been obtained using the Gillespie algorithm.

ate independently, Eq. (5.5.1), indicating that, in the collective phase, ϵ can be chosen appropriately to lead to better performance even as a pump. This result further strengthens the role of interactions and collective operations in an engine model with Ising-like interactions.

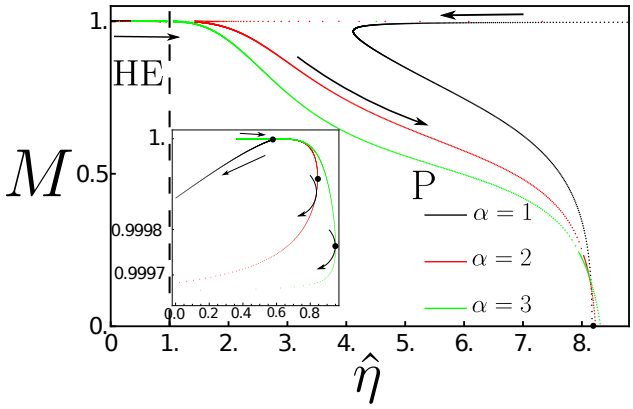

Figure 5.12: For the same parameters as in Fig. 5.13a, we show the order parameter $M = p_{\downarrow}^{st} - p_{\uparrow}^{st}$ versus system efficiency $\hat{\eta}$ for the collective (HE, i.e., heat engine) and independent (P, i.e., pump) regimes. Inset: Zoom of the curves in the heat engine regime, where • indicates where the maximum value of efficiency is attained. Arrows represent the direction of increasing ϵ.

5.6 Splitting of nonequilibrium phase transitions in driven Ising models

Until now, we have presented a system inspired by an equilibrium Ising model, considered in two variants (models A and B) according to the different phase interaction strength α. For both models, we split the phases into two according to the dominant state of the spins: a collective (ordered) and an independent (disordered) phase. We also mentioned a phase transition between these phases for $\alpha = 1$ (for $\alpha > 1$ there is no phase transition, only a crossover), and we now investigate it in more detail. One important question that arises from this analysis is how strong the interplay of non-equilibrium ingredients is and how these values affect crucial quantities for describing phase transitions, such as the magnetization and the critical exponents. For fixed $\alpha = 1$ and for model A, we split the system into two phases, A and B (not to be confused with the model, which is fixed in this analysis), according to which phase dominates at the start of the dynamics (spins up and down, respectively). We reveal an innovative phenomenon in which the interplay between different temperatures

and driving forces splits the order-disorder (or collective-independent) transition points depending on which ordered state initially dominates. Not only the point, but also the order of the transition changes, being of second order for A and of first order for B. The non-equilibrium effects also affect the critical exponents, yielding a continuous transition (phase A) with an exponent different from the classical one ($\beta = 1/2$). In addition, we study the engine regime and the entropy production in the vicinity of the phase transition, expanding in the criticality (in the continuous case). It is of great importance to understand this critical behavior not only to construct a clear relation between the phase and the engine regime, but also to emphasize the role of entropy production as an important quantity for characterizing a non-equilibrium phase transition, since it captures the irreversible character that the usual order parameter does not [126–128].

The interplay between biased driving forces and different ordered phases results in unique features of phase transitions with no equilibrium analog. Each ordered phase is associated with a distinct transition point, X_A or X_B (X being either ϵ or Δ) for $m > 0$ and $m < 0$, respectively, and, remarkably, these transitions can have different orders, with one being continuous and the other discontinuous (see Fig. 5.13a). This contrasts with typical phase transitions characterized by spontaneous symmetry breaking, where the splitting of a transition point associated with hysteresis involves transitions which are *both* discontinuous, and which are related to stability limits of the ordered and disordered phases. To illustrate these features, we analyze interactions on both square lattice arrangements (coordination number $k = 4$) and the all-to-all version ($k = N \to \infty$), the latter case yielding exact results which we now describe.

Following previous work [27–29, 129] and also as described in Sec.(3.3.1), we describe the all-to-all dynamics via the densities of units in each of the possible individual states, $n_i = \langle N_i/N \rangle$, with $i \in \{-, 0, +\}$. Here, $N_\pm$ represents the number of units in the local states $s = \pm 1$, and N_0 is the number of units for which $s = 0$. The dynamics of $\{n_i\}$ is governed by the master equation

$$\dot{p}_i(t) = \sum_{\nu=1}^{2} \sum_{j \neq i} J_{ij}^{(\nu)}(t), \tag{5.6.1}$$

where $J_{ij}^{(\nu)}(t) = \omega_{ij}^{(\nu)} n_j(t) - \omega_{ji}^{(\nu)} n_i(t)$, with density-dependent transition rates $\omega_{ji}^{(\nu)}$

whose explicit expressions are presented in Appendix A.4. The order parameter m and the quadrupole moment q are given by $m = n_- - n_+$ and $q = n_- + n_+$. In the absence of individual energies ($\Delta = 0$), and for $|\beta_\nu \epsilon| \gg 1$, the steady state of the system corresponds to one of the two different ordered phases (A or B), depending on the initial condition. At fixed β_1 and β_2, by taking $X = \epsilon$ as the control parameter, as $\epsilon < 0$ increases the phase transition from phase A (B) to the disordered phase occurs at ϵ_A (ϵ_B), with $\epsilon_A < \epsilon_B < 0$. On the other hand, for $\epsilon > \epsilon_B$, the system is in the disordered phase, for which steady-state densities are equal, $n_+^{\text{st}} = n_-^{\text{st}} = n_0^{\text{st}} = 1/3$, yielding $m = 0$ and $q = 2/3$. Finally, in the intermediate case $\epsilon_A < \epsilon < \epsilon_B$, the dynamics evolves to the disordered phase or to phase B, depending on the initial condition.

We notice that, by combining the master equations for n_- and n_+, it is possible to derive master equations for m and q. In the steady state, $dm/dt = dq/dt = 0$, from which an implicit relation $q = q(m)$ can be obtained.

If there is a continuous phase transition to the disordered phase, the NESS values (m, q) continuously approach $(0, 2/3)$ as $\epsilon < 0$ is increased from the ordered phase at fixed β_1 and β_2. Therefore, it is possible to expand the master equation for dm/dt in m and, taking into account the implicit relation $q(m)$, the time evolution of m reads

$$\frac{dm}{dt} \approx a(\epsilon - \epsilon_A)m + bm^2 + cm^3 + \dots, \tag{5.6.2}$$

where ϵ_A is given by

$$\epsilon_A = -\frac{e^{\frac{1}{2}F(\beta_1-\beta_2)} + e^{\frac{1}{2}F(\beta_2-\beta_1)} + e^{\frac{1}{2}F(\beta_1+\beta_2)} + e^{\beta_1 F} + e^{\beta_2 F} + 1}{\left(e^{\frac{\beta_1 F}{2}} + e^{\frac{\beta_2 F}{2}}\right)\left(\beta_1 \cosh\left(\frac{\beta_1 F}{2}\right) + \beta_2 \cosh\left(\frac{\beta_2 F}{2}\right)\right)},$$

while

$$b = \sinh\left(\frac{F}{4}(\beta_1 - \beta_2)\right) f(\beta_1, \beta_2, F),$$

with explicit expressions for $f(\beta_1, \beta_2, F)$ and the coefficients $a > 0$ and c provided in Appendix A.7.

A few observations about Eq. (5.6.2) are in order. First, the presence of a term proportional to m^2 for $F \neq 0$ and $\beta_1 \neq \beta_2$ leads to the critical behavior $m \sim a(\epsilon_A - \epsilon)/b$, with a critical exponent $\beta = 1$ (not to be confused with

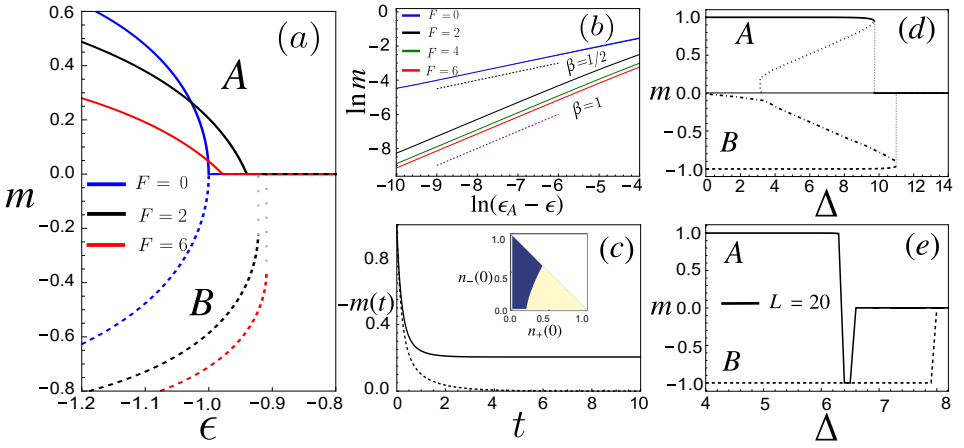

Figure 5.13: (a) For all-to-all interactions and $\Delta = 0$, we show the order parameter for different arrangements, with $m > 0$ (solid line) and $m < 0$ (dashed line), plotted against ϵ for various driving strengths F's. For comparison, the $F = 0$ case in which $\epsilon_A = \epsilon_B$ is shown. Dotted lines for $F \neq 0$ indicate discontinuous phase transitions. (b) Critical behavior associated with the ordered phase A, highlighting the difference between the $F = 0$ and the $F \neq 0$ cases. (c) Bistability of the magnetization close to the transition from the ordered phase B to the disordered phase, for $\epsilon = -0.9219$. Initial conditions are $n_+(0) = 0.8$, $n_-(0) = 0.2$ (solid line) and $n_+(0) = 0.2$ and $n_-(0) = 0.8$ (dotted line). The inset shows the basins of attraction of the ordered (yellow area) and disordered (blue area) phases according to the values of $n_+(0)$ and $n_-(0)$. (d) Behavior of the order parameter as a function of Δ at fixed $\epsilon = -13$ for the all-to-all case. Dotted and dotted-dashed lines denote the unstable solutions for the phases A and B, respectively. For phase A (B), initial conditions $m(0)$ lying above (below) the unstable solution will converge to the ordered solution. Otherwise, the disordered stationary solution will be reached. (e) Behavior of the order parameter as a function of Δ at fixed $\epsilon = -13$ for the square-lattice topology. The sudden jump from $m \approx 1$ to $m \approx -1$ is due to finite-size effects. Unless stated otherwise, parameters are $F = 2$, $\beta_1 = 2$ and $\beta_2 = 1$.

the inverse bath temperatures β_1 and β_2), markedly different from the standard mean-field behavior in order-disorder phase transitions $|m| \sim \sqrt{a(\epsilon_A - \epsilon)/c}$, where $\beta = 1/2$, obtained when $F = 0$ and/or $\beta_1 = \beta_2$. The appearance of a critical exponent $\beta = 1$, illustrated in Fig. 5.13b, is a consequence of breaking the Z_2-"up-down" symmetry which is often present in equilibrium and nonequilibrium phase transitions for mean-field systems [126, 130]. Two additional distinctions from standard order-disorder phase transitions are that $\epsilon_B \neq \epsilon_A$ and, for $\Delta = 0$, the classifications of the corresponding phase transitions differ. While the transition from $m > 0$ to the disordered phase is continuous, the one from $m < 0$ is discontinuous, as shown in Fig. 5.13a. Unlike a critical transition, the latter case features a spinodal region where the system may reach two distinct steady states depending on the initial configuration (see Fig. 5.13c). This behavior remains qualitatively the same as long as $F \neq 0$. In the absence of the nonconservative force, the splitting of the phase transitions disappears.

The existence of two distinct transition points is robust, as shown in Figs. 5.13d and 5.13e, where we fix the values of β_1, β_2 and ϵ while varying the individual-energy parameter Δ, both in the all-to-all case (Fig. 5.13d) and in the square lattice (Fig. 5.13e), the latter case having been studied by numerical simulations via the Gillespie algorithm [73]. Notice that now both transitions are discontinuous, with the jumps in the order parameter and the spinodal regions being more pronounced (dotted and dot-dashed lines) than for $\Delta = 0$. Notably, hints of a similar scenario have been observed in a simpler two-state model [27, 121], where the $m > 0$ phase exhibits a discontinuous phase transition, absent for $m < 0$.

These findings are also reflected in the peculiar thermodynamic properties of this class of systems. In the following, we analyze the average power $\langle \mathcal{P} \rangle$ and the power fluctuations $\gamma_{\mathcal{P}} \equiv \langle \mathcal{P}^2 \rangle - \langle \mathcal{P} \rangle^2$, the efficiency $\eta = -\langle \mathcal{P} \rangle / \langle \dot{Q}_2 \rangle$, and the dissipation $\langle \sigma \rangle$. We use the superscripts (A) and (B) to distinguish between quantities associated with phases A ($m > 0$) and B ($m < 0$). In the all-to-all limit, by expanding $\langle \sigma^{(A)} \rangle$ and $\gamma_{\mathcal{P}}^{(A)}$ in terms of the order parameter near ϵ_A, we arrive at the following expressions:

$$\begin{aligned} \langle \sigma^{(A)} \rangle &\sim \langle \sigma_c \rangle + c_\sigma m^2 + \cdots \\ \gamma_{\mathcal{P}}^{(A)} &\sim \gamma_{\mathcal{P}}^{(c)} + c_v m^2 + \cdots , \end{aligned}$$

where $\langle\sigma_c\rangle = 2F\left[\beta_1 \sinh(\beta_1 F/2) + \beta_2 \sinh(\beta_2 F/2)\right]$ and $\gamma_{\mathcal{P}}^{(c)} = 2F^2\left[\cosh(\beta_1 F/2) + \cosh(\beta_2 F/2)\right]$ respectively denote the entropy production and power variance for $\epsilon \geq \epsilon_A$. The coefficients c_σ and c_v are provided in Appendix A.7. This dependence on the order parameter implies another scaling behavior, i.e., $\langle\sigma^{(A)}\rangle - \langle\sigma_c\rangle \sim a c_\sigma (\epsilon_A - \epsilon)^\delta / b$ and $\gamma_{\mathcal{P}}^{(A)} - \gamma_{\mathcal{P}}^{(c)} \sim a c_v (\epsilon_A - \epsilon)^\delta / b$, with $\delta = 2\beta = 2$. The average entropy production and power fluctuations as functions of ϵ are shown in Figs. 5.14a and 5.14b.

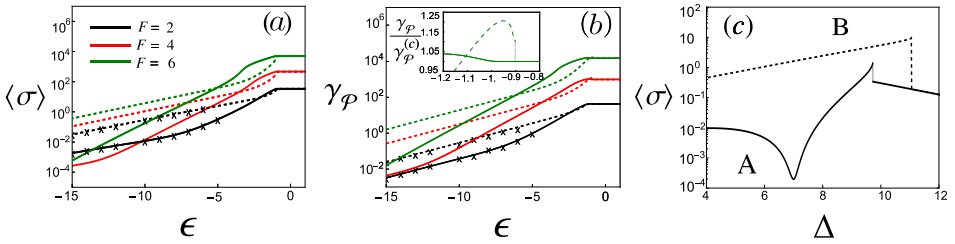

Figure 5.14: (a) Average entropy production as a function of ϵ in phases A (solid lines) and B (dashed lines). (b) Same as panel (a) but for power fluctuations. The inset provides a close-up of $\gamma_{\mathcal{P}}$ near the phase transitions (dashed line indicates phase B). These findings are robust beyond the all-to-all interaction case, holding also for square-lattice interactions (data marked by $\times$). (c) Entropy production as a function of Δ for the same parameters as in Fig. 5.13 for phases A (solid line) and B (dashed line). As in Fig. 5.13d, discontinuities occur at $\Delta_A = 9.73$ and $\Delta_B = 11.06$, respectively.

5.6.1 Linear stability of disordered phase solution for models A and B for q=3

Alternatively (but equivalently), the critical point can be obtained via the linear analysis of the stability of the disordered phase, as described below, examining the crossover between collective and independent regimes for model A (when $\alpha = 1$) and B for $q = 3$, which manifests through continuous and discontinuous phase transitions, respectively. These phenomena can be analyzed in a similar way to their equilibrium counterparts, by means of two order parameters: M for model A and $\phi = (3p_{max} - 1)/2$ ($p_{max} = \max\{p_\downarrow^{st}, p_0^{st}, p_\uparrow^{st}\}$) for model B, with the first one characterized by the classical exponent $\beta = 1/2$ in the equilibrium

realm [131, 132]. However, we will see in this section that the non-equilibrium ingredients change the classical exponent for model A (see Fig. 5.13) and modify the phase transition for model B from a continuous to a discontinuous one, as shown in panel (b) of Fig. 5.15, contrasting with the equilibrium Potts model.

A systematic investigation can be performed by means of a linear expansion of the master equation around a fixed point as follows: $\dot{p}_m = \sum_n A_{mn} p_n$, where A is the Jacobian matrix with elements $A_{mn} = \partial(\omega^{(1)}_{mn} + \omega^{(2)}_{mn})/\partial p_n|_{p_n = p^*}$ evaluated at fixed points satisfying $\sum_n A_{mn} p^*_n = 0$. In particular, the solution p^*_n is linearly stable if the real parts of the eigenvalues of the Jacobian matrix are negative. In both cases, the independent regime is characterized by equal populations $p^*_\downarrow = p^*_0 = p^*_\uparrow = 1/3$ for $\epsilon \geq \epsilon_c$. In both cases introduced above, the corresponding eigenvalues can be written as $\lambda_\pm = \lambda_0 \pm \lambda_1$, with λ_0 given by

$$\lambda_0 = -(3 + \beta_1 \epsilon) \cosh\left(\frac{\beta_1 F}{2}\right) - (3 + \beta_2 \epsilon) \cosh\left(\frac{\beta_2 F}{2}\right), \tag{5.6.3}$$

whereas λ_1, for model A, reads:

$$\lambda_1 = \Big[6 + \epsilon^2\left(\beta_1^2 + \beta_2^2\right) + \left(\beta_1^2 \epsilon^2 - 3\right) \cosh(\beta_1 F) - 3\cosh(\beta_2 F) + \beta_2 \epsilon^2 \left(4\beta_1 \cosh\left(\frac{\beta_1 F}{2}\right) \cosh\left(\frac{\beta_2 F}{2}\right) + \beta_2 \cosh(\beta_2 F)\right) + 12 \sinh\left(\frac{\beta_1 F}{2}\right) \sinh\left(\frac{\beta_2 F}{2}\right)\Big]^{1/2}, \tag{5.6.4}$$

while, for model B, we have:

$$\lambda_1 = i\sqrt{3}\left[\sinh\left(\frac{\beta_1 F}{2}\right) - \sinh\left(\frac{\beta_2 F}{2}\right)\right], \tag{5.6.5}$$

Since λ_1 is imaginary for model B, the linear stability of the disordered solution is guaranteed provided $\lambda_0 < 0$. Conversely, for model A, due to the fact that β_1 and β_2 are always positive, λ_- is always negative. Conversely, λ_+ is always negative for sufficiently large and positive ϵ, with the order-disorder phase transition corresponding to a transcritical bifurcation when $\lambda_+ = 0$. Clearly, λ_+ becomes positive as ϵ decreases, meaning that the independent regime becomes unstable.

Fig. 5.15 depicts the phase diagrams $\Delta\beta = \beta_1 - \beta_2$ versus ϵ for different F obtained from the linear analysis. In particular, for $F = 0$, λ_+ and λ_- read -6 and $-2[3+\epsilon(\beta_1+\beta_2)]$ (model A) and $-[6+\epsilon(\beta_1+\beta_2)]$ (model B), respectively, consistent

with phase transitions taking place at $\epsilon_c = -3/(\beta_1 + \beta_2)$ and $\epsilon_c = -6/(\beta_1 + \beta_2)$. The crossover from collective to independent regime changes smoothly with the driving and is more sensitive to the difference of temperatures. Note the excellent agreement between the values of ϵ_c obtained from the linear analysis and those from the order parameter behaviors (bottom panels for $F = 1$).

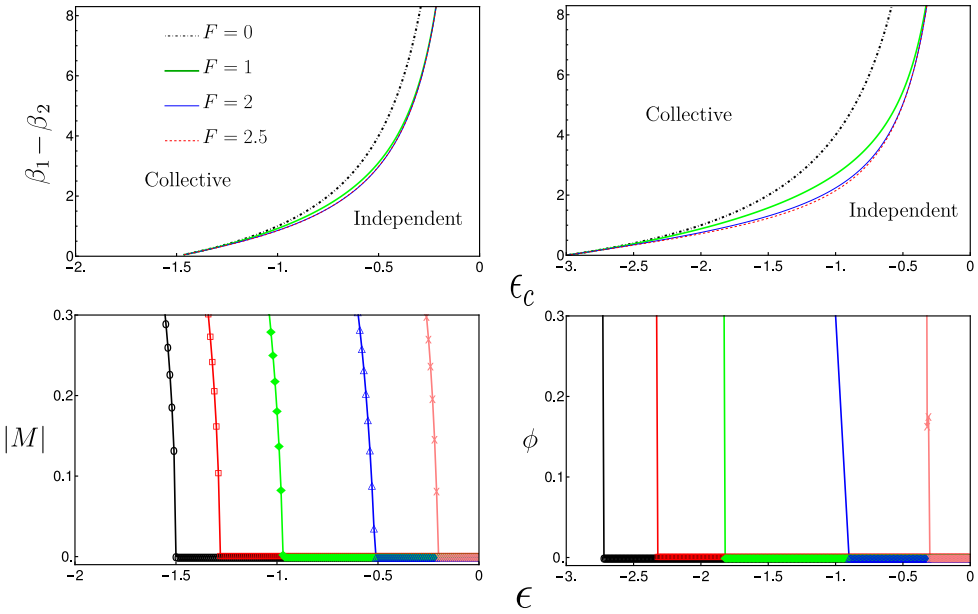

Figure 5.15: For $q = 3$ and distinct F, left and right top panels show the phase diagrams $\Delta\beta = \beta_1 - \beta_2$ versus ϵ_c for model A and B, respectively. They are obtained from the linear stability analysis of the disordered phase. For the sake of comparison, the bottom panels show (for $F = 1$) the location of phase transitions from the order-parameter behaviors. From left to right, $\beta_1 - \beta_2 = 0$, $1/3$, 1, 3, and 9. In all cases, we set $\beta_2 = 1$.

5.6.2 Engine performance near to the critical point

The system's performance, particularly its efficiency η, also exhibits a scaling behavior characterizing phase A. To examine this, we expand $\langle \dot{Q}_i^{(A)} \rangle$ around ϵ_A, yielding $\langle \dot{Q}_i^{(A)} \rangle \sim \langle \dot{Q}_i^{(c)} \rangle + c_{q_i} m^2 + \cdots$, where $\langle \dot{Q}_i^{(c)} \rangle = -2F \sinh(\beta_i F/2)$ and the

coefficients c_{q_1} and c_{q_2} are listed in Appendix A.7. Using the expressions for $\langle \dot{Q}_2^{(A)} \rangle$ and $\langle \mathcal{P}^{(A)} \rangle$, we derive an asymptotic form of the efficiency $\eta^{(A)}$,

$$\eta^{(A)} \sim \eta^{(c)} + \frac{1}{\langle \dot{Q}_2^{(c)} \rangle} \left(c_{q_1} - \frac{c_{q_2} \langle \dot{Q}_1^{(c)} \rangle}{\langle \dot{Q}_2^{(c)} \rangle} \right) (\epsilon_A - \epsilon)^{\delta},$$

where $\eta^{(c)} = 1 + \sinh(\beta_1 F/2)/\sinh(\beta_2 F/2)$ and $\delta = 2\beta$. Thus, the efficiency exhibits the same critical exponent as entropy production, power, and power fluctuations, as illustrated in Fig. 5.16. Although closed-form expressions are unavailable near ϵ_B, Fig. 5.14b (dashed line in the inset) shows that the discontinuity in the order parameter can also be found in the power fluctuations $\gamma_{\mathcal{P}}$. Moreover, when analyzing the system in the ordered phases, we notice that phase A ($m > 0$) exhibits notably lower dissipation and power fluctuations than phase B ($m < 0$), as shown in Figs. 5.14a and 5.14b.

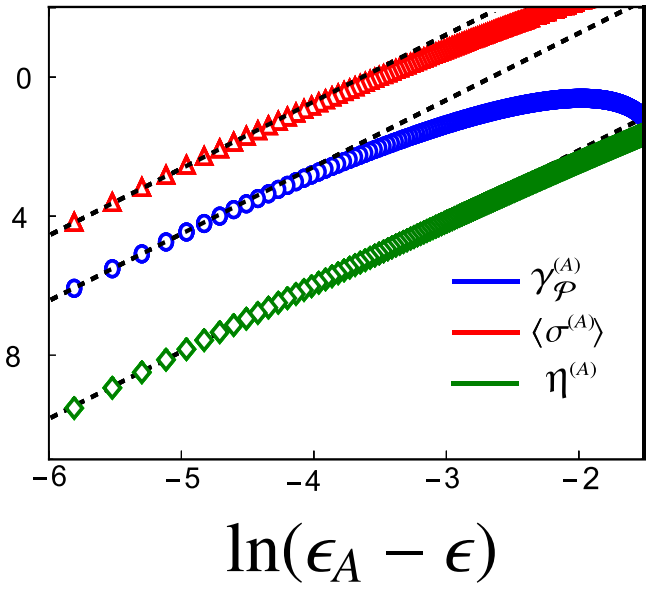

Figure 5.16: Log-log plots of the above quantities near the critical point ϵ_A, with slopes consistent with $\delta = 2$.

To gain more intuition about the system's behavior, we develop a phenomenological model valid when $|m| \approx 1$, using an approach analogous to that introduced in Ref. [121]. Under this condition, the state densities are approx-

imately given by $n_- = 1$ ($n_- = 0$) and $n_+ = 0$ ($n_+ = 1$) for phase A (B). Applying the spanning-tree method [133], we derive approximate steady-state solutions, depending only on model parameters (details in Appendix A.7). For $|\beta_\nu(\epsilon + \Delta)| \gg 1$, the effective expressions for the entropy production are given by

$$\langle \sigma_{\text{eff}}^{(A)} \rangle \approx -e^{\frac{1}{2}\beta_2(\Delta - F + \epsilon)}[F(\beta_1 + \beta_2) + (\beta_1 - \beta_2)(\Delta + \epsilon)]$$

and

$$\langle \sigma_{\text{eff}}^{(B)} \rangle \approx e^{\frac{\beta_2}{2}(\Delta + F + \epsilon)}[F(\beta_1 + \beta_2) - (\beta_1 - \beta_2)(\Delta + \epsilon)]$$

for phases A and B, respectively. Notice that $0 < \langle \sigma_{\text{eff}}^{(A)} \rangle < \langle \sigma_{\text{eff}}^{(B)} \rangle$. Similarly, expressions for the power fluctuations $\gamma_{\mathcal{P}}$ are obtained via the large-deviation method [134, 135], with leading terms given by $\gamma_{\mathcal{P}}^{(A)} \approx 4F^2 \left[e^{\frac{\beta_1}{2}(\epsilon + F)} + e^{\frac{\beta_2}{2}(\epsilon - F)} \right]$ and $\gamma_{\mathcal{P}}^{(B)} \approx 4F^2 e^{\frac{\beta_2}{2}(\epsilon + F)}$ for phases A and B, respectively. Here again, $\gamma_{\mathcal{P}}^{(A)} < \gamma_{\mathcal{P}}^{(B)}$, consistent with phase A exhibiting lower power fluctuations than phase B. These results are also valid for the square-lattice topology (see data marked by the symbols $\times$ in Figs. 5.14a and 5.14b).

Also, in Fig. 5.14d, we show the behavior of $\langle \sigma \rangle$ in the square lattice as Δ varies. Again, $\langle \sigma^{(A)} \rangle$ (solid lines) remains smaller than $\langle \sigma^{(B)} \rangle$ (dashed lines). The entropy production, like the order parameter, again captures the phase transitions occurring at two distinct values of Δ, $\Delta_A \neq \Delta_B$.

5.7 Exploring other topologies: Triangular Sublattices

Despite the fact that the all-to-all approach is mapped onto a 2D spin lattice, there is no topology in this configuration. However, we can still define a kind of topology in the interaction by introducing sublattices. Here we propose a minimal nonequilibrium model for addressing energetic frustration by introducing a triangular topology. Let us take, for instance, a regular lattice of N sites, divided into three sublattices named A, B, and C. In such a case, the system is composed of N spins, with each one interacting with its six nearest neighbor sites, forming a triangular lattice. More specifically, the i-th spin $\sigma_i^{(\alpha)}$ be-

longing to sublattice $\alpha \in \{A, B, C\}$ interacts with its $k = 6$ nearest neighbors belonging to the remaining sublattices $\tilde{\alpha} \neq \alpha$. In such a case, the system is characterized by the populations $N_{\pm}^{(\alpha)}$ of each sublattice, in such a way that $N^{(\alpha)} = N_{+}^{(\alpha)} + N_{-}^{\alpha} = N/3$ and $N = N^{(A)} + N^{(B)} + N^{(C)}$.

If we turn to the same system but in the all-to-all limit, the system will be composed of each sublattice α interacting with all the spins in the other sublattices $\tilde{\alpha} \neq \alpha$. The "topology" here is mapped into the interactions between the sublattices, since each sublattice A, B, and C will act as one spin with total magnetization M_A, M_B, and M_C interacting in a triangular structure, which is a highly frustrated structure [136].

Applying Eq.(3.3.19) to the sublattice and also considering the all-to-all approach, we write

$$E(M_A, M_B, M_C) = \frac{1}{N}(J_{AB}M_AM_B + J_{BC}M_BM_C + J_{CA}M_CM_A) - HM, \quad (5.7.1)$$

where $M = M_A + M_B + M_C$ and $M_\alpha = N_{+}^{(\alpha)} - N_{-}^{(\alpha)}$, and $J_{\alpha\alpha'} = J_{\alpha'\alpha}$ denotes the strength of interaction between the spins belonging to sublattices α and $\alpha' \neq \alpha$. The sign of $J_{\alpha\alpha'}$ plays a crucial role in the system's behavior. While $J_{\alpha\alpha'} < 0$ favors parallel alignment of the spins of sublattices α and α', the opposite holds for $J_{\alpha\alpha'} > 0$, where anti-parallel alignment is favored in such a case [136, 137]. A given spin flip corresponds to the transitions $N_{\pm}^{(\alpha)} \to N_{\mp}^{(\alpha)}$, which means $N_{\pm}^{(\alpha)} \to N_{\pm}^{(\alpha)} - 1$ and $N_{\mp}^{(\alpha)} \to N_{\mp}^{(\alpha)} + 1$, or equivalently $M_\alpha \to M_\alpha \pm 2$. We define the density of spins in each sublattice α as $\bar{n}_{\pm}^{(\alpha)} = \langle N_{\pm}^{(\alpha)} \rangle / N$, and by taking $N \to \infty$, the system dynamics reduces to three dynamical variables $\bar{n}_{\pm}^{(\alpha)}$ ($\alpha \in \{A, B, C\}$), for which the total magnetization per site is simply $m = \sum_{\alpha \in \{A,B,C\}} m_\alpha$. The system will be constrained in an ordered phase where $\bar{n}_{+}^{(A)} = \bar{n}_{+}^{(B)} = \bar{n}_{+}^{(C)} = 1/3$ and $\bar{n}_{-}^{(\alpha)} = 0$ for all α. Conversely, the disordered system is defined by $\bar{n}_{-}^{(\alpha)} = \bar{n}_{+}^{(\alpha)} = 1/6$, and $m_\alpha = 2\bar{n}_{+}^{(\alpha)} - 1/3$.

Since our goal is to investigate the interplay between non-conservative drivings in a minimal model exhibiting frustration, we repeat the same approach applied in this section, in which the system is simultaneously placed in contact with two different thermal reservoirs $\nu = 1, 2$. The dynamics of the spin state is entirely mapped in terms of the population of spins by Eq.(5.7.1), which makes it more convenient to describe its dynamics in terms of the average density

$\bar{n}_{\pm}^{(\alpha)}$ for each sublattice α. Also, following the same approach from previous works [27–29, 129, 138], we write the master equation in terms of the density $\bar{n}_{+}^{(\alpha)}$,

$$\dot{\bar{n}}_{+}^{(\alpha)}(t) = \sum_{\nu=1}^{2} \omega_{+-}^{(\alpha,\nu)} \left[\frac{1}{3} - \bar{n}_{+}^{(\alpha)}(t)\right] - \omega_{-+}^{(\alpha,\nu)} \bar{n}_{+}^{(\alpha)}(t), \tag{5.7.2}$$

where $\omega_{ij}^{(\nu,\alpha)}$ denotes the transition rate from $j \to i$ in sublattice α due to reservoir ν, and it is expressed as defined in Sec.(3.5), but now also split in terms of the sublattices α:

$$\omega_{ij}^{(\nu,\alpha)} = \exp\left[-\frac{\beta_\nu}{2}\left(\Delta E_{ij}^{(\alpha)} + F d_{ij}^{(\nu)}\right)\right], \tag{5.7.3}$$

where $\Delta E_{ij}^{(\alpha)}$ is the energy difference associated with the transition $j \to i$ in sublattice α. From Eq.(5.7.1) as $N \to \infty$, one has that $\Delta E_{-+}^{(\alpha)} = -2\big[J_{\alpha\beta}(2\bar{n}_{+}^{(\beta)}(t) - 1/3) + J_{\alpha\gamma}(2\bar{n}_{+}^{(\gamma)}(t) - 1/3)\big]$ for the transition $+ \to -$, where $\alpha, \beta, \gamma \in \{A, B, C\}$ are distinct sublattice indices. It is immediate to see that $\Delta E_{ij} = -\Delta E_{ji}$. As stated previously, the work source stems from a biased "force" of strength F, with its sign accounted for in the element $d_{ij}^{(\nu)} = -1$ if a local spin flip $-1(+1) \to +1(-1)$ is associated with contact with the cold (hot) thermal bath, and $+1$ otherwise. The dynamics evolve to a non-equilibrium steady state (NESS) $\bar{n}_{\beta}^{\alpha}(t) \to \bar{n}_{\beta}^{\alpha(\mathrm{st})}$ depending on the initial condition from which the dynamics starts. As will be shown further, the set of NESS solutions are different depending on whether the interactions are ferromagnetic or antiferromagnetic. The former case leads to different ferromagnetic systems in which $m_A = m_B = m_C = m/3$, with $m > 0$ and $m < 0$ depending on the initial condition, whereas $m_A = m_C = m$ and $m_B = -m$ for $J_{AB} = J_{BC} > 0$ and $J_{CA} < 0$. In all cases, a disordered solution $m = 0$ emerges as parameters are varied.

We now turn to the system thermodynamics, portrayed here via the evaluation of the entropy production, a central quantity for discerning equilibrium from nonequilibrium systems [39, 139], as discussed in Sec.(2.1). Also, as already stated in this thesis, it has been considered to capture the irreversible character of a non-equilibrium phase transition. From the definition in Eq.(3.4.9) we rewrite it as the expression $S(t) = -\sum_\alpha \sum_j \bar{n}_j^{(\alpha)} \ln \bar{n}_j^{(\alpha)}$, taking $k_B = 1$. By taking its time derivative $\dot{S}$ together with Eq. (5.7.2), we repeat the procedure done in Eq.(3.4.10) for each sublattice, and one has that $\dot{S}(t) = \langle\sigma\rangle - \langle\phi\rangle$, where $\langle\sigma\rangle \geq 0$

denotes the entropy production rate given by

$$\langle\sigma\rangle = \sum_{\nu}\sum_{(j<i)}\sum_{\alpha} J_{ij}^{(\alpha,\nu)} \ln\left(\frac{\omega_{ij}^{(\alpha,\nu)}\bar{n}_j^{(\alpha)}}{\omega_{ji}^{(\alpha,\nu)}\bar{n}_i^{(\alpha)}}\right), \tag{5.7.4}$$

where $J_{ij}^{(\alpha,\nu)}(t) = \omega_{ij}^{(\alpha,\nu)}\bar{n}_j^{(\alpha)}(t) - \omega_{ji}^{(\alpha,\nu)}\bar{n}_i^{(\alpha)}(t)$ denotes the probability current. In the NESS, the above expression for $\langle\sigma\rangle$ acquires the simpler form expressed as $\langle\sigma\rangle = \langle\phi\rangle = -\sum_\nu \beta_\nu\langle\dot{Q}_\nu\rangle$, where $\langle\dot{Q}_\nu\rangle$ denotes the heat exchanged with the ν-th thermal reservoir, given by

$$\langle\dot{Q}_\nu\rangle = \sum_{\alpha}(\Delta E_{+-}^{(\alpha)} + Fd_{+-}^{(\nu)})J_{+-}^{(\alpha,\nu)}, \tag{5.7.5}$$

$$J_{+-}^{(\alpha,\nu)} = \frac{\omega_{+-}^{(\alpha,\nu)}}{3} - (\omega_{+-}^{(\alpha,\nu)} + \omega_{-+}^{(\alpha,\nu)})\bar{n}_+^{(\alpha)}. \tag{5.7.6}$$

In the first set of results, we perform an analysis for two cases: $J_{AB} = J_{BC} = J_{CA} = -J$ and $J_{AB} = J_{BC} = J$ and $J_{CA} = -J$, consistent with ferromagnetic and antiferromagnetic interactions, respectively, for different temperature differences $\Delta\beta$ and drivings F.

5.7.1 Antiferromagnetic interaction

In this section we investigate the antiferromagnetic interaction between the sublattices, which can be imposed by setting $J_{AB} = J_{BC} = J$ and $J_{AC} = -J$ with $J < 0$. In equilibrium ($\Delta\beta = F = 0$), this interaction results in a set of solutions of the form $m_1 = m_A = m_C < 0$ and $m_2 = m_B = -m_1 > 0$, which reproduces the results from Ref. [136]. In Fig. (5.17 (c)), we report some results in equilibrium, where the system is constrained to the set of solutions described above (similarly for the opposite case $m_1 \to -m_1$) as $-\beta J$ is large, and a disordered phase ($m_1 = m_2 = 0$) emerges as $-\beta J$ decreases at a critical point $\beta J_0 = -3/2$. Its ordered phase ($m_1 = m_A = m_C < 0$ and $m_2 = m_B = -m_1 > 0$) is characterized by approximately 2/3 of the spins being up and 1/3 being down below a critical temperature, which is a ferrimagnetic state, as shown in Fig. (5.17(c)). Although similar findings can be observed for the nonequilibrium case with $F = 0$ and $\Delta\beta \neq 0$, remarkable differences appear when $F \neq 0$ and $\Delta\beta \neq 0$.

We observe that for $F \neq 0$ and/or $\Delta\beta \neq 0$, the sublattice solutions of the form $m_A = m_C = m_1$ and $m_B = m_2$ are preserved, with some new features arising due to the nonequilibrium conditions. If we set $J_{AB} = J_{BC} = 1$ and $J_{CA} = -1$, we still obtain stable solutions for a range of $\Delta\beta \neq 0$ and $F \neq 0$; however, the NESS solution for the magnetization now takes the form $m_A = m_C = m_1$ and $m_B = m_2 = \Gamma m_1$. If $m_1 > 0$ ($m_1 < 0$), then $-1 \leq \Gamma \leq 0$ ($0 \leq \Gamma \leq 1$), and the total magnetization is given by $m = 2m_1 + m_2 = (2 + \Gamma)m_1$. A transition to $m \to -m$ is also observed in this case (see Fig.(5.17 a)), however, the fact that the total magnetization in absolute value is less than 1 leads us to change the way we study such a transition. In fact, the change in the sign of the total magnetization suggests that the nonequilibrium ingredients affect the direction of the magnetization relative to a defined positive axis. Furthermore, the solution retains its symmetry before and after the transitions $m_1 \to -m_1$ and $m_2(\Gamma m_1) \to -m_2(-\Gamma m_1)$, and once we know m_1, we can describe the total magnetization in the ordered case, which suggests that we can focus our attention on only one sublattice to describe the entire lattice. The solution $m_1 = m_2 = 0$ is broken for sufficiently large F and $\Delta\beta$, as exemplified in Fig. 5.17 c) and in the inset.

In order to describe the key features (rotation and preserved symmetry) of the ferrimagnetism under nonequilibrium conditions, we propose the following quantity: $\theta = 3|\text{sign}(m)|(1 - \text{sign}(m_1))|m_1|$. This quantity will be zero if $m_1 = 0$ or if $m_1 > 0$ ($\text{sign}(m_1) = 1$) and non-zero otherwise. Thus, it will be zero if m_1 points along the positive axis and non-zero if it points in the opposite direction, characterizing the rotational transition $m_1 \to -m_1$. Figures (5.17 b) and (5.17 d) provide a first insight into its behavior. We show that θ is an order parameter exhibiting an order-disorder phase transition (Z_2 symmetry), presenting both discontinuous and continuous transitions connected by a tricritical point, as we will show throughout this section. In Fig.(5.17 b), we show the effect of the external drive for fixed $\Delta\beta$ and J, where the discontinuity point depends on the initial conditions, occurring at $|F|$ and $-|F|$ for the initial conditions $(m_1(0), m_2(0)) = (-1/3, 1/3)$ and $(m_1(0), m_2(0)) = (1/3, -1/3)$, respectively. In Fig.(5.17 d) we show the effect of the interaction strength J on the rotation. For the equilibrium case ($F = 0$ and $\Delta\beta = 0$), the continuous transition of θ corresponds to the order-disorder transition of m at the same critical point (see

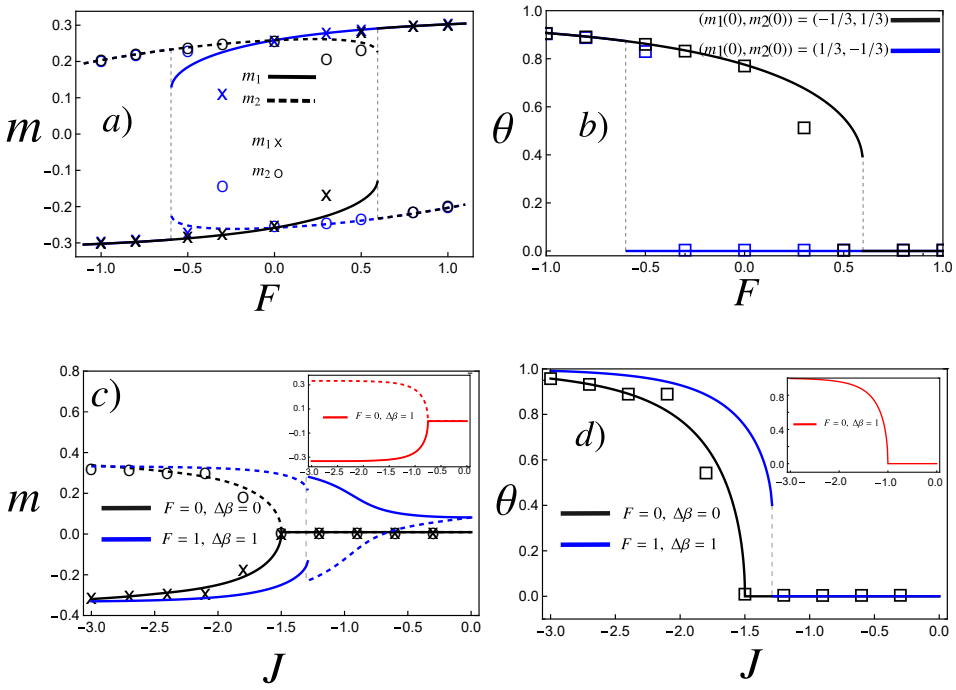

Figure 5.17: Panel $a)$ shows the magnetization m for $m_A = m_C = m_1$ (solid) and $m_B = m_2$ (dashed) as a function of the drive F in the antiferromagnetic case described in Sec. 5.7.2. Black and blue curves correspond to initial conditions $(m_1(0), m_2(0)) = (-1/3, 1/3)$ and $(1/3, -1/3)$, respectively. The symbols "x" and "o" give m_1 and m_2 from a Gillespie simulation with $N = 300$ spins. Panel $b)$ shows the order parameter θ under the same conditions, with $J_{AB} = J_{BC} = J$ and $J_{AC} = -J < 0$; the symbol "□" indicates the Gillespie results. Panels $c)$ and $d)$ compare m and θ at equilibrium (black curve) and out of equilibrium ($F \neq 0$, $\Delta\beta \neq 0$) as functions of J, using $(m_1(0), m_2(0)) = (-1/3, 1/3)$. Solid and dashed curves again denote $m_A = m_C = m_1$ and $m_B = m_2$. Insets show the case $F = 0$ and $\Delta\beta = 1$, highlighting the combined nonequilibrium effects. In $a)$ and $b)$ we set $|J_{AB}| = |J_{BC}| = |J_{CA}| = 1$ and $\beta_2 = 1$.

Fig.(5.17 c)).

In order to better understand this magnetization rotation as a phase transition, we plot a phase diagram. In Fig.(5.18 a) we depict the phase diagram for the transition of the form $m_1, m_2 = \Gamma m_1 \rightarrow -m_1, -\Gamma m_2$ for $\Gamma < 0$, considering $(m_1(0), m_2(0)) = (1/3, -1/3)$, with a tricritical point separating first-order and second-order phase transitions. The transition points in both cases depend on the initial condition beyond a certain threshold $F > F_C$. A similar phenomenon is observed in Ref. [138] and described in Sec.(5.6). On the right side, in Fig.(5.18 b), we show the corresponding transition for θ for some points of the phase diagram. In Fig.(5.18 c) and Fig.(5.18 d) we plot the same transition for the initial condition $(m_1(0), m_2(0)) = (1/3, -1/3)$.

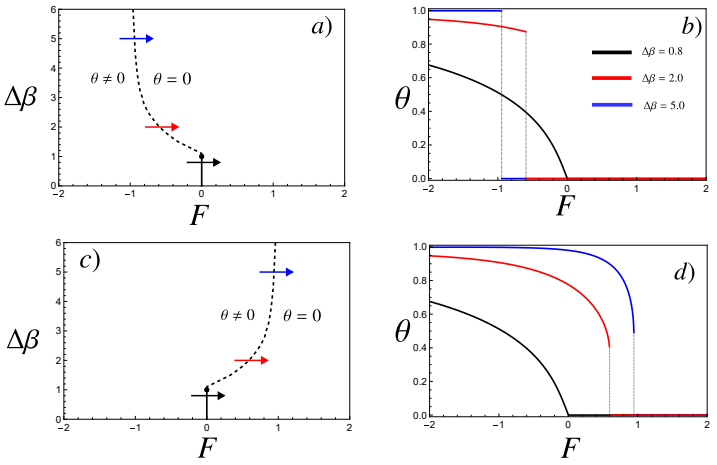

Figure 5.18: In panel $a)$ we represent a phase diagram for the antiferromagnetic case considering the initial condition $(m_1(0), m_2(0)) = (1/3, -1/3)$. The dashed line represents a discontinuous phase transition, the continuous line represents a continuous transition, and the bullet point is a tricritical point, $(F_C, \Delta\beta_C) = (0.0, 1.0)$. The colored arrows represent the plots for the respective values of $\Delta\beta$ in panel $b)$, where we show the order parameter θ for fixed values of $\Delta\beta$. In panels $c)$ and $d)$ we perform the same procedure with the initial condition $(m_1(0), m_2(0)) = (-1/3, 1/3)$.

To assure that the point $(F_C, \Delta\beta_C) = (0.0, 1.0)$ is a tricritical point, we must

investigate how the magnetization and the order parameter θ scale close to the critical point. The transition from one state to another changes the mean value of the total magnetization of the system, $m = 2m_1 + m_2$, which is described by θ. Also, θ is an important quantity for describing the transition within the sublattice, since it captures the specific sign change in the sublattice magnetization $m_1 \to -m_1$. We define $\theta \neq 0$ for states where the total magnetization is negative, with $m_1 < 0$ and $m_2 > 0$, also including the state $m_1 = m_2 < 0$ (present for larger negative values of $-|F|$) as part of it. Conversely, $\theta = 0$ for the positive and disordered cases, including the states $m_1 > 0$ and $m_2 < 0$, as well as $m_1 = m_2 = 0$ and $m_1 = m_2 > 0$ (see Fig. 5.18), where the latter state occurs for large positive F (see Fig. 5.17). Extensions for other sets of temperatures and drivings are depicted in Fig. 5.17. The main features can be briefly understood via series expansions of the order parameter: $d\theta/dt = (a - a_c)\theta + b\theta^2 + c\theta^3 + \cdots$, where, unlike the equilibrium version, the existence of biased drivings can lead to $b > 0$ and hence give rise to a different set of critical exponents compared to the equilibrium case. Such an expansion is similar to the Ising model description from Ref. [138]. The existence of a discontinuous phase transition is signaled by $b < 0$, with the critical and discontinuous lines meeting at a tricritical point, characterized by $b = 0$ and $c > 0$. We can explicitly derive this expansion starting from a logistic equation for m_A, which can be obtained from the dynamics of the magnetization, expanded in the form $\frac{dm}{dt} = a_1(J - J_c)m + a_2m^2 + a_3m^3 + \cdots$, where J_c is the critical value of the interaction strength between spins. One can derive the dynamics for the magnetization starting from Eq. 5.7.2, considering that $p_+^{(\alpha)}(t) = (m_\alpha(t) + 1/3)/2$. In the ferrimagnetic case, we represent the transition $m_1 \to -m_1$ ($m_2 \to -m_2$) with an order parameter θ which is order-disorder-like, reproducing the symmetry of a Z_2 model. It is reasonable to suppose that the expansion for θ will be similar to that for m_1, since θ is proportional to $|m_1|$. Also, because m_1 and m_2 are linked by the relation $m_2 = \Gamma m_1$, we capture information about both m_1 and m_2 from θ. Starting from the fact that $m_1 = m_A = m_C$ and $\theta \sim |m_A|$, it is justifiable to write...

$$\frac{dm_A}{dt} = \frac{d\theta}{dt} = a^\theta(\Delta\beta - \Delta\beta_C)\theta - b^\theta\theta^3, \tag{5.7.7}$$

with $a^\theta = 2/9$ and $b^\theta = -28/243$. This expansion converges with the result found in the scaling analysis shown in Fig. 5.19. The scaling analysis reveals

some important results: first, it guarantees that the second-order transition below the critical point ($0 < \Delta\beta < \Delta\beta_C = 1$) follows what is expected from mean-field theory, with the same critical exponent $\beta = 1/2$. Furthermore, the right panel of Fig. 5.19 shows that, in the vicinity of the critical point, the critical exponent equals $\beta = 1$, which is characteristic of a tricritical point, separating the system into first-order and second-order phase transitions. The scaling for the entropy production $\langle\sigma\rangle$ follows the expected value for the mean-field approximation, $\delta = 2\beta$.

We also draw attention to another interesting feature of θ: it exhibits different discontinuity values beyond the critical point, depending on the initially dominant state in the dynamics, as observed in the ferromagnetic case. The second-order phase transition always occurs at $F = 0$ until the temperature gradient reaches the critical point. Beyond that, the force acts to change the sign of the total magnetization at different points, as shown in Figs. 5.17 and 5.18.

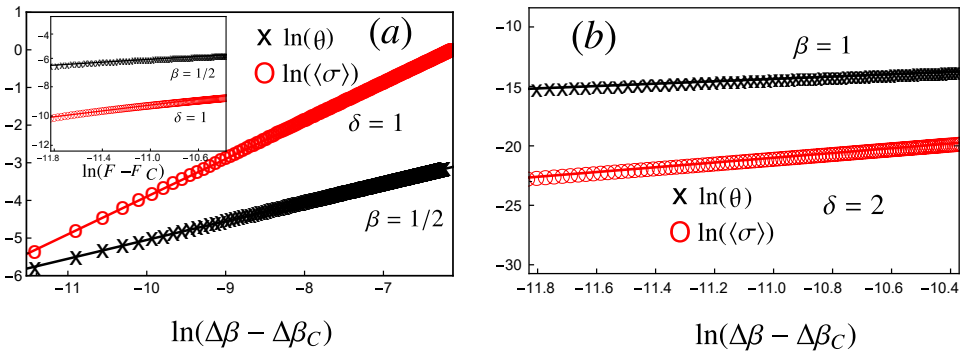

Figure 5.19: In panel $a)$ we show the scaling for the order parameter θ and the mean entropy production $\langle\sigma\rangle$ for $\Delta\beta = 0.8$, in the region where a second-order phase transition occurs. In panel $b)$, we show the same for the critical $\Delta\beta_C = 1$. As shown in both plots, we obtain the entropy production coefficient $\delta = 2\beta$ as expected from an order-disorder phase transition.

5.7.2 Ferromagnetic Interaction

It is instructive to draw a comparison with the ferromagnetic case, corresponding to $J_{AB} = J_{BC} = J_{CA} = J = -1$, which also reproduces the cases investigated for Model A with $\alpha = 1$ in this section. In such a case, the all-to-all approach on sublattices exhibits similar behavior but plays no important role, being equivalent (apart from a constant factor) to the all-to-all version consistent with two-state dynamics, $q = 2$, in Model A. The introduction of nonequilibrium ingredients splits the system into two transitions, of two different types, separated by a critical point, as shown in Fig. 5.20. In order to better understand such a transition, we focus on finding the nonequilibrium steady state (NESS) solution for the master equation given in Eq. 5.7.2. As argued in the previous section, the triangular sublattice approach presents a general solution of the form $m_A = m_C = m_1$ and $m_B = m_2$. In the ferromagnetic case, we have the special case $m_A = m_B = m_C = m/3$, resulting in $m_1 = m_2 = m/3$. In such a case, we can focus our attention on the total magnetization $m = 2m_1 + m_2$ as an order parameter.

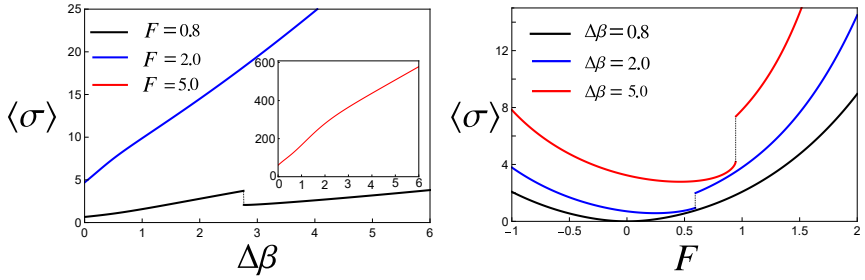

Figure 5.21: The diagrams represent the entropy production for fixed force (left) and for fixed temperature differences (right).

As observed in Fig. 5.20, for any temperature difference in the range $0 < \Delta\beta < 1$, there is a crossover transition of $m \to -m$. For $\Delta\beta > \Delta\beta_C = 1$, the increase of the external force F gives rise to a discontinuous transition, with the jump point depending on which phase initially dominates the system. A similar result is observed in the driven Ising model in Ref. [138]. As shown in Fig. 5.20 b), the discontinuity occurs at $-|F|$ and $|F|$ for the initial conditions $m(0) = 1$

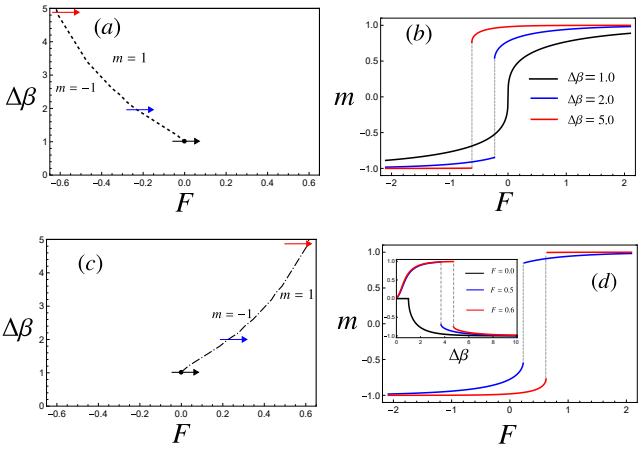

Figure 5.20: In panels $a)$ and $c)$, we present a phase diagram for the ferromagnetic case for initial conditions $p_+(0) = 1$ and $p_+(0) = 0$, respectively. The dashed line represents a discontinuous phase transition, and the bullet point indicates a critical point that separates the discontinuous transition from a crossover (see black curve in diagram b). The colored arrows correspond to the curve colors in diagrams $b)$ and $d)$, where we plot the total magnetization m *versus* F for fixed $\Delta\beta$ and for the respective initial conditions. In the inset of $d)$, we plot the total magnetization m *versus* $\Delta\beta$ for fixed F for the initial condition $p_+(0) = 0$.

and $m(0) = -1$, respectively. This discontinuity is also observed for a fixed force $F \neq 0$ while varying $\Delta\beta$, as shown in panel $c)$ of Fig. 5.20. The influence of the initial condition on the different phase transitions is only observed beyond the critical point, i.e., for $\Delta\beta > \Delta\beta_C$. We also examine the scaling of such a critical point via an expansion of the master equation. This critical point separates the crossover from a discontinuous phase transition, with the critical exponents of the magnetization m and the entropy production $\langle\sigma\rangle$ being $\beta = 1/2$ and $\delta = 2\beta = 1$, respectively. The effects of the nonequilibrium characteristics on the entropy production (dissipation) will be investigated in more detail later. In order to understand such criticality, we address the dynamics of the sublattice, taking into consideration a particular solution where $m_A(t) = m_B(t) = m_C(t) = m(t)/3$. Thus, the three master equations given in Eq.(5.7.2) reduce to a single equation that can be expanded in a general logistic form. In particular, for the ferromagnetic case we write $m_\alpha = m/3$ in the NESS, and the general logistic

form for the total magnetization under a continuous phase transition, $\frac{dm}{dt} = a(J - J_C)m - bm^3$, reduces to

$$\frac{dm_\alpha}{dt} = a_\alpha(J - J_c)m_\alpha - b_\alpha m_\alpha^3, \tag{5.7.8}$$

where $a_\alpha = a$ and $b_\alpha = 9b$. The critical value J_c can be found via a stability analysis around the disordered solution, which reads:

$$J_c = -\frac{3(1 + e^{F\Delta\beta/2})(1 + e^{F\beta_2 + F\Delta\beta/2})}{2(\beta_2 + e^{F\Delta\beta_2}(1 + e^{F\beta_2})\beta_2 + \Delta\beta + e^{F(\beta_2+\Delta\beta)}(\beta_2 + \Delta\beta))}. \tag{5.7.9}$$

Clearly, J_C is a negative number, as expected for a ferromagnetic configuration [138]. The coefficients a, b, and c are given by:

$$\begin{aligned} a = a_\alpha =& 2e^{\frac{F}{4}(\beta_1 - \beta_2)} \cosh\left[\frac{F}{4}(\beta_1 - \beta_2)\right]\left[\beta_1 \cosh\left(\frac{F\beta_1}{2}\right) + \right. \\ &\left. + \beta_2 \cosh\left(\frac{F\beta_2}{2}\right)\right], \end{aligned} \tag{5.7.10}$$

$$\begin{aligned} b =& b_\alpha/9 = -e^{\frac{1}{4}F(3\beta 1 + \beta 2)} \sinh\left(\frac{1}{4}F(\beta 1 - \beta 2)\right)\left(2\cosh\left(\frac{1}{2}F(\beta 1 - \beta 2)\right) + 1\right)^2 \\ & \cosh\left(\frac{1}{4}F(\beta 1 + \beta 2)\right)\left(\left(\beta 1^2 - 4\beta 1\beta 2 + \beta 2^2\right)\cosh\left(\frac{1}{4}F(\beta 1 - \beta 2)\right)\right. \\ & + \beta 1^2\left(-\cosh\left(\frac{1}{4}F(3\beta 1 + \beta 2)\right)\right) \\ & \left. - \beta 2^2 \cosh\left(\frac{1}{4}F(\beta 1 + 3\beta 2)\right)\right) \times \left[\left(e^{\frac{\beta 1 F}{2}} + e^{\frac{\beta 2 F}{2}}\right)^2\left(\beta 1 \cosh\left(\frac{\beta 1 F}{2}\right) + \beta 2 \cosh\left(\frac{\beta 2 F}{2}\right)\right)^2\right]^{-1} \end{aligned} \tag{5.7.11}$$

Since we fix the interaction strength $J = -1$, we do not perturb the master equation around J_C for fixed values of $\Delta\beta$ and F, as was done in previous Refs. [85, 138]. Instead, we are doing quite the opposite: fixing J and perturbing around a critical point given by F and $\Delta\beta$. Taking the expression from Eq. (5.7.9), imposing $J_C = -1$ and fixing $\beta_2 = 1$, we obtain as a unique solution the pair $F = 0$ and $\Delta\beta = 1$, corresponding to the critical points plotted in Figs. 5.20 and 5.18 for both the ferromagnetic and ferrimagnetic cases. Fixing these quantities and expanding in $\Delta\beta$, we obtain for the ferromagnetic case:

$$\frac{dm_\alpha}{dt} = \tilde{a}_\alpha(\Delta\beta - \Delta\beta_c)m_\alpha - \tilde{b}_\alpha m^3, \tag{5.7.12}$$

with $\tilde{a}_\alpha = 2/9$ and $\tilde{b}_\alpha = -28/243$.

As shown in Figs. 5.20 and 5.18, the continuous transition occurs only at $F = 0$. Since we fixed $|J| = 1$ and $\beta_2 = 1$, as in most of the results in this work, Eq. (5.7.12) leads to $F_C = 0$ and $\Delta\beta = 1$, with the coefficients described in the expansion of the equation above. Setting Eq.(5.7.12) to zero, we obtain three stable solutions: a disordered solution $m^D = 0$ and two ordered solutions $m^O = \pm\sqrt{(9/4)(\Delta\beta - \Delta\beta_C)}$, where $\Delta\beta_C = 1$, corresponding to the point shown in the phase diagram in Fig. 5.20. The phase transition follows the mean-field exponent $\beta_{mf} = 1/2$, in similarity to the critical exponent expected for the traditional Ising model. We also apply the scaling analysis to the entropy production, which is expected to also be continuous around the critical point, presenting a divergence in the first derivative [127]. As demonstrated in Fig. 5.19, the critical exponent for the entropy production is $\delta = 2\beta$, with $\langle\sigma\rangle - \langle\sigma_C\rangle \sim a_\sigma (J_C - J)^\delta / b_\sigma$ for $F = 0$.

We identify that some specific behaviors of $\langle\sigma\rangle$ are important signatures of the properties of the phase diagram, as depicted in Fig. 5.18, being a hallmark of the interaction choice and its interplay with the nonequilibrium ingredients present here. First, we stress that the entropy production has a symmetric bilinear form for $\Delta\beta < \Delta\beta_C = 1$ (see Fig. 5.21 b)), with a parabolic behavior and a minimum at $F = 0$. However, there is a displacement of the minimum of $\langle\sigma\rangle$ near the discontinuous transition for $\Delta\beta > \Delta\beta_C$, located at a nonzero F value. Such a discontinuity is also visible for fixed F while varying $\Delta\beta$. While we observe a divergence in $\langle\sigma\rangle$ corresponding to the points of discontinuity in $\Delta\beta$ in the phase diagram, we also observe a discontinuity in $\frac{d\langle\sigma\rangle}{d\Delta\beta}$, which is a signature of a second-order phase transition [126, 127]..

5.8 Final Remarks About Collective Heat Engines

In this chapter, we introduced a minimal class of reliable engines composed of several interacting units. In the collective phase, where all spins operate in a synchronized way, the engine can exhibit distinct regimes, along with max-

imal optimization outputs, in contrast to its independent phase. The interplay between the driving forces and the temperature gradient from two distinct thermal reservoirs results in a unique phase transition characterized by two distinct transition points. These results highlight an ordered phase with two contrasting behaviors, where one of the phases is less dissipative, offering ideal performance under optimal energy choices. The introduction of sublattices in an energetically frustrated structure reveals that the different transition points depend starkly on the set of interactions between the spins. We also reveal that the two transition points are reached after a critical point, above which all transitions have a single critical point, not depending on the initial condition.

Chapter 6

Quantum-Dot Collisonal engines: Role of stages

In this Chapter we study another important example of collisional (or sequential) engines: the quantum dot pump, which describes a setup composed of a single quantum-dot (QD) that interacts with two or more reservoirs that deliver/receive fermions (in general, electrons) that occupy/deoccupy the QD's energy level. This setup was broadly applied to address different investigations in the theoretical and experimental realms [51, 59, 60, 63, 63–65, 140, 141] in the statistical mechanics and nanoscience/nanotechnology territories. In equilibrium, this model is approached as a two-level system described by a Fermi-Dirac distribution [42] (See Sec.(3.3.1)). In the non-equilibrium realm, some variables are introduced such as chemical potential gradient (due to reservoirs) or ratchet potentials (external forces). Even in the far-from-equilibrium regime, the solution remains exact irrespective of the number of strokes and model parameters [60, 64, 140, 141]. Another advantage of working with the QD pump is the fact that the setup can work both as a heat engine and a work-to-work converter depending on the kind of external drivings and temperature gradient, unlike the Brownian case studied in Chap.(4), which is limited to operating as a work-to-work converter. In this thesis we present an alternative route to

improve its power output and efficiency by applying different ”collisions” along the engine cycle. More precisely, we investigate the role of adding new stages and how this procedure affects several thermodynamic quantities such as flux of particles, heat, and entropy production. We compute all former quantities exactly, exploring how one can choose the stage with respect to the experimental quantities such as voltage (chemical potential) and temperature in order to improve its output. This research was started by another PhD student (Carlos Noa) and some of the results of this Chapter are also found in his PhD thesis [142]. Here, we add the current analysis and the physical interpretation of adding new stages, which was lacking in the last work.

6.1 Stochastic Thermodynamics for a QD Pump

In this thesis, we study the collisional (or sequential) approach for the quantum-dot pump. The details of this approach are better described in Chapter (4), but in summary, the system (in this case the quantum-dot) will interact with one reservoir during a time interval and exchange heat under an adiabatic transition. In the vicinity of the transition, the probability must obey a boundary condition in order to keep its continuity. The time spent in each reservoir is given by τ/N, where τ is the total time of the cycle and N the number of reservoirs. The time spent in each reservoir is the same, and this is why we usually call this approach ”symmetric” [60]. As described in Sec.(3.3.1), the dynamics of the two-level system that describes the QD pump is given by a master equation,

$$\dot{p}_i(t) = [1 - p_i(t)]\,\omega_{01}^{(i)} - p_i(t)\omega_{10}^{(i)}, \tag{6.1.1}$$

where the rates $\omega_{01}^{(i)}$ and $\omega_{10}^{(i)}$ account for filling up $(0 \to 1)$ and vice versa $(1 \to 0)$, respectively. Considering a weak coupling between the reservoir and the system, these rates depend on ϵ_i and μ_i in such a way that:

$$\omega_{01}^{(i)} = \frac{\Gamma_0}{1 + e^{A_i}} \qquad \text{and} \qquad \omega_{10}^{(i)} = \frac{\Gamma_0 e^{A_i}}{1 + e^{A_i}}. \tag{6.1.2}$$

The index (i) is related to which reservoir the system will interact with. Here, we already consider the notation that will be adopted in Chap.(6) for the collisional model.

Exactly as described in Sec.(3.4), the thermodynamic relations are derived starting from the system energy given by $E(t) = \epsilon(t)p(t)$ where we introduce $\epsilon(t)$ / $p(t)$ as the energy level / occupation probability of the QD at time t. In the context of the sequential approach, the time derivative of $E(t)$ gives two contributing terms:

$$\dot{E}(t) \quad = \quad \dot{\epsilon}(t)p(t) + \epsilon(t)\dot{p}(t) \tag{6.1.3}$$

the former identified as direct driving and appearing only during the external driving phases (during which $\dot{\epsilon}(t) \neq 0$), and identified as the direct work $\dot{W}_{\mathsf{d}}$ given by

$$\dot{W}_{\mathsf{d}}(t) = \sum_{i=1}^{N} (\epsilon_{i+1} - \epsilon_i)\, \delta\left(t - \frac{i\tau}{N}\right) p_i(t), \tag{6.1.4}$$

where periodic boundary conditions for the index i, i.e. $\epsilon_{i+N} = \epsilon_i$, have been employed. We stress that $\dot{W}_{\mathsf{d}}(t) > 0$ according to whether the energy of the QD increases. By averaging it over one full period, one has that

$$\overline{\dot{W}}_{\mathsf{d}} \equiv \frac{1}{\tau}\int_0^{\tau} \dot{W}_{\mathsf{d}}(t)dt = \frac{1}{\tau}\sum_{i=1}^{N} (\epsilon_{i+1} - \epsilon_i)\, p_i\left(\frac{i\tau}{N}\right). \tag{6.1.5}$$

The second term $\epsilon(t)\dot{p}(t)$ appears during the exchange phases and it is different from zero provided an exchange of particles takes place. From the integration of $\dot{p}(t)$ from $\tau_{i-1} = (i-1)\tau/N$ to τ_i, one can re-express it as $\overline{J}_i \equiv dN_i/\tau$, the average net number of particles exchanged during stage i per period, given by

$$\overline{J}_i = \frac{1}{\tau}\left[p_i\left(\frac{i\tau}{N}\right) - p_i\left(\frac{(i-1)\tau}{N}\right)\right]. \tag{6.1.6}$$

The total energy exchange dE_i during the exchange phase of stage i is rewritten as

$$dE_i \equiv \int_{\frac{(i-1)\tau}{N}}^{\frac{i\tau}{N}} \epsilon(t)\dot{p}_i(t)dt = \epsilon_i dN_i. \tag{6.1.7}$$

From the reservoir viewpoint, the above expression can be split into two parts: $dE_i = (\epsilon_i - \mu_i)\, dN_i + \mu_i dN_i$, the former and latter terms identified as heat and chemical work respectively, counted as positive when delivered to the QD, i.e. when the energy of the QD increases. We can interpret this expression as

$$dE_i \quad = \quad (\epsilon_i - \mu_i)\, dN_i + \mu_i dN_i \tag{6.1.8}$$

$$\tag{6.1.9}$$

By averaging Eqs. (6.1.3) and (6.1.7) over one full period and using Eq. (6.1.6), it follows that $\overline{\dot{W}}_{\mathsf{d}} + \overline{\dot{Q}} + \overline{\dot{W}}_{\mathsf{ch}} = 0$, where $\overline{\dot{Q}}$ and $\overline{\dot{W}}_{\mathsf{ch}}$ are given by

$$\overline{\dot{Q}} = \sum_{i=1}^{N} (\epsilon_i - \mu_i)\, \overline{J}_i \; ; \tag{6.1.10}$$

$$\overline{\dot{W}}_{\mathsf{ch}} = \sum_{i=1}^{N} \mu_i \overline{J}_i \; ; \tag{6.1.11}$$

$$\overline{\dot{W}}_{\mathsf{d}} = -\sum_{i=1}^{N} \epsilon_i \overline{J}_i, \tag{6.1.12}$$

which reproduce exactly Eqs. (3.4.22) - (3.4.24) derived above. The entropy production averaged over one full cycle can be determined using Gibbs' expression for a Markov Chain 3.4.9:

$$\overline{\dot{S}} = \frac{k_B}{\tau} \sum_{i=1}^{N} \int_{\frac{(i-1)\tau}{N}}^{\frac{i\tau}{N}} [\omega_{01}^{(i)} - (\omega_{01}^{(i)} + \omega_{10}^{(i)}) p_i(t)] \ln \frac{\omega_{01}^{(i)}(1 - p_i(t))}{\omega_{10}^{(i)} p_i(t)} \mathrm{d}t, \tag{6.1.13}$$

where from now on we set $k_B T = 1$. Taking into account the periodicity of $p_i(t)$, the term $\sum_i [\omega_{01}^{(i)} - (\omega_{01}^{(i)} + \omega_{10}^{(i)}) p_i(t)] \ln(1 - p_i(t))/p_i(t)$ allows Eq. (6.1.13) to be expressed in the form $\overline{\dot{S}} = -\sum_i \overline{\dot{Q}}_i / T_i$, where $\overline{\dot{Q}}_i$ is given by Eq. (6.1.10). For equal temperatures and by using the first law of thermodynamics, this expression can be rewritten in the following form:

$$\overline{\dot{S}} = -\frac{\overline{\dot{Q}}}{T} = \frac{\overline{\dot{W}}_{\mathsf{d}} + \overline{\dot{W}}_{\mathsf{ch}}}{T}, \tag{6.1.14}$$

consistent with the ratio between the total average heat and the system temperature, as expected.

The collisional system can operate as an engine or as a pump depending on the suitable choice of parameters. To start, a short comment about the sign of thermodynamic quantities in each regime is useful in order to establish a reliable definition of efficiency. A particle pump typically consumes direct work $\overline{\dot{W}}_{\mathsf{d}}$ in order to move a particle from a lower to a higher chemical potential, which is consistent with $\overline{\dot{W}}_{\mathsf{ch}} < 0$ and $\overline{\dot{W}}_{\mathsf{d}} > 0$ (see e.g. top panel of Fig. 6.1). Since there is no particle accumulation in the QD, such delivered chemical work can only be the result of transferring particles from reservoirs at lower to those at higher chemical potentials. A reliable definition of power is given by $\mathcal{P}_{\mathsf{pump}} = -\overline{\dot{W}}_{\mathsf{ch}}$

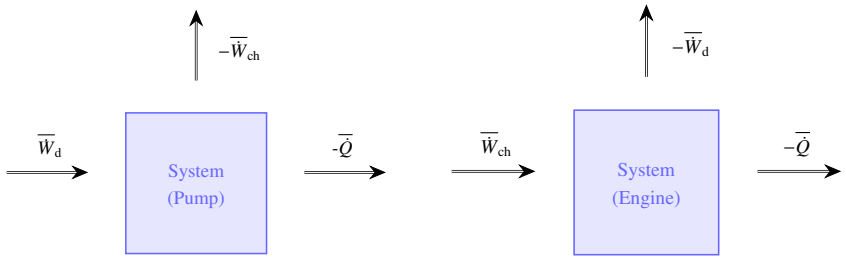

Figure 6.1: Sketch of a pump (top) and engine (bottom) working operation.

with associated efficiency η_{pump} given by

$$\eta_{\mathsf{pump}} = \frac{\mathcal{P}_{\mathsf{pump}}}{\overline{\dot{W}}_{\mathsf{d}}}, \tag{6.1.15}$$

respectively. By construction, the above efficiency definition implies that $0 \leq \eta_{\mathsf{pump}} \leq 1$. The system can also operate as an engine ($\overline{\dot{W}}_{\mathsf{d}} < 0$ and $\overline{\dot{W}}_{\mathsf{ch}} > 0$), as sketched in the bottom panel of Fig. 6.1. The dynamics are similar, but in this case the power output is given by $\mathcal{P}_{\mathsf{engine}} = -\overline{\dot{W}}_{\mathsf{d}} \geq 0$ according to the efficiency definition:

$$\eta_{\mathsf{engine}} = \frac{\mathcal{P}_{\mathsf{engine}}}{\overline{\dot{W}}_{\mathsf{ch}}}, \tag{6.1.16}$$

where $0 \leq \eta_{\mathsf{engine}} \leq 1$. It is worth pointing out that such efficiency definitions state that $\eta_{\mathsf{pump}} = 1/\eta_{\mathsf{engine}}$.

6.1.1 General expressions for the probability distribution and average flux

Although the QD evolves to the equilibrium regime when it is in contact with only one thermal bath, this is no longer true when it is periodically connected to different reservoirs [143]. From Eq. (6.1.1) together with the continuity of $p_i(t)$ at each reservoir switching and taking into account that the QD is thermalized with reservoir $i = 1$ at $t = 0$ and the system returns to its initial state after a complete period, one obtains the following (generic) expression for $p_i(t)$ for the i-th stage and N strokes [144]:

$$p_i(t) = p_i^{\text{eq}} + \left[p\left(\frac{(i-1)\tau}{N}\right) - p_i^{\text{eq}} \right] e^{-(\omega_{01}^{(i)}+\omega_{10}^{(i)})(t-\frac{(i-1)\tau}{N})}, \tag{6.1.17}$$

where $p_i^{eq} = \omega_{01}^{(i)}/(\omega_{01}^{(i)} + \omega_{10}^{(i)}) = (1 + e^{\frac{1}{T}(\epsilon_i - \mu_i)})^{-1}$ is obtained from transition rates $\omega_{01}^{(i)}$ and $\omega_{10}^{(i)}$ at stage i for $(i-1)\tau/N \leq t < i\tau/N$. By expressing $p\left((i-1)\tau/N\right)$ in terms of probabilities from previous strokes, we finally arrive at the generic form for $p_i(t)$:

$$p_i(t) = p_i^{\text{eq}} + e^{-(\omega_{01}^{(i)}+\omega_{10}^{(i)})(t-\frac{(i-1)\tau}{N})} \left\{ \sum_{m=2}^{i} \xi_{m,i-1}\Delta_{m-1,m} + \frac{\xi_{1,i-1}}{1-\xi_{1,N}} \left[\Delta_{N,1} + \sum_{n=2}^{N} \xi_{n,N}\Delta_{n-1,n} \right] \right\}, \tag{6.1.18}$$

solely expressed in terms of quantities $\Delta_{i,j} \equiv p_i^{\text{eq}} - p_j^{\text{eq}}$ and $\xi_{i,j} \equiv \exp\left\{ -\frac{\tau}{N} \sum_{n=i}^{j} (\omega_{01}^{(n)} + \omega_{10}^{(n)}) \right\}$. It is worth pointing out that $p_i(t)$ is the exact time-periodic occupation probability of the quantum dot at the i-th stage. We stress that since the system is ergodic and is periodically driven, the relation $p_i(t+\tau) = p_i(t)$ holds for any stroke i. Having $p_i(t)$, average fluxes can be obtained. From Eqs. (6.1.6) and (6.1.17) the average flux $\overline{J}_i$ during stage i reads

$$\overline{J}_i = \frac{1}{\tau} \left\{ \frac{\xi_{1,i-1}}{1-\xi_{1,N}} \left[\Delta_{N,1} + \sum_{n=2}^{N} \xi_{n,N}\Delta_{n-1,n} \right] + \sum_{m=2}^{i} \xi_{m,i-1}\Delta_{m-1,m} \right\} (\xi_{i,i} - 1). \tag{6.1.19}$$

From Eq. (6.1.19), the mean flux and thermodynamic quantities can be obtained for a generic N.

6.2 Overview about the two (N=2) and three (N=3) stages collisional engine

We describe the QD model exactly as defined in the Sec.(6.1). The QD interacts with several reservoirs with different energies and chemical potentials. The equations defined in the Sec(6.1) are broadly applied. In this section, we made an overview about two simple cases, when the QD interacts with two [60] and three symmetric strokes. As discussed in the Sec.(2.2.2) that the time of interaction between reservoirs plays an important role [60]. However, for

simplicity, we keep our attention to the called "symmetric case", in which the time durations of the interaction between the QD and all reservoirs are all the same, $\tau_j = \tau/N$, where τ is the total period of the engine and N the number of reservoirs. In the Fig.(6.2) we present a sketch representing the collisional interaction between the system and the reservoirs at all stages.

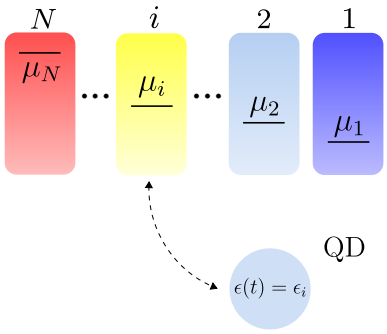

Figure 6.2: Sketch of a Quantum-dot setup sequentially exposed to N different thermal baths, each one at the interval $\tau_{i-1} \leq t < \tau_i = i\tau/N$ characterized by chemical potential μ_i and temperature $T_i = T$.

We describe the QD model exactly as defined in Sec.(6.1). The QD interacts with several reservoirs with different energies and chemical potentials. The equations defined in Sec.(6.1) are broadly applied. In this section, we give an overview of two simple cases, when the QD interacts with two [60] and three symmetric strokes. As discussed in Sec.(2.2.2), the time of interaction between reservoirs plays an important role [60]. However, for simplicity, we focus our attention on the so-called "symmetric case", in which the time durations of the interaction between the QD and all reservoirs are all the same, $\tau_j = \tau/N$, where τ is the total period of the engine and N the number of reservoirs. In Fig.(6.2) we present a sketch representing the collisional interaction between the system and the reservoirs at all stages. Despite the simplicity, various aspects comprising the role of parameters for equal [145] and asymmetric switching and different maximization routes [85] have been considered. In the former case, the first and second stages have time durations $0 < t < \tau^*$ and $\tau^* < t < \tau$, respectively, during which the system is in contact with the right reservoir (and disconnected from the left reservoir) and connected to the left reservoir (and

disconnected from the right reservoir), respectively. By curbing our analysis to the simplest symmetric case $\tau^* = \tau/2$, Eq. (6.1.19) reduces to:

$$\overline{J_l} = \frac{1}{2\tau}\left[\tanh\left(\frac{A_r}{2}\right) - \tanh\left(\frac{A_l}{2}\right)\right]\tanh\left(\frac{\Gamma_0\tau}{4}\right), \tag{6.2.1}$$

where $\overline{J_r} = -\overline{J_l}$ and indexes $i = r, l$ are associated with the right or left reservoir, respectively. From Eq. (6.1.10), the total heat exchanged $\overline{\dot{Q}} = \overline{\dot{Q}}_r + \overline{\dot{Q}}_l$ is given by

$$\overline{\dot{Q}} = (\epsilon_r - \mu_r - \epsilon_l + \mu_l)\overline{J_l}, \tag{6.2.2}$$

whereas chemical work and direct work, obtained from Eq. (6.1.11) and (6.1.12) respectively, read $\overline{\dot{W}}_{\text{chem}} = (\mu_r - \mu_l)\overline{J}_l$ and $\overline{\dot{W}}_{\text{d}} = (\epsilon_l - \epsilon_r)\overline{J}_l$. Note that the pump and engine operation occurs for different values of parameters $\epsilon_l, \epsilon_r, \mu_l$ and μ_r provided $\overline{\dot{W}}_{\text{chem}} < 0$ and $\overline{\dot{W}}_{\text{d}} > 0$ and $\overline{\dot{W}}_{\text{chem}} > 0$ and $\overline{\dot{W}}_{\text{d}} < 0$, respectively. The associated efficiency is given by

$$\eta_{\text{engine},N=2} = \frac{\epsilon_l - \epsilon_r}{\mu_l - \mu_r}, \tag{6.2.3}$$

due to the fact that $\overline{J}_l = -\overline{J}_r$, respectively, and it depends solely on $\epsilon_l, \epsilon_r, \mu_l$ and μ_r. Note that the engine regime corresponds to $\epsilon_l - \epsilon_r < \mu_l - \mu_r$, whereas the pump corresponds to $\epsilon_l - \epsilon_r > \mu_l - \mu_r$. Furthermore, the ideal regime $\eta_{\text{engine},N=2} = 1$ implies that $\overline{\dot{W}}_{\text{chem}} = -\overline{\dot{W}}_{\text{d}}$ and $\overline{\dot{S}} = 0$.

Our goal is to tackle the role of intermediate stages. We present a detailed analysis of the simplest setup with an intermediate stage, namely a cycle composed of $N = 3$ stages. More concretely, the system is placed in contact with the right reservoir during the first third of the time, with the middle reservoir in the second stage, and with the left reservoir in the final stage, completing a periodic cycle after τ. From Eq. (6.1.17), the probability distribution $p_i(t)$ at the i-th stage reduces to the following expression:

$$p_i(t) = \frac{1}{e^{A_i}+1} - \frac{e^{\Gamma_0(\frac{i\tau}{3}-t)}}{\phi}\left(\frac{1+e^{\frac{\Gamma_0\tau}{3}}}{e^{A_i}+1} - \frac{1}{e^{A_{i+1}}+1} - \frac{e^{\frac{\Gamma_0\tau}{3}}}{e^{A_{i+2}}+1}\right), \tag{6.2.4}$$

where $\phi = 1 + e^{\frac{\Gamma_0\tau}{3}} + e^{\frac{2\Gamma_0\tau}{3}} \geq 3$. From Eq. (6.1.19) for $N = 3$, each mean flux $\overline{J_i}$ reduces to the following expression:

$$\overline{J_i} = \Omega\left[\left(1+e^{A_{i+1}}\right)\left(e^{A_i} - e^{A_{i-1}}\right)e^{\frac{\Gamma_0\tau}{3}} + \left(e^{A_{i-1}}+1\right)\left(e^{A_i} - e^{A_{i+1}}\right)\right], \tag{6.2.5}$$

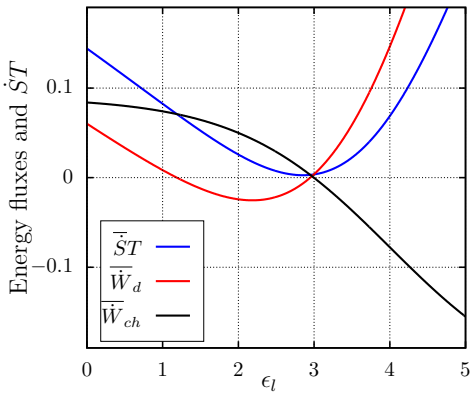

Figure 6.3: For the three-stage case, the entropy production times temperature $\overline{\dot{S}T}$ (blue), direct work $\overline{\dot{W}}_{\mathsf{d}}$ (red) and chemical work $\overline{\dot{W}}_{\mathsf{ch}}$ (black) vs ϵ_l. Parameters: $\tau = 0.1$, $\Gamma_0 = 1$, $\epsilon_r = 1$, $\mu_r = 2$, $\epsilon_m = 1.7$, $\mu_m = 3$ and $\mu_l = 4$.

where

$$\Omega = \frac{e^{\frac{\Gamma_0 \tau}{3}} - 1}{(e^{A_r} + 1)(e^{A_m} + 1)(e^{A_l} + 1)\phi\tau} > 0. \tag{6.2.6}$$

The quantities $\overline{\dot{W}}_{\mathsf{chem}}$ and $\overline{\dot{W}}_{\mathsf{d}}$ are straightforwardly obtained from Eqs. (6.1.11), (6.1.12) and (6.2.5), given by $\overline{\dot{W}}_{\mathsf{chem}} = (\mu_l - \mu_m)\overline{J}_l + (\mu_r - \mu_m)\overline{J}_r$ and $\overline{\dot{W}}_{\mathsf{d}} = (\epsilon_m - \epsilon_l)\overline{J}_l + (\epsilon_m - \epsilon_r)\overline{J}_r$, respectively.

Figs. 6.3 and 6.4 depict ($T\overline{\dot{S}}$, $\overline{\dot{W}}_{\mathsf{d}}$ and $\overline{\dot{W}}_{\mathsf{ch}}$) upon varying the energy ϵ_l and chemical potential μ_l, respectively, for particular choices of parameters. In the former case, there is a closed region delimited by approximately $1 < \epsilon_l < 3$ in which $\overline{\dot{W}}_{\mathsf{d}} < 0$ and $\overline{\dot{W}}_{\mathsf{ch}} > 0$, and the system operates as an engine. Conversely, for $\epsilon_l > 3$, one has that $\overline{\dot{W}}_{\mathsf{d}} > 0$ and $\overline{\dot{W}}_{\mathsf{ch}} < 0$, consistent with a pump behavior. Similar findings are depicted in Fig. 6.4, but as μ_l is varied the pump regime is delimited by a closed region $2.5 < \mu_l < 6$, whereas the engine mode operation extends to $\mu_l > 6.2$.

The associated efficiency is given by

$$\eta_{\mathsf{engine},N=3} = \frac{(\epsilon_l - \epsilon_m)\overline{J}_l + (\epsilon_r - \epsilon_m)\overline{J}_r}{(\mu_m - \mu_l)\overline{J}_l + (\mu_m - \mu_r)\overline{J}_r}. \tag{6.2.7}$$

Unlike the $N = 2$ case, the present case is more revealing, and the efficiencies depend on the interplay with intermediate parameters (μ_m, ϵ_m) and the period

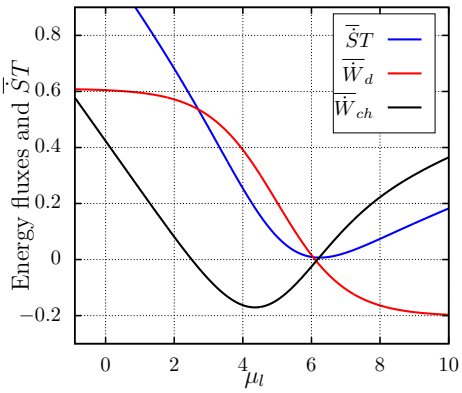

Figure 6.4: For the three-stage case, the entropy production times temperature $\overline{\dot{S}}T$ (blue), direct work $\overline{\dot{W}}_{\mathrm{d}}$ (red) and chemical work $\overline{\dot{W}}_{\mathrm{ch}}$ (black) vs μ_l. Parameters: $\tau = 0.1$, $\Gamma_0 = 1$, $\epsilon_r = 1$, $\mu_r = 2$, $\epsilon_m = 1.7$, $\mu_m = 3$ and $\epsilon_l = 5$.

τ. Analogous expressions are straightforwardly obtained for $N > 3$. Given that they are longer (and less instructive), they will be omitted here.

6.3 Influence of intermediate reservoirs

Below we investigate the influence of adding stages on the performance (efficiency and power). Our motivation for doing so is twofold. First, there is a fundamental difference between the $N = 2$ and $N > 2$ setups. As follows from the previous analysis, the $N = 2$ setup is a so-called thermodynamically strongly coupled system [146]. It is well known that in the regime of linear thermodynamics, the efficiency can be made optimal for such systems (see for example [123, 147]). Yet, beyond the linear regime, it is not at all clear whether these strongly coupled systems always do better than systems with $N > 2$. Second, the performance of any setup is the result of an intricate interplay between thermodynamics and dynamics (due to the periodic driving). Inserting additional stages makes the corresponding gradients (for example in chemical energy) smaller and hence might reduce the strong fluxes and corresponding dissipation/entropy production. The downside is, of course, that

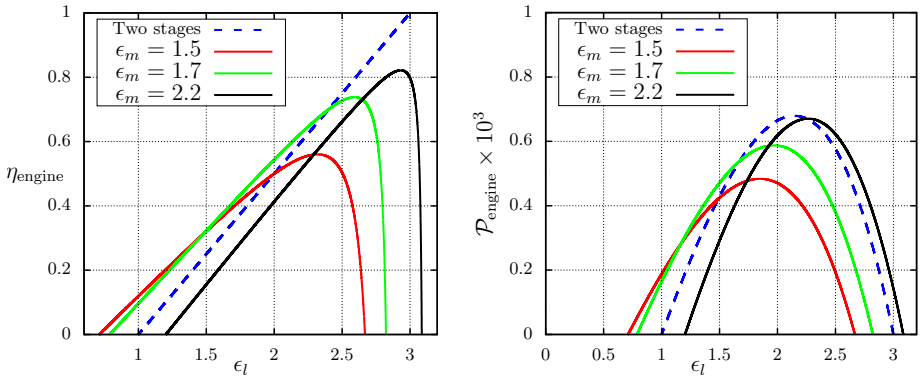

Figure 6.5: For the engine operation mode and different ϵ_m's, the depiction of efficiency η (top) and power $\mathcal{P}_{\text{engine}}$ (bottom) versus ϵ_l for $N = 2$ and $N = 3$ stages. Parameters: $\tau = 15$, $\Gamma_0 = 1$, $\epsilon_r = 1$, $\mu_r = 2$, $\mu_m = 3$ and $\mu_l = 4$.

the number of steps increases, adding to the overall complexity. It is far from obvious how this influences the performance.

As the number of stages increases, so too does the number of parameters. Below we optimise each setup by fine-tuning a number of these parameters. This is a relevant situation in an experimental context, in which adjusting each and every parameter continuously in order to reach a global optimum may not always be feasible nor realizable. For this reason, our analysis will be undertaken by means of various strategies, as described throughout Secs. 6.3 and 6.3.1. In order to gain a first insight into the influence of model parameters, Figs. 6.5 and 6.6 depict the behavior of $\mathcal{P}$ and η for $N = 3$ and three different values of ϵ_m by varying ϵ_l and τ (while the remaining parameters ϵ_r, μ_r, μ_m and μ_l are held fixed, respectively). In the former case (fixed τ), the system efficiency is solely improved via adjustment of ϵ_l (or ϵ_r). For $N = 2$, the efficiency η exhibits a linear dependence on ϵ_l, reaching the maximum (ideal) limit $\eta_{ME} = 1$ with $\mathcal{P}_{ME} = 0$ (consistent with the reversible operation mode). For $N = 3$, different routes for optimization become feasible, such as by varying ϵ_m and ϵ_l, resulting in some regions in the set of parameters in which the addition of stages can confer a larger performance. Fig. 6.7 extends the above analysis by tackling the number of strokes for N ranging from 2 to 5, depicting η and $\mathcal{P}$ for various values of ϵ_l, with ϵ_r, μ_r, μ_l held fixed. For this analysis, the interme-

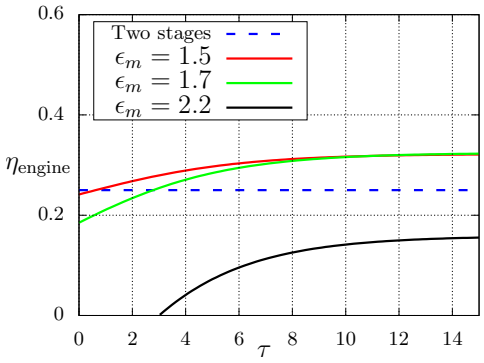

Figure 6.6: For fixed ϵ_l and different ϵ_m's, the depiction of efficiency η versus period τ for $N = 2$ and $N = 3$. Parameters: $\Gamma_0 = 1$, $\epsilon_r = 1$, $\epsilon_l = 1.5$, $\mu_r = 2$, $\mu_m = 3$ and $\mu_l = 4$.

diate μ_m's are determined by $\mu_m = \mu_{m-1} + \Delta\mu$, with $\Delta\mu = (\mu_l - \mu_r)/(N-1)$. The corresponding ϵ_m's are determined by $\epsilon_m = \alpha\mu_m$. As was the case for $N = 3$, the system performance can be improved by a suitable choice of parameters and by increasing the number of stages. In Figure 6.8 we compare both power and efficiency of $N = 3$ and $N = 4$ setups against the power and efficiency of an $N = 2$ setup which has been optimised for maximum power. That is, for $N = 2$ and the parameters μ_l, ϵ_r and μ_r held fixed, ϵ_l is determined by maximizing $\mathcal{P}$. In the (α, μ_l)-space shown in Figure 6.8, the blue and red areas are those for which respectively the power and efficiency for the $N = 3$ and $N = 4$ setups are improved compared to the $N = 2$ setup. Furthermore, in the case of $N = 4$, there is an overlap between these regions (indicated in purple) for which both performance indicators are higher. This again supports our claim that the addition of stages can improve the performance.

The above findings can be understood from the interplay among parameters (energies ϵ_i's and chemical potentials μ_i) and the period τ. In all previous cases and in Fig. 6.9 (left), the increase in the number of stages improves the system performance whenever τ is larger and the intermediate μ_m's lie between μ_l and μ_r ($\mu_l < \mu_m < \mu_r$). Such improvement can be linked to the steady fluxes and currents (and the QD occupation itself). We stress the role of the time period spent by the QD in each reservoir, since adding new steps reduces the interaction time of the QD with each thermal reservoir. The strongly

coupled system ($N = 2$) with $\tau/2$ for each reservoir in the symmetric case was investigated in Ref. [148], which also discusses the influence of the time spent in each step on a collisional QD pump. The interaction time with each reservoir can also be used as a maximization variable, and one can improve its performance by manipulating it as an independent variable.

For an interaction time much shorter than the thermalization time, the necessary exchanges (flux of particles and heat) due to the gradients will be insufficient to ensure any proper performance. On the other hand, an interaction time much larger than the thermalization time also has a negative influence, as no exchanges take place once the QD is in close thermal equilibrium with the corresponding reservoir (hence $J_i(t) \to 0$, as illustrated for example by the continuous lines in the bottom-left panel of Fig. 6.9). This lack of exchange strongly reduces the power output.

If the QD does not spend sufficient time, the thermalization and all necessary gradient exchanges (flux of particles and heat) will not happen, implying that fast interactions can result in an engine with lower performance (dotted and dashed lines of the bottom-left panel of Fig. 6.9). Longer interaction times also must have a negative influence, since they can expose the system to the reservoir for a sufficient time to make it thermalize and cause the current of the given step $J_i(t)$ to reach a null value (continuous line of the bottom-left panel of Fig. 6.9). Adding more steps in the long time period case will also increase the chemical potential gradient, moving the current of each step away from the null value, and the fine tuning of the ϵ_n's plays an important role in making this maximization route more efficient. To better visualize this result, we plot in Fig. 6.9 the power output (top) and the current at the i-th step $J_i(t)$ (bottom) considering a long ($\tau = 15$) and a short ($\tau = 1$) period interval.

Having discussed the role of interaction time in each step, we are now in a position to explain the improvement achieved by adding new steps in all previous cases and in Fig. 6.9 (left) in terms of occupation probabilities. The probability increases from the left to the right strokes (associated currents $J_i(t) > 0$), indicating that the particle flux goes from the i-th reservoir to the dot. We emphasize the fact that the intermediate μ_m's must lie between μ_l and

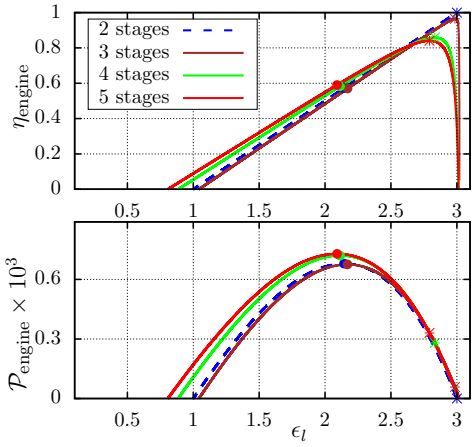

Figure 6.7: For the engine regime operation mode, the comparison between the efficiencies η's (top) and power outputs $\mathcal{P}$'s (bottom) for the two-stage system (blue), the three-stage system (brown), four-stage (green) and five-stage (red) systems in the engine regime vs. ϵ_l. Symbols $*$ and $\bullet$ correspond to the maximization of η and $\mathcal{P}$, respectively. Parameters: $\alpha = 0.68$, $\tau = 15$, $\Gamma_0 = 1$, $\epsilon_r = 1$, $\mu_r = 2$ and $\mu_l = 4$.

μ_r ($\mu_l < \mu_m < \mu_r$). Otherwise, if the μ's do not increase monotonically from μ_l to μ_r, the probabilities do not increase monotonically either, leading to negative $J_i(t)$'s (flux from the dot to the reservoir). As a consequence, the increase in the number of stages does not result in better performance.

6.3.1 Optimal parameters and maximization for $N = 3$ stages

Because multiple independent fluxes coexist, optimizing the system for $N > 2$ differs substantially from the $N = 2$ case, being strongly influenced by the number of stages, especially in terms of efficiency. In this section, we explore several optimization paths for $N = 3$, where ϵ_m and μ_m are treated as independent variables. Our analysis focuses on the case $N = 3$, with the parameters (ϵ_r, μ_r) kept fixed while varying (ϵ_l, ϵ_m) [for fixed (μ_l, μ_m)], and vice versa.

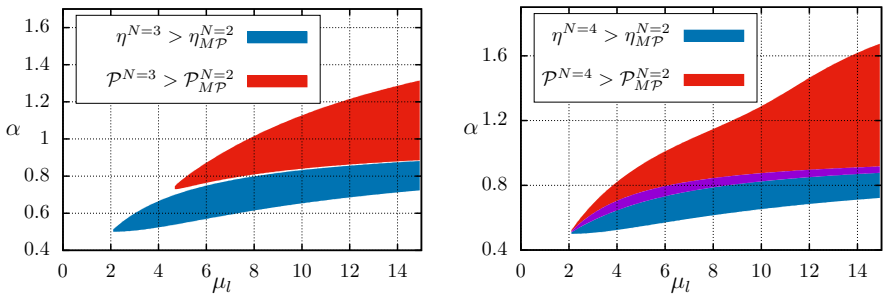

Figure 6.8: Top (bottom) panels depict, for the engine regime operation mode, the set of α values for which $\mathcal{P}$ (red area) and η (blue area) are, for $N = 3$ ($N = 4$), greater than the two-stage power and efficiency at the maximum power regime versus μ_l. The purple area (bottom) shows the intersection between the red and blue areas. Parameters: $\tau = 15$, $\Gamma_0 = 1$, $\epsilon_r = 1$, $\mu_r = 2$.

Although all results are obtained exactly, the resulting expressions for the optimized quantities are rather cumbersome and must be determined numerically. In particular, the maximum powers $\mathcal{P}_{M\mathcal{P}}$ occur at ϵ_m^* (for fixed ϵ_l) and ϵ_l^* (for fixed ϵ_m), satisfying the following relations:

$$\overline{J}_r(\epsilon_m^*) + \overline{J}_l(\epsilon_m^*) = (\epsilon_l - \epsilon_m^*)\overline{J}_l'(\epsilon_m^*) + (\epsilon_r - \epsilon_m^*)\overline{J}_r'(\epsilon_m^*), \tag{6.3.1}$$

with maximum power

$$\mathcal{P}_{M\mathcal{P}} = (\epsilon_l - \epsilon_m^*)\overline{J}_l(\epsilon_m^*) + (\epsilon_r - \epsilon_m)\overline{J}_r(\epsilon_m^*) \tag{6.3.2}$$

and

$$\overline{J}_l(\epsilon_l^*) = \frac{1}{\epsilon_m}[\epsilon_l^*\overline{J}_l'(\epsilon_l^*) + (\epsilon_r - \epsilon_m)\overline{J}_r'(\epsilon_l^*)], \tag{6.3.3}$$

in the latter case with maximum power $\mathcal{P}_{M\mathcal{P}} = (\epsilon_l^* - \epsilon_m)\overline{J}_l(\epsilon_l^*) + (\epsilon_r - \epsilon_m)\overline{J}_r(\epsilon_l^*)$. In this analysis, $\overline{J}_X'(\epsilon_Y^*) \equiv \frac{\partial \overline{J}_X}{\partial \epsilon_X}$ is evaluated at ϵ_Y^*, and the notation $\overline{J}_Y(\epsilon_X)$ is used to indicate which energy variable was considered in the derivative. An interesting feature arises when the loci of the maxima ϵ_m^* (for fixed ϵ_l) and ϵ_l^* (for fixed ϵ_m) meet at a single point $(\bar{\epsilon}_m, \bar{\epsilon}_l^*)$, defining the condition for a global maximization of the power. The corresponding expression is given by $\mathcal{P}_{M\mathcal{P}}^* = (\bar{\epsilon}_l - \bar{\epsilon}_m)\overline{J}_l(\bar{\epsilon}_l) + (\bar{\epsilon}_r - \bar{\epsilon}_m)\overline{J}_r(\bar{\epsilon}_l)$. An analogous result applies to the pump regime after substituting $\epsilon_X \to \mu_X$.

For $N = 2$, the behavior is qualitatively different. In this case, $\eta_{ME} = 1$,

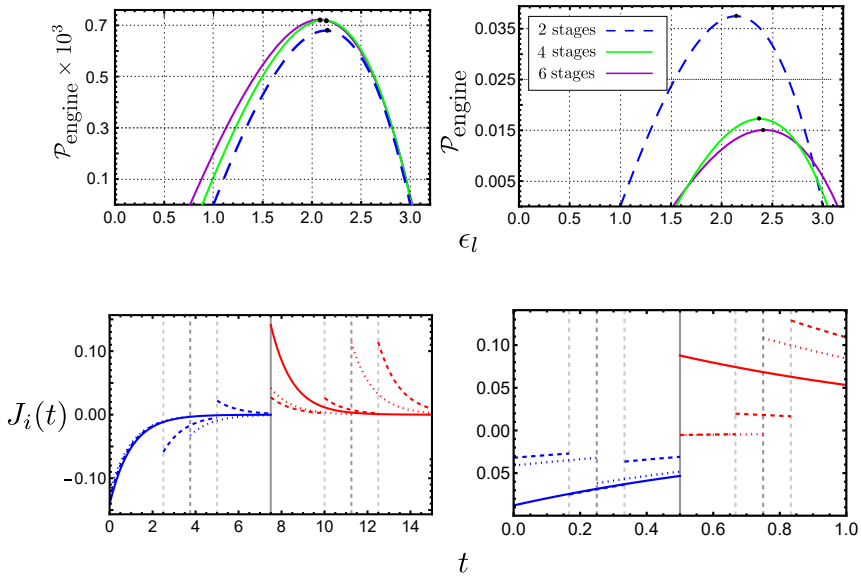

Figure 6.9: For the engine regime operation mode, the comparison between the power outputs $\mathcal{P}$'s (top) in two scales for the two-stage system (blue), four-stage (green) and six-stage (purple) systems in the engine regime vs. ϵ_l. The symbol • corresponds to the maximization of $\mathcal{P}$. The currents for each step $J_i(t)$ are shown at the bottom: the continuous line represents $N = 2$, the dotted line represents $N = 4$, and the dashed line represents $N = 6$. Red and blue colors correspond to the right and left sides of the symmetric $N = 2$ case, where the continuous grid line at the center is exactly at $t = \tau/2$. The dashed grid lines represent each step, with the lighter ones representing the $\tau/6$ steps and darker ones representing the $\tau/4$ divisions. The left side corresponds to $\tau = 15$ and the right side corresponds to $\tau = 1$. Parameters: $\alpha = 0.68$, $\Gamma_0 = 1$, $\epsilon_r = 1$, $\mu_r = 2$ and $\mu_l = 4$.

and the condition for power maximization at ϵ_l^* (with ϵ_r fixed) satisfies $\mathcal{P}^*_{M\mathcal{P}} = (\epsilon_r - \epsilon_l^*)^2 \bar{J}_l'(\epsilon_l^*)$, which highlights a distinct optimization condition compared to the $N = 3$ case.

Figs. 6.10 and 6.11 display a summary of our main results for the engine and pump regimes, respectively. Both $\mathcal{P}$ and η can be optimized through a proper selection of the intermediate parameters ϵ_m^* and μ_m^*. The dotted yellow

and black curves represent distinct optimization paths, corresponding to the power expressions given by Eqs. (6.3.1) and (6.3.3), respectively. The power can also be simultaneously maximized with respect to ϵ_l (or μ_l), which defines a central region at the intersection of these curves. The efficiency heat maps

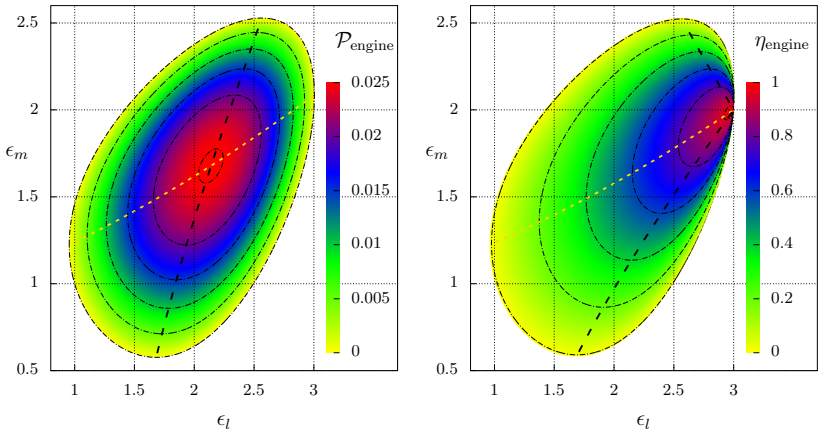

Figure 6.10: For the engine operation mode and $N = 3$, the power and efficiency heat maps for several values of ϵ_l and ϵ_m. Yellow and black dotted lines correspond to the maximization of power (left) and efficiency (right) for fixed ϵ_l while varying ϵ_m, and vice versa, respectively. White zones correspond to the dud regime. Parameters: $\tau = 1$, $\Gamma_0 = 1$, $\epsilon_r = 1$, $\mu_r = 2$, $\mu_m = 3$ and $\mu_l = 4$.

show patterns similar to those of the power-output maps, but the regions of higher efficiency are displaced toward larger values of ϵ_l/μ_l. In contrast to $\mathcal{P}$, the lines of maximum efficiency do not intersect; instead, they converge at the ideal operational limit $\eta \to 1$, consistent with the absence of dissipation $\overline{\dot{S}} = 0$.

We conclude this section by comparing the heat maps from Fig. 6.10 with the opposite configuration, $\mu_r = 4 > \mu_l = 2$ (not shown). Although the overall patterns remain similar, the optimal regions of power and efficiency are shifted toward smaller (ϵ_l, ϵ_m) values, including negative ones. The ideal operating regime occurs at $\epsilon_l = -1$ and $\epsilon_m \approx 0$. In this case, the global maximum power $\mathcal{P}^*_{M\mathcal{P}}$ is approximately half of that obtained in Fig. 6.10.

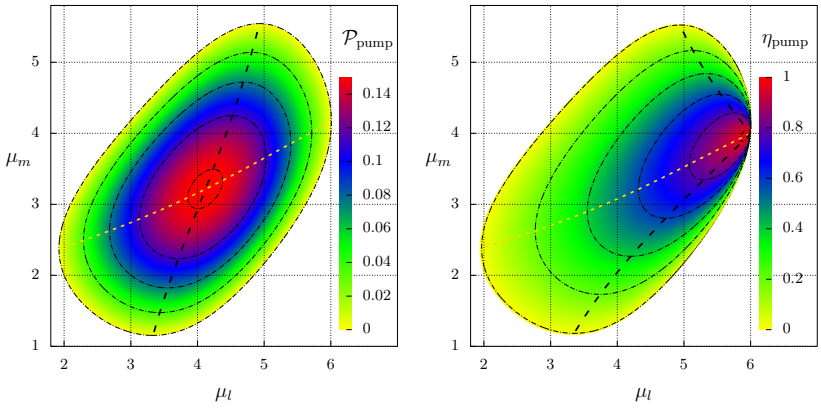

Figure 6.11: For the pump operation mode and $N = 3$, the power and efficiency heat maps for several values of μ_l and μ_m. Yellow and black dotted lines correspond to the maximization of power (left) and efficiency (right) for fixed μ_l while varying μ_m, and vice versa, respectively. White zones correspond to the dud regime. Parameters: $\tau = 1$, $\Gamma_0 = 1$, $\epsilon_r = 1$, $\mu_r = 2$, $\epsilon_m = 3$ and $\epsilon_l = 5$.

Chapter 7

Final Remarks

In this thesis, we introduced and analyzed different models for non-equilibrium heat engines, ranging from single-unit setups to collective engine systems, within the framework of stochastic thermodynamics. For the single-unit case, we focused on the sequential description, which is a suitable way for addressing contact with two different thermal reservoirs and different work sources at each stage (analogous to equilibrium heat engines). In this context, we introduced different external drivings and potentials that could be adjusted in order to optimize the engine output quantities (power and efficiency). For the Brownian case, we explored how different shapes of driving protocols can affect its thermodynamic quantities, obtaining exact expressions for power, dissipation, and efficiency, expressed in a linear form, regardless of the shape of the imposed protocol. We also addressed the resonance phenomenon in the underdamped case and how it can overcome certain trade-off relations in NESS, and introduced the joint probability maximization for power and efficiency, analyzing how to overcome the trade-off limitations and how to derive it from mean values. We also investigated the role of the number of strokes in the collisional approach in order to improve the output of a stochastic pump thermal engine composed of a single quantum dot, showing how the non-trivial interplay between the probability currents, the number of stages, and the chemical

potential of each reservoir affects the engine outputs.

The collective model for heat engines exhibits a richness of phenomena not only compared with heat engines composed of few units but also in terms of phase transitions with no equilibrium or nonequilibrium analogs. In particular, the collective operation of units can be used for improving the power and efficiency, or even giving rise to operations close to maximum power and efficiency, rarely observed in nonequilibrium heat engines. Additionally, the interplay between biased forces and different temperatures shifts the phase transition points with different classifications, constituting a new kind of phase transition, not observed elsewhere. The robustness of such findings also extends to other systems, such as the Potts model and other topologies, including triangular lattices and interactions with energetic frustrations.

Our results show the crucial importance of the synchronization of units to enhance an optimized output of stochastic heat engines. These results also pave the way for new future approaches, such as extension to more network topologies, since the working fluid of an engine regime using the triangular configuration is still under development, and also how other engine approaches, such as the collisional one, can affect the phase transitions and the engine output itself. Therefore, our results also highlight the emergence of phase transitions and new non-equilibrium phenomena without any known analog in the literature.

Bibliography

[1] Sadi Carnot. Réflexions sur la puissance motrice du feu et sur les machines propres à développer cette puissance. In Annales scientifiques de l'École normale supérieure, volume 1, pages 393–457, 1872.

[2] II Novikov. Efficiency of atomic energy installation. At. Energiya, 3:409–412, 1957.

[3] Bjarne Andresen, Peter Salamon, and R Stephen Berry. Thermodynamics in finite time: Extremals for imperfect heat engines. The Journal of Chemical Physics, 66(4):1571–1577, 1977.

[4] Claude E Shannon. A mathematical theory of communication. The Bell system technical journal, 27(3):379–423, 1948.

[5] Leo Szilard. Über die entropieverminderung in einem thermodynamischen system bei eingriffen intelligenter wesen. Zeitschrift für Physik, 53(11):840–856, 1929.

[6] C. Jarzynski. Equilibrium free-energy differences from nonequilibrium measurements: A master-equation approach. Physical Review E, 56(5):5018–5035, November 1997.

[7] Jascha Sohl-Dickstein, Eric Weiss, Niru Maheswaranathan, and Surya Ganguli. Deep unsupervised learning using nonequilibrium thermodynamics. In International conference on machine learning, pages 2256–2265. pmlr, 2015.

[8] Udo Seifert. Stochastic thermodynamics, fluctuation theorems and molecular machines. Reports on progress in physics, 75(12):126001, 2012.

[9] Sergio Ciliberto. Experiments in stochastic thermodynamics: Short history and perspectives. Physical Review X, 7(2):021051, 2017.

[10] Jordan M. Horowitz and Todd R. Gingrich. Thermodynamic uncertainty relations constrain non-equilibrium fluctuations. Nature Physics, 16(1):15–20, 2020.

[11] C. Van den Broeck and M. Esposito. Ensemble and trajectory thermodynamics: A brief introduction. Physica A: Statistical Mechanics and its Applications, 418:6 – 16, 2015.

[12] Parker Smith and Martin Schuster. Public goods and cheating in microbes. Current Biology, 29(11):R442–R447, 2019.

[13] Christopher W Lynn, Eli J Cornblath, Lia Papadopoulos, Maxwell A Bertolero, and Danielle S Bassett. Broken detailed balance and entropy production in the human brain. Proceedings of the National Academy of Sciences, 118(47):e2109889118, 2021.

[14] Riccardo Rao and Massimiliano Esposito. Nonequilibrium thermodynamics of chemical reaction networks: wisdom from stochastic thermodynamics. Physical Review X, 6(4):041064, 2016.

[15] Daniel Maria Busiello, Shiling Liang, Francesco Piazza, and Paolo De Los Rios. Dissipation-driven selection of states in non-equilibrium chemical networks. Communications Chemistry, 4(1):1–7, 2021.

[16] Avinash Vicholous Dass, Thomas Georgelin, Frances Westall, Frédéric Foucher, Paolo De Los Rios, Daniel Maria Busiello, Shiling Liang, and Francesco Piazza. Equilibrium and non-equilibrium furanose selection in the ribose isomerisation network. Nature communications, 12(1):1–10, 2021.

[17] Paolo Bonifazi, Miri Goldin, Michel A Picardo, Isabel Jorquera, A Cattani, Gregory Bianconi, Alfonso Represa, Yehezkel Ben-Ari, and Rosa Cossart.

Gabaergic hub neurons orchestrate synchrony in developing hippocampal networks. Science, 326(5958):1419–1424, 2009.

[18] Elad Schneidman, Michael J Berry, Ronen Segev, and William Bialek. Weak pairwise correlations imply strongly correlated network states in a neural population. Nature, 440(7087):1007–1012, 2006.

[19] György Buzsáki and Kenji Mizuseki. The log-dynamic brain: how skewed distributions affect network operations. Nature Reviews Neuroscience, 15(4):264–278, 2014.

[20] Eyal Gal, Michael London, Amir Globerson, Srikanth Ramaswamy, Michael W Reimann, Eilif Muller, Henry Markram, and Idan Segev. Rich cell-type-specific network topology in neocortical microcircuitry. Nature neuroscience, 20(7):1004–1013, 2017.

[21] Ralf Tönjes, Carlos E Fiore, and Tiago Pereira. Coherence resonance in influencer networks. Nature Communications, 12(1):1–8, 2021.

[22] Victor Mukherjee and Uma Divakaran. Many-body quantum thermal machines. Journal of Physics: Condensed Matter, 33(454001), 2021.

[23] Wolfgang Niedenzu and Gershon Kurizki. Cooperative many-body enhancement of quantum thermal machine power. New Journal of Physics, 20:113038, 2018.

[24] Dmytro Kolisnyk and Gernot Schaller. Performance boost of a collective qutrit refrigerator. Phys. Rev. Appl., 19:034023, Mar 2023.

[25] Latune C., L., Sinayskiy I., and Petruccione F. Collective heat capacity for quantum thermometry and quantum engine enhancements. New Journal of Physics, 22:083049, 2020.

[26] Shunsuke Kamimura, Hideaki Hakoshimam, Yuichiro Matsuzaki, Kyo Yoshida, and Yasuhiro Tokura. Quantum-enhanced heat engine based on superabsorption. Physical Review Letter, 128:180602, 2022.

[27] Hadrien Vroylandt, Massimiliano Esposito, and Gatien Verley. Collective effects enhancing power and efficiency. EPL (Europhysics Letters), 120(3):30009, nov 2017.

[28] Tim Herpich, Juzar Thingna, and Massimiliano Esposito. Collective power: Minimal model for thermodynamics of nonequilibrium phase transitions. Phys. Rev. X, 8:031056, Sep 2018.

[29] Tim Herpich and Massimiliano Esposito. Universality in driven potts models. Phys. Rev. E, 99:022135, Feb 2019.

[30] Michele Campisi and Rosario Fazio. The power of a critical heat engine. Nature communications, 7(1):1–5, 2016.

[31] Marc Suñé and Alberto Imparato. Out-of-equilibrium clock model at the verge of criticality. Physical Review Letters, 123(7):070601, 2019.

[32] Jeremy T Young, Alexey V Gorshkov, Michael Foss-Feig, and Mohammad F Maghrebi. Nonequilibrium fixed points of coupled ising models. Physical Review X, 10(1):011039, 2020.

[33] Julia M Yeomans. Statistical mechanics of phase transitions. Clarendon Press, 1992.

[34] E Kussell and M Vucelja. Non-equilibrium physics and evolution—adaptation, extinction, and ecology: a key issues review. Reports on Progress in Physics, 77(10):102602, oct 2014.

[35] Tânia Tomé and Mário J de Oliveira. Stochastic thermodynamics of ecosystems. Brazilian Journal of Physics, 55(5):236, 2025.

[36] Xiaofang Guo, Da-Jiang Liu, and James W Evans. Schloegl's second model for autocatalysis with particle diffusion: Lattice-gas realization exhibiting generic two-phase coexistence. The Journal of chemical physics, 130(7), 2009.

[37] Ta-you Wu. Lectures on the Kinetic Theory of Gases, Non-equilibrium Thermodynamics and Statistical Theories. National Tsing Hua University Press, 2002.

[38] Shigeyuki Komura. Non-equilibrium soft matter physics, volume 4. World Scientific, 2012.

[39] Tânia Tomé and Mário J de Oliveira. Stochastic approach to equilibrium and nonequilibrium thermodynamics. Physical review E, 91(4):042140, 2015.

[40] Kotaro Ikeda, Tomoya Uda, Daisuke Okanohara, and Sosuke Ito. Speed-accuracy relations for diffusion models: Wisdom from nonequilibrium thermodynamics and optimal transport. Phys. Rev. X, 15:031031, Jul 2025.

[41] Sebastian Goldt and Udo Seifert. Stochastic thermodynamics of learning. Physical review letters, 118(1):010601, 2017.

[42] Silvio Salinas. Introduction to statistical physics. Springer Science & Business Media, 2013.

[43] Herbert B Callen. Thermodynamics and an introduction to thermostatistics, 1998.

[44] Mário J De Oliveira et al. Equilibrium thermodynamics. Springer, 2013.

[45] SR De Groot and P Mazur. North-holland, 1962.

[46] Andre C Barato and Udo Seifert. Thermodynamic uncertainty relation for biomolecular processes. Physical review letters, 114(15):158101, 2015.

[47] C. E. Fernández Noa, Angel L. L. Stable, William G. C. Oropesa, Alexandre Rosas, and C. E. Fiore. Efficient asymmetric collisional brownian particle engines. Phys. Rev. Res., 3:043152, Dec 2021.

[48] Lars Onsager. Reciprocal relations in irreversible processes. i. Physical review, 37(4):405, 1931.

[49] Jean Charles Athanase Peltier. Nouvelles expériences sur la caloricité des courans électriques. 1834.

[50] Sheldon Axler. Linear algebra done right. Springer Nature, 2024.

[51] Alexandre Rosas, Christian Van den Broeck, and Katja Lindenberg. Three-stage stochastic pump: Another type of onsager-casimir symmetry and results far from equilibrium. Phys. Rev. E, 97:062103, Jun 2018.

[52] Karel Proesmans, Bart Cleuren, and Christian Van den Broeck. Power-efficiency-dissipation relations in linear thermodynamics. Physical review letters, 116(22):220601, 2016.

[53] Karel Proesmans and Christian Van den Broeck. Onsager coefficients in periodically driven systems. Physical review letters, 115(9):090601, 2015.

[54] Karel Proesmans, Yannik Dreher, Mom čilo Gavrilov, John Bechhoefer, and Christian Van den Broeck. Brownian duet: A novel tale of thermodynamic efficiency. Phys. Rev. X, 6:041010, Oct 2016.

[55] Karel Proesmans and Carlos E Fiore. General linear thermodynamics for periodically driven systems with multiple reservoirs. Physical Review E, 100(2):022141, 2019.

[56] Henri B Reitlinger and M Armand Duchesne. Sur l'utilisation de la chaleur dans les machines à feu. Vaillant-Carmanne, 1929.

[57] P Chambadal. Les centrales nucleaires (paris: A colin). 1957.

[58] FL Curzon and B Ahlborn. Efficiency of a carnot engine at maximum power output. American Journal of Physics, 43(1):22–24, 1975.

[59] Sang Hoon Lee, Jaegon Um, and Hyunggyu Park. Nonuniversality of heat-engine efficiency at maximum power. Phys. Rev. E, 98:052137, Nov 2018.

[60] Pedro E. Harunari, Fernando S. Filho, Carlos E. Fiore, and Alexandre Rosas. Maximal power for heat engines: Role of asymmetric interaction times. Phys. Rev. Research, 3:023194, Jun 2021.

[61] Tânia Tomé and Mário J De Oliveira. Stochastic dynamics and irreversibility. Springer, 2015.

[62] Martin Josefsson, Artis Svilans, Adam M Burke, Eric A Hoffmann, Sofia Fahlvik, Claes Thelander, Martin Leijnse, and Heiner Linke. A quantum-dot heat engine operating close to the thermodynamic efficiency limits. Nature nanotechnology, 13(10):920–924, 2018.

[63] Waqar Khan, Patrick P Potts, Sebastian Lehmann, Claes Thelander, Kimberly A Dick, Peter Samuelsson, and Ville F Maisi. Efficient and continuous microwave photoconversion in hybrid cavity-semiconductor nanowire double quantum dot diodes. Nature communications, 12(1):5130, 2021.

[64] Evžen Šubrt and Petr Chvosta. Exact analysis of work fluctuations in two-level systems. Journal of Statistical Mechanics: Theory and Experiment, 2007(09):P09019, sep 2007.

[65] Alexandre Rosas, Christian Van den Broeck, and Katja Lindenberg. Stochastic thermodynamics for a periodically driven single-particle pump. Phys. Rev. E, 96:052135, Nov 2017.

[66] Stephen G Brush. History of the lenz-ising model. Reviews of modern physics, 39(4):883, 1967.

[67] Ernst Ising. Beitrag zur theorie des ferromagnetismus. Zeitschrift für Physik, 31(1):253–258, 1925.

[68] Massimiliano Esposito. Stochastic thermodynamics under coarse graining. Physical Review E, 85(4):041125, 2012.

[69] Daniel M Busiello, Jorge Hidalgo, and Amos Maritan. Entropy production for coarse-grained dynamics. New Journal of Physics, 21(7):073004, 2019.

[70] Daniel Maria Busiello and Amos Maritan. Entropy production in master equations and fokker–planck equations: facing the coarse-graining and recovering the information loss. Journal of Statistical Mechanics: Theory and Experiment, 2019(10):104013, 2019.

[71] Ilya Prigogine. Introduction to thermodynamics of irreversible processes. Interscience New York, 1965.

[72] C. Van den Broeck and M. Esposito. Ensemble and trajectory thermodynamics: A brief introduction. Physica A: Statistical Mechanics and its Applications, 418:6–16, 2015. Proceedings of the 13th International Summer School on Fundamental Problems in Statistical Physics.

[73] Daniel T Gillespie. Exact stochastic simulation of coupled chemical reactions. The journal of physical chemistry, 81(25):2340–2361, 1977.

[74] Angel L. L. Stable, C. E. Fernández Noa, William G. C. Oropesa, and C. E. Fiore. Thermodynamics of collisional models for brownian particles: General properties and efficiency. Phys. Rev. Res., 2:043016, Oct 2020.

[75] Udo Seifert. Entropy production along a stochastic trajectory and an integral fluctuation theorem. Phys. Rev. Lett., 95:040602, Jul 2005.

[76] Steffen Liepelt and Reinhard Lipowsky. Kinesin's network of chemomechanical motor cycles. Phys. Rev. Lett., 98:258102, Jun 2007.

[77] S. Liepelt and R. Lipowsky. Operation modes of the molecular motor kinesin. Phys. Rev. E, 79:011917, Jan 2009.

[78] Cesare Berton, Daniel Maria Busiello, Stefano Zamuner, Euro Solari, Rosario Scopelliti, Farzaneh Fadaei-Tirani, Kay Severin, and Cristian Pezzato. Thermodynamics and kinetics of protonated merocyanine photoacids in water. Chemical Science, 11(32):8457–8468, 2020.

[79] Paolo De Los Rios and Alessandro Barducci. Hsp70 chaperones are non-equilibrium machines that achieve ultra-affinity by energy consumption. Elife, 3:e02218, 2014.

[80] Solange Flatt, Daniel Maria Busiello, Stefano Zamuner, and Paolo De Los Rios. Abc transporters are billion-year-old maxwell demons. Communications Physics, 6(1):205, 2023.

[81] Rahil N. Valani. Anomalous transport of a classical wave-particle entity in a tilted potential. Phys. Rev. E, 105:L012101, Jan 2022.

[82] Rahil N. Valani and Bruno S. Dandogbessi. Asymmetric limit cycles within lorenz chaos induce anomalous mobility for a memory-driven active particle. Phys. Rev. E, 110:L052203, Nov 2024.

[83] Paul Langevin et al. Sur la théorie du mouvement brownien. CR Acad. Sci. Paris, 146(530-533):530, 1908.

[84] Angel L. L. Stable, C. E. Fernández Noa, William G. C. Oropesa, and C. E. Fiore. Thermodynamics of collisional models for brownian particles: General properties and efficiency. Phys. Rev. Res., 2:043016, Oct 2020.

[85] Fernando S. Filho, Bruno A. N. Akasaki, Carlos E. F. Noa, Bart Cleuren, and Carlos E. Fiore. Thermodynamics and efficiency of sequentially collisional brownian particles: The role of drivings. Phys. Rev. E, 106:044134, Oct 2022.

[86] Franklin LS Rodrigues, Gabriele De Chiara, Mauro Paternostro, and Gabriel T Landi. Thermodynamics of weakly coherent collisional models. Physical review letters, 123(14):140601, 2019.

[87] Matthias Grimm, Thomas Franosch, and Sylvia Jeney. High-resolution detection of brownian motion for quantitative optical tweezers experiments. Physical Review E—Statistical, Nonlinear, and Soft Matter Physics, 86(2):021912, 2012.

[88] Gary W Slater, Pascal Mayer, and Paul D Grossman. Diffusion, joule heating, and band broadening in capillary gel electrophoresis of dna. Electrophoresis, 16(1):75–83, 1995.

[89] LP Filippov. Methods of simultaneous measurement of heat conductivity, heat capacity and thermal diffusivity of solid and liquid metals at high temperatures. International Journal of Heat and Mass Transfer, 9(7):681–691, 1966.

[90] Iago N. Mamede, Pedro E. Harunari, Bruno A. N. Akasaki, Karel Proesmans, and C. E. Fiore. Obtaining efficient thermal engines from interacting brownian particles under time-periodic drivings. Phys. Rev. E, 105:024106, Feb 2022.

[91] Bruno AN Akasaki, Mário J de Oliveira, and Carlos E Fiore. Entropy production and heat transport in harmonic chains under time-dependent periodic drivings. Physical Review E, 101(1):012132, 2020.

[92] Benjamin J Lopez, Nathan J Kuwada, Erin M Craig, Brian R Long, and Heiner Linke. Realization of a feedback controlled flashing ratchet. Physical Review Letters, 101(22):220601, 2008.

[93] Jacques Prost, Jean-François Chauwin, Luca Peliti, and Armand Ajdari. Asymmetric pumping of particles. Physical Review Letters, 72(16):2652, 1994.

[94] R Dean Astumian and Martin Bier. Fluctuation driven ratchets: molecular motors. Physical review letters, 72(11):1766, 1994.

[95] Jana Tóthová and Vladimír Lisỳ. Overdamped and underdamped langevin equations in the interpretation of experiments and simulations. European Journal of Physics, 43(6):065103, 2022.

[96] Hadiseh Safdari, Andrey G. Cherstvy, Aleksei V. Chechkin, Anna Bodrova, and Ralf Metzler. Aging underdamped scaled brownian motion: Ensemble- and time-averaged particle displacements, nonergodicity, and the failure of the overdamping approximation. Phys. Rev. E, 95:012120, Jan 2017.

[97] M. F. Kepnang Pebeu, R. L. Woulaché, and T. C. Kofane. Brownian motors in variable-shape medium: Overdamped versus underdamped cases. Phys. Rev. E, 98:052107, Nov 2018.

[98] Michael E Fisher and Anatoly B Kolomeisky. The force exerted by a molecular motor. Proceedings of the National Academy of Sciences, 96(12):6597–6602, 1999.

[99] S Leibler. Moving forward noisily. Nature, 370(6489), 1994.

[100] Anna S Bodrova, Aleksei V Chechkin, Andrey G Cherstvy, Hadiseh Safdari, Igor M Sokolov, and Ralf Metzler. Underdamped scaled brownian motion:(non-) existence of the overdamped limit in anomalous diffusion. Scientific reports, 6(1):30520, 2016.

[101] Pierre Nazé, Sebastian Deffner, and Marcus VS Bonança. Optimal finite-time processes in weakly driven overdamped brownian motion. Journal of Physics Communications, 6(8):083001, 2022.

[102] Soumen De Karmakar and Rajaraman Ganesh. Phase transition and emergence of active temperature in an active brownian system in underdamped background. Physical Review E, 101(3):032121, 2020.

[103] Yuhui Luo, Chunhua Zeng, and Baowen Li. A perfect probe: Resonance of underdamped scaled brownian motion. Europhysics Letters, 137(2):21002, 2022.

[104] Patrick Pietzonka and Udo Seifert. Universal trade-off between power, efficiency, and constancy in steady-state heat engines. Physical review letters, 120(19):190602, 2018.

[105] B. Suassuna, B. Melo, and T. Guerreiro. Path integrals and nonlinear optical tweezers. Phys. Rev. A, 103:013110, Jan 2021.

[106] Lucien P Ghislain, Neil A Switz, and Watt W Webb. Measurement of small forces using an optical trap. Review of Scientific Instruments, 65(9):2762–2768, 1994.

[107] TJ Davis. Brownian diffusion of nano-particles in optical traps. Optics express, 15(5):2702–2712, 2007.

[108] Miles J Padgett, Justin Molloy, and David McGloin. Optical Tweezers: methods and applications. CRC press, 2010.

[109] Karel Proesmans and Christian Van den Broeck. The underdamped brownian duet and stochastic linear irreversible thermodynamics. Chaos: An Interdisciplinary Journal of Nonlinear Science, 27(10):104601, 2017.

[110] Karel Proesmans and Christian Van den Broeck. Stochastic efficiency: five case studies. New J. Phys., 17(6):065004, June 2015. Publisher: IOP Publishing.

[111] Karel Proesmans, Yannik Dreher, Momčilo Gavrilov, John Bechhoefer, and Christian Van den Broeck. Brownian duet: a novel tale of thermodynamic efficiency. Physical Review X, 6(4):041010, 2016.

[112] K. Proesmans, B. Cleuren, and C. Van den Broeck. Stochastic efficiency for effusion as a thermal engine. EPL, 109(2):20004, February 2015. Publisher: EDP Sciences, IOP Publishing and SocietÃ Italiana di Fisica.

[113] Gustavo AL Forão, Fernando S Filho, Bruno AN Akasaki, and Carlos E Fiore. Thermodynamics of underdamped brownian collisional engines: General features and resonant phenomena. Physical Review E, 110(5):054125, 2024.

[114] Federico S Gnesotto, Federica Mura, Jannes Gladrow, and Chase P Broedersz. Broken detailed balance and non-equilibrium dynamics in living systems: a review. Reports on Progress in Physics, 81(6):066601, 2018.

[115] Mihai Macovei, A. Performance of the collective three-level quantum thermal engine. Physical Review A, 105:043708, 2022.

[116] F. Y. Wu. The potts model. Rev. Mod. Phys., 54:235–268, Jan 1982.

[117] M. Blume, V. J. Emery, and Robert B. Griffiths. Ising model for the λ transition and phase separation in he^3-he^4 mixtures. Phys. Rev. A, 4:1071–1077, Sep 1971.

[118] William Hoston and A. Nihat Berker. Multicritical phase diagrams of the blume-emery-griffiths model with repulsive biquadratic coupling. Phys. Rev. Lett., 67:1027–1030, Aug 1991.

[119] Alberto Rolandi, Paolo Abiuso, and Martí Perarnau-Llobet. Collective advantages in finite-time thermodynamics. Phys. Rev. Lett., 131:210401, Nov 2023.

[120] Jan Meibohm and Massimiliano Esposito. Minimum-dissipation principle for synchronized stochastic oscillators far from equilibrium. Phys. Rev. E, 110:L042102, Oct 2024.

[121] Fernando S. Filho, Gustavo A. L. Forão, Daniel M. Busiello, B. Cleuren, and Carlos E. Fiore. Powerful ordered collective heat engines. Phys. Rev. Res., 5:043067, Oct 2023.

[122] Shiling Liang, Yu-Han Ma, Daniel Maria Busiello, and Paolo De Los Rios. Minimal model for carnot efficiency at maximum power. Phys. Rev. Lett., 134:027101, Jan 2025.

[123] Bart Cleuren, Bob Rutten, and Christian Van den Broeck. Universality of efficiency at maximum power. The European Physical Journal Special Topics, 224(5):879–889, 2015.

[124] O. Kedem and S. R. Caplan. Degree of coupling and its relation to efficiency of energy conversion. Trans. Faraday Soc., 61:1897–1911, 1965.

[125] Jürgen Schnakenberg. Network theory of microscopic and macroscopic behavior of master equation systems. Reviews of Modern physics, 48(4):571, 1976.

[126] CE Fernández Noa, Pedro E Harunari, MJ de Oliveira, and CE Fiore. Entropy production as a tool for characterizing nonequilibrium phase transitions. Physical Review E, 100(1):012104, 2019.

[127] Leonardo Crochik and Tânia Tomé. Entropy production in the majority-vote model. Physical Review E—Statistical, Nonlinear, and Soft Matter Physics, 72(5):057103, 2005.

[128] Jesus M Encinas, Pedro E Harunari, MM de Oliveira, and Carlos E Fiore. Fundamental ingredients for discontinuous phase transitions in the inertial majority vote model. Scientific reports, 8(1):9338, 2018.

[129] Iago N. Mamede, Karel Proesmans, and Carlos E. Fiore. Thermodynamics of interacting systems: The role of the topology and collective effects. Phys. Rev. Res., 5:043278, Dec 2023.

[130] Miguel Aguilera, Masanao Igarashi, and Hideaki Shimazaki. Nonequilibrium thermodynamics of the asymmetric sherrington-kirkpatrick model. Nature Communications, 14(1):3685, 2023.

[131] Carlos. E. Fiore and M. G. E. da Luz. Exploiting a semi-analytic approach to study first order phase transitions. The Journal of Chemical Physics, 138(1):014105, 2013.

[132] Murty S. S. Challa, D. P. Landau, and K. Binder. Finite-size effects at temperature-driven first-order transitions. Phys. Rev. B, 34:1841–1852, Aug 1986.

[133] Jürgen Schnakenberg. Network theory of microscopic and macroscopic behavior of master equation systems. Reviews of Modern physics, 48(4):571, 1976.

[134] Hugo Touchette. The large deviation approach to statistical mechanics. Physics Reports, 478(1-3):1–69, 2009.

[135] Niraj Kumar, Christian Van den Broeck, Massimiliano Esposito, and Katja Lindenberg. Thermodynamics of a stochastic twin elevator. Physical Review E, 84(5):051134, 2011.

[136] Mário Noboru Tamashiro and SR Salinas. Bethe-peierls approximation for the triangular ising antiferromagnet in a field. Physical Review B, 56(13):8241, 1997.

[137] Hung T Diep et al. Frustrated spin systems. World scientific, 2013.

[138] Gustavo A. L. Forão, Fernando S. Filho, André P. Vieira, Bart Cleuren, Daniel M. Busiello, and Carlos E. Fiore. Splitting of nonequilibrium phase transitions in driven ising models. Phys. Rev. Res., 7:L032049, Sep 2025.

[139] Tânia Tomé. Entropy production in nonequilibrium systems described by a fokker-planck equation. Brazilian journal of physics, 36:1285–1289, 2006.

[140] Petr Chvosta, Viktor Holubec, Artem Ryabov, Mario Einax, and Philipp Maass. Thermodynamics of two-stroke engine based on periodically driven two-level system. Physica E: Low-dimensional Systems and Nanostructures, 42(3):472–476, 2010. Proceedings of the international conference Frontiers of Quantum and Mesoscopic Thermodynamics FQMT '08.

[141] Gatien Verley, Christian Van den Broeck, and Massimiliano Esposito. Modulated two-level system: Exact work statistics. Phys. Rev. E, 88:032137, Sep 2013.

[142] Carlos Ernesto Fernández Noa. Stochastic thermodynamics of collisional thermal machines and phase transition. Doctoral thesis in física, Instituto de Física, University of São Paulo, São Paulo, 2023.

[143] Samuel Herrmann and Damien Landon. Statistics of transitions for markov chains with periodic forcing. Stochastics and Dynamics, 15(04):1550022, 2015.

[144] Pedro E Harunari, Carlos E Fiore, and Karel Proesmans. Exact statistics and thermodynamic uncertainty relations for a periodically driven electron pump. Journal of Physics A: Mathematical and Theoretical, 53(37):374001, aug 2020.

[145] Alexandre Rosas, Christian Van den Broeck, and Katja Lindenberg. Stochastic thermodynamics for a periodically driven single-particle pump. Phys. Rev. E, 96:052135, Nov 2017.

[146] O. Kedem and S. R. Caplan. Degree of coupling and its relation to efficiency of energy conversion. Trans. Faraday Soc., 61:1897–1911, 1965.

[147] Christian Van den Broeck. Thermodynamic efficiency at maximum power. Physical Review Letters, 95(19):190602, 2005.

[148] Pedro E. Harunari, Fernando S. Filho, Carlos E. Fiore, and Alexandre Rosas. Maximal power for heat engines: Role of asymmetric interaction times. Phys. Rev. Res., 3:023194, Jun 2021.

[149] Artur Wachtel, Jürgen Vollmer, and Bernhard Altaner. Fluctuating currents in stochastic thermodynamics. i. gauge invariance of asymptotic statistics. Physical Review E, 92(4):042132, 2015.

[150] Tânia Tomé and Mário J. de Oliveira. Entropy production in nonequilibrium systems at stationary states. Phys. Rev. Lett., 108:020601, Jan 2012.

Appendix A

Appendix

A.1 Onsager coefficients for generic periodically driving

Onsager coeficients for a generic periodic driving in each half stage are listed below:

$$L_{11} = \frac{mT}{\tau(e^{\gamma\tau}-1)} \sum_{n=0}^{\infty}\sum_{m=0}^{\infty} \Big\{ (e^{\gamma\tau}-1) \int_0^{\tau/2} [a_m^{(1)} \cos(\frac{4\pi m}{\tau}t) + b_m^{(1)} \sin(\frac{4\pi m}{\tau}t)][a_n^{(1)} C_n^{(1)}(t) + b_n^{(1)} S_n^{(1)}(t)] \times$$
$$\times e^{-\gamma t} dt + [a_n^{(1)} C_n^{(1)}(\tau/2) + b_n^{(1)} S_n^{(1)}(\tau/2)][a_m^{(1)} \overline{C}_m^{(1)}(\tau/2) + b_m^{(1)} \overline{S}_m^{(1)}(\tau/2)] \Big\}, \tag{A.1.1}$$

$$L_{22} = \frac{mT}{\tau(e^{\gamma\tau}-1)} \sum_{n=0}^{\infty}\sum_{m=0}^{\infty} \Big\{ (e^{\gamma\tau}-1) \int_{\tau/2}^{\tau} [a_m^{(2)} \cos(\frac{4\pi m}{\tau}t) + b_m^{(2)} \sin(\frac{4\pi m}{\tau}t)]\{a_n^{(2)}[C_n^{(1)}(t) - C_n^{(1)}(\tau/2)]$$
$$+ b_n^{(2)}[S_n^{(1)}(t) - S_n^{(1)}(\tau/2)]\} e^{-\gamma t} dt + \{a_n^{(2)}[C_n^{(1)}(\tau) - C_n^{(1)}(\tau/2)] + b_n^{(2)}[S_n^{(1)}(\tau) - S_n^{(1)}(\tau/2)]\} \times$$
$$\times \{a_m^{(2)}[\overline{C}_m^{(1)}(\tau) - \overline{C}_m^{(1)}(\tau/2)] + b_m^{(2)}[\overline{S}_m^{(1)}(\tau) - \overline{S}_m^{(1)}(\tau/2)]\} \Big\} \tag{A.1.2}$$

$$L_{12} = \frac{mT}{\tau(e^{\gamma\tau}-1)} \sum_{n=0}^{\infty}\sum_{m=0}^{\infty} \{a_n^{(2)}[C_n^{(1)}(\tau) - C_n^{(1)}(\tau/2)] + b_n^{(2)}[S_n^{(1)}(\tau) - S_n^{(1)}(\tau/2)]\} \times$$
$$\times [a_m^{(1)}\overline{C}_m^{(1)}(\tau/2) + b_m^{(1)}\overline{S}_m^{(1)}(\tau/2)] \tag{A.1.3}$$

$$L_{21} = \frac{mTe^{\gamma\tau}}{\tau(e^{\gamma\tau}-1)} \sum_{n=0}^{\infty}\sum_{m=0}^{\infty} [a_n^{(1)}C_n^{(1)}(\tau/2) + b_n^{(1)}S_n^{(1)}(\tau/2)]\{a_m^{(2)}[\overline{C}_m^{(1)}(\tau) - \overline{C}_m^{(1)}(\tau/2)] +$$
$$b_m^{(2)}[\overline{S}_m^{(1)}(\tau) - \overline{S}_m^{(1)}(\tau/2)]\}, \tag{A.1.4}$$

where we introduce the following shorthand notation involving quantities $\overline{C}_m^{(i)}(t)$, $C_m^{(i)}(t)$, $\overline{S}_m^{(i)}(t)$ and $S_m^{(i)}(t)$

$$C_n^{(1)}(t) = \int_0^t e^{\gamma t'} \cos(\frac{4\pi n}{\tau}t')dt' \tag{A.1.5}$$
$$\overline{C}_n^{(1)}(t) = \int_0^t e^{-\gamma t'} \cos(\frac{4\pi n}{\tau}t')dt' \tag{A.1.6}$$
$$S_n^{(1)}(t) = \int_0^t e^{\gamma t'} \sin(\frac{4\pi n}{\tau}t')dt' \tag{A.1.7}$$
$$\overline{S}_n^{(1)}(t) = \int_0^t e^{-\gamma t'} \sin(\frac{4\pi n}{\tau}t')dt' \tag{A.1.8}$$
$$\tag{A.1.9}$$

For the particular set of drivings from Eq. (4.1.50),and considering $\omega_j = 2\pi/\tau$, Onsager coefficients reduce to the following expressions:

$$L_{11} = \frac{mT\tau\left[\gamma^3\tau^3 + 4\pi^2\gamma\tau + 16\pi^2\coth\left(\frac{\gamma\tau}{4}\right)\right]}{4\left(\gamma^2\tau^2 + 4\pi^2\right)^2}, \tag{A.1.10}$$

$$L_{22} = \frac{mT\tau\left[\gamma\tau\left(\left(e^{\frac{\gamma\tau}{2}}-1\right)\left(\gamma^2\tau^2+4\pi^2\right) - 4\gamma\tau\left(e^{\frac{\gamma\tau}{2}}+1\right)\sin^2(\phi)\right) + 16\pi^2\left(e^{\frac{\gamma\tau}{2}}+1\right)\cos^2(\phi)\right]}{4\left(e^{\frac{\gamma\tau}{2}}-1\right)\left(\gamma^2\tau^2+4\pi^2\right)^2}, \tag{A.1.11}$$

$$L_{12} = -\frac{2\pi mT\tau\coth\left(\frac{\gamma\tau}{4}\right)\left(\gamma\tau\sin(\phi) + 2\pi\cos(\phi)\right)}{\left(\gamma^2\tau^2+4\pi^2\right)^2}, \tag{A.1.12}$$

and

$$L_{21} = \frac{2\pi m T \tau \coth\left(\frac{\gamma\tau}{4}\right)\left(\gamma\tau \sin(\phi) - 2\pi\cos(\phi)\right)}{\left(\gamma^2\tau^2 + 4\pi^2\right)^2}, \tag{A.1.13}$$

respectively.

A.2 Onsager coefficients for power-law drivings

For generic algebraic (power-law) drivings, Onsager coefficients are listed below:

$$L_{11} = \frac{mT}{\tau}\int_0^{\tau/2}\left[4^\alpha e^{-t}\left(\frac{t}{\tau}\right)^\alpha\left(\frac{(-\tau)^{-\alpha}\left(\Gamma\left(\alpha+1,-\frac{\tau}{2}\right)-\Gamma(\alpha+1)\right)}{e^\tau-1}+(-t)^{-\alpha}\left(\frac{t}{\tau}\right)^\alpha\right.\right.$$
$$\left.\left.\left(\Gamma(\alpha+1,-t)-\alpha\Gamma(\alpha)\right)\right)\right]dt, \tag{A.2.1}$$

$$L_{12} = \frac{mT}{\tau}\int_0^{\tau/2}\left[(-1)^\beta e^{-t}2^{\alpha+\beta-1}(-\tau)^{-\beta}\operatorname{csch}\left(\frac{\tau}{2}\right)\left(\frac{t}{\tau}\right)^\alpha\left(\Gamma\left(\beta+1,-\frac{\tau}{2}\right)-\Gamma(\beta+1)\right)\right]dt, \tag{A.2.2}$$

$$L_{21} = \frac{mT}{\tau}\int_{\tau/2}^{\tau}\left[\frac{2^\alpha(-\tau)^{-\alpha}e^{\tau-t}\left(1-\frac{2t}{\tau}\right)^\beta\left(\Gamma\left(\alpha+1,-\frac{\tau}{2}\right)-\Gamma(\alpha+1)\right)}{e^\tau-1}\right]dt, \tag{A.2.3}$$

and

$$L_{22} = -\frac{mT}{\tau(e^\tau-1)}\int_{\tau/2}^{\tau}\left\{e^{\frac{\tau}{2}-t}\left(1-\frac{2t}{\tau}\right)^\beta\left[\left(\frac{2}{\tau}\right)^\beta\left(\Gamma(\beta+1)-\Gamma\left(\beta+1,-\frac{\tau}{2}\right)\right)+(e^\tau-1)\left(2-\frac{4t}{\tau}\right)^{-\beta}\right.\right.$$
$$\left.\left.\left(\Gamma(\beta+1)-\Gamma\left(\beta+1,\frac{\tau}{2}-t\right)\right)\right]\right\}dt, \tag{A.2.4}$$

respectively, where $\Gamma(x)$ and $\Gamma(x,y)$ denote gamma and incomplete gamma functions, respectively.

A.3 General Fourier coefficients of the mean velocity and General Onsager coefficients

For the underdamped case, Fourier coefficients for the mean velocity, obtained via the solution of the system equations, are listed below:

$$a_{1kv} = \frac{8\,\pi\,k\,\tau\,\left(8\,\pi\,\gamma\,k\,\tau\,a_n + b_n\,\left(\tau^2\,(\gamma^2 - \omega_{\mathsf{D}}^2) - 16\,\pi^2\,k^2\right)\right)}{(\tau^2\,(\gamma - \omega_{\mathsf{D}})^2 + 16\,\pi^2\,k^2)\,(\tau^2\,(\gamma + \omega_{\mathsf{D}})^2 + 16\,\pi^2\,k^2)},$$

$$a_{2kv} = \frac{8\,\pi\,k\,\tau\,\left(8\,\pi\,\gamma\,k\,\tau\,c_n\,+\,d_n\,\left(\tau^2\,(\gamma^2 - \omega_{\mathsf{D}}^2) - 16\,\pi^2\,k^2\right)\right)}{(\tau^2\,(\gamma - \omega_{\mathsf{D}})^2 + 16\,\pi^2 k^2)\,(\tau^2\,(\gamma + \omega_{\mathsf{D}})^2 + 16\,\pi^2\,k^2)},$$

$$b_{1kv} = \frac{8\,\pi\,k\,\tau\,\left(a_n\,\left(\tau^2\,\left(\omega_{\mathsf{D}}^2 - \gamma^2\right) + 16\,\pi^2\,k^2\right) + 8\,\pi\,\gamma\,k\,\tau\,b_n\right)}{(\tau^2\,(\gamma - \omega_{\mathsf{D}})^2 + 16\,\pi^2\,k^2)\,(\tau^2\,(\gamma + \omega_{\mathsf{D}})^2 + 16\,\pi^2\,k^2)},$$

and

$$b_{2kv} = \frac{8\,\pi\,k\,\tau\,\left(c_n\,\left(\tau^2\,\left(\omega_{\mathsf{D}}^i - \gamma^2\right) + 16\,\pi^2\,k^2\right) + 8\,\pi\,\gamma\,k\,\tau\,d_n\right)}{(\tau^2\,(\gamma - \omega_{\mathsf{D}})^2 + 16\,\pi^2\,k^2)\,(\tau^2\,(\gamma + \omega_{\mathsf{D}})^2 + 16\,\pi^2\,k^2)},$$

expressed in terms of Fourier coefficients a_n, b_n, c_n and d_n for $g_1(t)$ and $g_2(t)$, respectively, and $\omega_{\mathsf{D}} = \sqrt{\gamma^2 - 4\,\kappa}$ is the damped oscillation frequency of the system. Onsager coefficients are related to coefficients a_{ikv} and b_{ikv} via the following expressions

$$L_{11} = T\sum_{n=1}^{\infty}\sum_{k=1}^{\infty}\frac{\left(\pi\,k\,a_{1kv}\,a_k - b_{1kv}\,\left(a_0\,\left((-1)^k - 1\right) - \pi\,k\,b_k\right)\right)}{4\,\pi\,k} + (1 - \delta_{n,k})\cdot\left(-\frac{\left((-1)^{k+n} - 1\right)\,\left(k\,a_n\,b_{1kv} - n\,a_{1kv}\,b_n\right)}{2\,\pi\,\left(k^2 - n^2\right)}\right),$$

$$L_{12} = T\sum_{n=1}^{\infty}\sum_{k=1}^{\infty}\frac{\left(\pi\,k a_{2kv}\,a_k - b_{2kv}\,\left(a_0\,\left((-1)^k - 1\right) - \pi\,k\,b_k\right)\right)}{4\,\pi\,k} + (1 - \delta_{n,k})\cdot\left(-\frac{\left((-1)^{k+n} - 1\right)\,\left(k\,a_n\,b_{2kv} - n\,a_{2kv}\,b_n\right)}{2\,\pi\,\left(k^2 - n^2\right)}\right),$$

$$L_{21} = T \sum_{n=1}^{\infty} \sum_{k=1}^{\infty} \frac{1}{4} \left(a_{1kv}\, c_k + \frac{c_0 \, \left((-1)^k - 1\right) \, b_{1kv}}{\pi \, k} + b_{1kv}\, d_k \right) + (1 - \delta_{n,k}) \cdot \left(\frac{\left((-1)^{k+n} - 1\right) \, (k \, b_{1kv}\, c_n - n \, a_{1kv}\, d_n)}{2\,\pi \, (k^2 - n^2)} \right),$$

and

$$L_{22} = T \sum_{n=1}^{\infty} \sum_{k=1}^{\infty} \frac{1}{4} \left(a_{2kv}\, c_k + \frac{c_0 \, \left((-1)^k - 1\right) \, b_{2kv}}{\pi \, k} + b_{2kv}\, d_k \right) + (1 - \delta_{n,k}) \cdot \left(\frac{\left((-1)^{k+n} - 1\right) \, (k \, b_{2kv}\, c_n - n \, a_{2kv}\, d_n)}{2\,\pi \, (k^2 - n^2)} \right).$$

For constant and linear drivings, coefficients a_n, b_n, c_n and d_n's are listed below:

$$a_0 = c_0 = 1, \qquad a_n = c_n = 0, \qquad b_n = -d_n = \frac{-1 + (-1)^n}{\pi n}, \tag{A.3.1}$$

for constant drivings and

$$a_0 = c_0 = \tau/4, \qquad a_n = -c_n = \frac{((-1)^n - 1)\,\tau}{2\pi^2 n^2}, \qquad d_n = -\frac{\tau}{2\pi n}, \tag{A.3.2}$$

and $b_n = (-1)^n d_n$ for linear drivings, respectively. For harmonic drivings, Fourier coefficients read $a_1 = d_1 = 1/2$, $a_n = d_n = 0 \; \forall \; n \neq 1$, $b_1 = c_1 = 0$, $b_n = (1 + (-1^n))n/((n^2 - 1)\pi) = n \cdot c_n \; \forall \; n \neq 1$ and $c_0 = -2/\pi$. By inserting them into expressions for $a_{1kv}, a_{2kv}, b_{1kv}$ and b_{2kv}, Onsager coefficients can be promptly evaluated.

A.4 Model, all-to-all version and phenomenological descriptions for the non-equilibrium Ising model ($\alpha = 1, q = 3$)

As stated in the main text, the dynamics is described by Eq. (3.5.1), with transition rates $\omega^{(\nu)}_{s's}$ which depend on the amount of heat $Q^{(\nu)}_{s's}$ exchanged between the reservoir ν and the system when its configuration changes from $s \equiv \{s_1, \ldots, s_{j-1}, s_j, s_{j+1}, \ldots, s_N\}$ to $s' \equiv \{s_1, \ldots, s_{j-1}, \tilde{s}_j, s_{j+1}, \ldots, s_N\}$ (where $\tilde{s}_j \neq s_j$).

The heat itself depends on the energy difference $E(s') - E(s)$ and on the work $W^{(\nu)}_{s's} = (-1)^{(\nu-1)} d_{s's} F$ performed by the nonconservative force of magnitude F acting on spin s_j during its flip to $\tilde{s}_j$. The factor $d_{s's}$ equals $+1$ (-1) if the flip $s_j \to \tilde{s}_j$ follows clockwise (counterclockwise) the cycle $-1 \to 0 \to +1 \to -1$. Therefore, taking F to be positive, the cold thermal bath ($\nu = 1$) favors clockwise flips, while the hot bath ($\nu = 2$) favors counterclockwise flips. This is illustrated in the figure below.

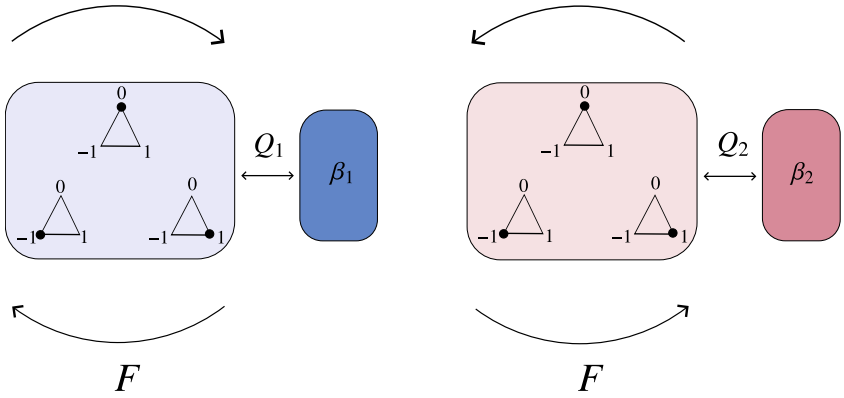

Figure A.1: Schematics of the driving operation for the three-state Ising model in contact with the cold (left) and hot (right) thermal baths. Arrows denote the spin transitions $s_j \to \tilde{s}_j$ favored by the non-conservative driving of strength F.

Next, we begin with the all-to-all version of Eq. (3.3.22), given by

$$E(s) \to E(N_+, N_-) = \frac{\epsilon}{2N} \left\{ N_+(N_+ - 1) + N_-(N_- - 1) - 2N_+N_- \right\} + \Delta \left(N_+ + N_- \right). \tag{A.4.1}$$

The energy differences ΔE_{+-}, ΔE_{+0}, and ΔE_{0-} are defined as

$$\begin{aligned} \Delta E_{+-} &= E_+ - E_- = \frac{2\epsilon}{N} \left(N_+ - N_- + 1 \right), \\ \Delta E_{+0} &= E_+ - E_0 = \frac{\epsilon}{N} \left(N_+ - N_- \right) + \Delta, \\ \Delta E_{0-} &= E_0 - E_- = \frac{\epsilon}{N} \left(N_+ - N_- + 1 \right) - \Delta. \end{aligned} \tag{A.4.2}$$

In the limit $N \to \infty$, where $N_\pm / N \to n_\pm$, transition rates assume the form

$\omega_{ij}^{(\nu)} = \Gamma \exp\left(-\frac{\beta_\nu}{2} Q_{ij}^{(\nu)}\right)$, where the quantities $Q_{ij}^{(\nu)}$ are given by

$$Q_{+-}^{(\nu)} = 2\epsilon(n_+ - n_-) + (-1)^{\nu-1} F, \quad Q_{+0}^{(\nu)} = \epsilon(n_+ - n_-) + \Delta - (-1)^{\nu-1} F, \quad Q_{0-}^{(\nu)} = \epsilon(n_+ - n_-) - \Delta - (-1)^{\nu-1} F \tag{A.4.3}$$

with $Q_{ji}^{(\nu)} = -Q_{ij}^{(\nu)}$ for any (i,j) and ν.

As outlined in the main text, steady-state densities are determined by the master equations

$$\dot{n}_i(t) = \sum_{\nu=1}^{2} \sum_{j \neq i} \left(\omega_{ij}^{(\nu)} n_j(t) - \omega_{ji}^{(\nu)} n_i(t) \right) = \sum_{\nu=1}^{2} \sum_{j \neq i} J_{ij}^{(\nu)}(t), \tag{A.4.4}$$

where $(i,j) \in (0, \pm)$. Since $n_- + n_0 + n_+ = 1$, the steady-state densities and their associated thermodynamic quantities are derived from two coupled transcendental equations.

To explore the thermodynamic behavior of the system in strong collective regimes, we apply a phenomenological description that is valid for $|m| \approx 1$. In this limit, we neglect the density dependence in the transition rates. Approximate steady-state densities are derived using the spanning-tree method [133], following the same approach proposed in [121]. We introduce the following definitions:

$$\gamma_+ = \tilde{\omega}_{+-}\,\tilde{\omega}_{-0} + \tilde{\omega}_{+0}\,\tilde{\omega}_{0-} + \tilde{\omega}_{+0}\,\tilde{\omega}_{+-}\,, \tag{A.4.5}$$

$$\gamma_0 = \tilde{\omega}_{0-}\,\tilde{\omega}_{-+} + \tilde{\omega}_{0+}\,\tilde{\omega}_{+-} + \tilde{\omega}_{0+}\,\tilde{\omega}_{0-}\,, \tag{A.4.6}$$

$$\gamma_- = \tilde{\omega}_{-+}\,\tilde{\omega}_{+0} + \tilde{\omega}_{-0}\,\tilde{\omega}_{0+} + \tilde{\omega}_{-0}\,\tilde{\omega}_{-+}, \tag{A.4.7}$$

where $\tilde{\omega}_{ij} = \omega_{ij}^{(1)} + \omega_{ij}^{(2)}$.

Using $n_- = 1$ and $n_+ = 0$ in the transition rates, the steady-state densities for phase A are

$$n_-^{\mathsf{st(A)}} = \frac{\gamma_-}{\gamma_+ + \gamma_0 + \gamma_-} \approx \frac{1}{e^{\frac{1}{2}((\beta_1+\beta_2)(\Delta+\epsilon)+F(\beta_1-\beta_2))} + e^{\epsilon(\beta_1+\beta_2)+\frac{1}{2}F(\beta_2-\beta_1)} + 1}, \tag{A.4.8}$$

$$n_+^{\mathsf{st(A)}} = \frac{\gamma_+}{\gamma_+ + \gamma_0 + \gamma_-} \approx \frac{1}{e^{\frac{1}{2}(\beta_1+\beta_2)(\Delta-\epsilon)+F(\beta_1-\beta_2)} + e^{\frac{1}{2}F(\beta_1-\beta_2)-\epsilon(\beta_1+\beta_2)} + 1}, \tag{A.4.9}$$

and, as a consequence, we also have:

$$n_0^{\mathsf{st(A)}} = \frac{\gamma_0}{\gamma_+ + \gamma_0 + \gamma_-} \approx 1 - n_+^{\mathsf{st(A)}} - n_-^{\mathsf{st(A)}}. \tag{A.4.10}$$

Similarly, for phase B, using $n_- = 0$ and $n_+ = 1$ in the transition rates, the steady-state densities are

$$n_-^{\mathrm{st(B)}} = \frac{\gamma_-}{\gamma_+ + \gamma_0 + \gamma_-} \approx \frac{1}{e^{\frac{1}{2}(\beta_1+\beta_2)(\Delta-\epsilon)-F(\beta_1-\beta_2)} + e^{\frac{1}{2}F(\beta_2-\beta_1)-(\beta_1+\beta_2)\epsilon} + 1}, \tag{A.4.11}$$

$$n_+^{\mathrm{st(B)}} \approx \frac{\gamma_+}{\gamma_+ + \gamma_0 + \gamma_-} = \frac{1}{e^{\frac{1}{2}((\beta_1+\beta_2)(\Delta+\epsilon)-F(\beta_1-\beta_2))} + e^{(\beta_1+\beta_2)\epsilon+\frac{1}{2}F(\beta_1-\beta_2)} + 1}, \tag{A.4.12}$$

so that:

$$n_0^{\mathrm{st(B)}} = \frac{\gamma_0}{\gamma_+ + \gamma_0 + \gamma_-} \approx 1 - n_+^{\mathrm{st(B)}} - n_-^{\mathrm{st(B)}}. \tag{A.4.13}$$

With these approximate steady-state densities, we can calculate all desired thermodynamic quantities, as shown in the main text. Due to their analytical complexity, we do not list them here.

A.5 Heat maps for q=3 and N=2 engines

This section discusses two important aspects introduced in the main text: the reliability of numerical simulations for finite N and the fact that a minimal setup of $N = 2$ interacting units already captures the essential ingredients of the model. Results are shown for $\beta_1 = 1$ and $\beta_2 = 0.4$ only for the sake of a better visualization. Fig. A.2 compares thermodynamic quantities evaluated from numerical simulations (Gillespie algorithm) and those from exact steady probabilities computed from the microscopic master equation for $N = 2$. Fig. A.3 extends the heat maps to $N = 2$, showing that despite the substantial reduced performance, all characteristics from collective effects are already present in this minimal setup.

A.6 Evaluation of the power variance $\gamma_{\mathcal{P}}$

In this section, we evaluate power fluctuations that are captured by the power variance, $\gamma_{\mathcal{P}}$.

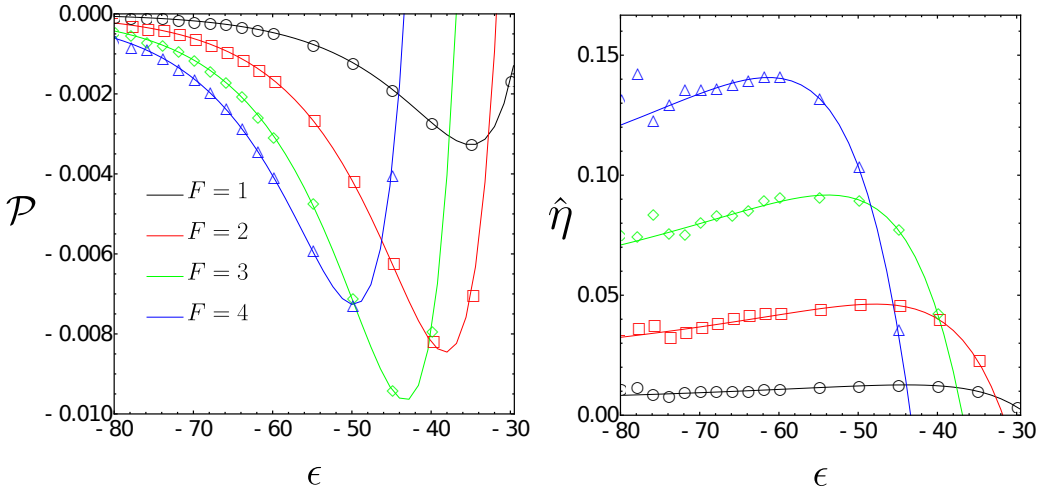

Figure A.2: Model A, $q = 3$. Left and right panels show the power per unit $\mathcal{P} = \langle \mathrm{P} \rangle / N$ and efficiency $\hat{\eta}$ for $N = 2$ for different values of F. Continuous lines are exact solutions obtained from the microscopic master equation, while symbols come from numerical simulations using the Gillespie algorithm. Parameters: $\alpha = 1$, $\beta_1 = 1$, and $\beta_2 = 0.4$.

For the all-to-all topology, the evaluation employs the large deviation method [134, 135]. Let $P(i, \mathcal{P}, t)$ denote the probability of the system being in state i at time t with power $\mathcal{P}$. The time evolution of $P(i, \mathcal{P}, t)$ is governed by the master equation

$$\frac{\partial}{\partial t} P(i, \mathcal{P}, t) = \sum_{\nu=1}^{2} \sum_{j} \left\{ \omega_{ij}^{(\nu)} P(j, \mathcal{P} - \Delta\mathcal{P}, t) - \omega_{ji}^{(\nu)} P(i, \mathcal{P}, t) \right\},$$

where $\omega_{ji}^{(\nu)}$ is the transition rate as defined in Sec. 3.4, and $\Delta\mathcal{P} = \pm F$ for transitions between states j and i, where different signs are associated with clockwise or counterclockwise transitions with the system in contact with the cold and hot thermal baths, respectively (see the main text for modeling details).

The characteristic function of the power is defined as $\rho_p(i, \alpha, t) = \int_{-\infty}^{\infty} d\mathcal{P}\, e^{-\alpha \mathcal{P}} P(i, \mathcal{P}, t)$, whose time evolution is described by

$$\frac{\partial}{\partial t} \rho_p(i, \alpha, t) = \sum_{\nu=1}^{2} \sum_{j} \left\{ \omega_{ij}^{(\nu)} \rho_p(j, \alpha, t) e^{-\alpha \Delta\mathcal{P}} - \omega_{ji}^{(\nu)} \rho_p(i, \alpha, t) \right\}.$$

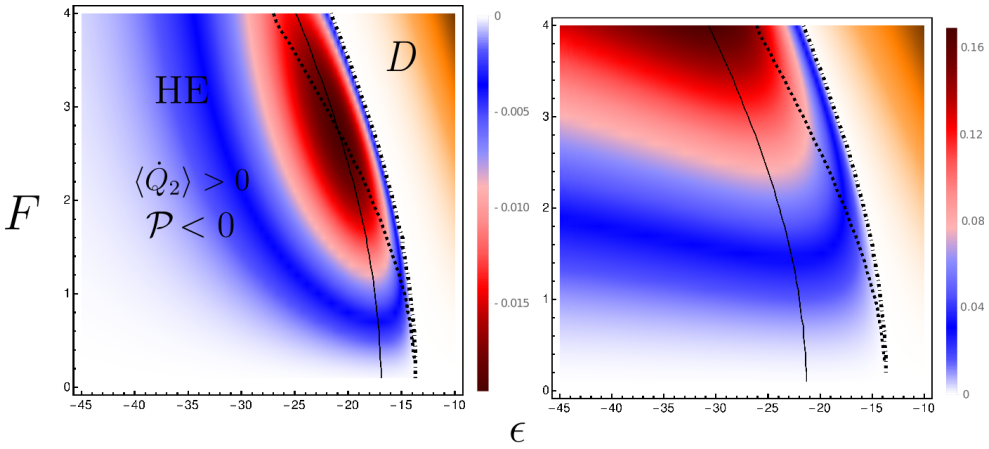

Figure A.3: Model A, $q = 3$ and $N = 2$. From left to right, top panels depict power per unit $\mathcal{P} = \langle \mathrm{P} \rangle / N$ and efficiency $\hat{\eta}$ heat maps. Heat engine and dud regimes are denoted by HE and D, respectively. For a better visualization, the pump regime has not been indicated. Parameters: $\alpha = 1$, $\beta_1 = 1$ and $\beta_2 = 0.4$.

This equation can be rewritten as

$$\frac{\partial \rho_p(i,\alpha,t)}{\partial t} = M_p(\alpha)\rho_p(i,\alpha,t),$$

where $M_p(\alpha)$ is the tilted matrix, explicitly given as

$$M_p(\alpha) = \begin{pmatrix} -(\omega_{0-}^{(1)} + \omega_{+-}^{(1)} + \omega_{0-}^{(2)} + \omega_{+-}^{(2)}) & \omega_{-0}^{(1)} e^{-\alpha F} + \omega_{-0}^{(2)} e^{\alpha F} & \omega_{-+}^{(1)} e^{\alpha F} + \omega_{-+}^{(2)} e^{-\alpha F} \\ \omega_{0-}^{(1)} e^{-\alpha F} + \omega_{0-}^{(2)} e^{\alpha F} & -(\omega_{-0}^{(1)} + \omega_{+0}^{(1)} + \omega_{-0}^{(2)} + \omega_{+0}^{(2)}) & \omega_{0+}^{(1)} e^{-\alpha F} + \omega_{0+}^{(2)} e^{\alpha F} \\ \omega_{+-}^{(1)} e^{-\alpha F} + \omega_{+-}^{(2)} e^{\alpha F} & \omega_{+0}^{(1)} e^{\alpha F} + \omega_{+0}^{(2)} e^{-\alpha F} & -(\omega_{-+}^{(1)} + \omega_{0+}^{(1)} + \omega_{-+}^{(2)} + \omega_{0+}^{(2)}) \end{pmatrix}. \tag{A.6.1}$$

Using the large-deviation method [134, 135], the scaled cumulant generating function is determined by the largest eigenvalue $\lambda_p(\alpha)$ of $M_p(\alpha)$. From $\lambda_p(\alpha)$, the mean $\langle \mathcal{P} \rangle$ and variance $\gamma_{\mathcal{P}}$ are given by

$$\langle \mathcal{P} \rangle = \left. \frac{\partial \lambda_p(\alpha)}{\partial \alpha} \right|_{\alpha=0}, \quad \gamma_{\mathcal{P}} = \left. \frac{\partial^2 \lambda_p(\alpha)}{\partial \alpha^2} \right|_{\alpha=0}.$$

Since the expression for $\lambda_p(\alpha)$ is generally cumbersome, we instead use an alternative approach [149]. In this method, the coefficients of the characteristic

function satisfy the cubic equation

$$a_0 + a_1\lambda_p(\alpha) + a_2\lambda_p^2(\alpha) - \lambda_p^3(\alpha) = 0,$$

allowing $\langle\mathcal{P}\rangle$ and $\gamma_{\mathcal{P}}$ to be evaluated as

$$\langle\mathcal{P}\rangle = -\frac{1}{a_1}\left(\frac{\partial a_0}{\partial\alpha}\right)_{\alpha=0}, \quad \gamma_{\mathcal{P}} = \frac{1}{a_1^3}\left[a_1^2\frac{\partial^2 a_0}{\partial\alpha^2} - 2a_1\frac{\partial a_0}{\partial\alpha}\frac{\partial a_1}{\partial\alpha} + 2a_2\left(\frac{\partial a_0}{\partial\alpha}\right)^2\right]_{\alpha=0}.$$

Exact values of $\langle\mathcal{P}\rangle$ and $\gamma_{\mathcal{P}}$ are obtained by inserting the steady-state probabilities $\{p_i^{\mathrm{st}}\}$ into these derivatives. Approximate expressions for $\gamma_{\mathcal{P}}^{(A)}$ and $\gamma_{\mathcal{P}}^{(B)}$ in the phenomenological description are obtained by assuming $n_- = 1$ ($n_+ = 0$) and $n_- = 0$ ($n_+ = 1$), respectively, in the transition rates.

At ϵ_A, $\gamma_{\mathcal{P}}^{(A)}$ behaves as $\gamma_{\mathcal{P}}^{(A)} \sim (\gamma_{\mathcal{P}})^{(c)} + b_v m + c_v m^2 + \ldots$, where $b_v = 0$, and the expression for c_v is omitted due to its length.

For the square-lattice topology, $\gamma_{\mathcal{P}}$ is computed via Gillespie simulations [73]. For the i-th stochastic trajectory up to time t_{max}, the total power and its square are recorded as $\mathcal{P}_i = \sum_{t=0}^{t_{\mathsf{max}}}\mathcal{P}_{it}$ and $\mathcal{P}_i^2 = \sum_{t=0}^{t_{\mathsf{max}}}\mathcal{P}_{it}^2$. Repeating this process M times (with $M = 10^4$), the averages are calculated as

$$\langle\mathcal{P}\rangle_{t_{\mathsf{max}}} = \frac{1}{M}\sum_{i=1}^{M}\mathcal{P}_i, \quad \langle\mathcal{P}^2\rangle_{t_{\mathsf{max}}} = \frac{1}{M}\sum_{i=1}^{M}\mathcal{P}_i^2.$$

Finally, $\langle\mathcal{P}\rangle = \langle\mathcal{P}\rangle_{t_{\mathsf{max}}}/t_{\mathsf{max}}$ and $\gamma_{\mathcal{P}} = (\langle\mathcal{P}^2\rangle_{t_{\mathsf{max}}} - \langle\mathcal{P}\rangle_{t_{\mathsf{max}}}^2)/t_{\mathsf{max}}$.

Figure 5.14 compares $\gamma_{\mathcal{P}}$ for all-to-all (continuous and dashed lines) and square-lattice topologies (symbols $\times$ for a system size $N = 10^2$). As shown, the estimates agree well.

A.7 Expressions for coefficients in the series expansions of m, $\langle\sigma^{(A)}\rangle$ and $\gamma_{\mathcal{P}}^{(A)}$ in the case $\Delta = 0$

As stated in the main text, the phase transition at ϵ_A for $\Delta = 0$ is continuous. The time evolution of the order parameter near criticality can be described by the expansion

$$\frac{dm}{dt} \approx a(\epsilon - \epsilon_A)m + bm^2 + cm^3 + \ldots,$$

where the coefficient a has been defined in the main text as

$$a = 2e^{\frac{F}{4}(\beta_1-\beta_2)} \cosh\left(\frac{F}{4}(\beta_1-\beta_2)\right)\left(\beta_1 \cosh\left(\frac{\beta_1 F}{2}\right) + \beta_2 \cosh\left(\frac{\beta_2 F}{2}\right)\right),$$

and b is given by

$$b = \sinh\left(\frac{F}{4}(\beta_1-\beta_2)\right) f(\beta_1,\beta_2,F).$$

Here, the function $f(\beta_1,\beta_2,F)$ can be explicitly written as

$$\begin{aligned} f(\beta_1,\beta_2,F) = -\Bigg[& e^{\frac{F}{4}(3\beta_1+\beta_2)}\left(2\cosh\left(\frac{F}{2}(\beta_1-\beta_2)\right)+1\right)^2 \cosh\left(\frac{F}{4}(\beta_1+\beta_2)\right) \\ & \times\Bigg(\left(\beta_1^2 - 4\beta_1\beta_2 + \beta_2^2\right)\cosh\left(\frac{F}{4}(\beta_1-\beta_2)\right) - \beta_1^2 \cosh\left(\frac{F}{4}(3\beta_1+\beta_2)\right) \\ & - \beta_2^2 \cosh\left(\frac{F}{4}(\beta_1+3\beta_2)\right)\Bigg)\Bigg] \\ & \times\left[\left(e^{\frac{\beta_1 F}{2}} + e^{\frac{\beta_2 F}{2}}\right)^2\left(\beta_1 \cosh\left(\frac{\beta_1 F}{2}\right) + \beta_2 \cosh\left(\frac{\beta_2 F}{2}\right)\right)^2\right]^{-1}, \end{aligned} \quad \text{(A.7.1)}$$

and the coefficient c reads

$$
\begin{aligned}
c = \Bigg[& e^{-\frac{1}{4}F(13\beta_1+15\beta_2)}\left(e^{F\beta_1}+e^{F\beta_2}+e^{\frac{1}{2}F(\beta_1+\beta_2)}\right)^2\Bigg(e^{\frac{1}{2}F(\beta_1+5\beta_2)}\beta_1^3+e^{5F\beta_1+2F\beta_2}\beta_1^3+e^{\frac{1}{2}F(7\beta_1+\beta_2)} \\
& \times(\beta_1-5\beta_2)\beta_2\beta_1+e^{\frac{3}{2}F(3\beta_1+\beta_2)}(5\beta_1-\beta_2)\beta_2\beta_1+e^{\frac{7}{2}F(\beta_1+\beta_2)}\left(\beta_1^2-4\beta_2\beta_1-4\beta_2^2\right)\beta_1+ \\
& e^{\frac{1}{2}F(9\beta_1+5\beta_2)}\left(\beta_1^2+\beta_2^2\right)\beta_1+2e^{2F(2\beta_1+\beta_2)}\left(\beta_1^2+\beta_2\beta_1+2\beta_2^2\right)\beta_1+e^{3F\beta_1}\beta_2^3+e^{\frac{1}{2}F(5\beta_1+9\beta_2)}\beta_2^3 \\
& +e^{\frac{3}{2}F(\beta_1+\beta_2)}\beta_2\left(4\beta_1^2+4\beta_2\beta_1-\beta_2^2\right)+e^{\frac{1}{2}F(5\beta_1+\beta_2)}\beta_2\left(\beta_1^2+\beta_2^2\right)+e^{F(4\beta_1+\beta_2)}(\beta_1+\beta_2)\times \\
& \left(\beta_1^2-5\beta_2\beta_1+\beta_2^2\right)+e^{\frac{1}{2}F(3\beta_1+7\beta_2)}(\beta_1+\beta_2)\left(\beta_1^2+\beta_2\beta_1+\beta_2^2\right)+ \\
& +2e^{F(3\beta_1+\beta_2)}\beta_2\left(2\beta_1^2+\beta_2\beta_1+\beta_2^2\right)+e^{\frac{1}{2}F(7\beta_1+3\beta_2)}(\beta_1+\beta_2)\left((\beta_1^2+4\beta_2\beta_1+\beta_2^2\right)+ \\
& e^{2F\beta_1+3F\beta_2}(\beta_1+\beta_2)\left(\beta_1^2+4\beta_2\beta_1+\beta_2^2\right)+e^{3F\beta_1+2F\beta_2}(\beta_1+\beta_2)\left((\beta 1^2+7\beta_2\beta_1+\beta_2^2\right)+ \\
& 3e^{\frac{5}{2}F(\beta_1+\beta_2)}(\beta_1+\beta_2)\left((3\beta_1^2+\beta_2\beta_1+3\beta_2^2\right)+e^{2F(\beta_1+2\beta_2)}\left(\beta_1^3-4\beta_2\beta_1^2+2\beta_2^2\beta_1-3\beta_2^3\right)+ \\
& e^{\frac{1}{2}F(7\beta_1+5\beta_2)}\left((5\beta_1^3+4\beta_2\beta_1^2+6\beta_2^2\beta_1-3\beta_2^3\right)+e^{F(\beta_1+2\beta_2)}\left((2\beta_1^3+\beta_2\beta_1^2-\beta_2^3\right)+ \\
& e^{4F\beta_1+3F\beta_2}\left((2\beta_1^3+2\beta_2\beta_1^2-\beta_2^3\right)+2e^{\frac{1}{2}F(3\beta_1+5\beta_2)}\left((2\beta 1^3+2\beta_2\beta_1^2+\beta_2^2\beta_1-\beta_2^3\right)+e^{F(\beta_1+3\beta_2)}\times \\
& \left((3\beta_1^3-2\beta_2\beta_1^2+4\beta_2^2\beta_1-\beta_2^3\right)+e^{3F\beta_1+4F\beta 2}\left(-\beta_1^3+\beta_2^2\beta_1+2\beta_2^3\right)+e^{F(2\beta_1+\beta_2)}\times \\
& \left((-\beta 1^3+2\beta_2^2\beta_1+2\beta_2^3\right)+e^{\frac{1}{2}F(5\beta_1+7\beta_2)}\left((-2\beta_1^3+2\beta_2\beta_1^2+4\beta_2^2\beta_1+4\beta_2^3\right)+ \\
& e^{2F(\beta_1+\beta_2)}\left((4\beta_1^3+13\beta_2\beta_1^2+7\beta_2^2\beta_1+4\beta_2^3\right)+e^{3F(\beta_1+\beta 2)}\left(4\beta_1^3+7\beta_2\beta_1^2+13\beta_2^2\beta_1+4\beta_2^3\right)+ \\
& e^{\frac{1}{2}F(5\beta_1+3\beta_2)}\left(-3\beta_1^3+6\beta_2\beta_1^2+4\beta_2^2\beta_1+5\beta_2^3\right)\Bigg)\mathrm{sech}^3\left(\frac{1}{4}F(\beta_1-\beta_2)\right)\Bigg]\times \\
& \left[128\Big((\beta_1\cosh\left(\left(\frac{F\beta 1}{2}\right)+\beta_2\cosh\left(\left(\frac{F\beta_2}{2}\right)\right)^3\right]^{-1}. \qquad \text{(A.7.2)}
\end{aligned}
$$

In a similar fashion, the behavior of distinct thermodynamic quantities near the phase transition reinforces the findings in the main text. For instance, the entropy production $\langle\sigma^{(A)}\rangle$ expressed in terms of m near ϵ_A is given by

$$\langle\sigma^{(A)}\rangle \sim \langle\sigma_c\rangle + b_\sigma m + c_\sigma m^2 + \ldots,$$

where

$$\langle\sigma_c\rangle = 2F\left[\beta_1 \sinh\left(\frac{\beta_1 F}{2}\right)+\beta_2\sinh\left(\frac{\beta_2 F}{2}\right)\right], \quad b_\sigma = 0,$$

and c_σ is given by

$$
\begin{aligned}
c_\sigma = -\Big[& e^{-\frac{3}{2}(\beta_1+\beta_2)F}\Big(e^{\frac{1}{2}(\beta_1+\beta_2)F}+1\Big)\Big(e^{\beta_1 F}+e^{\beta_2 F}+e^{\frac{1}{2}(\beta_1+\beta_2)F}\Big)\Big(-\beta_1^3 F e^{\frac{3\beta_2 F}{2}}+\beta_1^3 F e^{\left(\frac{5\beta_1}{2}+\beta_2\right)F}- \\
& \beta_2^3 F e^{\frac{3\beta_1 F}{2}}+\beta_2^3 F e^{\left(\beta_1+\frac{5\beta_2}{2}\right)F}-\Big(\beta_1-\beta_2\Big)e^{\frac{1}{2}\Big(4\beta_1+\beta_2\Big)F}\Big(\beta_2^2 F-\beta_2\Big(\beta_1 F+4\Big)+ \\
& \beta_1\Big(\beta_1 F+4\Big)\Big)+e^{\frac{3\beta_1 F}{2}+2\beta_2 F}\Big(-\Big(\beta_1^2\Big(\beta_1 F+4\Big)\Big)+\beta_2\beta_1\Big(\beta_1 F+6\Big)+2\beta_2^2\Big(\beta_1 F-1\Big)\Big) \\
& +e^{\beta_1 F+\frac{\beta_2 F}{2}}\Big(\beta_1^2\Big(\beta_1 F-4\Big)+\beta_2\beta_1\Big(6-\beta_1 F\Big)-2\beta_2^2\Big(\beta_1 F+1\Big)\Big)-\Big(\beta_1-\beta_2\Big)e^{\left(\beta_1+\frac{3\beta_2}{2}\right)F} \\
& \times\Big(\beta_1^2 F+2\beta_1\Big(\beta_2 F+1\Big)+\beta_2\Big(\beta_2 F-2\Big)\Big)-e^{\frac{\beta_1 F}{2}+\beta_2 F}\Big(2\beta_1^2\Big(\beta_2 F+1\Big)+\beta_2\beta_1\Big(\beta_2 F-6\Big) \\
& +\beta_2^2\Big(4-\beta_2 F\Big)\Big)+\Big(\beta_1-\beta_2\Big)e^{\left(\frac{3\beta_1}{2}+\beta_2\right)F}\Big(\beta_1^2 F+2\beta_1\Big(\beta_2 F-1\Big)+\beta_2\Big(\beta_2 F+2\Big)\Big)+ \\
& \Big(\beta_1-\beta_2\Big)e^{\frac{1}{2}\left(\beta_1+4\beta_2\right)F}\Big(\beta_1^2 F-\beta_1\Big(\beta_2 F+4\Big)+\beta_2\Big(\beta_2 F+4\Big)\Big)+ \\
& e^{2\beta_1 F+\frac{3\beta_2 F}{2}}\Big(2\beta_1^2\Big(\beta_2 F-1\Big)+\beta_2\beta_1\Big(\beta_2 F+6\Big)-\beta_2^2\Big(\beta_2 F+4\Big)\Big)\Big)\Big] \\
& \times\Big[4\Big(e^{\frac{\beta_1 F}{2}}+e^{\frac{\beta_2 F}{2}}\Big)^2\Big(\beta_1\cosh\Big(\frac{\beta_1 F}{2}\Big)+\beta_2\cosh\Big(\frac{\beta_2 F}{2}\Big)\Big)^2\Big]^{-1}. \qquad \text{(A.7.3)}
\end{aligned}
$$

From the scaling behavior $m \sim (\epsilon_A - \epsilon)$, it follows that $\langle \sigma^{(A)} \rangle - \langle \sigma_c \rangle \sim (\epsilon_A - \epsilon)^2$, where $\delta = 2\beta = 2$. This result differs from $\delta = 1$, which is typically observed in standard order-disorder phase transitions [126, 150].

The evaluation of $\langle \dot{Q}_i^{(A)} \rangle$ near ϵ_A can be carried out analogously to $\langle \sigma \rangle$. Specifically, these fluxes behave as $\langle \dot{Q}_i^{(A)} \rangle \sim \langle \dot{Q}_i^{(c)} \rangle + b_{q_i} m + c_{q_i} m^2 + \ldots$, where $\langle \dot{Q}_i^{(c)} \rangle = -2F \sinh(\beta_i F/2)$, $b_{q_i} = 0$, $c_{q1} = d_{q1}/d$ and $c_{q2} = d_{q2}/d$, with

$$
\begin{aligned}
d_{q1} = -\Big[& e^{-F(\frac{3\beta_1}{2}+\beta_2)}(e^{\frac{1}{2}F(\beta_1+\beta_2)}+1)(e^{\frac{1}{2}F(\beta_1+\beta_2)}+e^{\beta_1 F}+e^{\beta_2 F})(\beta_1^2 F e^{\beta_2 F}-\beta_1^2 F e^{\frac{1}{2}F(5\beta_1+\beta_2)}+ \\
& 2e^{\frac{1}{2}F(\beta_1+\beta_2)}(\beta_1-2\beta_2+\beta_1\beta_2 F)+e^{2\beta_1 F}(\beta_1(\beta_1 F+4)-2\beta_2(\beta_1 F+2))+ \\
& e^{\frac{3}{2}F(\beta_1+\beta_2)}(\beta_1(\beta_1 F+4)-\beta_2(\beta_1 F+2))-2e^{F(2\beta_1+\beta_2)}(2\beta_2+\beta_1(\beta_2 F-1))+ \\
& e^{\frac{1}{2}F(\beta_1+3\beta_2)}(\beta_1(\beta_1(-F)+2\beta_2 F+4)-4\beta_2)+e^{\beta_1 F}(\beta_1(F(\beta_2-\beta_1)+4)-2\beta_2)- \\
& e^{\frac{1}{2}F(3\beta_1+\beta_2)}(2\beta_2+\beta_1(F(\beta_1+\beta_2)-2))+e^{F(\beta_1+\beta_2)}(\beta_1(F(\beta_1+\beta_2)+2)-2\beta_2))\Big],
\end{aligned}
\qquad \text{(A.7.4)}
$$

$$
\begin{aligned}
d_{q2} =& e^{-F(\beta_1+\frac{3\beta_2}{2})}(e^{\frac{1}{2}F(\beta_1+\beta_2)}+1)(e^{\frac{1}{2}F(\beta_1+\beta_2)}+e^{\beta_1 F}+e^{\beta_2 F})(\beta_2^2 F\left(-e^{\beta_1 F}\right)+\beta_2^2 F e^{\frac{1}{2}F(\beta_1+5\beta_2)}+\\
& e^{\frac{1}{2}F(3\beta_1+\beta_2)}(\beta_1(4-2\beta_2 F)+\beta_2(\beta_2 F-4))+e^{\beta_2 F}(\beta_1(2-\beta_2 F)+\beta_2(\beta_2 F-4))-\\
& 2e^{\frac{1}{2}F(\beta_1+\beta_2)}(\beta_2+\beta_1(\beta_2 F-2))+2e^{F(\beta_1+2\beta_2)}(\beta_1(\beta_2 F+2)-\beta_2)+e^{\frac{1}{2}F(\beta_1+3\beta_2)}(\beta_1(\beta_2 F+2)+\\
& \beta_2(\beta_2 F-2))-e^{F(\beta_1+\beta_2)}(\beta_1(\beta_2 F-2)+\beta_2(\beta_2 F+2))+e^{\frac{3}{2}F(\beta_1+\beta_2)}(\beta_1(\beta_2 F+2)-\beta_2(\beta_2 F+4))\\
& e^{2\beta_2 F}(2\beta_1(\beta_2 F+2)-\beta_2(\beta_2 F+4))), \qquad \text{(A.7.5)}
\end{aligned}
$$

and

$$
d = 4\left(e^{\frac{\beta_1 F}{2}}+e^{\frac{\beta_2 F}{2}}\right)^2\left(\beta_1\cosh\left(\frac{\beta_1 F}{2}\right)+\beta_2\cosh\left(\frac{\beta_2 F}{2}\right)\right)^2.
$$

As a consequence, the power $\langle \mathcal{P}^{(A)}\rangle = -\langle \dot{Q}_1^{(A)}\rangle - \langle \dot{Q}_2^{(A)}\rangle$ and the efficiency $\eta^{(A)} = 1+\langle \dot{Q}_1^{(A)}\rangle/\langle \dot{Q}_2^{(A)}\rangle$ exhibit the same scaling behavior. We also note that the coefficient c_σ is related to c_{q1} and c_{q2} through the relation $c_\sigma = -\beta_1 c_{q1} - \beta_2 c_{q2}$.

Conversely, the bistability observed at ϵ_B is also reflected in all thermodynamic quantities. However, the linear analysis is unsuitable in this case. Instead, numerical solutions of the full master equations for m and q can be substituted into the expressions for thermodynamic quantities, as illustrated in Fig. (5.14) in the main text.

Front page of the papers

Here, we present the first page of each published paper.

Thermodynamics and efficiency of sequentially collisional Brownian particles: The role of drivings

Fernando S. Filho,[1] Bruno A. N. Akasaki,[1] Carlos E. F. Noa,[1] Bart Cleuren,[2] and Carlos E. Fiore[1]
[1]*Universidade de São Paulo, Instituto de Física, Rua do Matão, 1371, 05508-090 São Paulo, SP, Brasil*
[2]*UHasselt, Faculty of Sciences, Theory Lab, Agoralaan, 3590 Diepenbeek, Belgium*

(Received 13 June 2022; accepted 30 September 2022; published 24 October 2022)

Brownian particles placed sequentially in contact with distinct thermal reservoirs and subjected to external driving forces are promising candidates for the construction of reliable engine setups. In this contribution, we address the role of driving forces for enhancing the collisional machine performance. Analytical expressions for thermodynamic quantities such as power output and efficiency are obtained for general driving schemes. A proper choice of these driving schemes substantially increases both power output and efficiency and extends the working regime. Maximizations of power and efficiency, whether with respect to the strength of the force, driving scheme, or both have been considered and exemplified for two kind of drivings: generic power-law and harmonic (sinusoidal) drivings.

DOI: 10.1103/PhysRevE.106.044134

I. INTRODUCTION

The construction of nanoscale engines has received a great deal of attention and recent technological breakthroughs have made feasible not only the realization of distinct setups composed of quantum dots [1], colloidal particles [2–5], single and coupled systems [6–8] but also coarse-grained approaches for systems presenting different degrees of freedom [9,10]. In contrast with their macroscopic counterparts, their main features are strongly influenced by fluctuations when operating at the nanoscale, having several features described within the framework of stochastic thermodynamics [11–16].

Recently a novel approach, coined collisional, has been put forward as a candidate for the realization of reliable thermal engines [17,18] and novel engine setups [19–21]. They consist of sequentially placing the system (a Brownian particle) in contact with distinct thermal reservoirs and subjected to external driving forces during each stage (stroke) of the cycle. Each stage is characterized by the temperature of the connected thermal reservoir and the external driving force. The time needed to switch between the thermal baths at the end of each stage is neglected. Despite its reliability in distinct situations, such as systems interacting only with a small fraction of the environment and those presenting distinct drivings over each member of the system [22–25], the engine can operate rather inefficiently depending on the way it is projected (temperatures, kind of driving, and duration of each stroke). Hence the importance for strategies to enhance its performance [20,21]. Among the distinct approaches, we cite those based on the maximization of power [1,6,14,26–33], efficiency [20,34,35], low or finite dissipation [36,37] and even the assumption of maximization via the largest dissipation [38].

This paper deals with the above points but it focuses on a different direction, namely, the optimization of the engine performance by fine-tuning the driving at each stroke. Such an idea is illustrated in a collisional Brownian machine, which has been considered as a working substance in several works, both from the theoretical [7,39–43] and experimental points of view [3,35,44–46]. The collisional description allows us to derive general (and exact) expressions for thermodynamic quantities, such as output power and efficiency, irrespective of the kind of driving [20]. To exploit the consequences of a distinct driving each stroke and possible optimizations, two representative examples will be considered: generic harmonic and power-law drivings. The former consists of a simpler and feasible way to drive Brownian particles out of equilibrium [35,45,47–49] and providing simultaneous maximizations of the engine [7]. Since the engine performance is substantially reduced for linear drivings when compared with constant ones [19,20], generic power-law drivings have been considered not only for generalizing the machine performance beyond constant and linear drivings but also to exploit the possibility of obtaining a gain by changing its form at each stroke.

This paper is organized as follows: Section II presents the model and the main expressions for the thermodynamic quantities. Efficiency and optimization is discussed in detail for both classes of drivings in Sec. III. Conclusions and perspectives are addressed in Sec. IV.

II. THERMODYNAMICS AND MAIN EXPRESSIONS

We focus on the simplest projection of an engine composed of only two strokes and returning to the initial step after one cycle. The time it takes to complete one cycle is set to τ, with each stroke $\in\{1,2\}$ lasting a time $\tau/2$. During stroke i the Brownian particle of mass m is in contact with a thermal bath at temperature T_i and described by the Langevin equation.[1]

$$\frac{dv_i(t)}{dt} = -\gamma_i v_i(t) + \tilde{f}_i(t) + \zeta_i(t), \tag{1}$$

[1]Eq. (1) is formally identical to description of the overdamped harmonic oscillator subject to the harmonic force $\tilde{f}_h = -\tilde{k}x$ just by replacing $x \to v$, $\tilde{k}/\alpha \to \gamma_i$, $1/\alpha \to \gamma_i/m$.

Thermodynamics of underdamped Brownian collisional engines: General features and resonant phenomena

Gustavo A. L. Forão,[1] Fernando S. Filho,[1,2] Bruno A. N. Akasaki,[1] and Carlos E. Fiore[1]
[1]*Universidade de São Paulo, Instituto de Física, Rua do Matão, 1371, 05508-090 São Paulo, SP, Brazil*
[2]*UHasselt, Faculty of Sciences, Theory Lab, Agoralaan, 3590 Diepenbeek, Belgium*

(Received 5 July 2024; revised 17 September 2024; accepted 11 October 2024; published 20 November 2024)

Collisional Brownian engines have been proposed as alternatives to nonequilibrium nanoscale engines. However, most studies have focused on the simpler overdamped case, leaving the role of inertia much less explored. In this work, we introduce the idea of collisional engines to underdamped Brownian particles, where at each stage the particle is sequentially subjected to a distinct driving force. A careful comparison between the performance of underdamped and overdamped Brownian work-to-work engines has been undertaken. The results show that underdamped Brownian engines generally outperform their overdamped counterparts. A key difference is the presence of a resonant regime in underdamped engines, in which both efficiency and power output are enhanced across a broad set of parameters. Our study highlights the importance of carefully selecting dynamics and driving protocols to achieve optimal engine performance.

DOI: 10.1103/PhysRevE.110.054125

I. INTRODUCTION

The performance of engines and the search for protocol optimizations constitute fundamental issues in thermodynamics since the seminal work by Carnot [1,2] in 1872. Notwithstanding, the construction of different and reliable engine setups aimed at converting one kind of energy into another one has become more sophisticated, above all with the advent of nanotechnology and new experimental procedures for investigating and creating nanoscale engines. Contrasting with macroscopic engines, fluctuations in nanoscale systems can become important, making necessary the use of stochastic methods in order to describe their dynamics and thermodynamic properties, as well as its relationship with the system performance. Stochastic thermodynamics (ST) constitutes a unified tool for describing nanoscale systems operating far from equilibrium [3–6] and addressing the role of fluctuations and dissipation.

Recently, a collisional (or sequential) description has been proposed and extended for Brownian systems [7–10]. In its simplest version, a single particle interacts sequentially with a thermal bath and is subjected to a specific work source at each stage. This approach differs from the situation where the system interacts with all thermal baths simultaneously [11,12] and has been studied in distinct cases of nonequilibrium thermodynamics [13,14], open quantum systems [14–17], and information and computational processing [14,18–20]. Under suitable conditions, the sequential interaction operates as a heat engine or work-to-work converters, generating useful power. Despite this, its performance can be small or strongly reduced depending on the way it is designed, suggesting the choice of ingredients such as period, the duration of each stage, temperatures, the strength of driving worksources, and others as fundamental [7–9,13,21].

For describing the motion of particles in a colloidal environment subjected to random forces, a fundamental framework is the Langevin equation or Fokker-Planck approach [22,23]. Its two employed variants, namely the underdamped and overdamped cases, capture distinct and essential aspects of particle dynamics and stochasticity. The underdamped variant emphasizes inertia and retains the correlation between particle and position, while the overdamped variant simplifies the description and is suitable for systems with rapid relaxation. Despite the extensive research about them [24–31], little is known about their thermodynamic implications and the influence of inertial considerations on system performance and dissipation [11,12].

In this paper, we advance upon previous works [7–10] by introducing and extending the concept of collisional Brownian engines to underdamped systems. For equal temperatures at each stage, we obtain exact expressions for Thermodynamic quantities such as work, heat, and dissipation, solely expressed in terms of Onsager coefficients, irrespective of the driving protocol. For distinct driving worksources, we provide a comparative study between underdamped and overdamped dynamics. The underdamped case is significantly different [7–10] due to the presence of a resonance phenomenon, resulting in a specific region on the phase space in which the engine operates at maximum power and maximum efficiency. The present study sheds light on the importance of dynamics and driving protocols for achieving optimal engine performances.

This paper is structured as follows: In Sec. I, we introduce the model, present the main expressions for the underdamped system, and discuss the optimization approaches. In Sec. II, we compare the performance and dissipation of engines governed by each dynamic and highlight the resonant phenomena in the underdamped engine. Finally, conclusions are drawn in Sec. III.

Statistics of power and efficiency for collisional Brownian engines

Gustavo A. L. Forão [1], Fernando S. Filho [1,2] and Pedro V. Paraguassú [3]
[1] *Universidade de São Paulo, Instituto de Física, Rua do Matão, 1371, 05508-090 São Paulo, SP, Brazil*
[2] *UHasselt, Faculty of Sciences, Theory Lab, Agoralaan, 3590 Diepenbeek, Belgium*
[3] *Departamento de Física, Pontifícia Universidade Católica 22452-970, Rio de Janeiro, Brazil*

(Received 11 April 2025; accepted 16 July 2025; published 6 August 2025)

Collisional Brownian engines have attracted significant attention due to their simplicity, experimental accessibility, and amenability to exact analytical solutions. While previous research has predominantly focused on optimizing mean values of power and efficiency, the joint statistical properties of these performance metrics remain largely unexplored. Using stochastic thermodynamics, we investigate the joint probability distributions of power and efficiency for collisional Brownian engines, revealing how thermodynamic fluctuations influence the probability of observing values exceeding their respective mean maxima. Our conditional probability analysis demonstrates that when power fluctuates above its maximum mean value, the probability of achieving high efficiency increases substantially, suggesting fluctuation regimes where the classical power-efficiency trade-off can be probabilistically overcome. Notably, our framework extends to a broader class of engines, as the essential features of the statistics of the system are fully determined by the Onsager coefficients. Our results contribute to a deeper understanding of the role of fluctuations in Brownian engines, highlighting how stochastic behavior can enable performance beyond traditional thermodynamic bounds.

DOI: 10.1103/n6bd-jv9j

I. INTRODUCTION

In recent decades, the construction and characterization of nonequilibrium small engines have been broadly studied in the realm of stochastic thermodynamics [1–3]. On such scale, the fluctuations are unavoidable and play an important role in the system [3–5]. Among the relevant small-scale frameworks that deal with fluctuations within the realm of stochastic methods, we highlight molecular motors and rotors in cellular environments [6–12], single active and inactive Brownian particles in thermal environment [13–28], quantum-dot pumps in open systems [29–33], nonequilibrium chemical reactions [34–37], and others. Typically, such examples involve a nonequilibrium steady state (NESS) arising from either constant or periodic external forces, or from a sequential setup where the system interacts with an uncorrelated thermal bath and a specific worksource at each stage. In the collisional approach, the system is modeled by assuming that the particle interacts sequentially with different, uncorrelated portions of the medium. In any given interval, it collides with one small fraction before moving on to another. Due to its simplicity and robustness, this approach has been applied across various scenarios and shown to be a viable alternative for efficient thermal engines with engineered reservoirs, including Brownian particle systems operating as work-to-work converters [21,22], quantum dot pumps functioning as heat engines [30–33], or even minimal interacting systems [38]. In particular, the collisional approach has also been widely used in open quantum systems [33,39] and to study memory degradation in quantum and classical systems [40].

A key difference between equilibrium and nonequilibrium statistical mechanics is that the latter allows for obtaining statistical distributions of quantities such as heat flux, power, and entropy production rather than just their average values. This reveals additional features, such as the existence of forbidden values, including negative entropy production or efficiencies greater than Carnot [41–45], which, although rare, can still occur. It also opens the possibility of measuring values greater than the optimized mean quantities for power and efficiency. While this approach has been applied in a variety of classical [13,46–52] and quantum systems [53–57], there are still open questions about measuring of rare events in collisional frameworks and such a scenario is far from being fully understood.

In this contribution, we address this gap by studying rare event statistics in a well-known collisional work-to-work converter, where a single Brownian particle is placed sequentially with two thermal reservoir with different time-dependent external drives [21,22,58]. While related studies have examined efficiency distributions [45,48], our work focuses on collisional Brownian systems and investigates regimes in which power and efficiency surpass their mean-optimal values, along with a detailed analysis of their joint and conditional distributions. In doing so, we extend the scope of previous investigations [13,45–57] by examining the full probability landscape of performance, including both marginal and joint distributions of power and efficiency. This enables a deeper investigation into their statistical behavior and the chances of specific events, allowing us to ask questions such as: What is the probability of the efficiency falling within a certain range, given that the power already meets a specific value? Furthermore, we examine the full distribution of these quantities, both conditionally and unconditionally, to understand how they influence one another. This analysis sheds light on the rare but significant occurrences of forbidden events and explores the possibility of measuring values greater than the optimized mean quantities of power and efficiency. Overall,

Powerful ordered collective heat engines

Fernando S. Filho [1], Gustavo A. L. Forão [1], Daniel M. Busiello [2,*], B. Cleuren [3] and Carlos E. Fiore [1]

[1] *Universidade de São Paulo, Instituto de Física, Rua do Matão, 1371, 05508-090 São Paulo, SP, Brazil*

[2] *Max Planck Institute for the Physics of Complex Systems, 01187 Dresden, Germany*

[3] *UHasselt, Faculty of Sciences, Theory Lab, Agoralaan, 3590 Diepenbeek, Belgium*

(Received 6 February 2023; accepted 26 September 2023; published 20 October 2023)

We introduce a class of stochastic engines in which the regime of units operating synchronously can boost the performance. Our approach encompasses a minimal setup composed of N interacting units placed in contact with two thermal baths and subjected to a constant driving worksource. The interplay between unit synchronization and interaction leads to an efficiency at maximum power between the Carnot η_c and the Curzon-Ahlborn bound η_{CA}. Moreover, these limits can be respectively saturated maximizing the efficiency, and by simultaneous optimization of power and efficiency. We show that the interplay between Ising-like interactions and a collective ordered regime is crucial to operate as a heat engine. The main system features are investigated by means of a linear analysis near equilibrium, and developing an effective discrete-state model that captures the effects of the synchronous phase. The robustness of our findings extends beyond the all-to-all interactions and paves the way for the building of promising nonequilibrium thermal machines based on ordered structures.

DOI: 10.1103/PhysRevResearch.5.043067

I. INTRODUCTION

The ambition to build efficient engines is not only prominent, but also pressing in thermodynamics since the pioneering work by Sadi Carnot [1], and gained new momentum with the development of nonequilibrium thermodynamics of small-scale systems [2,3]. Unlike thermodynamics, fluctuations become fundamental at the nanoscale and the study of their role attracted large attention, both theoretically [4–7] and experimentally [8–10]. As irreversibility is unavoidable, the search for new strategies in the realm of nonequilibrium stochastic thermodynamics is crucial and strongly desirable. Bearing this in mind, several distinct approaches have been proposed. Among them, we highlight the study of the maximum attainable power [11–19] and efficiency [16,20], the modulation of the system-bath interaction time [21,22], and the dynamical control via shortcuts to adiabaticy [23–25] or isothermality [26].

The above examples deal with engines composed of a single or a few units. However, nature is plenty of complex systems composed of many interacting entities, in which cooperative effects often play a crucial role. Examples span multiple biological scales [27], from microbes [28] to the human brain [29], and have been studied in a broad range of research fields, from nonequilibrium effects in chemical processes [30–33] to synchronization in biological networks [34–38]. This vast spectrum of applications highlights that the demand for implementable and robust optimal strategies to engineer collective engines is important and timely. Although the interplay between collective effects and system's performances has been extensively studied in quantum systems [39–44], the development of classical setups built from interacting units is comparatively much less known and still remains at a primary stage [19,45–49].

We introduce a general class of collective engines, inspired by ferromagnetic equilibrium models [50–53]. They have a longstanding importance in the context of collective effects and are at the heart of numerous theoretical and experimental advances, having distinct models (e.g., the Ising, Potts, XY, and Heisenberg) as ideal platforms for describing ferromagnetism. Optimizing power and efficiency by changing driving and coupling parameters, we show that synchronized operations under ordered (ferromagnetic) arrangements play a central role in improving system performances. The main features and optimization routes of the engine proposed here can be unveiled both using a linear analysis close to equilibrium and an effective discrete-state model capturing all relevant effects. Finally, we highlight that our results are robust beyond the case of all-to-all interactions and pave the way for the building of promising nonequilibrium thermal machines based on ordered structures.

II. GENERAL MODEL AND THERMODYNAMICS

Since our goal is to investigate main features and advantages of the cooperative behavior emerging from ordered agents, we design a system composed of N all-to-all interacting units. Each unit can occupy q different states, so that a microstate i of the system is an N-dimensional vector containing the states of all units. This system is placed in contact with two baths at different temperatures ($\nu = 1$ is the cold one, $\nu = 2$ the hot) to work as a heat engine. Moreover,

*Corresponding author: busiello@pks.mpg.de

Letter

Splitting of nonequilibrium phase transitions in driven Ising models

Gustavo A. L. Forão,[1] Fernando S. Filho,[1,2] André P. Vieira,[1] Bart Cleuren,[2] Daniel M. Busiello,[3,4] and Carlos E. Fiore[1,*]

[1]Universidade de São Paulo, Instituto de Física, Rua do Matão, 1371, 05508-090 São Paulo, SP, Brazil
[2]UHasselt, Faculty of Sciences, Theory Lab, Agoralaan, 3590 Diepenbeek, Belgium
[3]Max Planck Institute for the Physics of Complex Systems, 01187 Dresden, Germany
[4]Department of Physics and Astronomy, University of Padova, 35131 Padova, Italy

(Received 19 December 2024; revised 13 May 2025; accepted 29 July 2025; published 4 September 2025)

Spontaneous symmetry breaking occurs in various equilibrium and nonequilibrium systems, where phase transitions are typically marked by a single critical point that separates ordered and disordered regimes. We reveal an innovative phenomenon in which the interplay between different temperatures and driving forces splits the order-disorder transition into two distinct transition points depending on which ordered state initially dominates. Crucially, these two emerging phases have distinct scaling behaviors and thermodynamic properties. To study this, we propose a minimal variant of the Ising model where spins are coupled to two thermal baths and subjected to two opposite driving forces associated with them. Our findings, robust for both all-to-all interactions (where exact solutions are possible) and nearest-neighbor couplings on a square lattice, uncover unique nonequilibrium behaviors and scaling laws for crucial thermodynamic quantities, such as efficiency, dissipation, power and its fluctuations, that are different between the two ordered phases. We also highlight that one of these emerging phases enables heat-engine operations that are less dissipative and show reduced fluctuations. In this setup, the system can also operate near maximum power and maximum efficiency over a wide parameter range. Our results offer unique insights into the relevance of phase transitions under nonequilibrium conditions.

DOI: 10.1103/hzl3-hjnl

Introduction. Phase transitions and universal scaling are central topics in statistical physics, particularly for systems that display collective behavior. Examples can be found across diverse fields, including physics, chemistry, biology, and economics. Many of these systems operate out of equilibrium, where nonzero probability currents and specific symmetries can lead to unique classes of nonequilibrium phase transitions. Similar to their equilibrium counterparts, nonequilibrium phase transitions are often characterized by an order parameter. However, this approach can obscure the irreversible dynamics and its impact on the properties of phase transitions. Increasing attention has been given to entropy production—a key indicator of system dissipation—and related thermodynamic quantities as alternative descriptors of nonequilibrium phase transitions, although many aspects of this topic remain to be understood [1–4].

Beyond phase transitions and universality classes, systems exhibiting collective dynamics are of considerable interest for their potential to enhance the performance of nonequilibrium heat engines, in both classical [5–12] and quantum thermodynamics [10,13,14]. A key subset of collective-engine setups extract work from driving forces, often modeled as biases over specific transitions [5–8,15,16]. These biases arise in diverse systems, such as anomalous mobility in driven active particles [17,18], chemical potentials fueling kinesin motion [19,20], light-activated transitions in photoacids [21], thermodynamic forces in chemical reaction networks [22–24], and ATP-driven pathways in chaperones and molecular transporters [25,26]. Recent studies highlight a distinct phase transition that separates a functional heat-engine regime from a "dud" regime, where the system is purely dissipative [7,8,15,16]. Despite its relevance in biophysics and related fields, the interplay between biased forces and phase transition regimes remains poorly understood and explored only in a few examples.

In this Letter, we demonstrate that collective effects under driving forces yield unique phenomena with no analog in traditional equilibrium or nonequilibrium phase transitions. The uniqueness lies in the combination of the following features: (1) Order-disorder phase transitions occur at separate points depending on which ordered phase initially dominates; (2) each order-disorder phase transition may fall into a different classification, with, for instance, the "down"-spin-dominated phase transition being critical and continuous, while the "up"-spin-dominated transition is discontinuous; and (3) unlike customary "up-down" (Z_2) symmetry-breaking phenomena [2,27], the continuous phase transition we observe exhibits critical exponents that, in the mean-field limit, differ from the classical result of $\beta = 1/2$. Our findings reveal different insights into the properties of the order parameter and uncover unique behaviors of key thermodynamic quantities, such as power and energy dissipation. We further show that the less dissipative ordered phase—characterized by lower power fluctuations—exhibits heat-engine behavior capable of

*Contact author: fiorecarlos.cf@gmail.com

IOP Publishing Journal of Physics A: Mathematical and Theoretical
J. Phys. A: Math. Theor. **57** (2024) 345001 (17pp) https://doi.org/10.1088/1751-8121/ad695e

Thermodynamics of a collisional quantum-dot machine: the role of stages

Fernando S Filho[1,2], C E Fernández Noa[1,2], Carlos E Fiore[1,*], B Wijns[2] and B Cleuren[2]

[1] Institute of Physics of São Paulo University, Rua do Matão, 1371, 05508-090 São Paulo, SP, Brazil
[2] UHasselt, Faculty of Sciences, Theory Lab, Agoralaan, Diepenbeek, 3590, Belgium

E-mail: fiore@if.usp.br

Received 6 December 2023; revised 24 July 2024
Accepted for publication 29 July 2024
Published 9 August 2024

Abstract

Sequential (or collisional) engines have been put forward as an alternative candidate for the realisation of reliable engine setups. Despite this, the role of the different stages and the influence of the intermediate reservoirs is not well understood. We introduce the idea of conveniently adjusting/choosing intermediate reservoirs at engine devices as a strategy for optimizing its performance. This is done by considering a minimal model composed of a quantum-dot machine sequentially exposed to various reservoirs at each stage, and for which thermodynamic quantities (including power and efficiency) can be obtained exactly from the framework of stochastic thermodynamics, irrespective the number of stages. Results show that a significant gain can be obtained by increasing the number of stages and conveniently choosing their parameters.

Keywords: thermodynamics, nonequilibrium engines, stochastic processes, quantum-dot, entropy production

1. Introduction

Stochastic engines are devices that convert a given amount of energy, say heat**,** into work or vice-versa. In contrast to macroscopic engines, they operate at the nanoscale and consequently the relevant thermodynamic quantities are subjected to fluctuations at the microscopic level, above all in power and efficiency. Although an ideal engine is always desired to operate at high

* Author to whom any correspondence should be addressed.

www.uhasselt.be
Hasselt University
Martelarenlaan 42 | BE-3500 Hasselt